EnPress Publisher, LLC

Add: 9650 Telstar Avenue, Unit A, Suite 121, El Monte, CA 91731, USA.
Email: editorial_jgc@enpress-publisher.com

2024
Volume 7
Issue 2
ISSN: 2578-1979(Online)

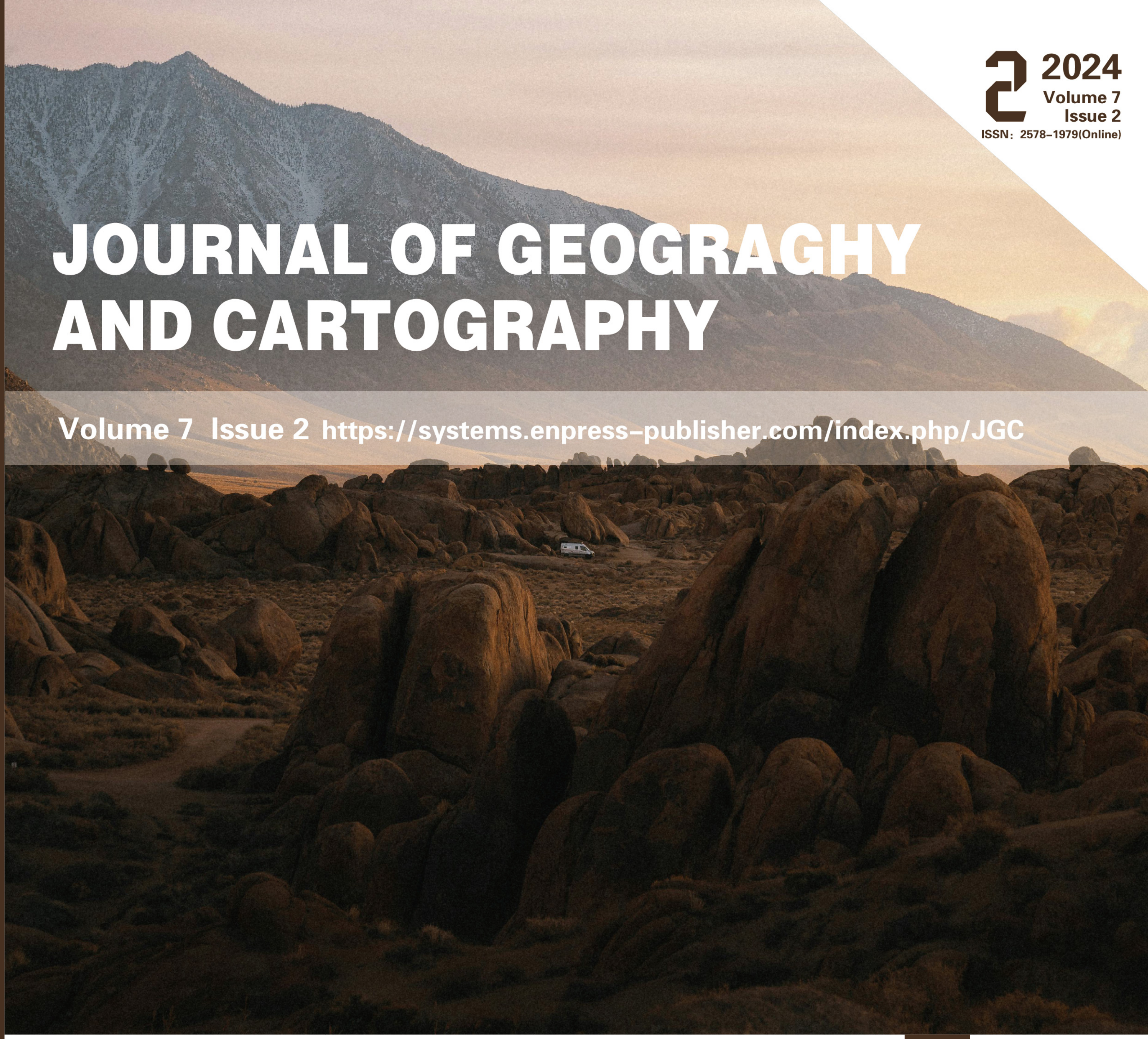

JOURNAL OF GEOGRAPHY AND CARTOGRAPHY

Volume 7 Issue 2 https://systems.enpress-publisher.com/index.php/JGC

JGC

ISSN 2578-1979
9 772578 197079 02

Ionut Cristi Nicu
Norsk Institutt for Kulturminneforskning (NIKU) | Flinders University
Norway

Pravat Kumar Shit
Vidyasagar University
India

Gouri Sankar Bhunia
Aarvee Associates Architects Engineers & Consultants Pvt Ltd.
India

Volume 7 Issue 2 • 2024

Journal of Geography and Cartography

EnPress Publisher

EnPress Publisher

2024 | Volume 7 | Issue 2

Journal of Geography and Cartography

https://systems.enpress-publisher.com/index.php/JGC

Contents

Articles

Review

*Journal of Geography and Cartography*2024, 7(2), 6400.
https://doi.org/10.24294/jgc.v7i2.6400

Article

Integrating in-situ hydraulic conductivity measurements and vertical electrical sounding for groundwater exploration in fractured shales within Alex Ekwueme Federal University Ndufu Alike (AE-FUNAI), South Eastern Nigeria

Amobi Ekwe*, Samuel Ekeoma, Georgebest Azuoko, Ayatu Usman, Omonona Victor, Ndidiamaka Eluwa

Department of Geology/Geophysics, Alex Ekwueme Federal University Ndufu Alike, P.M.B. 1010, Abakaliki 480242, Nigeria
*** Corresponding author:** Amobi Ekwe, amobiekwe@yahoo.com

CITATION

Ekwe A, Ekeoma S, Azuoko G, et al. Integrating in-situ hydraulic conductivity measurements and vertical electrical sounding for groundwater exploration in fractured shales within Alex Ekwueme Federal University Ndufu Alike (AE-FUNAI), South Eastern Nigeria. Journal of Geography and Cartography. 2024; 7(2): 6400. https://doi.org/10.24294/jgc.v7i2.6400

ARTICLE INFO

Received: 14 May 2024
Accepted: 19 June 2024
Available online: 19 July 2024

Abstract: An appraisal of the groundwater potential of Alex Ekwueme Federal University Ndufu Alike was carried out by integrating datasets from geology, geographic information system and electrical resistivity survey of the area. The study area is underlain by the Asu River group of Albian age. The Asu River Group in the Southern Benue Trough comprises of Shales, Limestones and Sandstone lenses of the Abakaliki Formation in Abakaliki and Ikwo areas. The shales are generally weathered, fissile, thinly laminated and highly fractured and varies between greyish brown to pinkish red in colour. Twenty (20) Vertical Electrical Sounding data were acquired using SAS 1000 ABEM Terrameter and processed to obtain layer parameters for the study area. A maximum current electrode spacing (AB) of 300 meters was used for data acquisition. Computer aided iterative modelling using IPI2 Win was used to determine layer parameters. In-situ Hydraulic Conductivity measurements at seven parametric locations within the study area were conducted and integrated with Electrical Resistivity measurements to determine aquifer parameters (e.g., Hydraulic conductivity and Transmissivity) in real time. This technique reduces the attendant huge costs associated with pumping tests and timelines required to carry out the technique. Accurate delineation of aquifer parameters and geometries will aid water resource planners and developers on favourable areas to site boreholes in the area. Several correlative cross-sections were generated from the interpreted results and used to assess the groundwater potential of the study area. Results show that the resistivity of the the aquifer ranges from 7.3 Ωm–530 Ωm while depth to water ranges from 11.4 m to 55.3 m. Aquifer thicknesses range from 8.7 m at VES 5 to 36.3 m at VES 6 locations. Hydraulic conductivity ranges from 1.55 m/day at VES 15.18, and 19 locations to 9.8 m/day at VES 3 and 4 locations respectively. Transmissivity varies from 17.48 m^2/day at VES 19 to 98 m^2/day at VES 3 locations respectively. Areas with relatively high transmissivities coupled with good aquifer thicknesses should be the target of water resource planners and developers when proposing sites for drilling productive boreholes within Alex Ekwueme federal University Ndufu Alike.

Keywords: groundwater; shale; hydraulic conductivity; transmissivity; VES

1. Introduction

Shales are portrayed as aquitards on hydrogeology maps and often ignored as a veritable source of water supply to rural, semi urban and urban communities whose geology does not include conventional aquifer materials like Sandstones and Carbonates [1]. Previous research works have shown that 70 million or more people in sub-saharan Africa live in semi-urban and rural communities underlain by low permeability formations like Shales and Mudstones [2–4]. Some of these rural communities can be found in Ikwo Local Government Area of Ebonyi state, Nigeria, where Alex Ekwueme Federal University Ndufu Alike is located. The area has continued to witness huge influx of both staff, students, entrepreneurs and artisans as a result of the establishment of the University since 2011. Alex Ekwueme Federal University Ndufu Alike and environs is underlain by the Asu River Shales; a Cretaceous Formation of Albian age, deposited within the Southern Benue Trough. Shales in their natural form cannot transmit water effectively but their transimissivity can be enhanced when the Shales are fractured. Fractured Shales can deliver substantial amount of water that can serve a rural community for domestic and Agricultural purposes. Several researchers applied electrical resistivity method to delineate aquifer types and geometry [5–8]. Some more recent works have been done by utilizing geosounding datasets to explore for water in low permeability formations (e.g. Shales and Mudstones) and hard rock terrains [9–11]. In Nigeria, a significant proportion of residents in rural areas lack reliable access to safe water sources. The quality of groundwater holds equal significance to its availability. The drive to grant access to potable water supply and the need to eradicate Guinea worm scourge(Dracunculus medinensis) in some of these rural communities propelled the Jimmy Carter Foundation, through collaboration with United Nations International Children Education Fund (UNICEF) and World Health Organization (WHO) to sink several boreholes to provide water to the rural populace [12]. Nigeria is faced with increasing demands for water resources due to high population growth rate and growing prosperity [13]. The advantages of groundwater as a source of supply cannot be overemphasized especially where populations are still largely rural and demand are dispersed over large areas [14]. Groundwater is a dependable and assured resource and can be exploited with greater ease and flexibility. The southern Benue trough is the southwestern part of the Benue depression [15]. It is distinctively characterized by the Abakaliki anticlinorium and the Afikpo syncline and bounded to the west by Anambra basin [16]. The major part of the Ikwo metropolis is underlain by aquicludes and aquitards, except in locations or zones where secondary aquiferous conditions were made possible by syn- and post depositional circumstances [17]. The resistivity of the subsurface material observed is a function of the magnitude of the current, the recorded potential difference and the geometry of the electrode array used [18]. Measurement of resistivity is, in general, a measure of water saturation and pore space connectivity. Resistivity measurements are associated with varying depths relative to the distance between the current and potential electrodes in the survey and can be interpreted qualitatively and quantitatively in terms of a lithologic and/or geohydrologic model of the subsurface [19]. The form of resistivity curve type obtained by sounding over a horizontally stratified medium is a function of the resistivities and thicknesses of the layers as well as the electrode configuration [20]. The objective of this study was to integrate in-situ Hydraulic conductivity measurements with results from the interpretation of electrical resistivity data to map fractures in Shales with the aim of determining favourable sites to drill boreholes within Alex Ekwueme Federal University Ndufu Alike and environs.

2. Location and geology

The study area is underlain by the Asu River Group shales of Albian age [21] and lies between latitude 6°7'10" to 6°8'10"N and 8°8'0 ' to 8°9'0"E (**Figure 1**).

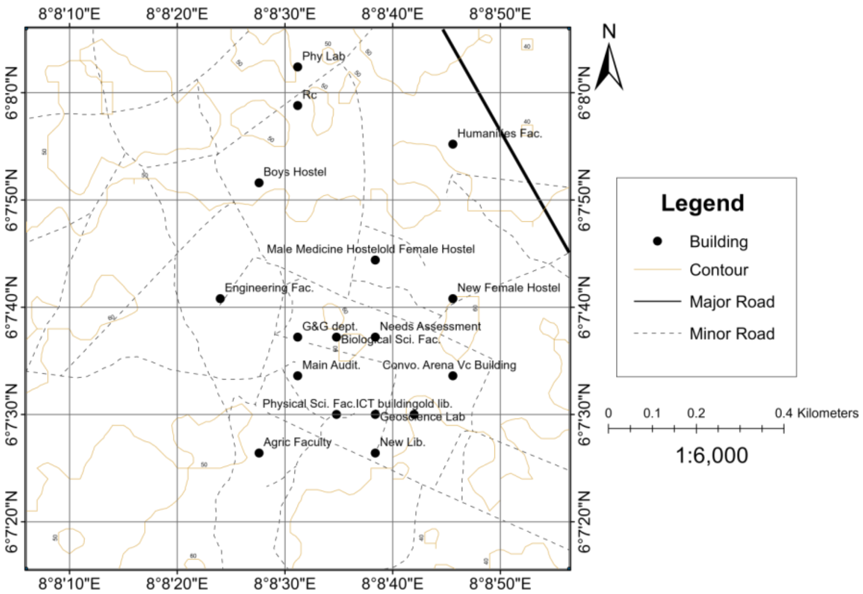

Figure 1. Topographic map of AE-FUNAI.

The Asu River Group (**Figure 2**) sediments are predominantly shales, and localized occurrences of sandstone, siltstone and limestone intercalations [22]. It was generally believed to have started depositing in the mid-Albian period and continued within the Southern Benue Trough, southeastern Nigeria. Emplaced within the Asu River Group sediments are intermediateto basic intrusive diorites and dolerites and pyroclastics [22–24]. The group has average thickness of about 2000 m and rests unconformably on the Precambrian Basement [25,26] have reported type localities of Asu River sediments at Abakaliki, and Ishiagu areas.

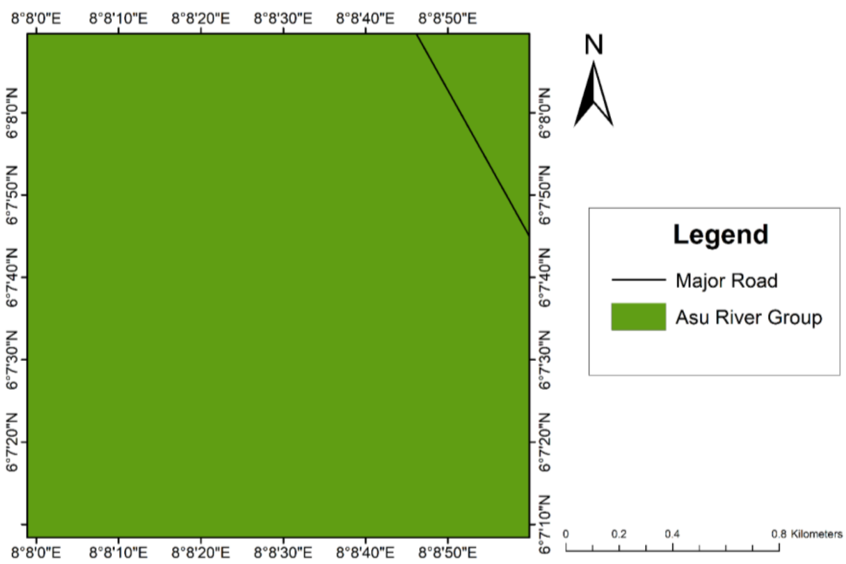

Figure 2. Geologic map of AE-FUNAI.

3. Materials and methods

The equipments/materials used for the present research include ABEM Terrameter, two current electrodes, two potential electrodes, 4 reels of wire,12V battery, GPS, common salt, measuring tape, hammer, Hand Auger, laptop, Jerry cans of water and measuring tape. The study started with a detailed literature review of past research works in the area and related studies in other areas with similar geology. This was followed by detailed geological studies of the study area. Subsequently, twenty (20) vertical electrical soundings (VES) were acquired using an ABEM SAS 1000 Terrameter with the Schlumberger configuration (**Figure 3**) and a maximum current electrode spacing (AB) of 200 meters. The Schlumberger technique involves the injection of direct current or low frequency alternating current into the earth through a pair of current electrodes and the measurement of the potential difference between another pair of potential electrodes. The method was adopted because it allows the acquisition of numerous data points within a short time. The Schlumberger technique allows a clearer mapping of the subsurface for a given current electrode spacing and the processing and interpretation softwares are readily available. Few soundings were taken near existing boreholes to facilitate comparison between the geologic and geoelectric sections. The data obtained was plotted as a graph of apparent resistivity against half current electrode spacing on a log-log graph sheet to provide insights into the layer resistivities and depths to the interfaces.

The apparent resistivity (ρ_a) for the Schlumberger array is given by

$$\rho = \pi[\frac{a^2}{b} - \frac{b}{4}]$$

$$\mathrm{K} = \sum \frac{2\pi}{(^1/_a)-(^b/_2)-(^1/_a)+(^b/_2)-(^1/_2)+(^b/_2)+(^1/_a)-(^b/_2)} \tag{1}$$

$$\mathrm{K} = \pi(\frac{a^2}{b} - \frac{b}{4}) = \{\frac{\left(\frac{AB}{2}\right)^2 - \left(\frac{MN}{2}\right)^2}{MN}\}\pi \tag{2}$$

$$\mathrm{K} = \pi\left(\frac{a^2}{b} - \frac{b}{4}\right)\frac{V}{1} or \rho = \pi\left(\frac{a^2}{b} - \frac{b}{4}\right)R \tag{3}$$

Recall $\rho = KR$

where K = Geometric factor which depends on the electrode configuration and R= measured resistance.

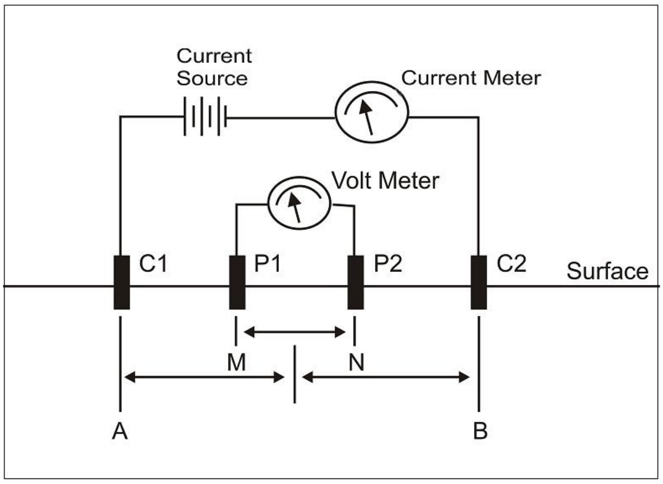

Figure 3. Schematic of the schlumberger array.

3.1. Estimation of aquifer parameters

Hydraulic conductivity and transmissivity are useful aquifer parameters for proper development and management of groundwater resources. Direct determination of hydraulic conductivity from field measurements has proven to be a cost effective technique for the estimation of transmissivity by utilizing the empirical relationship between transmissivity (m^2/day), hydraulic conductivity (m/day) and aquifer thickness (m). We measured hydraulic conductivity in the field by substituting several other field parameters into the well known Darcy's equation and used the calculated value to determine transmissivity in areas with known aquifer thickness.

3.2. Hydraulic conductivity

Hydraulic conductivity,*K* is used to describe the capacity of a porous material to transmit water [27]. Without hydraulic conductivity data, neither simple analytical solutions nor complex computer simulations of groundwater flow are possible.

Darcy formula for hydraulic conductivity (*K*) is given by

$$K = \frac{QL \times \mu L \times 1000}{A(P2-P1)} \tag{4}$$

where *K* = Hydraulic conductivity.

QL = flow rate = $\frac{\text{height of water (h)}}{\text{time of water to dry}}$ = (m/s)

μ_L = Viscosity of water (Centipose)

A = Cross–sectional (M^2) = $2\pi r^2 + 2\pi h$

L = Height of section

H = height of water

P_2 = Atmospheric Pressure (known)

P_1 = pressure of water (unknown)

$P_2 - P_1 = \Delta P \wp \Delta h$

$P_2 - P_1 = Patm - P_w = \wp \Delta h$

3.3. Determination of hydraulic conductivity in the field

Hydraulic conductivity, often denoted by the symbol *K*, is a property of porous materials like soil and rock that describes how easily a fluid (usually water) can move through the pore spaces or fractures within the material. A total of seven (7) hydraulic conductivity values were obtained in the field at the various VES locations. Field measurements of hydraulic conductivity were obtained using a simple infiltration test (**Figure 4**). A borehole was created, and three liters of water were poured in. The following parameters were monitored: water level change (height), borehole dimensions (diameter and radius), and time taken for water to infiltrate. Darcy's equation was then used to calculate hydraulic conductivity values at various locations across the study area. The above technique is very challenging because of the geology of the study area which comprises of shales and other low permeability rocks. The low permeability in shales dovetails to longer time for the water poured in the drill holes to drain and this translated to longer waiting time of up to 2 to 3 hours in the field.

Figure 4. In-situ hydraulic conductivity measurement in the field.

3.4. Transmissivity

Transmissivity describes the rate at which water can be transmitted horizontally through an aquifer. (a) water-bearing layer of soil or rock. Transmissivity (T) is calculated by multiplying the average hydraulic conductivity (K) of the aquifer by the thickness. (b) of the saturated zone.

Mathematically, $T = K \times b$.

Where T is the transmissivity (m^2/day), K is the Hydraulic conductivity and b is the aquifer thickness (m).

4. Results and discussion

Figure 5 shows the VES locations superimposed on the geologic map of the area while **Figure 6** shows the lithology log of the borehole at the Male hostel (close to VES 15), Alex Ekwueme Federal University Ndufu Alike. The lithologic succession comprises of top lateritic overburden, Dry clay, Gray shale, Partially fractured shale, fractured Shale section which serves as the aquifer and a non-fractured shale section of indeterminate thickness. **Figure 7** shows sample type curves from the study area. The fractured shale aquifer sections were discriminated from other sections in the curve by their characteristic low resistivities due to fluid filled fractures in secondary porosities.

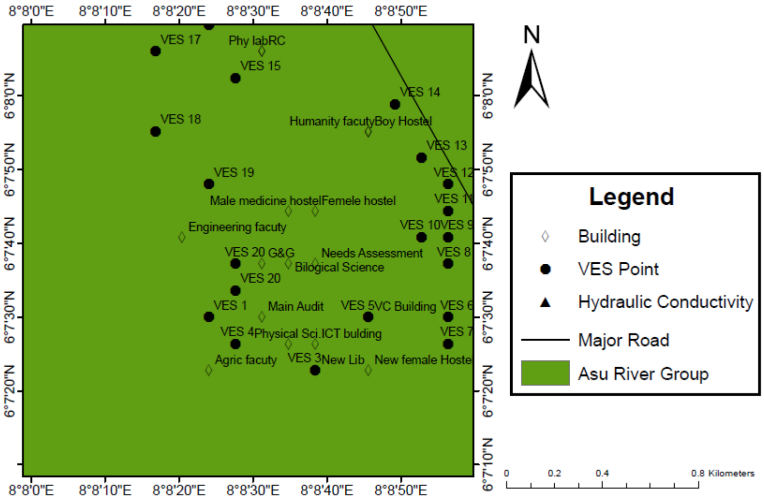

Figure 5. Geologic map of the study area showing the VES points.

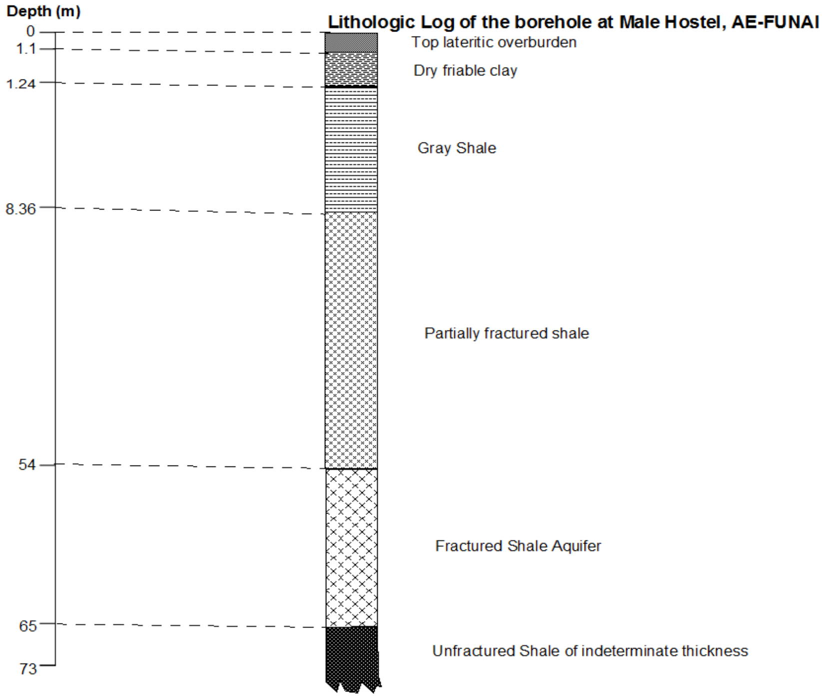

Figure 6. Lithology log of the borehole at the male hostel, AEFUNAI.

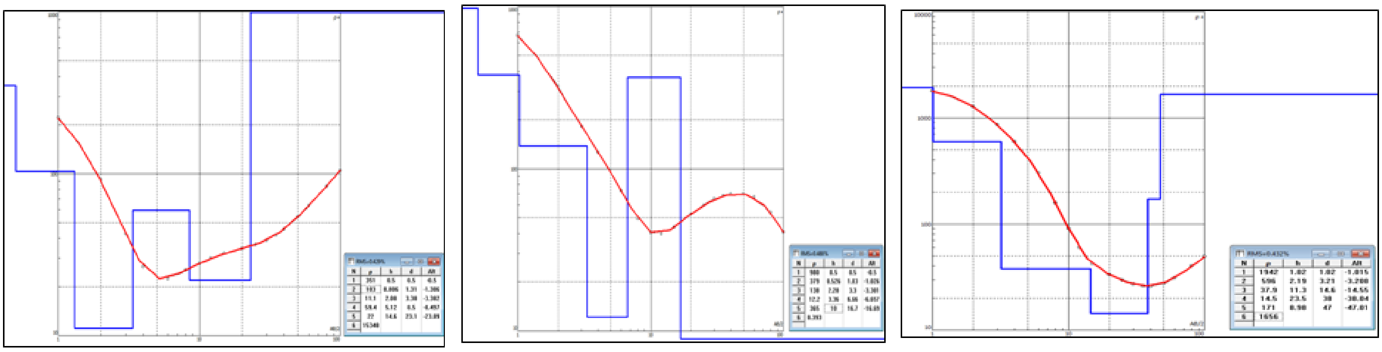

Figure 7. Sample curve types obtained from the study area.

4.1. Hydraulic conductivity

Table 1 shows in-situ hydraulic conductivity values obtained from measurements in the field while **Table 2** shows the derived Hydraulic conductivity values across the study area. Hydraulic conductivity values range from 1.546560 m/day at location 5 to 9.800300 m/day with variations across the vertical electrical sounding (VES) locations. The variations in measured hydraulic conductivity values was attributed to presence of fractures, weathering and mineralogy. The entire study area was sub-divided into three zones (A,B and C) with Hydraulic Conductivity varying from 7.5 to 9.8 m/day in Zone A; 4.5–7.5 m/day in Zone B and 1–4.5 m^2/day respectively (**Figure 8**).

Table 1. In-situ hydraulic conductivity (HC) values obtained in the field.

In-situ HC locations/Proximal VES points	Depth of hole (m)	Diameter (m)	Radius (m)	Height of water (m)	Drainage time (sec.)	Hydraulic conductivity (m/s)	Hydraulic conductivity (m/day)
1 (VES 2)	0.50	0.152	0.076	0.30	7200	2.5884×10^{-5}	2.236277
2 (VES 4)	0.60	0.177	0.088	0.35	10800	11.343×10^{-5}	9.800300
3 (VES 7)	0.70	0.160	0.080	0.50	7200	2.541×10^{-5}	2.195424
4 (VES 10)	0.90	0.203	0.101	0.65	5400	2.68×10^{-5}	2.315520
5 (VES 15)	0.70	0.152	0.072	0.50	10800	1.79×10^{-5}	1.546560
6 (VES 17)	0.50	0.120	0.060	0.30	7200	3.368×10^{-5}	2.909954
7 (VES 20)	0.70	0.127	0.064	0.50	10800	3.2432×10^{-5}	2.802120

Table 2. Hydraulic conductivity (HC) values across the study area.

VES points	In-situ HC values (m/day)	Aquifer Resistivity (m)	Aquifer Thickness (m)	Hydraulic conductivity (HC) values at other VES locations (m/day)
1	-	171.00	8.98	2.24
2	2.236	17.70	30.10	2.24
3	-	365.00	10.00	9.80
4	9.800	4.54	8.75	9.80
5	-	59.70	8.70	2.20
6	-	42.30	36.30	2.20
7	2.195	43.80	23.60	2.20
8	-	530.00	11.30	2.20
9	-	16.50	15.00	2.32
10	2.316	10.60	9.57	2.32
11	-	374.00	17.40	2.32
12	-	7.55	12.60	2.80
13	2.802	22.00	14.60	2.80
14	-	41.50	45.60	2.80
15	1.547	85.10	38.10	1.55
16	-	9.60	8.66	2.91
17	2.910	7.30	12.00	2.91
18	-	57.10	14.10	1.55
19	-	8.80	11.30	1.55
20	-	12.80	16.20	2.24

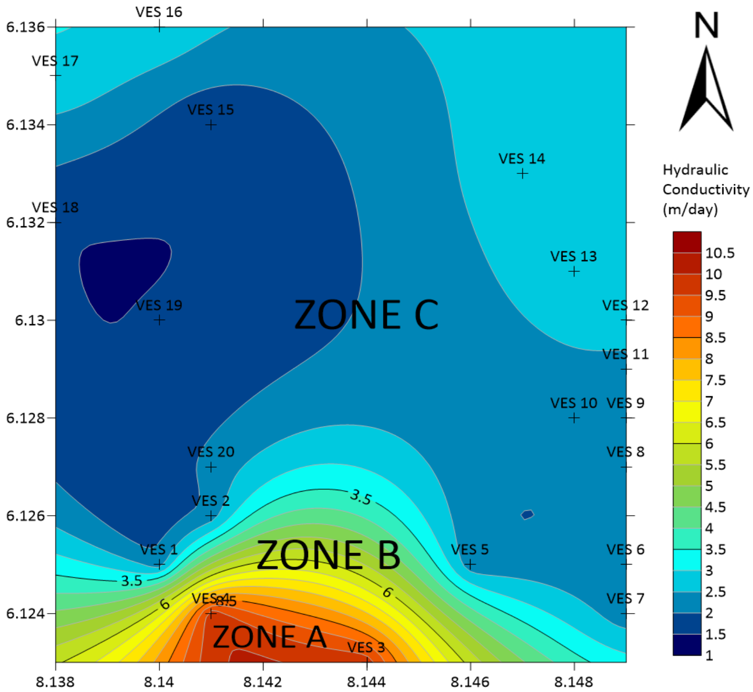

Figure 8. Hydraulic conductivity values across the study area.

4.2. Aquifer thickness across the study area

The thickness of the aquifer in the study area exhibits significant variability, which can be attributed to a combination of geological factors and human activities, particularly construction activities within the campus vicinity. The aquifer thickness ranges from high in certain areas to extremely low in others, reflecting the complex hydrogeological conditions that influence groundwater distribution. Aquifer thickness ranges from 8.66 m at VES 5 to 45.60 m at VES 14 locations respectively (**Figure 9**).

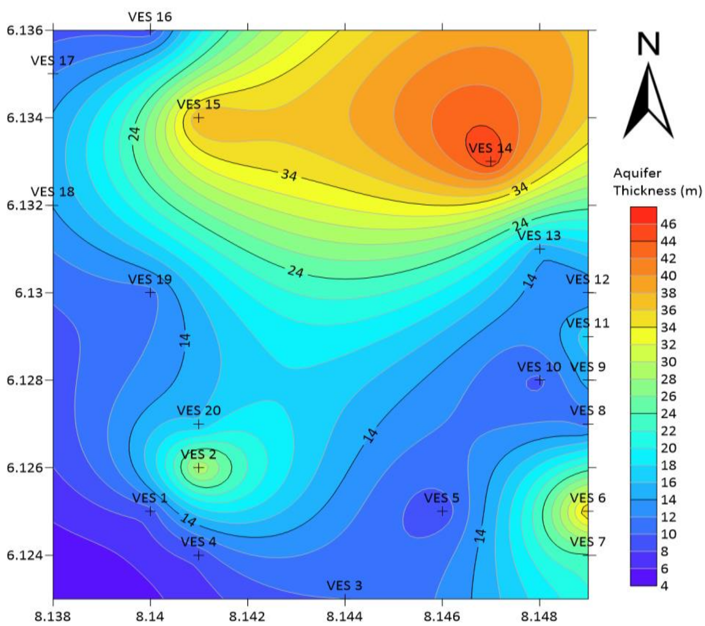

Figure 9. Aquifer thickness across the study area.

4.3. Depth to water table

Figure 10 shows the variation of depth to the fractured shale aquifers across the study area. Depth to water ranges from 11.4 m at Convocation arena (VES 5) to 55.3m at staff quarters. The variation in depths to the aquifer is geologically controlled. The area was affected by the Santonian tectonic activities which initiated fracturing in the shales at various depths. The shallow aquifers could be tapped by hand dug wells while the moderate and deeper aquifers would require borehole drilling in order to harness the water resouces.

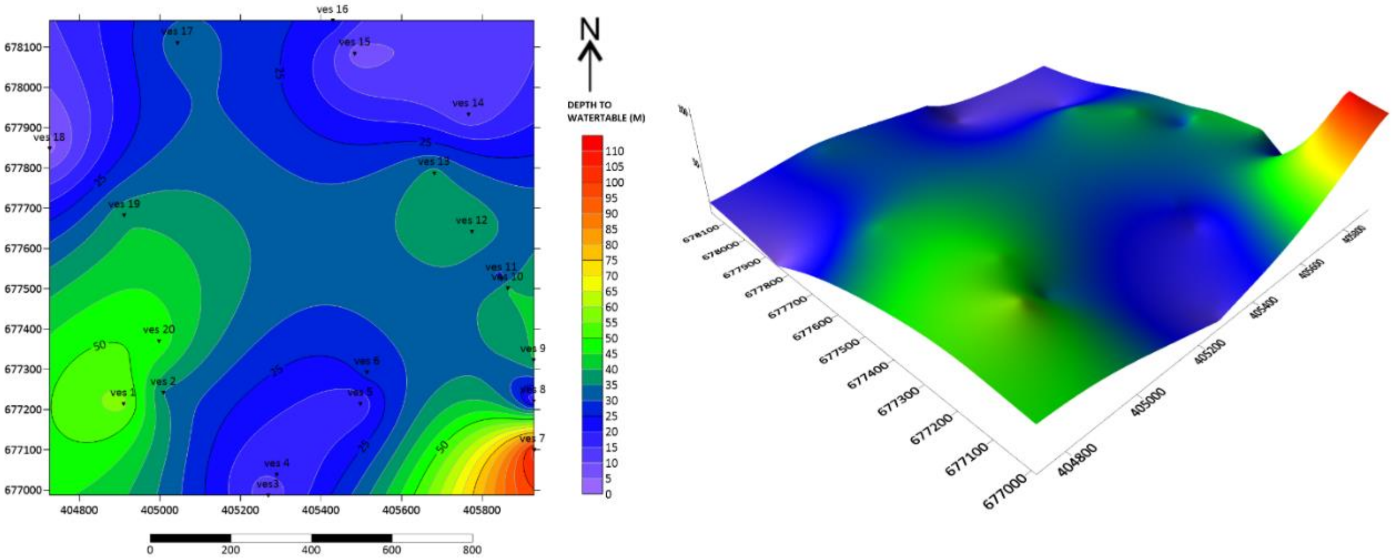

Figure 10. Depth to water across the study area.

4.4. Transmissivity

Table 3 shows the derived Transmissivity values across the study area. Transmissivity values range from 7.48 m^2/day at VES 19 location to 127.78 m^2/day at VES 14 respectively. **Figure 11** shows the variations of Transmissivity values across the study area with Zone A ranging from 90–130 m^2/day (high Transmissivity). Transmissivity values across Zone B ranges from 45–90 m^2/day (Moderate Transmissivity) while Zone C ranges from 10–45 m^2/day (Low Transmissivity). The transmissivity values are largely determined by the development of fractures in the shales due to tectonism and other secondary geologic processes. These results are consistent with earlier results from groundwater studies in low permeability formations [6,4,28].

Table 3. Transmissivity values across the study area.

VES points	In-situ HC values (m/day)	Aquifer Resistivity (m)	Aquifer Thickness (m)	Hydraulic conductivity (HC) values at other VES locations (m/day)	Transmissivity (m^2/day)
1	-	171.00	8.98	2.24	20.08
2	2.236	17.70	30.10	2.24	67.31
3	-	365.00	10.00	9.80	98.00
4	9.800	4.54	8.75	9.80	85.75
5	-	59.70	8.70	2.20	19.10

Table 3. (*Continued*).

VES points	In-situ HC values (m/day)	Aquifer Resistivity (m)	Aquifer Thickness (m)	Hydraulic conductivity (HC) values at other VES locations (m/day)	Transmissivity (m^2/day)
6	-	42.30	36.30	2.20	79.69
7	2.195	43.80	23.60	2.20	51.81
8	-	530.00	11.30	2.20	24.81
9	-	16.50	15.00	2.32	34.73
10	2.316	10.60	9.57	2.32	22.16
11	-	374.00	17.40	2.32	40.29
12	-	7.55	12.60	2.80	35.31
13	2.802	22.00	14.60	2.80	40.91
14	-	41.50	45.60	2.80	127.78
15	1.547	85.10	38.10	1.55	58.92
16	-	9.60	8.66	2.91	25.20
17	2.910	7.30	12.00	2.91	34.92
18	-	57.10	14.10	1.55	21.81
19	-	8.80	11.30	1.55	17.48
20	-	12.80	16.20	2.24	36.23

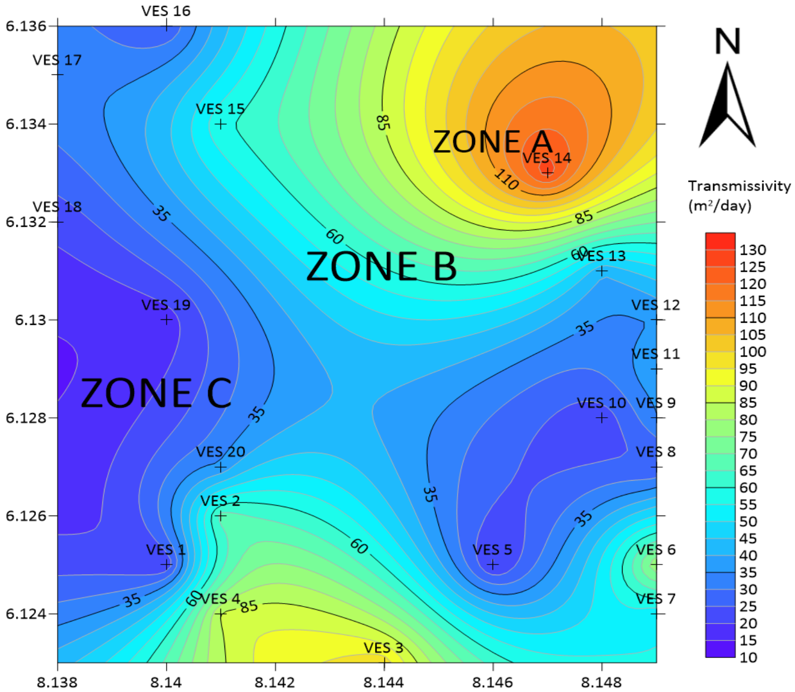

Figure 11. Transmissivity values across the study area.

5. Conclusion

The electrical resistivity method has proved to be a veritable technique in groundwater assessment within Alex Ekwueme Federal University Ndufu Alike; an area underlain by Shales of Albian age. The development of factures in the shales as a result of secondary tectonic activities improved the water storage capacity and transmissivity in shales, which ordinarily would have been considered an aquitard.

The fluid filled fractures created the required contrast which the electrical resistivity method responds to by their characteristically low to moderate resistivity values when compared with the non-fractured sections in the Shales. The resistivity of the fractured sections of the shales, which serves as the aquifer ranges from 7.3–530 Ωm while depth to water ranges from 11.4 m to 55.3 m. Aquifer thicknesses range from 8.7 m at VES 5 to 36.3 m at VES 6 locations. Hydraulic conductivity ranges from 1.55 m/day at VES 15.18, and 19 locations to 9.8 m/day at VES 3 and 4 locations respectively. Transmissivity varies from 17.48 m^2/day at VES 19 to 98 m^2/day at VES 3 locations respectively. It is therefore recommended that any water drilling scheme within the area should be preceded by detailed geophysical investigation to ensure prolific borehole within the campus. Areas with relatively high transmissivities coupled with good aquifer thicknesses should be the target of water resource planners and developers when proposing sites for drilling productive boreholes within Alex Ekwueme federal University Ndufu Alike.

Author contributions: Conceptualization, AE; methodology, AE, SE, VO and GA; software, SE and AE; validation, AU, NdidiamakaEluwa, VO and AE; formal analysis, SE, AE and AU; investigation, NE, VO and SE; resources, AE and GA; data curation, VO and AU; writing—original draft preparation, AE and SE; writing—review and editing, SE and GA; visualization, AE and NdidiamakaEluwa; supervision, AE; project administration, AE and GA; funding acquisition, AE, GA and AU. All authors have read and agreed to the published version of the manuscript.

Conflict of interest: The authors declare no conflict of interest.

References

1. Struckmeier WF, Margat, J. Hydrogeological Maps—A guide and a Standard Legend. International Association of Hydrogeologists (IAH). 1995; 17: 177.
2. MacDonald AM, DaviesJ. A brief review of groundwater for rural water supply in sub-Saharan Africa. British Geological Survey Technical Report 2000; WC/00/33.
3. MacDonald AM, Davies J, Peart RJ. Geophysical methods for locating groundwater in low permeability sedimentary rocks: Examples from southeast Nigeria. Journal of African Earth Sciences. 2001; 32: 115–131. doi: 10.1016/S0899-5362(01)90022-3
4. Neuzil CE. Groundwater Flow in Low-Permeability Environments. Water Resources Research. 1986; 22(8): 1163–1195. doi: 10.1029/wr022i008p01163
5. Onuoha KM, Mbazi FCC. Aquifer Transmissivity from Electrical Sounding Data. The Case of Ajali Sandstone Aquifers, South-West of Enugu. In: Ofoegbu CO (editor). Ground Water and Mineral Resources of Nigeria, Fried-vieweg and Sohn,Wiesbaden. 1988. pp. 17–29.
6. Ekwe AC, Onu NN, Onuoha KM. Estimation of aquifer hydraulic characteristics from electrical sounding data: The case of middle Imo River basin aquifers, southeastern Nigeria. Journal Spatial Hydrology. 2006; 6(2): 121–132.
7. Ekwe AC, Opara AI. Aquifer transmissivity from surface geo-electrical data: A case study of owerri and environs, southeastern Nigeria. Journal of the Geological Society of India. 2012; 80(1): 123–128. doi: 10.1007/s12594-012-0126-8
8. Opara AI, Onu NN, Okereafor DU. Geophysical Sounding for the Determination of Aquifer Hydraulic Characteristics from Dar- Zarrouk Parameters: Case study of Ngor Okpala, Imo River Basin, Southeastern Nigeria. Pacific Journal of Science and Technology. 2012; 13(1): 590–603.
9. Ekwe AC, Nnodu IN, Ugwumbah KI et al.. Estimation of Aquifer Hydraulic Characteristics of Low Permeability Formations from Geosounding Data: A case study of Oduma Town, Enugu State; Online Journal of Earth Sciences 2010; 4(1): 19-26. doi: 10.3923/ojesci.2010.19.26

10. Maxwell O, Ejike EJ,Ugwuoke PE. Geophysical Analysis of Basement Terrain Groundwater Using Vertical Electrical Sounding: A Case Study of Parts of Abuja North Central Nigeria. International Journal of Geophysics and Geochemistry. 2015; 2(4): 92–97.
11. Loke MH, Chambers JE, Rucker DF, et al. Recent developments in the direct-current geoelectrical imaging method. Journal of Applied Geophysics. 2013; 95: 135–156. doi: 10.1016/j.jappgeo.2013.02.017
12. Ekwe AC, Onuoha MK, Ugodulunwa FXO. Prospecting for groundwater in low permeability formations using the electrical resistivity method: The case of Ikwo and environs, southeastern Nigeria. International Workshop and Gravity, Electrical & Magnetic Methods and their Applications, Chenghu, China. 2015; 19–22.doi: 10.1190/gem2015-127.
13. Nwankwoala HO. An integrated approach to sustainable groundwater development and management in Nigeria. Journal of geology and mining research. 2011; 3(5): 123–130.
14. Nwankwoala HNL. Causes of Climate and Environmental Changes: The Need for Environmental-Friendly Education Policy in Nigeria. Journal of Education and Practice. 2015; 6(30): 224–234.
15. Ekwok SE, Akpan AE, Ebong ED, et al. Assessment of depth to magnetic sources using high resolution aeromagnetic data of some parts of the Lower Benue Trough and adjoining areas, Southeast Nigeria. Advances in Space Research. 2021; 67(7): 2104–2119. doi: 10.1016/j.asr.2021.01.007
16. Okolo GC, Emedo OC, Obumselu AC, et al. Lithofacies, particle size analysis and paleodepositional environment of the Eze-Aku Group (Cenomanian–Turonian) in the Itigidi-Ediba area, Afikpo Synclinorium, southeastern Nigeria. Journal of Sedimentary Environments. 2020; 5(4): 375–398. doi: 10.1007/s43217-020-00012-9
17. Okogbue CO, Aghamelu OP. Performance of pyroclastic rocks from Abakaliki Metropolis (southeastern Nigeria) in road construction projects. Bulletin of Engineering Geology and the Environment. 2013; 72(3–4): 433–446. doi: 10.1007/s10064-013-0489-0
18. Okpoli CC. Sensitivity and Resolution Capacity of Electrode Configurations. International Journal of Geophysics. 2013; 2013: 1–12. doi: 10.1155/2013/608037
19. Amadi AN, Olasehinde PI, Okosun EA, Yisa J. Assessment of the water quality index of Otamiri and Oramiriukwa Rivers. Physics International 2010; 1(2): 102-109.
20. A. Zohdy, “Application of Surface Geophysical (Elec- trical Methods to Groundwater Investigations),” Techni- ques of Water Resources Investigations of the United States Geological Survey, 1976, pp. 5-55.
21. Reyment RA. Aspects of the geology of Nigeria: the stratigraphy of the Cretaceous and Cenozoic deposits.Ibadan University Press; 1965. p. 133.
22. Ofoegbu CO, Amajor LC. A geochemical comparison of the pyroclastic rocks from Abakaliki and Ezillo, southeastern Benue Trough. J. Min. Geol. 1987; 23(1–2): 45–51.
23. Murat RC. Stratigraphy and paleogeography of the Cretaceous and Lower Tertiary in Southern Nigeria. African geology. 1972; 1(1): 251–266.
24. Nwachukwu SO. The tectonic evolution of the southern portion of the Benue Trough, Nigeria. Geological Magazine. 1972; 109(5): 411–419. doi: 10.1017/s0016756800039790
25. Benkhelil J. The origin and evolution of the Cretaceous Benue Trough (Nigeria). Journal of African Earth Sciences (and the Middle East). 1989; 8(2–4): 251–282. doi: 10.1016/S0899-5362(89)80028-4
26. Adejuwon BB, Obasi IA, Salami AA. Integrated geophysical study for mapping Pb–Zn sulfide deposits in Asu River Group shales in Nkpuma-Ekwoku, Abakaliki area, southeastern Nigeria. Arabian Journal of Geosciences. 2021; 14(14). doi: 10.1007/s12517-021-07770-4
27. Wang W, Zhao K, Zhang P, et al. Investigation of water ingress into uncracked and cracked cement-based materials using electrical capacitance volume tomography. Materials & Design. 2022; 220: 110877. doi: 10.1016/j.matdes.2022.110877
28. Oli IC, Opara AI, Okeke OC, et al. Evaluation of aquifer hydraulic conductivity and transmissivity of Ezza/Ikwo area, Southeastern Nigeria, using pumping test and surficial resistivity techniques. Environmental Monitoring and Assessment. 2022; 194(10). doi: 10.1007/s10661-022-10341-z

Journal of Geography and Cartography 2024, 7(2), 6588.
https://doi.org/10.24294/jgc.v7i2.6588

Article

A perennial controversy: The St. Peter Sandstone of the American Midwest

Greg Brick

Earth & Environmental Sciences Department, University of Minnesota, Minneapolis, MN 55455, USA; bric0004@umn.edu

CITATION

Brick G. A perennial controversy: The St. Peter Sandstone of the American Midwest. Journal of Geography and Cartography. 2024; 7(2): 6588.
https://doi.org/10.24294/jgc.v7i2.6588

ARTICLE INFO

Received: 24 May 2024
Accepted: 12 July 2024
Available online: 1 August 2024

Abstract: The St. Peter Sandstone of the American Midwest is presented today in textbooks as a simple and unproblematic example of "layer-cake geology." The thesis of this paper is that the very simplicity of St. Peter Sandstone has made it challenging to characterize. In widely separated states, the sandstone appeared under different names. Several theories about how it formed began to circulate. The story of the St. Peter is not only the story of the assemblage of a stratigraphic unit over a vast area during three centuries, but also the role the study of the provenance of this unit played in the development of sedimentology in the early twentieth century, research that was made all the more challenging by its "simple" mineralogy. Indeed, the St. Peter has been controversial since it was first described.

Keywords: St. Peter Sandstone; quartz arenite; Minnesota; Neptunism; Abraham Gottlob Werner; sedimentology; particle size analysis

1. Introduction

The St. Peter Sandstone of the American Midwest is presented today in textbooks as a simple and unproblematic example of "layer-cake geology." A largely horizontal formation of variable thickness, but averaging 30 m, this cratonic sheet sand underlies 585,000 square km in thirteen states. A brief lithological description is appropriate. The formation has been divided into various members according to the geological survey of the state concerned. In the state of Minnesota, locality of the St. Peter type section, the upper Tonti Member is the one usually exposed in cliff faces. The sandstone is fine to medium-grained, well sorted, and poorly cemented. The beds are internally structureless, with occasional cross-stratification. The lower, Pigs Eye Member, is less often exposed in outcrop [1]. The current consensus is that the sandstone was deposited in the nearshore of a shallow, transgressing epicontinental sea during Ordovician times, 450 million years ago, presenting a combination of eolian, fluvial, and marine characteristics [2]. It was the last great period of quartz deposition on the vegetation-free craton during the Paleozoic.

Its mineralogy, too, is usually presented as simple and unproblematic. Over much of the region, the sandstone is more than 99% quartz and dazzling white in outcrop. Its lack of cementation leads to its pronounced friability, or readiness to crumble, which led to it being compared to loaf sugar in the early days. Its most important economic uses have included glass manufacture, as an ingredient of mortars, and for foundry molds [3]. In various places, it also serves as an aquifer, a natural gas reservoir, and most recently, for carbon dioxide sequestration [4].

But geologists have long held mixed feelings about St. Peter. Kentucky geologist Willard R. Jillson declared in 1938 that "The Saint Peter is still an imperfectly known unit in American stratigraphy. Perhaps it will always be" [5]. Mazzullo and Ehrlich stated that, "The St. Peter Sandstone of southeastern Minnesota is a classic example of homogeneous, featureless, problematic lithology" [6]. Simo et al. lamented that "the formation was maddingly difficult to interpret" [7]. The most widely used textbook of Minnesota geology today, in its description of the St. Peter, asserted that, "The answers are not yet in. As scientists are so prone to say, further study is necessary" [8]. And as recently as 2014, Konstantinou et al. affirmed that, "Despite numerous studies, the century-long debate on how these [quartz] arenites formed is still unresolved" [9].

The thesis of this paper is that the very simplicity of the St. Peter Sandstone has made it difficult to characterize. In widely separated states, the sandstone appeared under different names. Several theories about the nature of this rock began to circulate. The story of St. Peter is not only the story of the assemblage of a stratigraphic unit over a vast area during three centuries, but also the role the study of the provenance of this unit played in the development of sedimentology in the early twentieth century, research that was made all the more challenging by its "simple" mineralogy. Indeed, the St. Peter has been controversial since it was first described.

2. The assemblage of a stratigraphic unit

Ever since the late seventeenth century, reports about a white-cliff-forming rock had come back from the wilderness in the interior of North America. The French explorers Jolliet and Marquette must have been the first Europeans to see the St. Peter Sandstone at the mouth of the Wisconsin River, where it enters the Mississippi, while canoeing the Fox-Wisconsin River portage route in 1673. At the junction of the Wisconsin and Mississippi rivers, they would have been confronted by the towering cliffs of St. Peter Sandstone on the western side of the river at what is now Pikes Peak State Park, in the state of Iowa. However, no description of the rock itself was left by these early explorers [10]. In 1682, another French explorer, René-Robert Cavelier, Sieur de La Salle (1643–1687), constructed Fort St. Louis atop Starved Rock, Illinois—cliffs of what is now known to be St. Peter Sandstone **(Figure 1)**. They called this "Le Rocher", meaning "The Rock" [11]. La Salle sent Father Louis Hennepin (1626–1704) to explore the Upper Mississippi River, and Jillson asserted, somewhat misleadingly, that "Father Hennepin first gazed upon … the Saint Peter Sandstone at the Falls of Saint Anthony" [5]. The problem is that Hennepin himself did not mention the sandstone in his description of the waterfall in 1680 [12]. And based on my own personal observation, the sandstone is not especially prominent at this particular location.

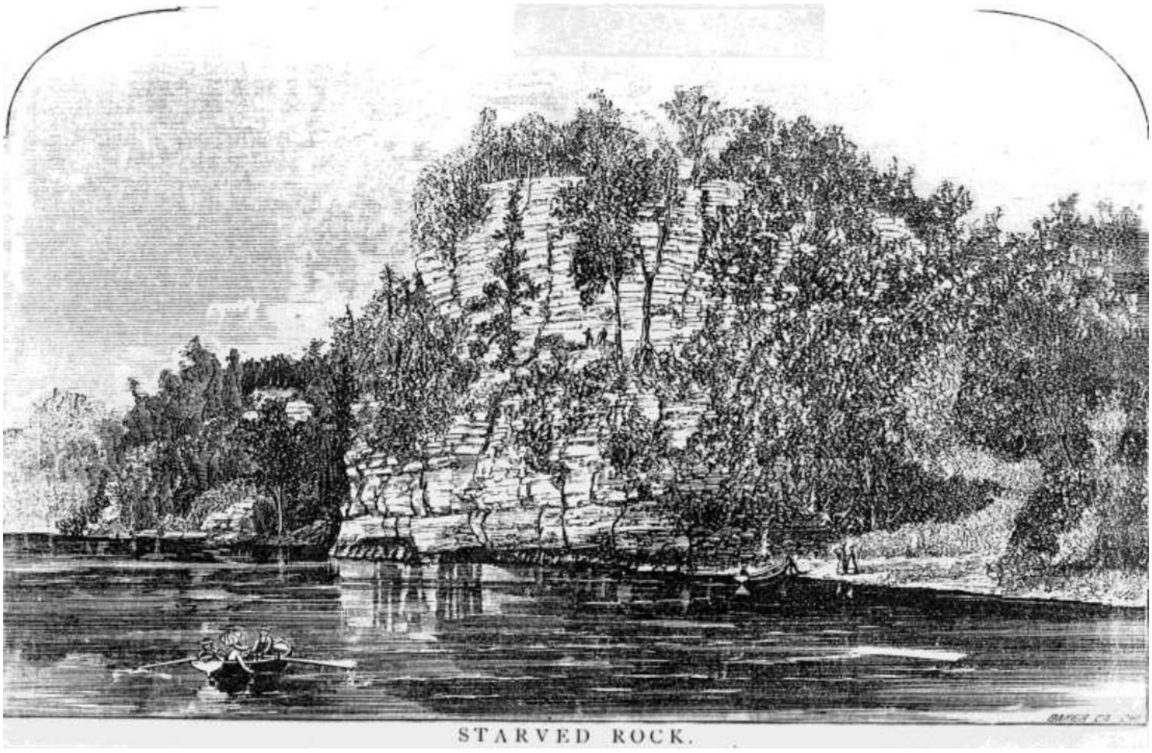

Figure 1. Starved Rock, a prominent historical landmark of St. Peter Sandstone on the Illinois River in the state of Illinois, known to Europeans since 1682 (From Kett [13]).

The first good St. Peter descriptions in the historical record are from the British colonial explorer Jonathan Carver (1710–1780), who traversed the Upper Mississippi in 1766–1767. Ascending the Mississippi River north of Prairie du Chien, Wisconsin, he reported that: "The mountains upon the Mississippi abound with a kind of stone as easily wrought as wood when newly taken out of the ground but hardens in the air. Much of it is white as snow and would serve for building in the best manner. Others have the color and quality of grindstone" [14]. Carver subsequently described the "white stone" at Carver's Cave. In what is perhaps the most heavily quoted passage from Carver's best-selling "Travels", we read that:

> "About thirty miles below the Falls of St. Anthony, at which I arrived the tenth day after I left Lake Pepin, is a remarkable cave of an amazing depth. The Indians term it Wakon-teebe, that is, the Dwelling of the Great Spirit …. I found in this cave many Indian hieroglyphicks, which appeared very ancient, for time had nearly covered them with moss, so that it was with difficulty I could trace them. They were cut in a rude manner upon the inside of the walls, which were composed of a stone so extremely soft that it might be easily penetrated with a knife: a stone everywhere to be found near the Mississippi" [15].

In 1820, Fort Snelling was established at the confluence of the Minnesota and Mississippi rivers, atop bluffs of this snowy white sandstone (**Figure 2**). What is now the nearby city of St. Paul, capital of Minnesota, was established in the 1840s at a place known as "White Cliffs" among the Native peoples [16]. The type locality was described by geologist David Dale Owen (1807–1860) in 1847 from outcrops at this confluence (see below). Due to the construction of extensive revetments at the fort in the years since then, these outcrops are no longer accessible.

Figure 2. The white cliffs of St. Peter Sandstone at the type section of the formation, Fort Snelling, 1844 (Courtesy Minnesota Historical Society).

Landscape artist Henry Lewis (1819–1904), preparing a moving panorama for public display, painted scenes along the Mississippi River from St. Anthony Falls to the Gulf of Mexico, many of which were included in his book, “Views of the Mississippi”, originally published in German in 1854. Lewis calls the St. Paul cliffs “The Cornice Cliffs,” perhaps an allusion to how erosion has sculpted them into quasi-architectural forms [17]. It’s important to note that in most places, where the St. Peter Sandstone manifests itself as cliffs, its soft, crumbly nature requires the presence of a hard limestone caprock, the Platteville Limestone, to protect it from erosion. Thus, a fanciful comparison to columns and entablatures seemed appropriate.

In the neighboring state of Wisconsin, the white cliffs also drew early attention, especially along the Mississippi River, an important steamboat route. One of Owen’s assistants during the geological reconnaissance of the Chippewa Land District was John Locke, who drafted a geological cross-section at Prairie du Chien in 1839 [18] (**Figure 3**).

In other states, widely separated from the type section in Minnesota, encounters with the St. Peter Sandstone appeared under different names and guises. George C. Swallow (1817–1899) reported a “Saccharoidal Sandstone” in his 1855 geological survey of Missouri [19] (**Figure 4**). Harvard geologist Nathaniel Southgate Shaler (1841–1906) identified what he called the “Calciferous Sand Rock” in the drilling logs of deep wells in Kentucky in 1877, and it was not until 1909 that its true identity was known [5].

Figure 3. John Locke's 1839 geological cross-section of the Mississippi cliffs, depicting the village of Prairie du Chien, Wisconsin, on the river bottoms. The St. Peter is here described as "soft sugar-like sandstone" (Courtesy Wisconsin Historical Society).

Figure 4. Saccharoidal Sandstone in the cliffs of the Pomme de Terre River, near Bolivar, Missouri, in 1855, from Swallow [19]. There were several units with the same name, creating confusion.

Indeed, the drilling of artesian wells, beginning in the late nineteenth century, greatly extended the known area of the St. Peter Sandstone. The first comprehensive map of these occurrences of white cliffs in the American Midwest was by Charles P. Berkey in 1906 [20]. It was seen that the outcrop of the sandstone is not broadly continuous, though the sea from which it was deposited was of vast extent. Ultimately it evolved into the map published by George A. Thiel in 1935 [21] **(Figure 5**). The sandstone manifests itself as an outcrop in the states of Arkansas, Illinois, Iowa, Minnesota, Missouri, and Wisconsin. Deep wells revealed its presence under Indiana, Kansas, Kentucky, Michigan, Nebraska, Ohio, and Tennessee. In 1938, Jillson [5] summarized that "Roughly, the paleogeographic pattern of deposition of the Saint Peter Sandstone is that of an ellipse," the east-west axis of which he estimated at 1,300 km, and the north-south axis as 950 km. In the states of Ohio, Kentucky, and Tennessee, where it serves as a host rock for oil and gas plays, the sandstone was of considerable economic interest [5].

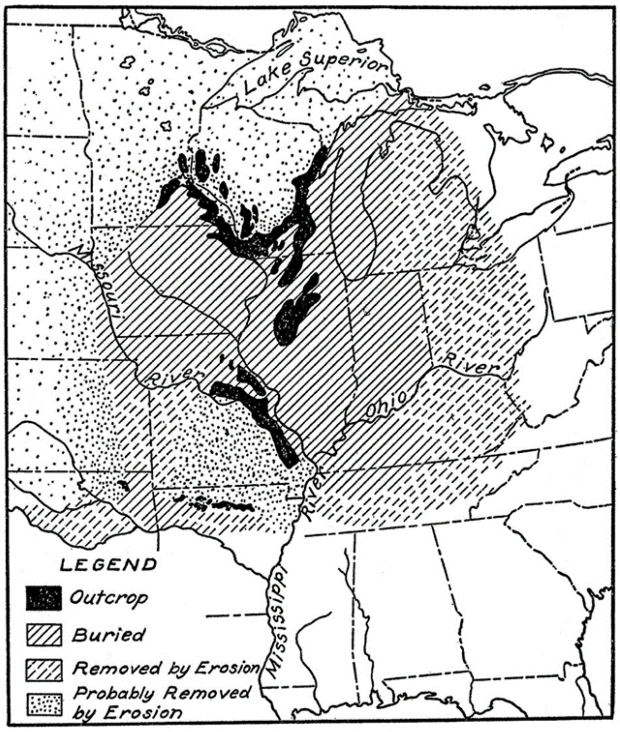

Figure 5. "Distribution of the St. Peter Sandstone" (modified from Thiel [21]). The type section at Fort Snelling, Minnesota, is located among the northernmost outcrop areas shown on the map, as indicated by the star. While this sandstone underlies much of the American Midwest, its vast subsurface extent was not realized until the widespread drilling of artesian wells.

The St. Peter Sandstone underwent wild swings of stratigraphic interpretation over the years. According to the Wernerians (see below), this sandstone fell into the "secondary or horizontal class of rocks." In 1825, William H. Keating (1799–1840) assigned this sandstone to the Lias [22], which in modern stratigraphy would place it in the Jurassic Period. By 1835, however, Roderick I. Murchison (1792–1871) had unveiled his new Silurian System in Europe. Traveling up the Minnesota River by canoe, George W. Featherstonhaugh (1780–1866), the first to use the title "U.S.

Geologist," became an early adopter, applying modern concepts and terminology from England [23]. "Featherstonhaugh was probably the first in America to use the terms Cambrian and Silurian in a geologic column" [24]. He was "highly scornful" of Amos Eaton (1776–1842), the prominent American stratigrapher, who "knew little about the importance of fossils" [25]. Based on "a great variety of fossils, such as orthoceras, bellerophon, fucoides, orthis," Featherstonhaugh classified "the great sandstone beds of the country," seen at Fort Snelling, as Silurian in age [26]. But not until 1903 did the U.S. Geological Survey officially adopt the name Ordovician, thereafter applied to these rocks [27].

Another early adopter of Murchison's terminology was David Dale Owen, the second "U.S. Geologist," who imported the Silurian label to the American Midwest in numerous geological surveys [28]. By the time Owen actually published the name "St. Peter Sandstone," after its type locality on the St. Peter's (now Minnesota) River in 1847, understanding of the stratigraphic position of the layer had been transformed [29,30]. The paleontologist James Hall was able to correlate trans-Appalachian geologic units, including the St. Peter, with the more familiar units of the New York Geological Survey, beginning with a traverse of the Ohio River valley in 1841. He found that sedimentary formations thinned out westwardly, one aspect of his discovery of the craton [31].

3. A problematic lithology

"Every theory of the Earth published in England between Steno's theory in 1671 and Kirwan's theory in 1799 has one feature in common: they all claim that a large proportion of the Earth's rocks are precipitates laid down in some chaotic fluid" [32]. The assumption that sea sands had been chemically precipitated from seawater was widespread in previous centuries; for example, the famous botanist Linnaeus held this belief [33].

Keating served as mineralogist on Major Stephen H. Long's 1823 expedition to the source of the St. Peter's River. He concluded, on the basis of grain shape, that the St. Peter Sandstone, at what was to become Owen's type section, was a chemical precipitate from seawater [22]. This appears to be an echo of the Neptunist teachings of Abraham Gottlob Werner (1749–1817). Precipitation of rock layers from a primitive ocean was a signature Neptunist teaching at the Freiberg Mining Academy in Saxony (**Figure 6**).

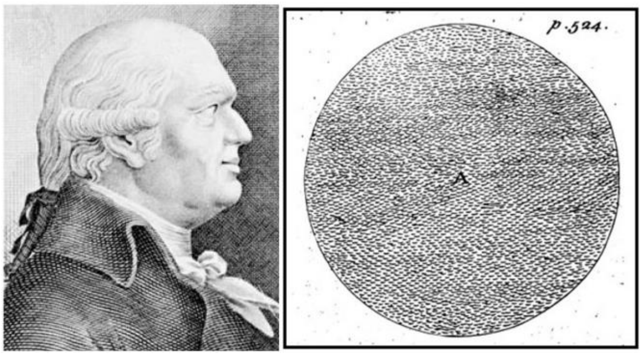

Figure 6. Abraham Werner, father of Neptunism (left) and his water world, showing the Universal Ocean, from Brick [34].

Werner’s influence on early American geology was pervasive. Prominent American Wernerians of that time included Eaton, Benjamin Silliman (1779–1864), and Parker Cleaveland (1780–1858) [35]. William Maclure (1763–1840), dubbed the “Father of American Geology” by Silliman, used the Wernerian scheme to map the eastern United States [36]. Indeed, Ospovat characterized the years from 1785 to 1829 as “the Wernerian Era of American geology” [35]. Even after Wernerian concepts had fallen out of favor with geologists themselves, they continued to be presented in popular works, such as John Hinton’s “History and Topography of the United States”, as late as 1852 [37].

“All American geological maps produced before 1825 were based on the Wernerian scheme” [38]. Maclure’s famous 1809 map of the geology of the United States, revised in 1817, extended as far west as the Mississippi River [39,40]. American geology was thus initially interpreted in Wernerian terms, which entailed mapping the extent of the Primitive, Transition, Secondary, and Alluvial formations. The American Midwest was at the western fringes of Maclure’s map and was shown as undifferentiated “Secondary”. But according to Schneer, “The principal error in Maclure’s map was in classifying the Paleozoic strata of the plateaus between the Mississippi River and the Appalachian Mountains as secondary on the basis of their attitude (nearly flat) and their lithology. They should have been Transition rocks in his scheme” [41].

Nonetheless, on Major Long’s previous expedition through the American Midwest to the Rocky Mountains in 1819, Werner was cited as the chief authority in matters geological [35]. Most of Long’s expeditions deployed Wernerian explanations for the geological phenomena encountered [42]. The geologist of this earlier expedition, Edwin James (1797–1861), extended Maclure’s Wernerian mapping program to the land between the Mississippi River and the Rocky Mountains [37,43].

The fullest account of Keating’s encounter with the St. Peter Sandstone on 9 July 1823 is contained in his “Narrative of an Expedition to the Source of St. Peter’s River”:

> “Immediately under this bed of [Platteville] limestone, in parallel stratification, we observed the [St. Peter] sandstone, which constitutes the principal mass of the bluff, being about sixty feet in thickness. It is a very friable stone, and in some cases the grains, of which it is formed, are so loosely united that it appears almost like sand. Every fragment, if examined with care, seems to be a regular crystal, and we incline much to the opinion that this sandstone must have been formed by a chemical precipitation and not by mere mechanical deposition. The process of its formation may have been a very rapid one, such as is obtained in the manufacture of fine salt, and to this may be attributed the circumstance of its loose texture. The grain is very fine; its colour is white, sometimes a little yellowish, in which case it resembles in texture, colour, &c. the finer varieties of Muscovado sugar. The loose texture of the rock is probably the cause of its presenting but few indications of stratification” [22].

Although Keating did not use the words “pure” or “purity” in the context of the St. Peter Sandstone, the purity concept, later to become part of petrographic rhetoric, was attributed to him by Frederick W. Sardeson in 1896 [44]. Owen appears to be the first, in 1852, to use the word “pure” consequent upon an actual chemical analysis, which showed "but two-tenths of one per cent of foreign matter," making it appropriate for "the glass-houses at Pittsburg" [30].

Keating's speculations about the St. Peter Sandstone projected Wernerian interpretations farther west than ever before. The "primitive ocean" from which the sandstone supposedly precipitated, named the "Saint Peter Sea' by Berkey, was epicontinental, extending northward from what is now the Gulf of Mexico [20].

While Werner's concept of basalt crystallizing from sea water had lost favor even among fervent Wernerians like Keating by this time, the chemical precipitation of sedimentary rocks from sea water appears to be the last surviving petrological concept of Werner among American geologists. With Keating, we see an actual reversion to chemical precipitation, a Wernerian mechanism, to account for a rock layer. Keating asserted that the St. Peter sand grains resemble tiny crystals. He had elsewhere described examining a sand sample with a microscope during the expedition [22], but he did not mention a microscope at Fort Snelling, and it is unknown what magnification (if any) he employed to view the grains. But it would not be the first time he had made a crystallographic blunder [45]. The Wisconsin geologist Thomas C. Chamberlin (1843–1928) later warned against precisely this error, emphasizing the necessity for distinguishing the angular grains of the St. Peter Sandstone from "freely-forming quartz crystals" [46]. The other St. Peter grain shape commonly found is rounded, and these also indicate a detrital origin because chemical precipitation would have produced an interlocking fabric [47].

Impressed by the discovery of the enormous siliceous sinter deposits of the Iceland geysers, some chemists, such as Richard Kirwan (1733–1812), became convinced that, if Werner's Universal Ocean was hot and alkaline, the deposition of silica was indeed feasible [48]. The German chemical geologist Gustav Bischof (1792–1870) asserted "investigations prove that sandstone strata have been formed, not only from quartzose detritus, but, also from siliceous deposits from water" [49], though it appears he was referring to the deposition of siliceous cements, not the body of the rock unit. This distinction is important because Bischof was a proponent of the so-called "neo-Neptunist" school of thought [50]. Among them, "particularly from the French and German-speaking parts of Europe, the old Wernerian idea of an aqueous origin for crystalline rocks was by no means defunct, well into the second half of the nineteenth century" [51]. While the precipitation of silica from seawater to form siliceous ooze and, ultimately, chert is a familiar process, enormous quartz sandstones like the St. Peter are not known to form in this way [52].

Keating did attract direct support from several American scientists. The Wisconsin antiquarian and topographer Increase A. Lapham (1811–1875) investigated the St. Peter in the last days of its anonymity before Owen formally bestowed a name upon it. "The sandstone is mostly pure, and white as the driven snow," he reported. "The grains appear to be perfect quartz crystals, and not beach sand smoothed and ground by the action of water and then hardened into rock" [53].

James Hall (1811–1898) and Josiah D. Whitney (1819–1896) were prominent geologists who endorsed Keating's notion of the chemical origin of the St. Peter Sandstone but put the emphasis on lack of fossils rather than presence of crystalline facets.

The origin of these immense accumulations of silicious matter in so pure a form and with such peculiarities of lithological character is a matter of great theoretical interest. It has been generally assumed, without much examination of the subject, that all such sandstones were originally formed by mechanical agencies, the material being supposed to have gradually accumulated from the grinding down of previously existing quartzose rocks. The facts collected above, however, seem rather to point to chemical than mechanical causes, as having been the chief agents in the deposition of the sandstones. If these silicious strata, developed over such an extensive surface and with such a thickness as they are, were the result of the trituration of the azoic rocks which everywhere underlie them, and it is difficult to conceive of any other source from which the material could have been obtained, unless we adopt the chemical theory, we can hardly understand how such an amount of quartzose sand could have been accumulated, without its containing, at the same time, a considerable quantity of detritus which could be recognized as having come from the destruction of the schistose, feldspathic and trappean rocks that make up the larger portion of the azoic series, wherever it has been examined. The uniform size of the grains of which the sandstone is composed and the tendency to the development of crystalline facets in them are additional facts that suggest the idea of chemical precipitation rather than of mechanical accumulation [54].

As late as 1862, Hall and Whitney reiterated that "no vestige of an organism, either of plant or animal, has been observed" in the St. Peter [55].

The grand finale of the chemical precipitation theory, however, took place in 1871, nearly a half century after Keating's original observations. John Murrish (1820–1886), a geologist working in the lead regions of southwestern Wisconsin, applied the Iceland geyser analogy directly to the St. Peter Sandstone, emphasizing "the fact that very different physical conditions prevailed then to what we find now." He seemed enamored with the "little crystals of quartz." "I have sometimes thought," he wrote, "that I would give almost anything if I could procure some of those crystals in their magnified forms as cabinet specimens" [56]. The historian Goerge P. Merrill, however, dismissed Murrish as a man of "slight training" who "was led into many errors" [18].

Soon after, in 1876, Newton H. Winchell (1839–1914) found a fossil brachiopod, "Lingulepis", at the very top of the St. Peter Sandstone in Minnesota, and subsequently Sardeson found many molluscan fossils within the lower third of the sandstone, again in Minnesota [44]. "They dispel the idea," Winchell asserted, "of the possible chemical origin of the St. Peter Sandstone, as an oceanic precipitate" [57].

4. New developments in sedimentology

Ultimately, three explanations emerged to account for the purity of the St. Peter Sandstone, and they would have implications for the understanding of its provenance. The first was Keating's chemical precipitation, which, although not directly linked to the issue of purity by him, was certainly in the forefront for his supporters, especially Hall and Whitney [54]. The second was Sardeson's "percolating waters," whereby "the Saint Peter has simply had all soluble material washed out of it" [44]. The third was Berkey's concept of recycled sandstones, whereby "wind and water" had winnowed away the impurities [20]. While there was certainly truth in Sardeson's conjecture, it was Berkey's that would get the most play as the field of sedimentology advanced.

A new method was being developed that would have a significant impact on the study of the St. Peter Sandstone. "Between about 1930 and 1950 particle size analysis seems to have been the single most important technique ... The method of particle size analysis was formulated and developed by two pioneer American sedimentologists, J. A. Udden and C. K. Wentworth, between 1890 and 1920" [58]. The subsequent maturation of sedimentology, with the application of statistical analysis to the St. Peter Sandstone, led to the realization that "the uniform size of the grains" of which Hall spoke was an unwarranted generalization when the "uniformity coefficient" was actually calculated [59].

Charles L. Dake (1883–1934) spent most of his career at the Missouri School of Mines and Metallurgy in Rolla [60]. His doctoral thesis, "The Problem of the St. Peter Sandstone," undertook to examine the "problem" of where the sand constituting this sandstone came from [59]. Implicit in the title was the assumption that it was, of course, a mechanical sediment, and the paper reads as one long argument against an eolian origin for the sandstone. Dake adopted Berkey's suggestion of a recycled sandstone, emphasizing a specific candidate for its precursor, the Cambrian-aged Potsdam sandstone of the Great Lakes region [59]. "A belt of Potsdam," he wrote, "fringes the pre-Cambrian shield" [59]. Berkey favored "the Basal Sandstone," which included the Potsdam along with other units [20]. According to Dake:

> "The purity of the St. Peter Sandstone, while very remarkable, as compared with that of average sandstones, is, in respect to content of clay, iron, mica, heavy minerals, and carbonate, not sufficiently different from that of associated marine sandstones to demand any essentially different explanation of origin; the degree of difference actually existing being satisfactorily accounted for by assuming its derivation from one of the older, already well-sorted sandstones, the Potsdam" [59].

Dake had employed elementary statistical arguments, but the rapid development of sedimentology soon added new parameters. George A. Thiel (1892–1979), long-time chairman of the geology department at the University of Minnesota, had undertaken to clarify the subject in the 1930s [61]. Thiel's classic study, "Sedimentary and Petrographic Analysis of the St. Peter Sandstone," published in 1935, was the first to fully describe the St. Peter statistically [62]. On the basis of the more rigorous procedures and reasoning of the day, Thiel broke with the monocyclic paradigm that had characterized St. Peter genealogy: "The accessory minerals in the St. Peter Sandstone suggest also that the sands have passed through several cycles of transportation and attrition ... The common rock-forming ferro-magnesian minerals are no longer present" [21]. Hard, durable accessory minerals such as "zircon, rutile, and tourmaline," were the only ones to survive. Ironically, the impurities were now driving the argument about purity.

Moreover, Thiel unseated the favored candidate for precursor status by introducing the "average median diameter." "If the St. Peter sands were derived from the Potsdam sandstones, as suggested by Dake, Lamar, and Giles, one would expect to find these Cambrian sandstones composed, for the most part, of sands coarser than, or at least as coarse as, the St. Peter sands," whereas the St. Peter grains had a larger average median diameter than their supposed source in the Potsdam. On the basis of samples from "the Kettle River sandstone taken at [the town of] Sandstone, Minnesota," he was able to identify a more suitable precursor [21]. It was the lower part of Berkey's "Basal Sandstone," what we now call the Hinckley Sandstone, of Upper Precambrian age [63].

Finally, Thiel broached a topic that returns us to the origins of the Keating controversy, perhaps providing an alternative resolution (literally). Keating claimed to have seen in the St. Peter grains "a regular crystal." But Thiel observed secondary growths on St. Peter grains, which often result from re-solution of surrounding grains: "Much of the present angularity of the larger quartz grains in the St. Peter sands is due to changes in shape resulting from fracturing or is due to recrystallization and enlargement produced by secondary growth," adding that "secondary growth tends to reconstruct quartz grains to their original hexagonal crystal structure" [21]. Or, as Krynine expressed it: "Pseudo-angularity produced by secondary silica overgrowths on the grains of quartzitic rocks should not be mistaken for original angularity" [64]. While Henry Clifton Sorby (1826–1908) was the first to describe overgrowths on quartz grains in 1880 [65,66], the possibility remains that Keating's real significance was in being the first to observe quartz overgrowths, mistaking them for primary growth (**Figure 7**).

Figure 7. Grains of St. Peter Sandstone, from Brick [3].

Many changes occurred in the field of sedimentology following Thiel, but the thread of purity arguments about the St. Peter Sandstone tapered off after the hey-day of particle-size analysis. There was a transition away from the word "purity," which was part of an "industrial-commercial parlance" [62], towards terms denoting petrological maturity, in particular, chemical maturity (as contrasted with textural maturity). Beginning in the 1940s, with the famous compositional triangles for sandstone classification stemming from the work of F. J. Pettijohn and P. D. Krynine, among others, the word purity rarely appears [67], although some sedimentologists continued to speak informally of "clean sands" [64]. In the new ternary diagrams, the St. Peter Sandstone is plotted as a quartzose sandstone or quartz arenite.

In recent decades, provenance studies of the St. Peter Sandstone have focused on newer methods. To determine the ultimate source of detrital zircons in the St. Peter, Johnson and Winter [68] studied source ages, finding two clusters: 1.1 billion years ago (suggestive of Midcontinental Rift origin) and 2.7 billion years ago (suggestive of the granite-greenstone terrane of the Superior Province). In both cases, the ultimate source is thought to be Precambrian felsic plutonic rocks such as granite. To determine the immediate source of the sandstone, however, they undertook isotopic studies of quartz grains, which contain zircon microinclusions. Their data indicates a sedimentary source, the lower Paleozoic quartz arenites, corroborating the results of past studies, especially those of Tyler, published in 1936 [69].

5. Conclusion

A vast region of white cliffs in the American Midwest perceived by early travelers from the late seventeenth century onwards was later named the St. Peter Sandstone, whose type section was described on the St. Peter's (now Minnesota) River. Widely separated occurrences were pieced together into a coherent unit by geologists. But the nature and origin of this sandstone were fiercely debated until quite recently. At first thought to be a primordial ocean deposit, or perhaps a vast sinter terrace, it was found to be a recycled sandstone from previous rock units in the region. This study has shown that the very simplicity of the St. Peter Sandstone, a veritable icon of "layer-cake geology," has made it challenging to characterize.

Acknowledgments: My essay on the St. Peter Sandstone was loosely inspired by the historical approach used by David Branagan in his study of the Desert Sandstone of Australia [70].

Conflict of interest: The author declares no conflict of interest.

References

1. Mossler JH. Paleozoic Stratigraphic Nomenclature for Minnesota. Minneapolis: Minnesota Geological Survey; 2008.
2. Runkel AC, Miller JF, McKay RM, et al. High-resolution sequence stratigraphy of lower Paleozoic sheet sandstones in central North America: The role of special conditions of cratonic interiors in development of stratal architecture. Geological Society of America Bulletin. 2007; 119(7-8): 860-881. doi: 10.1130/b26117.1
3. Brick GA. The far shoals of Neptunism: William H. Keating and the St. Peter Sandstone in the American Midwest. Earth Sciences History. 2022; 41(1): 64-76. doi: 10.17704/1944-6187-41.1.64
4. Barnes DA, Ellett KM, Rupp JA. Geologic-carbon-sequestration potential of the Ordovician St. Peter Sandstone, Michigan and Illinois Basins, United States. Environmental Geosciences. 2017; 24(1): 15-49. doi: 10.1306/eg.02071716007
5. Jillson WR. The Saint Peter Sandstone in Kentucky: An Account of the Discovery, Early Surveys, and Regional Geology of This Famous Clastic of the Upper Mississippi Valley Coupled with an Outline of Its Stratigraphic Correlatives in Kentucky to Which Are Added Notes on Its Oil and Gas Possibilities and a Bibliography. Louisville: Standard Printing Co; 1938.
6. Mazzullo JM, Ehrlich R. Grain-shape variation in the St. Peter Sandstone: A record of eolian and fluvial sedimentation of an early Paleozoic cratonic sheet sand. SEPM Journal of Sedimentary Research. 1983; 53. doi: 10.1306/212f8161-2b24-11d7-8648000102c1865d
7. Simo JA, Choi YS, Freiberg PG, et al. Sedimentology, sequence stratigraphy, and paleoceanography of the Middle and Upper Ordovician of eastern Wisconsin. In: Guide to Field Trips in Wisconsin and Adjacent Areas of Minnesota, 31st Annual Meeting, North-Central Section. Geological Society of America; 1997. pp. 95-114.
8. Ojakangas RW, Matsch CL. Minnesota's Geology. Minneapolis: University of Minnesota Press; 2001.
9. Konstantinou A, Wirth KR, Vervoort JD, et al. Provenance of quartz arenites of the early Paleozoic Midcontinent Region, USA. The Journal of Geology. 2014; 122(2): 201-216. doi: 10.1086/675327
10. Kellogg LP. Early Narratives of the Northwest, 1634-1699. New York: Charles Scribner's Sons; 1917.

11. Johnson DS. LaSalle: A Perilous Odyssey from Canada to the Gulf of Mexico. New York: Cooper Square Press, 2002.
12. Hennepin L. Father Louis Hennepin's Description of Louisiana Newly Discovered to the Southwest of New France by Order of the King. Translated by Marion E. Cross. Minneapolis: University of Minnesota Press; 1938.
13. Kett HF. The Past and Present of La Salle County, Illinois. Chicago: H.F. Kett; 1877.
14. Parker J. The Journals of Jonathan Carver and Related Documents 1766-1770. St. Paul: Minnesota Historical Society; 1976.
15. Carver J. Travels Through the Interior Parts of North America. (Facsimile reprint of the third London edition, 1781). Minneapolis, MN: Ross & Haines, Inc.; 1956.
16. Williams JF. A History of the City of Saint Paul, and of the County of Ramsey, Minnesota. St. Paul: Collections of the Minnesota Historical Society; 1876.
17. Lewis H. The Valley of the Mississippi Illustrated. St. Paul: Minnesota Historical Society; 1967.
18. Merrill GP. The First One Hundred Years of American Geology. New York: Hafner Publishing Company; 1969.
19. Swallow GC. The First and Second Annual Reports of the Geological Survey of Missouri. Jefferson City: James Lusk, Printer; 1855.
20. Berkey CP. Paleogeography of Saint Peter time. Geological Society of America Bulletin. 1906; 17(1): 229-250. doi: 10.1130/gsab-17-229
21. Thiel GA. Sedimentary and petrographic analysis of the St. Peter Sandstone. Geological Society of America Bulletin. 1935; 46(4): 559-614. doi: 10.1130/gsab-46-559
22. Keating WH. Narrative of an Expedition to the Source of St. Peter's River, Lake Winnepeek, Lake of the Woods, &c., Performed in the Year 1823. Minneapolis: Ross & Haines, Inc; 1959.
23. Schneer CJ. Ebenezer Emmons and the foundations of American Geology. Isis. 1969; 60(4): 439-450. doi: 10.1086/350535
24. White GW, Slanker BO. Early Geology in the Mississippi Valley. Urbana: University of Illinois; 1962.
25. Eyles JM. G. W. Featherstonhaugh (1780-1866), F.R.S., F.G.S., geologist and traveller. Journal of the Society for the Bibliography of Natural History. 1978; 8(4): 381-395. doi: 10.3366/jsbnh.1978.8.4.381
26. Featherstonhaugh GW. A Canoe Voyage Up the Minnay Sotor. Reprint edition. St. Paul: Minnesota Historical Society; 1970.
27. Yochelson E. The Decline of the use of "Lower Silurian" and the rise of "Ordovician" in U.S. geologic literature. Earth Sciences History. 1997; 16(1): 4-12. doi: 10.17704/eshi.16.1.6844363517t44154
28. Keyes C. Transplantation of English terranal classification to America by David Dale Owen. Pan-American Geologist. 1923; 39(2): 80-94.
29. Owen DD. Preliminary report, containing outlines of the progress of the geological survey of Wisconsin and Iowa, up to October 11, 1847. In: Senate Executive Document 2, 1st Session, 30th. U. S. Congress; 1847. pp. 160-174.
30. Owen DD, Leidy J, Norwood JG, et al. Report of a geological survey of Wisconsin, Iowa, and Minnesota; and incidentally of a portion of Nebraska Territory. Made under instructions from the United States Treasury Department. Philadelphia: Lippincott, Grambo, & Company; 1852. doi: 10.5962/bhl.title.58539
31. Dott RH. James Hall's discovery of the craton. Geologists and Ideas. 1985; 157-167. doi: 10.1130/dnag-cent-v1.157
32. Seddon G. Abraham Gottlob Werner: History and folk-history. Journal of the Geological Society of Australia. 1973; 20(4): 381-395. doi: 10.1080/00167617308728824
33. Adams FD. The Birth and Development of the Geological Sciences. New York: Dover Publications, Inc.; 1954.
34. Brick GA. "White as the Driven Snow": Neptunian Echoes from the Deep Sewers. Journal of Spelean History. 2022; 56(2): 31-35.
35. Ospovat AM. Werner's influence on American geology. Proceedings of the Oklahoma Academy of Science. 1960; 40: 98-103.
36. Lessing P. William Maclure's Wernerian Appalachians. Southeastern Geology. 1999; 38(3): 117-134.
37. Aalto KR. Edwin James' and John Hinton's revisions of Maclure's geologic map of the United States. History of Geo-and Space Sciences. 2012; 3(1): 75-86. doi: 10.5194/hgss-3-75-2012
38. Hazen RM. The founding of geology in America: 1771 to 1818. Geological Society of America Bulletin.1974; 85:12. 1827-1834. doi: 10.1130/0016-7606(1974)85<1827:TFOGIA>2.0.CO;2
39. Maclure W. Observations on the geology of the United States, explanatory of a geological map. Transactions of the American Philosophical Society. 1809; 6: 411. doi: 10.2307/1004821

40. White GW. William Maclure's maps of the geology of the United States. Journal of the Society for the Bibliography of Natural History. 1977; 8(3): 266-269. doi: 10.3366/jsbnh.1977.8.3.266
41. Schneer CJ. William Maclure's Geological Map of the United States. Journal of Geological Education. 1981; 29(5): 241-242. doi: 10.5408/0022-1368-29.5.241
42. Merriam D. Edwin James-Chronicler of geology in the American West. Earth Sciences History. 1994; 13(2): 115-120. doi: 10.17704/eshi.13.2.gn02226010571537
43. James EP. Remarks on the Sandstone and Floetz Trap Formations of the Western Part of the Valley of the Mississippi. Transactions of the American Philosophical Society. 1825; 2: 191. doi: 10.2307/1005059
44. Sardeson FW. The Saint Peter Sandstone. Journal of the Minnesota Academy of Science. 1896; 4(1): 64-88.
45. Greene JC, Burke JG. The Science of Minerals in the Age of Jefferson. Transactions of the American Philosophical Society. 1978; 68(4): 1. doi: 10.2307/1006294
46. Chamberlin TC. Geology of Wisconsin, Survey of 1873-1879. Madison: Commissioners of Public Printing; 1883.
47. Pettijohn FP, Potter PE, Siever R. Geology of Sand and Sandstone. Bloomington: Indiana Geological Survey and Indiana Department of Geology; 1965.
48. Newcomb S. Laboratory Evidence of Silica Solution Supporting Wernerian Theory. Ambix. 1986; 33(2-3): 88-93. doi: 10.1179/amb.1986.33.2-3.88
49. Bischof G. Elements of Chemical and Physical Geology, Volume III. London: Printed for the Cavendish Society by Harrison and Sons; 1859.
50. Amstutz GC. Bischof, Carl Gustav Christoph. In: Gillispie CC (editor). Dictionary of Scientific Biography. New York: Charles Scribner's Sons; 1970; pp. 158-159.
51. Oldroyd DR. The archaean controversy in Britain: Part IV—Some general theoretical and social issues. Annals of Science. 1994; 51(6): 571-592. doi: 10.1080/00033799400200441
52. Tréguer PJ, De La Rocha CL. The World Ocean Silica Cycle. Annual Review of Marine Science. 2013; 5(1): 477-501. doi: 10.1146/annurev-marine-121211-172346
53. Lapham IA. Wisconsin: Its Geography and Topography, History, Geology, and Mineralogy: Together with Brief Sketches of Its Antiquities, Natural History, Soil, Productions, Population, and Government, 2nd ed. Milwaukee: I. A. Hopkins; 1846.
54. Hall J, Whitney JD. Report on the Geological Survey of the State of Iowa, Volume 1. State Printer; 1858.
55. Hall J, Whitney JD. Report on the Geological Survey of the State of Wisconsin, Volume 1. State Printer; 1862.
56. Murrish J. Report on the Geological Survey of the Lead Regions. Wisconsin Geological, Mineralogical, and Agricultural Survey; 1871.
57. Winchell NH. Report on the Geology of Fillmore County. In: Fourth Annual Report of the Geological and Natural History Survey of Minnesota. St. Paul: The Pioneer-Press Company; 1876. pp. 13-74.
58. Law J. Fragmentation and investment in sedimentology. Social Studies of Science. 1980; 10(1): 1-22. doi: 10.1177/030631278001000101
59. Dake CL. The Problem of the St. Peter Sandstone. Rolla: University of Missouri; 1921.
60. Bridge J. Charles Laurence Dake. Bulletin of the American Association of Petroleum Geologists. 1935; 19(1): 143-147.
61. Swain FM. Memorial to George Alfred Thiel (1892-1979). Available online: https://www.geosociety.org/documents/gsa/memorials/v13/Thiel-GA.pdf (accessed on 12 January 2024).
62. Amaral EJ, Pryor WA. Depositional environment of the St. Peter Sandstone deduced by textural analysis. SEPM Journal of Sedimentary Research. 1977; 47. doi: 10.1306/212f70ea-2b24-11d7-8648000102c1865d
63. Tryhorn AD, Ojakangas RW. Sedimentation and petrology of the Upper Precambrian Hinckley Sandstone of east-central Minnesota. In: Sims, P. K., & Morey, G. B. (editors). Geology of Minnesota: A Centennial Volume. St. Paul: Minnesota Geological Survey; 1972. pp. 459-473.
64. Krynine PD. The megascopic study and field classification of sedimentary rocks. The Journal of Geology. 1948; 56(2): 130-165. doi: 10.1086/625492
65. Sorby HC. On the structure and origin of non-calcareous stratified rocks. Proceedings of the Geological Society of London. 1880; 36: 46-92.
66. Folk RL. Henry Clifton Sorby (1826-1908), the founder of petrography. Journal of Geological Education. 1965; 13(2): 43-47. doi: 10.5408/0022-1368-xiii.2.43

67. Klein GDV. Analysis and review of sandstone classifications in the North American geological literature, 1940-1960. Geological Society of America Bulletin. 1963; 74(5): 555-576. doi:10.1130/0016-7606(1963)74[555:AAROSC]2.0.CO;2
68. Johnson CM, Winter BL. Provenance analysis of lower Paleozoic cratonic quartz arenites of the North American midcontinent region: U-Pb and Sm-Nd isotope geochemistry. Geological Society of America Bulletin. 1999; 111(11): 1723-1738. doi:10.1130/0016-7606
69. Tyler SA. Heavy minerals of the Saint Peter Sandstone in Wisconsin. Journal of Sedimentary Research. 1936; 6(2): 55-84. doi: 10.1306/d4268f5e-2b26-11d7-8648000102c1865d
70. Branagan DF. The Desert Sandstone of Australia: A late-nineteenth-century enigma of deposition, fossils, and weathering. Earth Sciences History. 2004; 23(2): 208-256.

Journal of Geography and Cartography 2024, 7(2), 8282.
https://doi.org/10.24294/jgc.v7i2.8282

Article

LULC changes in the region of the proposed Pwalugu hydropower project using GIS and remote sensing technique

Emmanuel Kekle Ahialey[1,2,*], Amos T. Kabo–bah[1,3], Samuel Gyamfi[1,4]

[1] Regional Centre for Energy and Environmental Sustainability (RCEES), Sunyani P. O. Box 214, Ghana
[2] University of Energy and Natural Resources (UENR), Sunyani P. O. Box 214, Ghana
[3] Department of Civil and Environmental Engineering, University of Energy and Natural Resources (UENR), Sunyani P. O. Box 214, Ghana
[4] School of Energy University of Energy and Natural Resources (UENR), Sunyani P. O. Box 214, Ghana
*** Corresponding author:** Emmanuel Kekle Ahialey, emmanuel.ahialey.stu@uenr.edu.gh

CITATION

Ahialey EK, Kabo–bah AT, Gyamfi S. LULC changes in the region of the proposed Pwalugu hydropower project using GIS and remote sensing technique. Journal of Geography and Cartography. 2024; 7(2): 8282. https://doi.org/10.24294/jgc.v7i2.8282

ARTICLE INFO

Received: 29 May 2024
Accepted: 1 July 2024
Available online: 2 August 2024

Abstract: Proper understanding of LULC changes is considered an indispensable element for modeling. It is also central for planning and management activities as well as understanding the earth as a system. This study examined LULC changes in the region of the proposed Pwalugu hydropower project using remote sensing (RS) and geographic information systems (GIS) techniques. Data from the United States Geological Survey's Landsat satellite, specifically the Landsat Thematic Mapper (TM), the Enhanced Thematic Mapper (ETM), and the Operational Land Imager (OLI), were used. The Landsat 5 thematic mapper (TM) sensor data was processed for the year 1990; the Landsat 7 SLC data was processed for the year 2000; and the 2020 data was collected from Operation Land Image (OLI). Landsat images were extracted based on the years 1990, 2000, and 2020, which were used to develop three land cover maps. The region of the proposed Pwalugu hydropower project was divided into the following five primary LULC classes: settlements and barren lands; croplands; water bodies; grassland; and other areas. Within the three periods (1990–2000, 2000–2020, and 1990–2020), grassland has increased from 9%, 20%, and 40%, respectively. On the other hand, the change in the remaining four (4) classes varied. The findings suggest that population growth, changes in climate, and deforestation during this thirty-year period have been responsible for the variations in the LULC classes. The variations in the LULC changes could have a significant influence on the hydrological processes in the form of evapotranspiration, interception, and infiltration. This study will therefore assist in establishing patterns and will enable Ghana's resource managers to forecast realistic change scenarios that would be helpful for the management of the proposed Pwalugu hydropower project.

Keywords: land use land cover; change detection; GIS and remote sensing technique; Pwalugu

1. Introduction

Land use and land cover changes are used interchangeably for different purposes. Studies by researchers have therefore made abundantly clear the distinction between land cover and land use Quentin et al. [1] Lambin et al., [2] Chrysoulakis et al. [3] Zubair [4] and FAO [5] The activities carried out by man, such as the clearing of arable land for settlement, farming, mining, the construction of dams, and the destruction of forests for other purposes, are some of the activities that lead to the alteration of the land, which can be seen in many communities. The widespread consumption of land results in an increase in soil erosion, floods and droughts.

Several studies have identified different factors as drivers of land use and land cover changes. For instance, Lambin et al. [2] identify socioeconomic development, population growth, and pressures on land for agricultural use as the primary drivers of land use and land cover changes. Mather and Needle [6] also identify deforestation as having a high link with poverty as well as population growth in developing countries. The works of Campbell et al. [7], Briassoulis et al. [8], Auch et al. [9] and Kanianska et al. [10] classify the factors that drive land changes into distinct categories. The distinct categories were economic, cultural, social, and political. They again stated that the classifications may include two or more categories at the same time.

It is evident from previous studies that changes in LULC have an effect on the fundamental processes that govern the Earth System. For instance, Sanderson et al. [11] stated that deforestation leads to an increase in albedo as well as a reduction in evapotranspiration (ET). Perugini et al. [12] also stated that deforestation causes a warming effect due to a larger decrease in the ET. This happens as a result of changes in the latent and sensible heat fluxes due to the reduced leaf area index. Mariye [13] postulated that population growth, settlement patterns, and the expansion of farmlands can all be linked to the increase in cropland. Mehari [13] further stated that the increase in cropland has occurred as a direct result of the demand for more food. Moreover, Reid et al. [14] stated that the dynamics of LULC are the result of complex interactions between a number of different biophysical and socio-economic conditions. In addition, these interactions can take place on a variety of different temporal and spatial scales.

According to Sterling et al. [15], land use and land cover changes have an indirect impact on water cycles as a result of changes in albedo. They concluded that the changes alter the partitioning of precipitation into different components. The components are evaporation, transpiration, runoff, interception, and infiltration, which in turn affect soil moisture contents and the energy cycle. The works of Trimble and Crosson [16] mentioned changes in LULC as the primary source of soil degradation, while Sala et al. [17] indicated that it influences biotic diversity globally. In addition to this, it alters the functions of ecosystems and reduces the capacity of biological systems to meet the requirements of humans Vitousek et al. [18] and Praveen [19].

The findings of a number of other studies indicate that an increase in agricultural activities, as well as afforestation or deforestation, have a significant influence on the processes of hydrology. The processes specifically mentioned include interception, infiltration, and evapotranspiration. According to the findings of the studies, such processes also result in changes to the flows at both the surface and subsurface levels. Examples of such studies can be found in the following publications: Gashaw et al. [20] Jaksa and Sridhar [21] Ahiablame et al. [22] Kidane and Bogale [23] Wang et al. [24] Niraula et al. [25] Seong and Sridhar [26] Sridhar and Wedin [27] Sridhar and Anderson [28].

1.1. Relationship between LULC changes and hydrology

According to the findings of Wang et al. [29] the variations in the land surface are dependent on the changes that occur in the vegetation, the soil, and the climate. The study conducted by Mango et al. [30] agrees with Wang et al. [29]. The findings of Mango et al. [30] show a visible run-off reaction occurred in Kenya as a result of an increase in rainfall as well as an increase in temperature. Woyessa and Welderufae [31] discovered that an increase in forest cover could result in a reduction in yearly flow by up to 15% and yearly surface runoff by up to 30%. These findings were based on the fact that more trees would cover the land. As a consequence of this, the level of peak flow that occurs during floods may be reduced. On the other hand, this strategy can only be implemented in catchment areas that feature fully developed forest covers.

Other studies across the globe have studied the relationship that exists between LULC and hydrology [32–35]. They are of the opinion that the characteristics of land use changes are linked to the effects that the hydrologic cycle has on the catchment area.

In Ghana, Awotwi et al. [36] investigate the effect of shifting land cover on the various components of West Africa's White Volta Basin's water balance. The results show that grasslands and savannahs were being converted to farmlands at a faster rate than was previously thought. They also held the view that land use and land cover changes contribute to a range of effects on both the annual water yield and ET in the basin. In the Pra River Basin of Ghana, Awotwi et al. [37] discovered that there has been an increase in anthropogenic activities beginning in 1986 to a projected 2025. This leads to an increase in the surface runoff as well as water yield and a reduction in the base flow as well as ET.

1.2. The use of Remote Sensing (RS) and Geographic Information System (GIS) in determining LULC changes

Since the 1970s, remote sensing (RS) has been a source of data used to monitor and analyse LULC changes Chang et al. [38]. Several studies (e.g., Ayala-Silv et al. [39]; Rawart and Kumar [40]; Berrick [41] have suggested that the use of RS aids in determining land cover changes that have occurred in a short period of time, at a low cost, and with greater precision. According to Chaikaew [42], the Geographic Information System (GIS) in conjunction with RS is the preferred method for determining land cover changes. Halefom et al. [43], concurred, stating that both RS and GIS have been widely used to provide accurate and timely geographical data for the LULC change analysis.

There have been several studies conducted across the globe where RS and GIS were used to determine the trends of LULC changes. El-Kawy et al. [44], for instance, utilised Landsat imagery to provide current and historical LULC conditions for the western Nile delta. Dymond et al. [45] also utilised RS in New Zealand to estimate the change in forest cover and, thus, the area of afforestation and deforestation. Md Islam et al. [46] conducted a study on NijhumDwip National Park (NDNP) to determine the decadal changes in forest cover utilising freely accessible satellite RS data and GIS tools. In the southern district of Ethiopia, Mariye [13] used

RS, field observations, in-depth household interviews, key informants, and focus group discussions to determine LULC change dynamics on the Ojoje watershed.

Using RS and GIS at various locations, a number of studies have also been conducted in Ghana to evaluate the land changes that have occurred over time (e.g., Braimoh and Vlek [47]; Alo and Pontius [48]; Kusimi [49]; Kleeman et al. [50]; Karki et al. [51]; Kpienbaareh and Oduro-Appiah [52]; Oduro-Appiah et al. [53]. Although there are copious studies on LULC assessment across the globe and in Ghana, a search through the literature revealed a gap of no LULC change assessment in the region of the proposed Pwalugu hydropower project (PHP). LULC change assessments across regions and locations have not been the same across the board but differ from one location to another with their own consequences. Additionally, it has been recognised in literature (e.g., Mango et al. [30]; Woyessa and Welderufae, [31] that LULC changes have an influence on hydrology. LULC changes also have implications for water availability. Information on LULC changes has also served as a very important constituent for modelling and understanding the earth as a system. As a result, LULC studies have therefore become vital in enhancing our understanding and monitoring of environmental change. Therefore, the study of LULC changes in the region of the proposed PHP is justified.

The findings of LULC changes over the thirty-year period would aid governments and policymakers in providing optimal measures to meet the increasing demands of human needs, especially as the population increases. It would also help to aid environmental policy formulators and implementers in the adoption of more sustainable development strategies in line with sustainable development goals (SDGs) 11, 13, and 15.

2. Materials and methods

2.1. Description of the study area

The location of the proposed PHP is on the White Volta River, around 30 kilometres to the southwest of Bolgatanga, and lies between the Upper East and the North-East Regions of Ghana. This location may be found using the following coordinates: 10°34′59.54″ N, 0°41′33.81″ W [54].

According to the Ghana Statistical Service [55] the study area is covered with Guinea Savannah Forest with thin, small deciduous trees and grassy ground flora. As a result, the area is densely forested with trees such as acacia, baobab, dawadawa, and sheanuts [55]. Cereal crops such as maize, guinea corn, millet, beans, rice, and sorghum are cultivated in the catchment area. Based on the 2021 population and housing census of Ghana, 72.2% of the total population in the two regions lives in rural areas. It is not surprising that the main economic activity of the people in the catchment area is agriculture (farming and animal rearing).

The area has two climate seasons: dry and rainy. The rainy season is between May and October, and the dry season begins from November to April [55].

The main purpose of this study is to assess LULC changes in the region of the proposed PHP. This study is being conducted as the government of Ghana prepares to construct the three-throng project. These are solar, irrigation, and hydroelectric, all known as the Pwalugu Multipurpose Dam (PMD) project (**Figure 1**). To achieve the aforementioned, three objectives were established: first**,** to define and classify the various LULC kinds; second, to quantify the LULC changes. third, to determine the rate of LULC changes over the thirty-year period. The study area is shown in **Figure 2**.

Locations of the solar project site and the project site for the proposed PMD:

Figure 1. Scoping report (VRA).

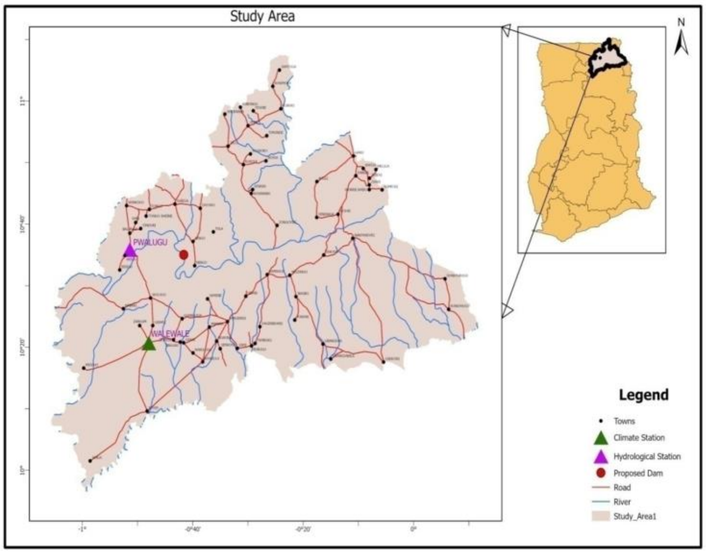

Figure 2. The study area (left) and Ghana map (right top).

2.2. Field data collection

Landsat Imagery

In fulfilling the purpose of this study, two sorts of data, namely satellite and ancillary data, were utilised. The satellite data consists of three (3) multi-temporal satellite images from different years. Landsat 5 images from 1990, whereas Landsat 7 and 8 images from 2000 and 2020 were acquired from the United States Geological Survey (USGS) GLOVIS website (**Table 1**). These Landsat pictures were selected to reflect the LULC conditions of the area. Ancillary data includes ground truth data for the LULC classes in the form of reference points gathered using the Global Positioning System (GPS) for the 2020 picture analysis. The observed land use conditions and recorded GPS locations were used for image classification and an overall accuracy assessment of the classification results. This satellite data is produced by the USGS and is freely accessible at the website [56].

The particular research strategies and conceptual frameworks that were utilised for this investigation are depicted in **Figure 3**.

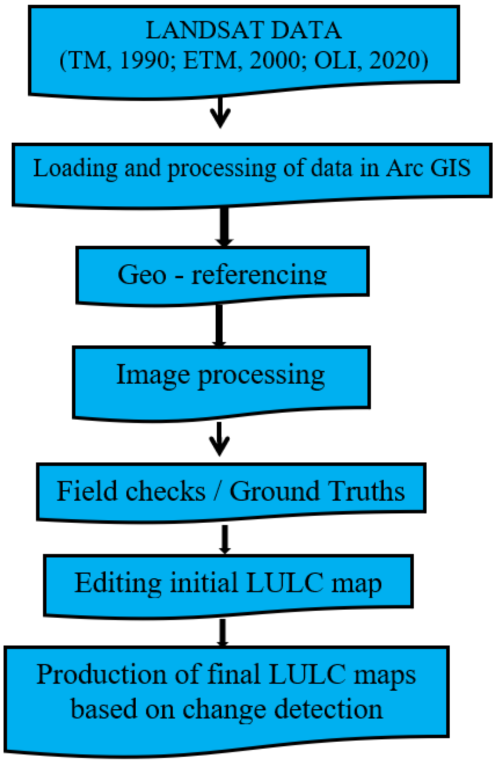

Figure 3. A Flow chart of LULC Change detection at the catchment area of the proposed PHP.

Table 1. Characteristics and properties of the Landsat images used.

Acquisition Date	Path/Row	Landsat	Sensor	Resolution	Source
5 October 1990	194/53 and 194/52	Landsat 5	TM	30 m	USGS
22 September 2000	194/52 and 194/53	Landsat 7	ETM+	30 m	USGS
16 May 2020	194/52 and 194/53	Landsat 8	OLI–TIRS	30 m	USGS

3. Results and analysis

As indicated earlier, our intention was to assess the LULC changes in the region of the proposed PHP using GIS and RS. After obtaining the raster image of LULC classes for Landsat 5, 7, and 8 images for classifications, three LULC maps were produced. **Figures 4–6** represent the LULC maps for the various years (1990, 2000, and 2020). Information on LULC definitions and classifications for supervised classifications in line with the first objective is in **Table 2**. A quantitative analysis of the LULC changes in line with the second objective can be seen in **Table 3**, which is further detailed in **Figure 7**. The third objective is to determine the rate of LULC changes over the thirty-year period. **Figures 8–10** are in fulfilment of the third objective of this study. The **Figures 8–10** show a graphical explanation of the rate of

LULC changes over the thirty-year period. Thus, LULC changes between 1990–2000, 2000–2020, and 1990–2020.

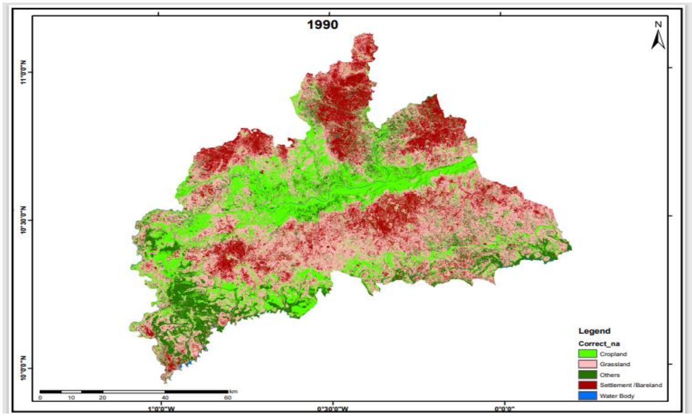

Figure 4. LULC classification map of the study area for the year 1990.

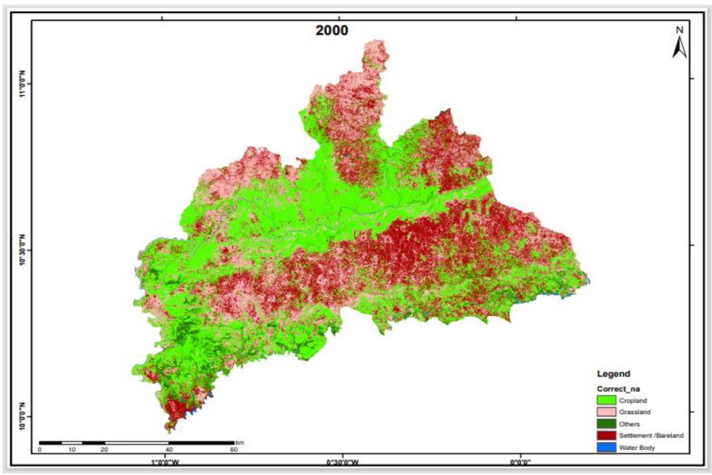

Figure 5. LULC classification map of the study area for the year 2000.

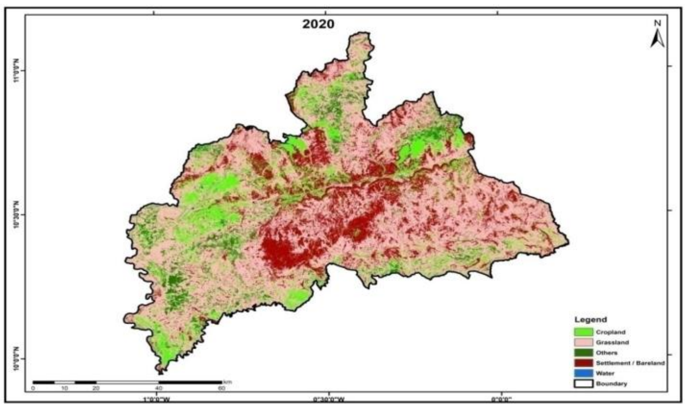

Figure 6. LULC classification map of the study area for the year 2020.

Table 2. LULC definition and classifications for supervised classifications.

Land cover	Description
Cropland	This land is used primarily for cultivating food crops such as corn, onions, beans, cassava, cabbages, carrots, Sorghum, millet, and mangoes. This region's crops are either irrigated or rain-fed.
Grassland	This category of land cover identifies grass as the predominant plant cover.
Settlement/Bare-land	This class describes the rural and urban land covered by buildings. It contains facilities for commerce, residence, industry, and transportation. It also refers to the land that is devoid of flora.
Waterbody	This category of land cover describes places covered with water along the riverbed or within earth dams, sand dams, and ponds created by humans.
Others	This defines the areas with evergreen trees primarily growing naturally on the reserved land, along the rivers, and on the hills, as well as the sparsely forested and shrubby regions.

Table 3. Area transition for LULC classes between 1990, 2000 and 2020.

LULC type	1990		2000		2020	
	Area (km^2)	**% Area**	**Area (km^2)**	**% Area**	**Area (km^2)**	**% Area**
Cropland	1781.94	21.92	3217.89	39.58	729.27	8.97
Grassland	3515.01	43.24	3845.06	47.30	4833.31	59.45
Settlement/Bareland	1303.83	16.04	338.44	4.16	720.19	8.86
Water body	29.69	0.37	43.26	0.53	23.07	0.28
Others	1498.97	18.44	684.78	8.42	1823.59	22.43
Total	8129.43	100.00	8129.43	100.00	8129.43	100.00

The figure below (**Figure 7**) shows the total area (in percentage) covered by each LULC class in 1990, 2000, and 2020.

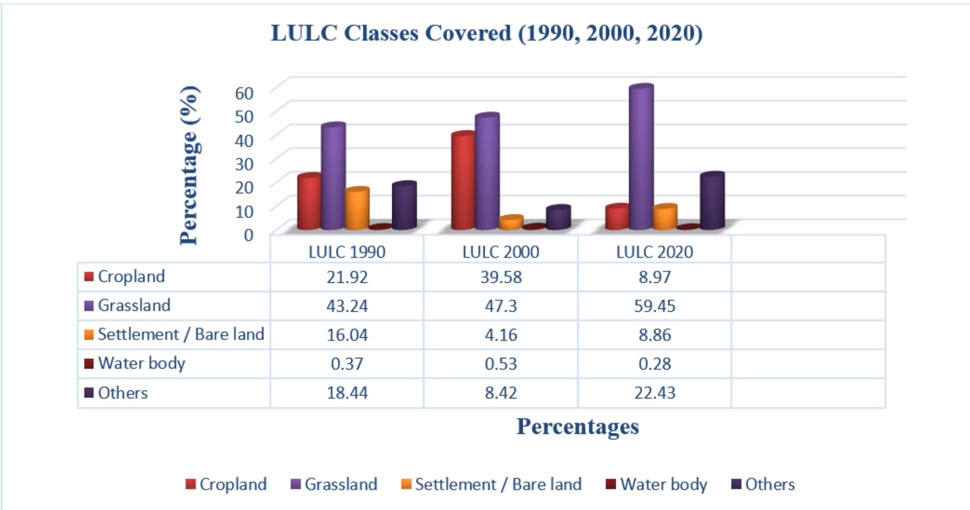

Figure 7. Total area (in percentage) covered by each LULC class in 1990, 2000, and 2020.

Figures 8–10 show the rate of LULC changes (gains or losses) between the period of years under consideration within the thirty-year period that the study lasts.

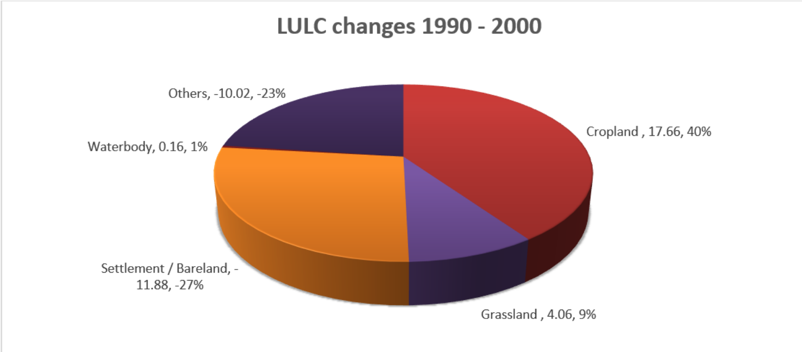

Figure 8. Graphical representation of the LULC changes (1990–2000).

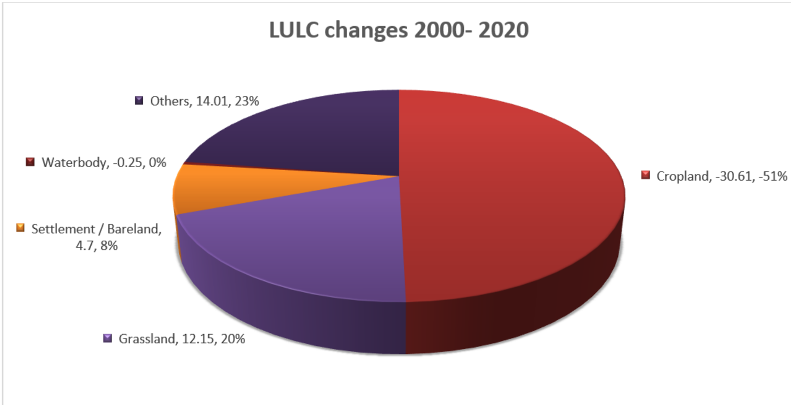

Figure 9. Graphical representation of the LULC changes (2000–2020).

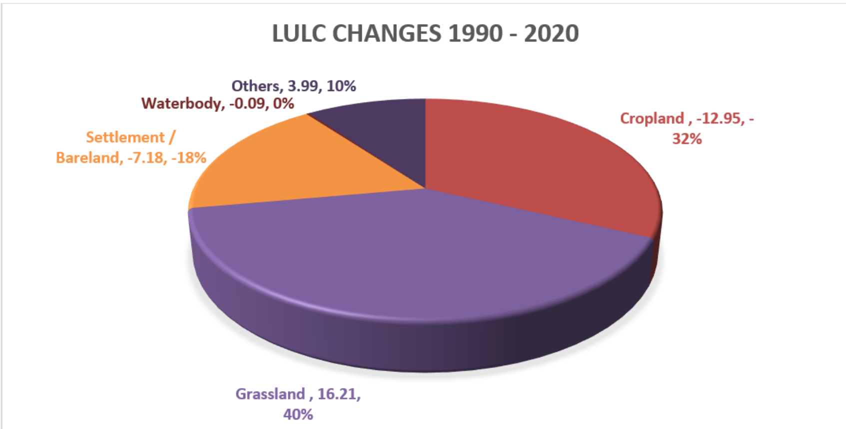

Figure 10. Graphical representation of the LULC changes (1990–2020).

The region of the proposed PHP always gets flooded, especially due to the spillage of the Bagre dam in Burkina Faso. Owing to climate variability coupled with human activities in the region of the proposed PHP, the water bodies are the most stressed natural resources (**Figures 8–10**). Thus, rivers, dams, and other dugouts in the region show significant morphological variations due to climate change. As the water body shrinks, this leads to an increase in the areas classified as others.

The rates of change of LULC within the region of the proposed PHP show an explicit net change in the form of gains and losses for each class during the periods (**Figures 8–10**). The first period (1990–2000) saw settlements, bare land, and areas classified as others record 27% and 23% losses, respectively. Within the same period, water bodies, grassland, and cropland had 1%, 9%, and 40% gains, respectively. The spatial analysis in this period (1990–2000) therefore indicated that cropland was the principal LULC (**Figure 8**).

The pattern of LULC changes in the second period (2000–2020), however, saw losses in cropland (49%) and water bodies (0%). The losses noticed in the two LULC classes could be due to early harvesting of crops, changes in climate, and anthropogenic activities. During the same period, settlements, bare land, grassland, and areas classified as others recorded 8%, 20%, and 23% gains, respectively. The area classified as others is the principal LULC change for the period 2000–2020.

Again, in the third period (1990–2020), water bodies, settlements, bare land, and cropland recorded (–0.09) 0%, 18%, and 32% losses, respectively. The period also registered 10% and 40% gains in grassland and areas classified as others, respectively. The net change for the period 1990–2020 shows grassland as the principal LULC change.

The area classified as others is defined as the areas with evergreen trees primarily growing naturally on the reserved land, along the rivers, and on the hills, as well as the sparsely forested and shrubby regions (**Table 2**). These LULC classes of area have a positive trend over the three periods. It increases from a 23% loss in 1990–2000 to a 23% gain in 2000–2020 and a further appreciation of 10% in the 1990–2020 periods. This means that the proposed region has vegetation that shows a positive trend.

The region of LULC classified as grassland has seen a steady increase or gain over the three periods. On the contrary, cropland as well as water bodies have seen a drastic shrink over the years. This implies that climate change has greatly impacted the region of the proposed PHP. It further shows that afforestation has also impacted the region, as the LULC classified as others remains stable throughout the period. It can therefore be concluded that climate change and afforestation would play a major role in the sustainability of the proposed PHP.

Charcoal production is one of the occupations of people living in rural Ghana. This could be the reason why the area classified as others increased from 2000–2020 (23%) but shrank in 1990–2020 (10%). Deforestation, a growing population, and a changing climate could be responsible for the changes.

Again, the findings suggest that, during this thirty-year period, cropland, settlements, bare land, water bodies, and areas classified as others shrank. The reason attributed to the shrinking of the settlement or bare land class could be due to the immigration of people to urban areas. Whereas it further suggests that climate change could be responsible for the shrinking of cropland and water body areas.

The housing and population figures of Ghana show that a great number of the populace lives in rural areas, especially in the study area. Since the main occupation of the populace in the study area is fishing and farming, the beginning and completion of the construction of the three-throng project (solar, irrigation, and dam), also known as the PMD, would go a long way towards boosting the economic activities of the farmers. It therefore behoves the government and other policymakers to take steps to make all-year-round farming a possibility for the many farmers in and around the proposed PHP.

4. Conclusion

This study analysed LULC changes for the years 1990, 2000, and 2020 using RS and GIS in the region of the proposed PHP. The utilisation of RS and GIS tools was helpful in detecting changes in the LULC that have taken place in the region of the proposed PHP over the period. This study unveils five LULC classes that has transformed significantly over this thirty-year period.

It is detected that grassland has increased from 9%, 20%, and 40% within the three periods (1990–2000, 2000–2020, and 1990–2020), whilst the remaining four (4) classes varied. The key factors responsible for the variations in the LULC classes are: population growth, changes in climate, deforestation and the decline of water bodies during this thirty-year period. In summary, LULC changes in the region of the proposed PHP are driven by natural and human activities. The variations in the LULC would have a significant influence on the hydrological processes in the form of evapotranspiration, interception, and infiltration.

The study also revealed that the combination of RS and GIS comes at a low cost, with greater precision and therefore have proven to be a powerful device for prompt decision-making in determining LULC changes in any area.

The decline in water bodies has resulted in irrigation problems thereby affecting all-year-round agriculture. It is therefore recommended that the preservation of the environment and the expansion of agriculture must be given precedence to help mitigate the challenges.

Author contributions: Conceptualization, EKA; methodology, EKA; software, EKA; validation, EKA; formal analysis, EKA; investigation, EKA; resources, EKA; data curation, EKA; writing—original draft preparation, EKA; writing—review and editing, EKA; visualization, EKA; supervision, ATK and SG. All authors have read and agreed to the published version of the manuscript.

Conflict of interest: The authors declare no conflict of interest.

References

1. Quentin FB, Jim C, Julia C, et al. Drivers of land use change, Final report: Matching opportunities to motivations, ESAI project 05116. Royal Melbourne Institute of Technology; 2006.
2. Lambin EF, Geist HJ, Lepers E. Dynamics of Land-Use and Land-Cover Change in Tropical Regions. Annual Review of Environment and Resources. 2003; 28(1): 205-241. doi: 10.1146/annurev.energy.28.050302.105459
3. Chrysoulakis N, Kamarianakis Y, Farsari Y, et al. Combining Satellite and Socio-economic data for Land-use Models estimation. Geography, Environmental Science; 2004.
4. Zubair AO. Change Detection in Land Use and land Cover Using Remote Sensing Data and GIS: A Case Study of Ilorin and Its Environs in Kwara State. Available online: https://www.geospatialworld.net/wpcontent/uploads/2016/04/OpeyemiZubair_ThesisPDF.pdf (accessed on 6 March 2024).
5. FAO (Food and Agriculture Organization of the United Nations). State of the World's Forests 2005. Available online: https://fao.org/docrep/pdf/007/y5574e/y5574e00.pdf (accessed on 17 March 2024).
6. Mather AS, Needle CL. The relationships of population and forest trends. Geography Journal. 2000; 166(1): 2–13.
7. Campbell DJ, Lusch DP, Smucker TA, et al. Multiple Methods in the Study of Driving Forces of Land Use and Land Cover Change: A Case Study of SE Kajiado District, Kenya. Human Ecology. 2005; 33(6): 763-794. doi: 10.1007/s10745-005-8210-y

8. Briassoulis H. Land Use, Land Cover and Soil Sciences—Land-use, land-cover changes and global aggregate impacts. Available online: https://www.eolss.net/sample-chapters/c19/E1-05-01-07.pdf (accessed on 6 March 2024).
9. Auch RF, Napton DE, Kambly S, et al. The Driving Forces of Land Change in the Northern Piedmont of the United States. Geographical Review. 2012; 102(1): 53-75. doi: 10.1111/j.1931-0846.2012.00130.x
10. Kanianska R, Kizeková M, Nováček J, et al. Land-use and land-cover changes in rural areas during different political systems: A case study of Slovakia from 1782 to 2006. Land Use Policy. 2014; 36: 554-566. doi: 10.1016/j.landusepol.2013.09.018
11. Sanderson MG, Wiltshire AJ, Betts RA. Projected changes in water availability in the United Kingdom. Water Resources Research. 2012; 48(8). doi: 10.1029/2012wr011881
12. Perugini L, Caporaso L, Marconi S, et al. Biophysical effects on temperature and precipitation due to land cover change. Environmental Research Letters. 2017; 12(5): 053002. doi: 10.1088/1748-9326/aa6b3f
13. Mehari M, Melesse M, Jianhua L. The study of land use and land cover (LULC) dynamics and the perception of local people in Aykoleba, Northern Ethiopia. African Journal of Environmental Science and Technology. 2021; 15(7): 282-297. doi: 10.5897/ajest2021.3022
14. Reid RS, Kruska RL, Muthui N, et al. Land-use and land-cover dynamics in response to changes in climatic, biological and socio-political forces: the case of southwestern Ethiopia. Landscape Ecology. 2000; 15: 339-355.
15. Sterling SM, Ducharne A, Polcher J. The impact of global land-cover change on the terrestrial water cycle. Nature Climate Change. 2012; 3(4): 385-390. doi: 10.1038/nclimate1690
16. Trimble SW, Crosson P. U.S. Soil Erosion Rates--Myth and Reality. Science. 2000; 289(5477): 248-250. doi: 10.1126/science.289.5477.248
17. Sala OE, Chapin FS, Armesto JJ, et al., Global Biodiversity Scenarios for the Year 2100. Science. 2000; 287: 1770-1774. doi: 10.1126/science.287.5459.1770 Science 287, 1770
18. Vitousek PM, Aber JD, Howarth RW, et al. Human alteration of the global nitrogen cycle: sources and consequences. Ecological Applications. 1997; 7: 737–750. doi: 10.1890/1051-0761(1997)007[0737:haotgn]2.0.co;2
19. Praveen K, Ganguly S, &Wakchaure R. Environmental pollution and safety measures international issues and its global impact. Global Progress in Development of Sustainable Environment. 2017; 40-65.
20. Gashaw T, Tulu T, Argaw M, et al. Modeling the hydrological impacts of land use/land cover changes in the Andassa watershed, Blue Nile Basin, Ethiopia. Science of The Total Environment. 2018; 619-620: 1394-1408. doi: 10.1016/j.scitotenv.2017.11.191
21. Jaksa WT, Sridhar V. Effect of irrigation in simulating long-term evapotranspiration climatology in a human-dominated river basin system. Agricultural and Forest Meteorology. 2015; 200: 109-118. doi: 10.1016/j.agrformet.2014.09.008
22. Ahiablame L, Sinha T, Paul M, et al. Streamflow response to potential land use and climate changes in the James River watershed, Upper Midwest United States. Journal of Hydrology: Regional Studies. 2017; 14: 150-166. doi: 10.1016/j.ejrh.2017.11.004
23. Welde K, Gebremariam B. Effect of land use land cover dynamics on hydrological response of watershed: Case study of Tekeze Dam watershed, northern Ethiopia. International Soil and Water Conservation Research. 2017; 5(1): 1-16. doi: 10.1016/j.iswcr.2017.03.002
24. Wang B, Yim SY, Lee JY, et al. Future change of Asian-Australian monsoon under RCP 4.5 anthropogenic warming scenario. Climate Dynamics. 2013; 42(1-2): 83-100. doi: 10.1007/s00382-013-1769-x
25. Niraula R, Meixner T, Norman LM. Determining the importance of model calibration for forecasting absolute/relative changes in streamflow from LULC and climate changes. Journal of Hydrology. 2015; 522: 439-451. doi: 10.1016/j.jhydrol.2015.01.007
26. Seong C, Sridhar V. Hydroclimatic variability and change in the Chesapeake Bay Watershed. Journal of Water and Climate Change. 2016; 8(2): 254-273. doi: 10.2166/wcc.2016.008
27. Sridhar V, Wedin DA. Hydrological behaviour of grasslands of the Sandhills of Nebraska: water and energy-balance assessment from measurements, treatments, and modelling. Ecohydrology. 2009; 2(2): 195-212. doi: 10.1002/eco.61
28. Sridhar V, Anderson KA. Human-induced modifications to land surface fluxes and their implications on water management under past and future climate change conditions. Agricultural and Forest Meteorology. 2017; 234-235: 66-79. doi: 10.1016/j.agrformet.2016.12.009

29. Wang YC, Hu BKH, Myint SW, et al. Patterns of land change and their potential impacts on land surface temperature change in Yangon, Myanmar. Science of The Total Environment. 2018; 643: 738-750. doi: 10.1016/j.scitotenv.2018.06.209
30. Mango LM, Melesse AM, McClain ME, et al. Land use and climate change impacts on the hydrology of the upper Mara River Basin, Kenya: results of a modeling study to support better resource management. Hydrology and Earth System Sciences. 2011; 15(7): 2245-2258. doi: 10.5194/hess-15-2245-2011
31. Woyessa YE, Welderufael WA. Impact of land-use change on catchment water balance: a case study in the central region of South Africa. Geoscience Letters. 2021; 8(1). doi: 10.1186/s40562-021-00204-9
32. Bronstert A, Niehoff D, Bürger G. Effects of climate and land-use change on storm runoff generation: present knowledge and modelling capabilities. Hydrological Processes. 2002; 16(2): 509-529. doi: 10.1002/hyp.326
33. Foley JA, DeFries R, Asner GP, et al. Global Consequences of Land Use. Science. 2005; 309(5734): 570-574. doi: 10.1126/science.1111772
34. Tang Z, Engel BA, Pijanowski BC, et al. Forecasting land use change and its environmental impact at a watershed scale. Journal of Environmental Management. 2005; 76(1): 35-45. doi: 10.1016/j.jenvman.2005.01.006
35. Ott B, Uhlenbrook S. Quantifying the impact of land-use changes at the event and seasonal time scale using a process-oriented catchment model. Hydrology and Earth System Sciences. 2004; 8(1): 62-78. doi: 10.5194/hess-8-62-2004
36. Awotwi A, Yeboah F, Kumi M. Assessing the impact of land cover changes on water balance components of White Volta Basin in West Africa. Water and Environment Journal. 2014; 29(2): 259-267. doi: 10.1111/wej.12100
37. Awotwi A, Anornu GK, Quaye-Ballard JA, et al. Water balance responses to land-use/land-cover changes in the Pra River Basin of Ghana, 1986–2025. CATENA. 2019; 182: 104129. doi: 10.1016/j.catena.2019.104129
38. Chang Y, Hou K, Li X, et al. Review of Land Use and Land Cover Change research progress. IOP Conference Series: Earth and Environmental Science. 2018; 113: 012087. doi: 10.1088/1755-1315/113/1/012087
39. Ayala-Silva T, Gordon G, Heath R. Use of Satellite Data to Study the Impact of Land-Cover/Land-Use Change in Madison County Alabama. American Journal of Applied Sciences. 2009; 6(4): 656-660. doi: 10.3844/ajassp.2009.656.660
40. Rawat JS, Kumar M. Monitoring land use/cover change using remote sensing and GIS techniques: A case study of Hawalbagh block, district Almora, Uttarakhand, India. The Egyptian Journal of Remote Sensing and Space Science. 2015; 18(1): 77-84. doi: 10.1016/j.ejrs.2015.02.002
41. Berrick NOS. What Is Remote Sensing? Available online: https://earthdata.nasa.gov/learn/ backgrounders/remote-sensing (accessed on 12 March 2024).
42. Chaikaew P. Land Use Change Monitoring and Modelling using GIS and Remote Sensing Data for Watershed Scale in Thailand. Land Use - Assessing the Past, Envisioning the Future. Published online March 13, 2019. doi: 10.5772/intechopen.79167
43. Halefom AT, Sisay E, Khare D, et al. Applications of remote sensing and gis in land use/land cover change detection: A case study of WoretaZuria watershed, Ethiopia. Applied Research Journal of Geographic Information System. 2018; 1: 1–9.
44. Abd El-Kawy OR, Rød JK, Ismail HA, et al. Land use and land cover change detection in the western Nile delta of Egypt using remote sensing data. Applied Geography. 2011; 31(2): 483-494. doi: 10.1016/j.apgeog.2010.10.012
45. Dymond JR, Shepherd JD, Newsome PF, et al. Remote sensing of land-use change for Kyoto Protocol reporting: the New Zealand case. Environmental Science & Policy. 2012; 16: 1-8. doi: 10.1016/j.envsci.2011.11.011
46. Md Islam R, Khan NI, Khan Z, Roy B. A three decade assessment of forest cover changes in Nijhumdwip national park using remote sensing and GIS. Environmental Challenges. 2021; 4: 100162.
47. Braimoh AK, Vlek PLG., Scale dependent relationships between land-use change and its determinants in the Volta Basin of Ghana. Earth Interact. 2004; 8: 1–23. doi:10.1175/1087-3562(2004)008.
48. Alo CA, Pontius RG. Identifying Systematic Land-Cover Transitions Using Remote Sensing and GIS: The Fate of Forests inside and outside Protected Areas of Southwestern Ghana. Environment and Planning B: Planning and Design. 2008; 35(2): 280-295. doi: 10.1068/b32091
49. Kusimi JM. Characterizing land disturbance in Atewa Range Forest Reserve and Buffer Zone. Land Use Policy. 2015; 49: 471-482. doi: 10.1016/j.landusepol.2015.08.020
50. Kleeman J, Baysal G, Bulley HNN, Furst C. Assessing driving forces of land use and land cover change by a mixed-method approach in North-Eastern Ghana. Journal of Environmental Management. 2017; 196: 411–442. doi: 10.1016/j.jenvman.2017. 01.053

51. Karki S, Thandar AM, Uddin K, et al. Impact of land use land cover change on ecosystem services: a comparative analysis on observed data and people's perception in Inle Lake, Myanmar. Environmental Systems Research. 2018; 7(1). doi: 10.1186/s40068-018-0128-7
52. Kpienbaareh D, Oduro Appiah J. A geospatial approach to assessing land change in the built-up landscape of Wa Municipality of Ghana. Geografisk Tidsskrift-Danish Journal of Geography. 2019; 119(2): 121-135. doi: 10.1080/00167223.2019.1587307
53. Oduro Appiah J, Kpienbaareh D, Adomako JAA. Built-up area expansion in the Wa Municipality of Ghana: implications for vegetation cover loss and fragmentation. African Geographical Review. 2021; 41(3): 364-384. doi: 10.1080/19376812.2021.1919532
54. VRA. Pwalugu Multipurpose Dam Project—Environmental Impact Assessment: Scoping Report. Available online: https://www.vra.com/media/2021/50%20MW%20Solar%20Hybrid%20-PMPDP%20-Scoping%20Report%20-%20Final%20Report_online.pdf (accessed on 6 March 2024).
55. GSS (Ghana Statistical Service). 2010 Population and Housing Census: District Analytical Report, Talensi District. Available online: https://www.google.com/url?sa=t&rct=j&q=&esrc=s&source=web&cd=&cad=rja&uact=8&ved=2ahUKEwiS_cD_iZ-HAxUrWUEAHcxnCA8QFnoECCQQAQ&url=https%3A%2F%2Fstatsghana.gov.gh%2Fgssmain%2FfileUpload%2Fpressrelease%2F2021%2520PHC%2520General%2520Report%2520Vol%25203A_Population%2520of%2520Regions%2520and%2520Districts_181121.pdf&usg=AOvVaw0oAt1cZCAn42icD1NZkTkc&opi=89978449 (accessed on 16 March 2024).
56. USGS. EarthExplorer. Available online: https://earthexplorer.usgs.gov/ (accessed on 24 March 2024).

Journal of Geography and Cartography 2024, 7(2), 6694.
https://doi.org/10.24294/jgc.v7i2.6694

Article

New definitions of isometric latitude and the Mercator projection of the ellipsoid

Miljenko Lapaine

University of Zagreb, Faculty of Geodesy, 10000 Zagreb, Croatia; mlapaine@geof.hr

CITATION

Lapaine M. New definitions of isometric latitude and the Mercator projection of the ellipsoid. Journal of Geography and Cartography. 2024; 7(2): 6694. https://doi.org/10.24294/jgc.v7i2.6694

ARTICLE INFO

Received: 27 May 2024
Accepted: 21 June 2024
Available online: 6 July 2024

Abstract: The article discusses the interrelationships of the loxodrome or rhumb line, isometric latitude, and the Mercator projection of the rotational ellipsoid. It is shown that by applying the isometric latitude, a very simple equation of the rhumb line on the ellipsoid is obtained. The consequence of this is that the isometric latitude can be defined using the generalized geodetic longitude and not only using the geodetic latitude, as was usual until now. Since the image of the rhumb line in the plane of the Mercator projection is a straight line, the isometric latitude can also be defined using this projection. Finally, a new definition of the normal aspect of the Mercator projection of the ellipsoid is given. It is a normal aspect cylindrical projection in which the images of the rhumb line on the ellipsoid are straight lines in the plane of projection that, together with the images of the meridians in the projection, form equal angles as the rhumb line forms with the meridians on the ellipsoid. The article provides essential knowledge to all those who are interested in the use of maps in navigation. It will be useful for teachers and students studying cartography and GIS, maritime, or applied mathematics. The author uses mathematical methods, especially differential geometry. The assumption is that the readers are no strangers to mathematical cartography.

Keywords: map projection; rhumb line; isometric latitude; generalized longitude; ellipsoid

1. Introduction

In this article, we begin with the derivation of the rhumb line equation on a rotational ellipsoid with geodetic parameterization. Then, instead of the geodetic latitude, we introduce isometric latitude as a parameter. It is shown that in this way a very simple equation of the rhumb line on the ellipsoid is arrived at. It is a linear relationship between the isometric latitude and geodetic longitude, with the fact that the geodetic longitude should be taken in a generalized sense, i.e., from the interval $(-\infty, \infty)$. This, in turn, allows us to define the isometric latitude on the ellipsoid using the rhumb line and geodetic longitude.

After that, we consider the normal aspect Mercator projection of the ellipsoid in the usual way and using the isometric latitude. Then we derive the equation of the rhumb line image in that projection. This gives us the possibility of a new interpretation of the isometric latitude using the normal aspect Mercator projection of the ellipsoid. Finally, the idea appears to approach the Mercator projection in a new way. We define it as a normal aspect cylindrical projection in which the images of the rhumb line from the ellipsoid are straight lines in the plane of the projection that make the same angles with the images of the meridians in the projection as the rhumb lines with the meridians on the ellipsoid.

The results of this article are generalizations to the ellipsoid of the results published in the article that dealt with the relationship between the rhumb line, the isometric latitude, and the Mercator projection of the sphere [1].

In geography, latitude is a coordinate that determines the position of a point on the Earth's surface in the north-south direction. It is an angle that ranges from −90° at the South Pole to 90° at the North Pole, with 0° at the equator. Lines of constant latitude, or parallels, run east-west as circles parallel to the equator. Latitude and longitude are used together as a pair of coordinates to determine a location on the Earth's ellipsoid.

There is relatively detailed cartographic literature on loxodromes, isometric latitude, and the Mercator projection [2−5].

Isometric latitude (see details in section 3) appears in conformal mappings [6,7]. For instance, isometric latitude is used in the derivation of the Gauss-Krüger projection, the normal and transverse aspects of the Mercator projection, and any other conformal map projection [8]. The name "isometric" derives from the fact that at any point on an ellipsoid, equal increments of isometric latitude and longitude lead to equal displacements of distance along the meridians and parallels. A cartographic network defined by lines of constant isometric latitude and constant longitude divides the surface of an ellipsoid into a network of squares (of different sizes). Isometric latitude is equal to zero at the equator but quickly deviates from geodetic latitude, tending to infinity at the poles.

The Mercator projection is one of the most famous map projections. Even in recent times, it has been researched and written about by many, e.g., Kawase [9], Abee [10], Lapaine and Frančula [11], Pápay [12] and Kerkovits [13]. Lapaine and Frančula [11] investigate a new variant of the Mercator projection, the web-Mercator projection. Kerkovits [13] deals with the transverse Mercator projection and the problem of secant cylinders.

The loxodrome and the Mercator projection are closely related to navigation [14−17]. The loxodrome was specially investigated by Alexander [18], Kos et al. [19,20], Elhashash [21], Petrović [22,23], Weintrit and Kopcz [24], Babaarslan and Yayli [25], Kovalchuk and Mladenov [26] and Lambrinos et al. [27].

Petrović [22] considers the rhumb line on the rotational ellipsoid, but only gives equations without a more detailed derivation and without concrete applications. Alexander [18] mainly deals with the historical development and connection of the rhumb line with the Mercator projection. In maritime and air navigation, ships and aircraft sailing or flying along fixed compass directions travel along a rhumb line, so knowing the properties of a rhumb line is important. It is known that the normal aspect of the Mercator projection (cylindrical conformal projection) has the unique property that rhumb lines from the Earth's ellipsoid are mapped as straight lines on the map. Tseng et al. [28] deal with solving the direct and inverse problem of navigation along the rhumb line.

The primary goal of the study and its novelty are found in the title of the article, i.e., a new definition of isometric latitude and the Mercator projection of the ellipsoid will be explained and given. Scientists from diverse fields will be able to grasp the essential aspects of the research if they know the basics of mathematics, especially differential geometry.

2. The equation of the rhumb line on the rotational ellipsoid

Let us recall that the following expressions define a rotational ellipsoid with the center at the origin of the coordinate system, the semi-major axis a, and the numerical eccentricity e:

$$\begin{gathered} x = x(\varphi,\lambda) = M\cos\varphi\cos\lambda,\; y = y(\varphi,\lambda) = M\cos\varphi\sin\lambda, \\ z = z(\varphi,\lambda) = N(1-e^2)\sin\varphi \\ (\varphi,\lambda) \in \left[-\frac{\pi}{2},\frac{\pi}{2}\right] \times [-\pi,\pi],\; (x,y,z) \in \mathrm{R}^3 \end{gathered} \tag{1}$$

here, φ is the geodetic latitude, λ is the geodetic longitude,

$$M = M(\varphi) = \frac{a(1-e^2)}{\sqrt{(1-e^2\sin^2\varphi)^3}} \tag{2}$$

is the radius of curvature of the meridian and

$$N = N(\varphi) = \frac{a}{\sqrt{1-e^2\sin^2\varphi}} \tag{3}$$

is the radius of curvature of the section along the first vertical. We call the mapping (1) the geodetic parametrization of the rotating ellipsoid. The coefficients of the first differential form of this mapping are:

$$E = M^2,\; F = 0,\; G = N^2\cos^2\varphi.$$

The differential expressions for any curve on the rotational ellipsoid are [29]:

$$ds^2 = M^2 d\varphi^2 + N^2\cos^2\varphi d\lambda^2 \tag{4}$$

$$\cos\alpha\, ds = M d\varphi \tag{5}$$

$$\sin\alpha\, ds = N\cos\varphi\, d\lambda \tag{6}$$

$$\tan\alpha = \frac{N\cos\varphi d\lambda}{M d\varphi}. \tag{7}$$

where α is the angle between the observed curve and the meridian. Let us agree that the angle α will have a value from the interval $[0,2\pi]$. It is the azimuth that will be measured clockwise so that the relationships shown in **Table 1** apply.

Table 1. Basic relations between geodetic latitude, geodetic longitude and azimuth.

$\varphi_1 < \varphi_2$	$\lambda_1 < \lambda_2$	$\alpha \in \left(0,\frac{\pi}{2}\right)$
$\varphi_1 > \varphi_2$	$\lambda_1 < \lambda_2$	$\alpha \in \left(\frac{\pi}{2},\pi\right)$
$\varphi_1 > \varphi_2$	$\lambda_1 > \lambda_2$	$\alpha \in \left(\pi,\frac{3\pi}{2}\right)$
$\varphi_1 < \varphi_2$	$\lambda_1 > \lambda_2$	$\alpha \in \left(\frac{3\pi}{2},2\pi\right)$
$\varphi_1 = \varphi_2$	$\lambda_1 < \lambda_2$	$\alpha = \frac{\pi}{2}$
$\varphi_1 = \varphi_2$	$\lambda_1 > \lambda_2$	$\alpha = \frac{3\pi}{2}$
$\varphi_1 < \varphi_2$	$\lambda_1 = \lambda_2$	$\alpha = 0$
$\varphi_1 > \varphi_2$	$\lambda_1 = \lambda_2$	$\alpha = \pi$

Let $\alpha = \text{const}$. The differential equation of the rhumb line on the ellipsoid is then e.g., Equation (5), and can be solved as follows:

$$\cos\alpha \int ds = \int M d\varphi,$$

which after integration gives

$$s\cos\alpha = s_m(\varphi) - s_m(\varphi_1), \tag{8}$$

where

$$s_m(\varphi) = \int_0^{\varphi} M d\varphi. \tag{9}$$

Equation (8) is the equation of the rhumb line connecting the geodetic latitude φ and the arc length s. This rhumb line passes through a point with geodetic latitude φ_1 and at that point the arc length is 0.

Unlike the derivation of the rhumb line equation on the sphere, the integral on the right side in Equation (9) is an elliptic integral that appears when calculating the length of the arc of the meridian on the rotational ellipsoid and which cannot be integrated directly, but instead, developments in series or some other mathematical methods are applied. Lapaine [30] showed that for calculating the length of the arc of the meridian from the equator to the geodetic latitude φ, a suitable formula reads

$$s_m(\varphi) = A[\varphi + \sin 2\varphi(c_1 + (c_2 + (c_3 + (c_4 + c_5\cos 2\varphi)\cos 2\varphi)\cos 2\varphi)\cos 2\varphi)] + \cdots \tag{10}$$

where A, c_1, c_2, …, c_5 are corresponding coefficients.

In Equation (10), the length of the arc of the rhumb line is expressed as a function of the geodetic latitude. If it is necessary to express the geodetic latitude as a function of the length of the arc of the rhumb line, then we can use the formula that determines the geodetic latitude of a point on the meridian for which the length of the arc of the meridian from the equator to that point is known [30]:

$$\varphi(s_m) = \psi + \sin 2\psi(c_1 + (c_2 + (c_3 + (c_4 + c_5\cos 2\psi)\cos 2\psi)\cos 2\psi)\cos 2\psi) + \cdots \tag{11}$$

where c_1, c_2, …, c_5 are the corresponding coefficients and

$$\psi = \frac{s_m(\varphi)}{A},\ s_m(\varphi) = s\cos\alpha + s_m(\varphi_1). \tag{12}$$

Rhumb lines on a rotational ellipsoid are generally spiral curves that wrap around each pole an infinite number of times (**Figure 1**) and never reach it, although their length is finite. The length of the rhumb line from pole to pole is equal to the length of the arc of the meridian divided by the cosine of the angle α.

Indeed, in Equation (8) we should put $\varphi_1 = -\frac{\pi}{2}$, $\varphi = \frac{\pi}{2}$, so we get

$$s = \frac{s_m\left(\frac{\pi}{2}\right) - s_m\left(-\frac{\pi}{2}\right)}{\cos\alpha} = \frac{2s_m\left(\frac{\pi}{2}\right)}{\cos\alpha},\ \alpha \neq \frac{\pi}{2},\ \alpha \neq \frac{3\pi}{2}.$$

If we start with the differential Equation (6), we cannot integrate it immediately, but first we should express φ by means of λ or s. Therefore, we prefer to take Equation (7), which can be integrated if we write it in the form

$$d\lambda = \tan\alpha\frac{Md\varphi}{N\cos\varphi}. \tag{13}$$

After integration we get

$$\lambda = \tan\alpha\left[\ln\tan\left(\frac{\pi}{4} + \frac{\varphi}{2}\right)\left(\frac{1 - e\sin\varphi}{1 + e\sin\varphi}\right)^{\frac{e}{2}}\right] + \beta. \tag{14}$$

We note that according to Equation (14) $\lambda \in (-\infty, \infty)$ for $\varphi \in \left(-\frac{\pi}{2}, \frac{\pi}{2}\right)$. Therefore, λ is a generalized geodetic longitude [29].

If we want the rhumb line to pass through a point with geodetic coordinates (φ_1, λ_1), it is necessary to take the integration constant β like this.

$$\beta = \lambda_1 - \tan\alpha\left[\ln\tan\left(\frac{\pi}{4} + \frac{\varphi_1}{2}\right)\left(\frac{1 - e\sin\varphi_1}{1 + e\sin\varphi_1}\right)^{\frac{e}{2}}\right]. \tag{15}$$

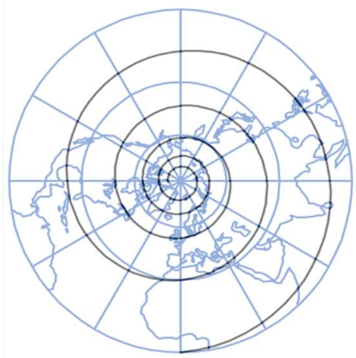

Figure 1. Rhumb line.

3. Isometric latitude and rhumb line

Taught by experience about the isometric latitude and rhumb line on a sphere [1], let us try an analogous approach on a rotating ellipsoid. In the theory of map projections, the isometric latitude q is defined by means of the geodetic latitude φ and the differential equation

$$dq = \frac{M d\varphi}{N \cos\varphi}. \tag{16}$$

The solution of the differential equation (16) is

$$q = \ln \tan\left(\frac{\pi}{4} + \frac{\varphi}{2}\right)\left(\frac{1 - e\sin\varphi}{1 + e\sin\varphi}\right)^{\frac{e}{2}} \tag{17}$$

with the assumption that for the integration constant we took the value that gives $q = 0$ for $\varphi = 0$. Note that $q \in (-\infty, \infty)$ for $\varphi \in \left(-\frac{\pi}{2}, \frac{\pi}{2}\right)$.

The inverse function cannot be written in its final form using elementary functions. Instead, different approximation procedures or approximate formulas are used [8].

If the conformal latitude χ is introduced as follows

$$\tan\left(\frac{\pi}{4} + \frac{\chi}{2}\right) = \tan\left(\frac{\pi}{4} + \frac{\varphi}{2}\right)\left(\frac{1 - e\sin\varphi}{1 + e\sin\varphi}\right)^{\frac{e}{2}} \tag{18}$$

then between it and the isometric latitude q, analogous to the relations for the sphere [1], the following relations apply:

$$\tanh q = \sin\chi,\ \sinh q = \tan\chi,\ \cosh q = \frac{1}{\cos\chi},$$
$$\tanh\frac{q}{2} = \tan\frac{\chi}{2},\ \exp(q) = \tan\left(\frac{\pi}{4} + \frac{\chi}{2}\right). \tag{19}$$

Furthermore, the differential Equation (7) written by using the isometric latitude q becomes very simple and reads

$$d\lambda = \tan\alpha\, dq. \tag{20}$$

After integration, we get the equation of the rhumb line on the ellipsoid in the form

$$\lambda = q\tan\alpha + \beta, \tag{21}$$

where β is a constant of integration. In that equation, λ is the generalized longitude or longitude in a broader sense. The corresponding value of longitude λ' from the interval $(-\pi, \pi)$ will be obtained as a remainder when dividing by 2π, i.e., by applying the Equation

$$\lambda' = \lambda - 2\pi \operatorname{sgn}(\lambda) \left[\frac{|\lambda|+\pi}{2\pi}\right], \tag{22}$$

where $\operatorname{sgn}(\lambda)$ is equal to 1, 0 or –1, according to whether λ is greater than, equal to or less than zero, and the square brackets indicate the largest integer function, i.e., $[x]$ is the largest integer that is smaller than x or equal to x.

If we want the rhumb line to pass through the point with coordinates (q_1, λ_1), it is necessary to take the integration constant β:

$$\beta = \lambda_1 - q_1 \tan\alpha\,. \tag{23}$$

Special cases

Meridians and parallels are special cases of rhumb lines (see **Table 1**). For meridians, $\alpha = k\pi$, $k = 0, 1$, and for parallels, $\alpha = \frac{\pi}{2} + k\pi$, $k = 0, 1$. Indeed, if we take $\alpha = k\pi$, $k = 0, 1$, then (5) turns into $s = \int_{\varphi_1}^{\varphi} M d\,\varphi$, and (6) into $\lambda = \lambda_1$.

For $\alpha = \frac{\pi}{2} + k\pi$, $k = 0, 1$, (5) becomes $\varphi = \varphi_1$, and the differential equation $ds = N(\varphi_1)\cos\varphi_1\, d\lambda$ gives the solution $s = N(\varphi_1)\cos\varphi_1\,(\lambda - \lambda_1)$.

4. Mercator projection of a rotational ellipsoid

The Mercator projection is a conformal cylindrical projection. This means that the basic equations of the normal aspect projection are

$$x = a\lambda,\; y = y(\varphi), \tag{24}$$

where φ and λ are geodetic latitude and longitude, respectively, a is a constant (it does not have to be the semi-axis of the ellipsoid!), while $y(\varphi)$ is a function that should be determined so that the projection is conformal. Let us suppose that the rotational ellipsoid given by Equation (1) should be conformally mapped into the plane according to Equation (24). The condition for this mapping to be conformal reads [2]:

$$h = k, \tag{25}$$

where *h* and *k* are local linear scale factors along the meridian and parallel, respectively. From the expression [2]

$$h = \frac{dy}{Md\varphi},\; k = \frac{a}{N\cos\varphi}, \tag{26}$$

it follows according to Equation (25)

$$\frac{dy}{Md\varphi} = \frac{a}{N\cos\varphi}, \tag{27}$$

i.e.,

$$dy = a\frac{Md\varphi}{N\cos\varphi}, \tag{28}$$

and from there

$$y = a\int\frac{Md\varphi}{N\cos\varphi} + K = a\ln\tan\left(\frac{\pi}{4}+\frac{\varphi}{2}\right)\left(\frac{1-e\sin\varphi}{1+e\sin\varphi}\right)^{\frac{e}{2}} + K, \tag{29}$$

where *K* is the constant of integration. The constants *a* and *K* can be chosen in different ways. For example, if we set the conditions $\varphi = 0$ and $y = 0$, it follows that $K = 0$. Finally, the normal aspect Mercator projection of the ellipsoid is given by

$$x = a\lambda,\; y = a\ln\tan\left(\frac{\pi}{4}+\frac{\varphi}{2}\right)\left(\frac{1-e\sin\varphi}{1+e\sin\varphi}\right)^{\frac{e}{2}}. \tag{30}$$

At the end, let us note that the equations of the Mercator projection (30) can be written in a very simple form using the isometric latitude q (17)

$$x = a\lambda, y = aq. \tag{31}$$

Rhumb line in the normal aspect Mercator projection of the ellipsoid

The equation of the rhumb line on the ellipsoid is Equation (21). If we substitute Equation (21) in Equation (31), we will get the equation of the image of the rhumb line in the Mercator projection

$$x = a(\tan\alpha\, q + \beta),\ y = aq. \tag{32}$$

Equation (32) represent the straight line equation in parametric notation. The parameter is the isometric latitude q. By eliminating that parameter, we can obtain the equation of the straight line in an explicit, implicit, or other form.

From Equation (21) we can get

$$q = \cot\alpha\,(\lambda - \beta) \tag{33}$$

and then from Equation (31)

$$x = a\lambda,\ y = a\cot\alpha\,(\lambda - \beta). \tag{34}$$

Equations (34) again represent the straight line equation in parametric notation. The parameter is now the generalized longitude λ, $\lambda \in (-\infty, \infty)$. If we need an ordinary geodetic longitude, we can get it using Equation (22). In a similar way, we could write the equation of the rhumb line in the Mercator projection plane parameterized by latitude φ or arc length s.

Figure 2 shows the rhumb line in the normal aspect Mercator projection with constants $\alpha = 75° = \frac{5\pi}{12}$, $\beta = 0$.

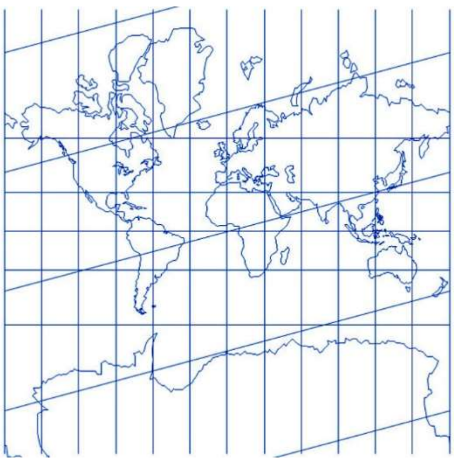

Figure 2. Rhumb line in the normal aspect Mercator projection.

Although the geometric interpretations of latitude and longitude on the ellipsoid as well as geocentric and reduced latitude are well known, a similar interpretation of isometric latitude is not easy to find. For example, Heck [31] says in his famous monograph: "While the geographic latitude φ can be given the geometric meaning of the direction of the normal on the surface, the numerical values of the isometric latitude cannot be clearly interpreted." A connection between rhumb line and isometric latitude was observed, and on this basis a new, very simple definition of isometric latitude was given. This definition is further generalized to the rotational ellipsoid [32]. This is also proof that the isometric latitude, contrary to Heck's claim, can be clearly interpreted.

Now we will give a new definition of the isometric latitude q on the ellipsoid using the Mercator projection of the ellipsoid.

Definition 1. *The isometric latitude of any point on the rotational ellipsoid is proportional to the y-ordinate of the image of that point in the normal aspect Mercator projection,* $q = \frac{y}{a}$. *The proportionality factor is* $\frac{1}{a} = \frac{1}{N(\varphi_0)\cos\varphi_0}$, *where* φ_0 *is the geodetic latitude of the standard parallel. If* $a = 1$, *then the isometric latitude of a point on the ellipsoid is equal to the y-ordinate of the image of that point in the normal aspect Mercator projection.*

5. A new approach to the Meractor projection

A common approach to deriving the equations of the normal aspect Mercator projection is to look for a cylindrical projection that satisfies the conformality condition (section 4 in this article). When we have the equations of the normal aspect Mercator projection, then we derive from them the equation of the rhumb line in that projection and show that it is always a straight line.

The new approach to the derivation of the equations of that projection does not start with setting the conformity condition. Instead, we set the condition that each rhumb line in the normal aspect cylindrical projection is mapped as a straight line. The equations of the normal aspect Mercator projection will emerge from this condition.

When Mercator made his map, he had in mind the rectilinearity of the loxodrome, not its conformality. Thus, the following derivation, in a way, connects Mercator's original idea with today's usual approach to his projection as a conformal cylindrical projection.

Let us start from the equations of a normal aspect cylindrical projection (24), where φ and λ are the geodetic latitude and longitude, respectively, a is a constant, and $y(\varphi)$ is a function to be determined assuming that each rhumb line on the ellipsoid is mapped in the normal aspect cylindrical projection to the straight line, which forms the same angle α with the positive direction of the y axis in the projection plane that the rhumb line encloses with all meridians on the ellipsoid. The equation of the rhumb line on the ellipsoid is (21), where α and β are constants, q is the isometric latitude, and λ is the generalized longitude. If we substitute Equation (21) in Equation (24), we will get the equation of the image of the rhumb line in the plane of the cylindrical projection

$$x = a(q\tan\alpha + \beta), y = y(\varphi). \tag{35}$$

In order for Equation (35) to be the equation of a straight line in parametric form with the parameter q, which closes the angle α with the positive direction of the y axis, the equation for y must be of the form

$$y = aq + b, \tag{36}$$

where b is a constant. According to Equation (17)

$$y = a\ln\tan\left(\frac{\pi}{4} + \frac{\varphi}{2}\right)\left(\frac{1-e\sin\varphi}{1+e\sin\varphi}\right)^{\frac{e}{2}} + b. \tag{37}$$

Therefore, the equations of the normal aspect cylindrical projection of the ellipsoid, which has the property that every rhumb line on the ellipsoid that encloses an angle α with the meridians is mapped to a straight line in the projection plane that encloses the same angle α with the images of the meridians are

$$x = a\lambda,\ y = a \ln \tan\left(\frac{\pi}{4} + \frac{\varphi}{2}\right)\left(\frac{1-e\sin\varphi}{1+e\sin\varphi}\right)^{\frac{e}{2}} + b. \tag{38}$$

With the usual condition in map projections that $y = 0$ for $\varphi = 0$, it follows $b = 0$, so we have

$$x = a\lambda,\ y = a \ln \tan\left(\frac{\pi}{4} + \frac{\varphi}{2}\right)\left(\frac{1-e\sin\varphi}{1+e\sin\varphi}\right)^{\frac{e}{2}}, \tag{39}$$

where we recognize the equations of the normal aspect Mercator projection of the rotational ellipsoid.

6. Conclusion

It is known that instead of the geodetic latitude, it is convenient to introduce the isometric latitude as a parameter when it comes to the issue of preserving angles. We have shown that in this way we arrive at a very simple equation of the rhumb line on the ellipsoid. This is a linear relationship between the isometric latitude and geodetic longitude, with the fact that geodetic longitude should be taken in a generalized sense, i.e., from the interval $(-\infty, \infty)$. This made it possible to define the isometric latitude using the rhumb line and geodetic longitude.

The traditional definition of isometric latitude is found in the article, Equation (17), and has nothing to do with the rhumb line. In the article, it was shown that isometric latitude is in a simple linear relationship with longitude, Equation (21). On the other hand, the ordinate of each point in the Mercator projection is also linearly related to the isometric latitude. From there follows a new definition of isometric latitude based on the Mercator projection.

The traditional definition of the Mercator projection can be found in the article, Equation (30). Since the image of each rhumb line in the Mercator projection is a straight line, thus the image of a linear function, this is a possible new definition of the Mercator projection as a projection in which each rhumb line is mapped as a straight line. So, one property of the Mercator projection gave its definition, and its previous definition as a conformal cylindrical projection became a property of that projection.

The new definitions shed new light on the issue and new insight, thus expanding the field of the theory of map projections. For isometric latitude, it was not known that it could be clearly interpreted with the help of longitude or with the help of the ordinate in the Mercator projection. The Mercator projection is always defined as a cylindrical conformal projection, although in Mercator's time such a classification did not exist. Mercator constructed his projection in a way that is called a new definition in the article, i.e., a projection in which all loxodromes from a sphere or ellipsoid are mapped into straight lines.

Future research could explore the impact of new definitions on solving practical tasks in maritime affairs.

Conflict of interest: The author declares no conflict of interest.

References

1. Lapaine M. New Definitions of the Isometric Latitude and the Mercator Projection. Revue Internationale de Géomatique. 2024; 33(1): 155-165. doi: 10.32604/rig.2024.052258

2. Snyder JP. Map projections: A working manual. Professional Paper. Geological Survey Professional Paper. 1987. doi: 10.3133/pp1395
3. Bugaevsky LM, Snyder JP. Map Projections: A Reference Manual. London, Bristol: Taylor & Francis; 1995.
4. Deakin RE. 3-D coordinate transformations. Surveying and land information systems. 1998; 58(4): 223−234. doi: 10.1017/S0373463315000181
5. Bian SF, Li HP. Mathematical Analysis in Cartography by Means of Computer Algebra System. Cartography - A Tool for Spatial Analysis. Published online August 17, 2012. doi: 10.5772/50159
6. Bermejo-Solera M, Otero J. Simple and highly accurate formulas for the computation of Transverse Mercator coordinates from longitude and isometric latitude. Journal of Geodesy. 2008; 83(1): 1-12. doi: 10.1007/s00190-008-0224-y
7. Li H, Bian S, Chen L. The direct calculating formulae for transformations between authalic latitude function and isometric latitude. Geomatics and Information Science of Wuhan University. 2011; 36(7): 843−846.
8. Thomas PD. Conformal projections in geodesy and cartography (United States. Coast and Geodetic Survey. Special publication). National Technical Information Service; 1977.
9. Kawase K. Concise derivation of extensive coordinate conversion formulae in the Gauss-Krüger projection. Bulletin of the Geospatial information authority of Japan. 2013; 60: 1−6.
10. Abee M. The Spread of the Mercator Projection in Western European and United States Cartography. The International Journal for Geographic Information and Geovisualization. 2021; 56(2): 151-165. doi: 10.3138/cart-2019-0024
11. Lapaine M, Frančula N. Web Mercator Projection – One of Cylindrical Projections of an Ellipsoid to a Plane. Kartografija i geoinformacije. 2021; 20(35): 30-47. doi: 10.32909/kg.20.35.2
12. Pápay G. Mercator's geometric method in the construction of his projection of 1569 (German). KN - Journal of Cartography and Geographic Information. 2022; 72(4): 261-267. doi: 10.1007/s42489-022-00115-5
13. Kerkovits K. Secant Cylinders Are Evil—A Case Study on the Standard Lines of the Universal Transverse Mercator and Universal Polar Stereographic Projections. ISPRS International Journal of Geo-Information. 2024; 13(2): 56. doi: 10.3390/ijgi13020056
14. Lenart AS. Orthodromes and Loxodromes in Marine Navigation. Journal of Navigation. 2016; 70(2): 432-439. doi: 10.1017/s0373463316000552
15. Gao M, Shi GY. Ship-handling behavior pattern recognition using AIS sub-trajectory clustering analysis based on the T-SNE and spectral clustering algorithms. Ocean Engineering. 2020; 205: 106919. doi: 10.1016/j.oceaneng.2020.106919
16. Nicolai R. The map projection of portolan charts. Nieuw archief voor wiskunde. 2021; 5(1): 33−41.
17. Jiao C, Wan X, Li H, et al. Dynamic Projection Method of Electronic Navigational Charts for Polar Navigation. Journal of Marine Science and Engineering. 2024; 12(4): 577. doi: 10.3390/jmse12040577
18. Alexander J. Loxodromes: A Rhumb Way to Go. Mathematics Magazine. 2004; 77(5): 349-356. doi: 10.1080/0025570x.2004.11953279
19. Kos S, Filjar R, Hess M. Differential Equation of the Loxodrome on a Rotational Surface. Available online: https://www.ion.org/publications/abstract.cfm?articleID=8379 (accessed on 9 March 2024).
20. Kos S, Vranić D, Zec D. Differential Equation of a Loxodrome on a Sphere. Journal of Navigation. 1999; 52(3): 418-420. doi: 10.1017/s0373463399008395
21. Elhashash A. Existence, Uniqueness and Angle Computation for the Loxodrome on an Ellipsoid of Revolution. Journal of Geometry and Symmetry in Physics; 2012. doi: 10.7546/jgsp-13-2009-75-88
22. Petrović M. Differential Equation of a Loxodrome on the Spheroid. Naše more. 2007; 54(3-4): 87-89.
23. Petrović M. Orthodrome-Loxodrome Correlation by the Middle Latitude Rule. Journal of Navigation. 2013; 67(3): 539-543. doi: 10.1017/s037346331300074x
24. Weintrit A, Kopcz P. A Novel Approach to Loxodrome (Rhumb Line), Orthodrome (Great Circle) and Geodesic Line in ECDIS and Navigation in General. In: Methods and Algorithms in Navigation. CRC Press; 2014.
25. Babaarslan M, Yayli Y. Differential Equation of the Loxodrome on a Helicoidal Surface. Journal of Navigation. 2015; 68(5): 962-970. doi: 10.1017/s0373463315000181
26. Kovalchuk V, Mladenov IM. λ-Spheres as a New Reference Model for Geoid: Explicit Solutions of the Direct and Inverse Problems for Loxodromes (Rhumb Lines). Mathematics. 2022; 10(18): 3356. doi: 10.3390/math10183356
27. Lambrinos N, Repanidou I, Intzidou G. A Didactical Approach of Rhumb Line vs. Great Circle in Web Mercator Projection for 6th Grade Pupils. Didactic Strategies and Resources for Innovative Geography Teaching. Published online June 10, 2022:

168-202. doi: 10.4018/978-1-7998-9598-5.ch008

28. Tseng WK, Earle MA, Guo JL. Direct and Inverse Solutions with Geodetic Latitude in Terms of Longitude for Rhumb Line Sailing. Journal of Navigation. 2012; 65(3): 549-559. doi: 10.1017/s0373463312000148
29. Viličić M, Lapaine M. Loxodrome and Isometric Latitude. Cartography and Geoinformation. 2024; 23(41).
30. Lapaine M. Mappings in the theory of map projections (Croatian) [PhD thesis]. University of Zagreb, Faculty of Geodesy; 1996.
31. Heck B. Calculation methods and evaluation models for land surveying (German). Herbert Wichmann Verlag, Karlsruhe; 1987.
32. Lapaine M. Isometric latitude and rhumb line (Croatian). Geodetski list. 1993; 1: 5−14.

Journal of Geography and Cartography 2024, 7(2), 7043.
https://doi.org/10.24294/jgc.v7i2.7043

Article

Improving the properties of alluvial sand, a potential alternative to standardized sand for geotechnical laboratory

Jules Hermann Keyangue Tchouata[1,*], Willy Chance Guimezap Kenou[2], Darman Japhet Taypondou[1,*], Moses Mbuh Kuma[3], Joseph Stephane Edzoa Akoa[1], François Ngapgue[4]

[1] School of Geology and Mining Engineering, University of Ngaoundere, Meiganga 115, Cameroon
[2] Research Center for Innovation and Entrepreneurship (PRIE), Institut Universitaire de la Cote, Douala 3001, Cameroon
[3] Civil Engineering and Forestry Techniques Department, Higher Technical Teacher Training College, University of Bamenda, Bambili 39, Cameroon
[4] Fotso Victor University, Institute of Technology, University of Dschang, Bandjoun 134, Cameroon
*** Corresponding authors:** Jules Hermann Keyangue Tchouata, keyanguetchouatajuleshermann@gmail.com; Darman Japhet Taypondou, japhet8darman@gmail.com

CITATION

Keyangue Tchouata JH, Guimezap Kenou WC, Taypondou DJ, et al. Improving the properties of alluvial sand, a potential alternative to standardized sand for geotechnical laboratory. Journal of Geography and Cartography. 2024; 7(2): 7043. https://doi.org/10.24294/jgc.v7i2.7043

ARTICLE INFO

Received: 10 June 2024
Accepted: 23 July 2024
Available online: 21 August 2024

Abstract: Despite Cameroon's immense sand reserves, several enterprises continue to import standardized sands to investigate the properties of concretes and mortars and to guarantee the durability of built structures. The present work not only falls within the scope of import substitution but also aims to characterize and improve the properties of local sand (Sanaga) and compare them with those of imported standardized sand widely used in laboratories. Sanaga sand was treated with HCl and then characterized in the laboratory. The constituent minerals of Sanaga sand are quartz, albite, biotite, and kaolinite. The silica content (SiO_2) of this untreated sand is 93.48 wt.%. After treatment, it rose 97.5 wt.% for 0.5 M and 97.3 wt.% for 1 M HCl concentration. The sand is clean (ES, 97.67%–98.87%), with fineness moduli of 2.45, 2.48, and 2.63 for untreated sand and sand treated with HCl concentrations of 0.5 and 1 M respectively. The mechanical strengths (39.59–42.4 MPa) obtained on mortars made with untreated Sanaga sand are unsatisfactory compared with those obtained on mortars made with standardized sand and with the expected strengths. The HCl treatment used in this study significantly improved these strengths (41.12–52.36 MPa), resulting in strength deficiencies of less than 10% after 28 curing days compared with expected values. Thus, the treatment of Sanaga sand with a 0.5 M HCl concentration offers better results for use as standardized sand.

Keywords: standardized sand; HCl treatment; mortars; mechanical strength; Sanaga

1. Introduction

Every year, an estimated 4 billion cubic meters of concrete and mortar are used for infrastructure development through the construction of various buildings such as administrative structures, residential complexes, bridges, freeways, dams, airports, etc. [1,2]. For the formulation of concrete, aggregates (sand and gravel) are the most widely exploited solid materials in the world, with production estimated at between 25.9 and 29.6 billion tonnes per year [3]. According to a new report by the United Nations Environment Programme (UNEP), sand is the second most used resource in the world after water [4].

Despite the general development of infrastructure, numerous problems, such as the collapse of buildings, bridges, and pipes and the premature deterioration of infrastructure, have recently been observed in developing countries, particularly in Cameroon. These problems are very often linked to the poor quality of the materials used and the poor formulation of the concretes and mortars employed. In addition, there is insufficient monitoring of compliance with standards. These standards, sometimes of foreign origin, are costly and not always available on time. It is therefore essential to study the various physico-chemical and mechanical properties of the materials used in the manufacture of mortars and concretes to guarantee their quality and performance in construction. Sand is a granular material composed of fine rock and mineral particles [5]. Alluvial sands are naturally occurring sands resulting from the weathering of pre-existing rocks. Depending on its qualities, sand is the element with the greatest influence on concrete. Indeed, cleanliness, fineness modulus, and particle size distribution are the main physical characteristics used to control sand quality [5]. In the laboratory, standardized sand is generally used to test cement, concrete, and mortars. To date, studies on the development of standardized sand in the tropics are rare as many African countries continue to import standardized sand. It should also be noted that, given the long distances involved in obtaining standardized sand (mainly imported from outside the continent), this sand, although indispensable, is becoming very expensive and may be inaccessible to many individuals [6,7]. More recently, several crises, notably the coronavirus (COVID-19), have disrupted the global economy and transactions. This has led to a shortage of standardized sand in markets south of the Sahara and Cameroon in particular. It would therefore appear that sand exploitation is of great importance to the African economy [6] and to the quality of built structures. This underlines the need to study the possibility of valorizing and standardizing local materials, particularly sand, according to their geotechnical specificities, for use in construction. In Congo, some researchers [7] have carried out work to develop local standardized sand by selecting local sands with characteristics close to the required standards and determining their chemical compositions.

In Cameroon, there are large reserves of alluvial sands in rivers and valleys that could have the characteristics required for the design of standardized sands and bring undeniable added value to the local material that sand represents. However, very little work has been devoted to the characterization and development of standardized sand. The present study therefore aims to: (1) characterize the natural alluvial sands of the Sanaga, improve their non-conforming characteristics, and obtain mechanical strengths that meet geotechnical standards; (2) formulate recommendations for the production of standardized sand locally, in compliance with current standards. The ultimate objective is to eliminate the undesirable elements contained in these sands, notably by hydrochloric acid treatment.

2. Localization

The Sanaga River stretches from latitude 3°32′ N to latitude 7°22′ N, with its most westerly point at meridian 9°45; it reaches meridian 14°57′E and drains a succession of plateaus bounded to the west by the Cameroon ridge and to the north by the Adamawa plateau. The Sanaga River is 918 km long and 20 m deep, stretching over some 130,000 km^2. The section of the Sanaga studied, from which the samples were collected, concerns the locality of Nanga-Eboko, a division in the Central region of Cameroon, 166 km from Yaoundé. The middle part of the Sanaga corresponds to the portion of this river in the study area. **Figure 1** illustrates the location and hydrographic network of the Sanaga at the mouth of Nanga-Eboko. Geologically, the Sanaga watershed is made up of a vast ensemble of crystalline schists composed of ectinites, migmatite, and concordant ancient eruptive rocks represented mainly by syntectonic granites [8].

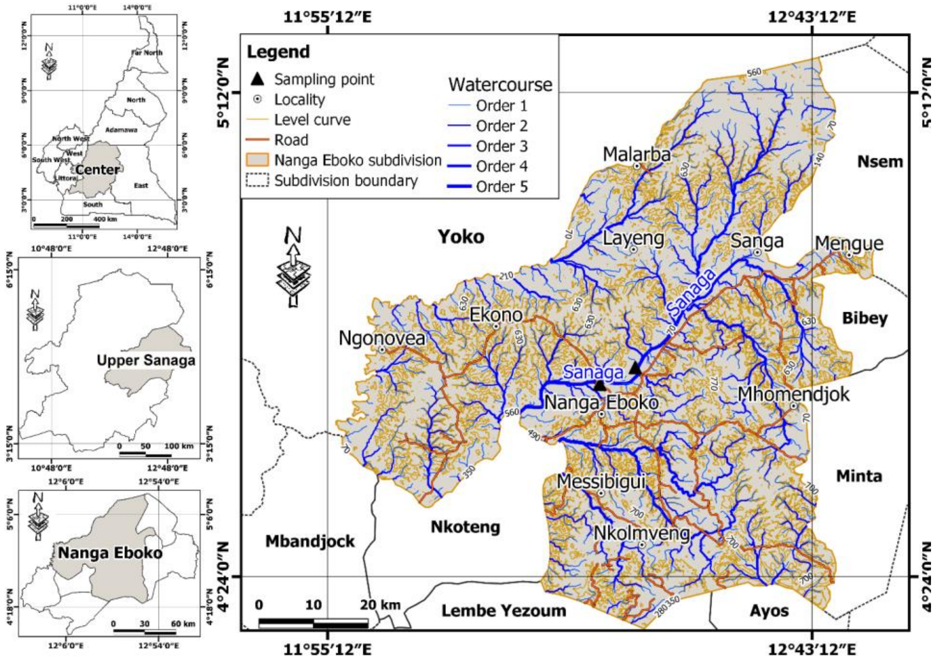

Figure 1. Localization map of the studied site.

3. Materials and methods

3.1. Materials

Figure 2. Representative sample of Sanaga sand.

Sanaga sand is in great demand and is used as aggregate for construction. The Sanaga sand reserve is the largest in Cameroon's center region. The sand samples (**Figure 2**) used for this study were local sands (a representative sample obtained from a mixture of several samples taken along the river) and the EN 196-1 standardized sand more widely used in laboratory tests in Cameroon and the sub-region. Samples were taken along the watercourse. After macroscopic description, the two samples shown on the map were selected. On the basis of the similarities observed between the samples, these two samples represent the sands of this watercourse. These samples were then mixed to obtain a representative sample.

Class 52.5R compound Portland cement (CEM II) was also used in this project. This cement was chosen for the mortar samples because of its mechanical performance, reduced water content, and rapid setting.

3.2. Methods

3.2.1. Physical characterization

The water content is used in this work to determine the moisture content by weight of the sample. This test was carried out following standard NF P 94-050 [9], using a series of successive weightings before and after oven drying (24 h at 105 ℃) of the representative sand sample.

Granulometric analysis consists of establishing a dimensional distribution of the different particles in the sand studied, expressed as a percentage by mass. The test consists of classifying the different grains making up a sample using a series of sieves nested one on top of the other, with openings decreasing in size from top to bottom. This test was carried out under standard NF P 94-056 [10].

The fineness modulus is obtained from particle size data. It expresses the fineness of sand. It is obtained by standard NF P 18-540 [11] and expressed as Equation (1).

$$\mathrm{fm} = \frac{\%R_{1.25} + \%R_{0.63} + \%R_{0.315} + \%R_{0.16}}{100} \tag{1}$$

where:

fm is fineness modulus.

*R*x is refusal corresponding to a sieve opening *x*.

Sand equivalent (SE) is used to measure the degree of cleanliness of sand. It consists in measuring the quantity of very fine elements contained in the sand. The test was carried out by flocculation on the 0/2 sand fraction following standard NF P 18-598 [12]. The sand equivalent value is expressed as Equation (2).

$$\mathrm{ES} = \frac{H_2}{H_1} \times 100 \tag{2}$$

where:

H_1 is flocculate height.

H_2 is height of clean sand.

Apparent density corresponds to the mass per unit apparent volume of the material, i.e., the volume made up of solid grains and voids. This test was carried out per standard NF EN 1097-3 [13]. Specific density does not take voids into account. It is obtained by the pycnometer method under standard NF P 94-054 [14].

Mortars were formulated from two different types of sands (sand extracted from the Sanaga River and standardized sand) using EN-196-1 [15] standard method. To determine compressive strength, specimens of formulated mortar were subjected to an increasing load until failure following NF EN 12390-3 [16] standard. The failure load is the maximum load recorded during the test, and the compressive strength is the ratio of the failure load to the cross-sectional area of the specimen; the results are obtained using Equation (3).

$$R = \frac{F}{S} \tag{3}$$

where:

R is compressive strength in MPa;

S is cross-sectional area of the specimen to which the compressive force is applied;

F is maximum load in Newtons.

Flexural strength is the limiting stress of a material before flexural failure. It is used to determine the relative variation in bond forces between particles of a material. This test was carried out following standard NF P 94-422 [17]. Flexural strength, in MPa, is given by Equation (4).

$$F = \frac{3}{2} \times \frac{Pd}{le^2} \tag{4}$$

where:

d is the distance between cylindrical supports in mm;

e is specimen thickness in mm;

P is the load applied at the failure in Newton (N);

l is the width of specimen in mm.

3.2.2. Chemical and mineralogical analysis

Chemical analysis by X-ray fluorescence (XRF) spectrometry

Chemical analysis by X-ray fluorescence (XRF) spectrometry was carried out in the laboratory of Société des Cimenteries du Cameroun (CIMENCAM). This technique aims to determine the mass content of major oxides such as SiO_2, Al_2O_3, Fe_2O_3, MgO, Na_2O, CaO, and K_2O. The chemical composition of the sand was obtained after heating and melting with a lithium tetraborate flux and analyzed using a Pan Analytical Axios Advanced PW4400. Loss on ignition is defined as the variation in mass resulting from heating a sample under specific conditions. It is used to assess the non-volatile organic matter content of waste, sludge, and sediment.

Sand treatment

The treatment aims to remove undesirable particles from Sanaga sand samples. The treatment consists mainly of removing oxides and alkalis by hydrochloric acid attack. Purification of sand with hydrochloric acid (HCl) is often preferred to simple washing with water for several scientific and technical reasons. Hydrochloric acid can dissolve certain mineral impurities present in sand, such as iron oxides, carbonates, and silicates. These impurities are not always soluble in water and may require chemical treatment to be effectively removed. Washing with water can remove surface particles and soluble contaminants. However, it is often insufficient to remove more stubborn contaminants or fine particles adhering to sand grains. Hydrochloric acid, on the other hand, can penetrate deeper and dissolve these contaminants for a more thorough cleaning. The procedure used for HCl treatment consisted of placing a 10 g mass of sand in a bath and adding 150 mL volumes of a hydrochloric acid (HCl) concentration corresponding to C = 0.5 M and C = 1 M. The mixture was homogenized and heated to 200 ℃ on a hot plate for 15 minutes. Finally, the hydrochloric acid solution was drawn off, and the sand was rinsed in a bath containing distilled water.

Mineralogical analysis by X-ray diffraction (XRD)

The mineralogical composition of the sample was carried out using an X-ray powder diffractometer, XRD (Bruker Advance D8), Cu-Kα radiation, and Ni filtered radiation (λ = 1.54184 Å). Radiation was generated by an electric current of 30 mA and at a voltage of 40 kV. Analysis of each powder sample ($\phi \leq 75$ µm) was performed in swept steps from 5° to 70° for random powder in 2θ range and integrated at the rate of 2s per step.

4. Results, interpretations, and discussions

4.1. Mineralogical and chemical composition

4.1.1. Mineralogical composition

The minerals identified by post-treatment diffractogram (XRD) analysis of studied sand samples include quartz, biotite, kaolinite, and albite (**Figure 3**). These minerals are thought to result from the disintegration of granites and similar rocks by natural weathering and erosion processes [18]. Quartz predominates the mineralogical composition (93% approx.) of the sand extracted from the Sanaga. The abundant presence of quartz is essential for the composition of standardized sands. Indeed, according to standard EN 196-1 [15], the most important and abundant mineral that a standardized sand must contain is quartz. It should be noted that the presence of clay minerals (kaolinite), even in small quantities, is not conducive to the manufacture of standardized sands; these sands should therefore be treated to effectively eliminate the level of fine clay particles.

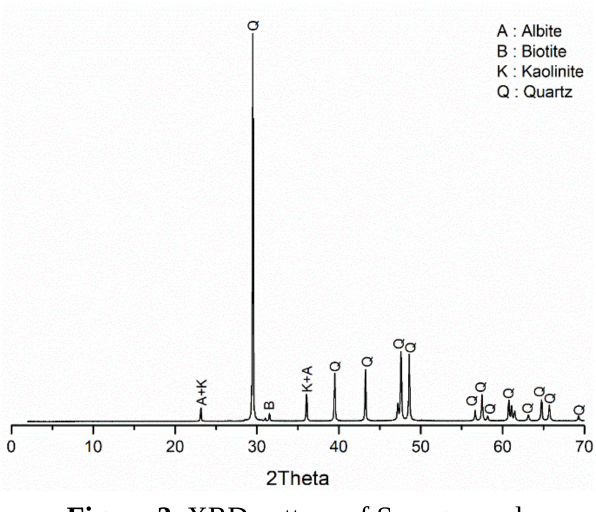

Figure 3. XRD pattern of Sanaga sand.

4.1.2. Chemical composition

Table 1 shows the results of the chemical analysis of untreated sand, sand treated with hydrochloric acid at different concentrations (0.5M and 1M), and reference sand.

Table 1. Major oxide composition of sands.

Oxides (%)	Untreated	Treated		Standard Sand
		0.5M	1M	
SiO_2	93.48	97.5	97.3	98.05
Al_2O_3	3.14	1.77	1.67	0.54
Na_2O	0.34	0.13	0.14	
MgO	0.13	0.03	0.08	
K_2O	0.89	0.13	0.12	
CaO	0.17	0.11	0.11	
TiO_2	0.3			
Fe_2O_3	1.55	0.33	0.57	0.07
LOI	3.01	1.31	1.43	0.16

The variations in chemical composition as a function of sand type are illustrated in **Figure 4.** The sands studied (treated and untreated Sanaga sand) have very high SiO_2 contents (93.48 wt.%–97.5 wt.%). These values are generally lower than those observed for standardized sand (98.05 wt%). Alumina content (Al_2O_3) is relatively low overall (1.67 wt.%–3.14 wt.%), with the highest value recorded for untreated Sanaga sand. Overall, iron oxide (Fe_2O_3) is also present in low proportions (0.33 wt.%–1.55% wt.%), with the highest value observed in the untreated Sanaga sand sample. The other oxides are present in very low proportions in both natural and treated Sanaga sand samples (cumulative percentage: <3 wt.%). Loss on ignition values is low (1.31 wt.%–3.01 wt.% by weight), with the highest value recorded in untreated Sanaga sand. This chemical composition of Sanaga sand is due to the petrographic, mineralogical, and therefore chemical composition of the basement rocks [8]. The Al_2O_3, K_2O, Na_2O, and Fe_2O_3 contents in the samples in **Table 1** are associated with the low presence of feldspar, clay, and micas (biotite) listed in **Figure 3**. High amounts of MgO, K_2O, and Na_2O are associated with high expansion [19]. Thus, HCl treatment resulting in a reduction of these oxides in Sanaga sand is a major advantage for the use of this sand in mortars. In addition, after hydrochloric acid treatment of local sand, it was found that the silica content of Sanaga sand increased between 3.82% and 4.02 wt.% compared to pure sand. The 0.5 M concentration offers better treatment than the 1 M concentration. These silica concentrations are very close to those recommended by reference standard EN 196-1 [15], which is 98.05 wt.%. The silica content shows a clear increase from 93.48 wt.% to 97.3 wt.% and 97.5 wt.% for the 1 M and 0.5 M concentrations, respectively. This increase is mainly due to a significant drop of alumina (Al_2O_3), magnesium (MgO), potassium (K_2O), and titanium (TiO_2).

The SiO_2/Al_2O_3 ratio of sand extracted from the Sanaga is 29.77% in its natural state, compared with 55.08% at 0.5 M and 58.26% at 1 M. This ratio, although lower than that of the reference standard EN 196-1 [15], would indicate an abundance of silica in Sanaga sand [20]. The results obtained after sand treatment are in line with Indian and Asian standards. This could be explained by the fact that the oxides present in the sand particles have been reduced by the attack of tetrachloro-silicate ions, as reported in certain works [21]. The purification equation is as follows:

$$SiO_2 + 4HCl \rightarrow SiCl_4 + 2H_2O.$$

This equation enabled considerable elimination of oxides such as Al_2O_3, Fe_2O_3, K_2O, CaO, etc., leading to an increase in silica content of the order of 3% to 4%. After treatment, the loss on ignition of the sand studied is down (1.31 wt.% for 0.5 M and 1.43 wt.% for 1 M) and relatively close to the recommendations of the European standard (0.1 wt.%–0.16 wt.%). This reduction also reflects the elimination of alumina, magnesium, and potassium oxides, mainly contained in clays.

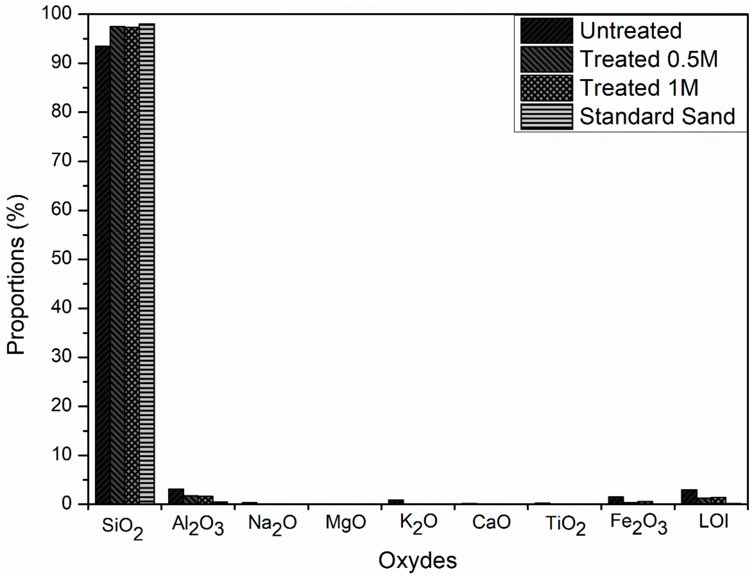

Figure 4. Chemical composition of untreated, treated, and standard sand.

4.2. Grain size distribution

The results of the particle size analysis of the various sands studied are shown in **Table 2** and presented in the particle size pattern in **Figure 5.**

Table 2. Physical parameters of sands.

Parameters	Untreated	Treated 0.5M	Treated 1M	Standard
cs (0.2mm < φ < 2 mm) (%)	95	98	99	86
fs (φ < 0.2 mm) (%)	5	2	1	14
fm	2.45	2.48	2.63	2.49
SE (%)	97.67	98.54	98.87	98.34
dh	1.49	1.38	1.41	/
dr	2.67	2.61	2.41	2.64
dd	1.46	1.34	1.37	/
W (%)	2.50	/	/	7.00
Cu	4.07	4.36	2.62	6.43
Cc	1.88	2.14	1.39	1.30

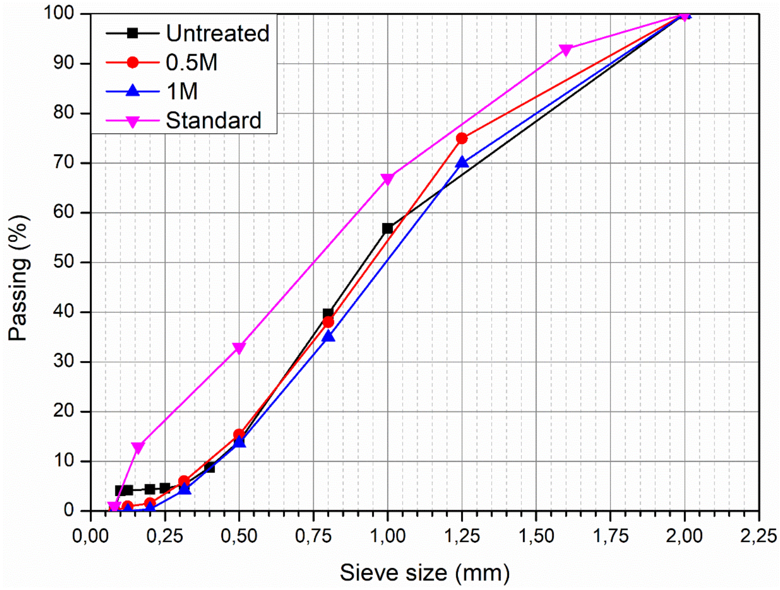

Figure 5. Particle size distribution pattern of Untreated, treated, and standard sand.

The sands studied show particle size distribution curves that follow an "S" shape (**Figure 5**). This curve is common for sands containing elements of different sizes [22]. The particle size patterns show that the particle sizes of the standardized sand and the sand extracted from the Sanaga River are globally continuous. Analysis of the sands' particle size curves shows that natural sand extracted from the Sanaga has a fine particle content (φ < 0.2 mm) of around 5% and a coarse particle content (0.2 mm < φ < 2 mm) of almost 95%. Research [23] has shown that particle size distribution in sand is crucial to both the workability and segregation of newly mixed concrete. According to various authors [24,25], the use of uniformly distributed mixes generally leads to better workability compared with discontinuously graded mixes. However, it should be noted that discontinuously graded mixes can lead to a greater slump. Analysis of the Sanaga sand grading curve clearly shows that the samples are made up of the main granular classes in varying proportions. The coefficients of uniformity (Cu) of the sands studied (2.62–6.43) are greater than 2, showing that these sands have spread or varied and continuous granulometries. The lowest value recorded on the sample treated with HCl at a concentration of 1 M reflects a more or less heterogeneous (i.e., less uniform) grain size, composed mainly of coarse elements. When mixtures are non-uniformly distributed, they tend to settle more, resulting in concrete of higher density and lower permeability [24].

The curvature coefficients of the Sanaga sand grading curves indicate that this sand has a well-graded grading (Cc < 3). The granulometric data show that Sanaga sand is coarse-grained (cs), with proportions ranging from 95% to 99%. The quantity of fine particles (fs) varies between 1% (1 M-treated sand) and 5% (untreated sand). Except for natural samples, all other samples can be classified as clean sands since their fine particle content ranges between 1% and 3.8%. However, the quantity of fine particles present has a significant impact on the amount of water required and the workability of the mortar [26]. According to standards [27–29], there is a limit to the amount of fine particles allowed. If the fine content exceeds 3 to 5%, it is advisable to treat the sand or reject it. Aggregate can contain fine particles in various forms. They may be present in the sand in the form of clay, silt, or stone dust. The presence of fines or silt can reduce the permeability of concrete. In addition, too much silt can reduce the workability of concrete and increase shrinkage. According to the European standard [30], sand is considered pure if particles larger than 2 mm account for no more than 20% of its total mass, and if particles smaller than 0.063 mm account for no more than 15% [31].

4.3. Fineness modulus

Table 2 shows that all fineness moduli (fm) are between 2.45 and 2.63. The fineness modulus of sand is one of the key factors affecting the workability, strength, durability, visco-plasticity, density, and permeability of fresh and hardened concrete [5,32]. Sand with a fineness modulus (fm) of 2.1 to 2.5 is considered too fine, while sand with an fm of 2.5 to 3.1 is considered medium, and sand with an fm of 3.1 to 3.5 is considered coarse. According to ASTM C 33 [27], the fineness modulus should be between 2.3 and 3.1. It is important to note that the use of very coarse or very fine sand can lead to poor-quality concrete mixes. Coarse sand can lead to hard concrete mixes that are more likely to bleed and segregate. To achieve the desired workability of concrete, a significant amount of water is required when using very fine sand. However, this type of sand can easily separate and may require a greater quantity of cement. According to some authors [5], optimizing fineness modulus can improve concrete strength by between 8% and 39%. The Ethiopian standard [29] specifies a slightly different range of 2 to 3.5, with a tolerance of ±0.2. If the fineness modulus is between 2.0 and 2.6, the material is fine sand. If it's between 2.6 and 2.9, it's medium sand. If it's between 2.9 and 3.5, it's coarse sand. If the sand's fineness modulus exceeds 3.5, it is considered unacceptable. The Sanaga sand samples meet the requirements of Ethiopian [29] and French [11], standards and the sand fineness modulus values show that all the sands are of good quality and suitable for construction.

4.4. Sand equivalent (SE) values

The sand equivalent results show that all the sands have the characteristics of very clean sand, due to the almost total absence of clay fines. Sand equivalent values for the material studied range from 97.67% to 98.87%. The best results were obtained after treatment of the sand with HCl. According to NF EN 933-8 [33], these sands are classified as very clean sands, with extremely negligible clay fines, which could however lead to plasticity defects in the concrete. Despite this, these sands can be used in conventional concrete structures if structural strength is required. In addition, high sand equivalent values have a positive impact on concrete properties [34]. When assessing the quality of fine particles in sand, a high sand equivalent value indicates positive effects of the fine fraction on concrete properties [34,35].

4.5. Densities

Table 2 shows the densities of sand samples before and after hydrochloric acid treatment.

The specific densities of the sands studied range from 2.41 to 2.67, as shown in

Table 2. The values are similar for the different samples. These results are comparable to those obtained in other studies carried out in the same region [36]. These results show that the densities of acid-treated sands extracted from the Sanaga River drop with reference to their initial state. Bulk and dry densities of Sanaga sand before and after HCl treatment vary between 1.38 and 1.49 and between 1.34 and 1.46 respectively. Like specific densities, bulk and dry density values also tend to decrease after treatment with HCL. These results mainly reflect a decrease in the oxides making up the clay minerals (alumina oxide, potassium oxide, and magnesium oxide) in terms of mass. It seems that the clay minerals acted as fillers (filler effect). Thus, before treatment, the volume of voids within the sand was occupied by clay particles.

However, although a decrease in density values was observed, the densities of the sand extracted from the Sanaga are within the range prescribed by EN 196-1 [15] (2.63–2.67), particularly for the 1 M concentration [22].

4.6. Water content

The average natural water content of the Sanaga sand sample is shown in **Table 2**.

The sand sample extracted from the Sanaga has a water content of 2.5%, which is very close to the water content of sand standardized to EN 196-1 [15]. The amount of water contained in the sand determines the effective water/cement ratio and the free water content. The water content value is attributed to the presence of clay minerals. Thus, a high amount of clay minerals may lead to high water content values for the sand. If the sand is dry or has a low water content, it requires a higher water/cement ratio for mix design, as the sand particles are quickly covered with cement paste. To calculate the amount of water required for the water/cement ratio, it is essential to know the water content of the sand. Standards [37–39] determine the water content of fine aggregates, which is generally between 2% and 6% for free water content. Fine aggregates can retain a maximum water content of around 2%–8%. Based on the water content results and the above description, Sanaga natural sand, and in particular treated sand, meets the free water content values prescribed by the standard.

4.7. Mechanical strength of mortars

Table 3 shows the different compressive strength results for sand mortars before and after treatment with hydrochloric acid at different concentrations.

Table 3. Mechanical strength of mortars.

Time	Compressive strength (MPa)				Flexural strength (MPa)			
	Untreated	0.5M	1M	Standard	Untreated	0.5M	1M	Standard
14 days	39.59	41.77	41.12	48.97	8.4	9.2	8.92	11.15
28 days	41.01	50.1	49.7	54.5	10.1	11.03	10.7	12
35 days	42.4	52.36	51.98	55.98	10.21	11.39	11.04	12.1

The compressive strength of mortar is the performance measurement most commonly used by engineers in the design of buildings and other structures. Mortar compressive strengths were determined at 14, 28, and 35 days. Compressive strengths obtained with treated and untreated Sanaga sand varied between 39.59–41.77 MPa, 41.01–50.1 MPa, and 42.4 and 52.36 MPa at 14, 28, and 35 days, respectively. In general, the compressive strengths of the various mortars show a relatively significant increase after hydrochloric acid treatment. Treatment of the sand with a concentration of 0.5 M hydrochloric acid gave the best results and most closely resembled the results obtained with the reference sand prescribed by standard EN 196-1 [15]. The graph in **Figure 6** shows this evolution between untreated sand mortar and sand treated with different concentrations.

The flexural strengths of the various mortars treated with hydrochloric acid also show increasing results close to the reference sand in standard EN 196-1 [15]. The graphs in **Figure 6** show this progression from untreated sand mortar to sand treated at different concentrations (0.5 M and 1 M), as well as that of sand, standardized in standard EN 196-1 [15], respectively. The strengths obtained with treated and untreated Sanaga sand varied between 8.4–9.2 MPa, 10.1–11.3 MPa, and 10.21 and 11.39 MPa at 14, 28, and 35 days, respectively. When the sand was treated with HCL, the 0.5 M concentration gave better results, close to those obtained with sand standardized to EN 196-1 [15].

Overall, the mortar strength histograms show that these values increase with time. The strength values of standardized sand remain higher than those of sand extracted from the Sanaga, whether treated or not; however, after HCl treatment, a significant overall increase is observed, with values in line with those expected and approaching those of standardized sand. As sand mainly acts as a reinforcing particle in a mortar [40], the nature (mineralogical and chemical composition) and particle size distribution of the sand are the main parameters influencing the mechanical behaviour of the mortar tested. The increase in strength after treatment is therefore justified by the greater or lesser reduction in the content of undesirable elements such as K_2O, Na_2O, etc. [41]. This slight difference in mechanical strength in favour of standardized sand may be due to a higher percentage of silica and therefore quartz (XRF and XRD results). Quartz had a positive effect on mechanical strength. Indeed, the abundant quartz in Sanaga sand reacts with calcium hydroxide from cement hydration to form hydrated calcium silicates (C-S-H), which constitute the main binding phase and ensure the long-term strength and durability of the materials [42]. Natural sand may have a higher organic matter content indicated by the LOI value (3.01%) than treated sand (LOI 0.5 M = 1.31% LOI 1 M = 1.43%), which is detrimental to cementitious matrices [41]. In the natural state, the compressive strength of mortars is lower than the 0.5 M compressive strength. This is attributed to the presence of clay in the natural sand, which, in contact with the binder, causes a loosening of the contacts and bonds between the aggregates and the cementitious matrix [41]. Furthermore, the presence of clay minerals can harm mechanical strength due to the reaction of the cement with the alumina silicates contained in the clays, producing hydrogen gas, which creates microcracks in the cementitious matrix [43]. Similarly, the finer particles of non-clay sand can also fill the pores of the mortar matrix, resulting in a denser material, leading to an increase in the mortar's mechanical properties.

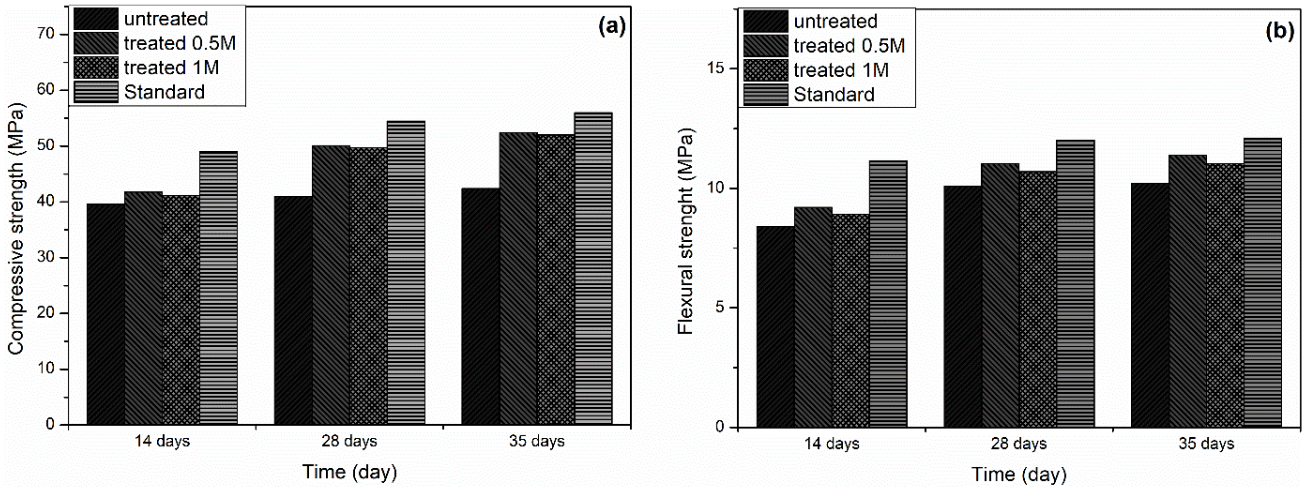

Figure 6. Evolution of mechanical properties according to time.

4.8. Statistics and comparative analysis of mechanical strength

Table 4. Comparative mechanical strength analysis.

	Compressive strength				Flexural strength			
	Untreated	**0.5M**	**1M**	**Standard**	**Untreated**	**0.5M**	**1M**	**Standard**
VR 14 days (%)	−19.15	−14.70	−16.03	/	−24.66	−17.49	−20.00	/
VR 28 days (%)	−24.75	−8.07	−8.81	/	−15.83	−8.08	−10.83	/
VR 35 days (%)	−24.26	−6.47	−7.15	/	−15.62	−5.87	−8.76	/
Min.	39.59	41.77	41.12	48.97	8.40	9.20	8.92	11.15
Max.	42.40	52.36	51.98	55.98	10.21	11.39	11.04	12.10
Mean	41.00	48.08	47.60	53.15	9.57	10.54	10.22	11.75
Std. dev.	1.41	5.58	5.73	3.69	1.01	1.17	1.14	0.52

Table 4 shows the rates of variation observed between the uniaxial compressive strengths of mortars made from standardized sand and those made from untreated Sanaga sand treated with HCl at different concentrations (0.5 and 1 M). In the natural state, compared with the values obtained with standardized sand, those obtained with Sanaga sand show a compressive strength deficit of −19.15, −24.75, and −24.26% at 14, 28, and 35 days of curing, respectively. These values highlight a very significant strength deficit of almost 25% compared with standardized values. However, mortars made from HCl-treated sand showed better variation rates. For a concentration of 0.5 M, the variation rates show a slight strength deficiency. The rates of change obtained at 0.5 M are −14.70, −8.07, and −6.47% respectively, at 14, 28, and 35 days of curing. For treatment with 1 M concentrated HCl, the rates of change obtained were −16.03, −8.81, and −7.15% respectively, at 14, 28, and 35 days of treatment. In general, at 28 days and beyond, the strengths obtained with Sanaga sand treated with 0.5 and 1 M concentrated HCl offer less than 10% difference compared with those obtained with standardized sand. According to some authors [5], this can be the result of optimizing the effect of fineness modulus by HCl treatment that can improve the mechanical strength. The strength results therefore show that treating Sanaga sand with a 0.5 M concentration of HCl results in higher mechanical strengths. These results are justified

by the disappearance of the clay mineral phase containing certain oxides whose presence is detrimental to the hardening reaction. In general, flexural (**Table 4**) strengths describe the same phenomenon as that observed for compressive strengths.

5. Conclusion

This study aimed to characterize and improve the geotechnical, chemical, and mechanical properties of sand extracted from the Sanaga River, for the production of standardized local sand and overcome the failure observed in mortars caused by the use of inappropriate sands. Imported EN 196-1 sand, with known characteristics, was used as the main reference for various comparisons. The ultimate aim was to improve the properties of local sand. Sanaga sand was therefore subjected to physical, mineralogical, and chemical characterization. The sand was also tested in mortar production to assess its mechanical resistance.

Physical parameters such as fineness modulus, which is 2.96 for sand extracted from the Sanaga River, have been corrected in the laboratory with HCl treatment to obtain a fineness modulus, which is now 2.45 after treatment and complies with standard EN 196-1 for imported standardized sands. Post-treatment densities were reduced from 2.67 to 2.61 for 0.5 M and 2.64 for 1 M in the case of Sanaga sand, in line with EN 196-1, which recommends a value of 2.6. Other physical parameters, such as water content and sand cleanliness, showed acceptable properties in line with current standards.

Chemical parameters showed 93.01% silica for sand extracted from the Sanaga River; HCl-based purification further enriched this sand in silica. The 0.5 M concentration gave a better result than that of 1 M since the silica content of the Sanaga sand is 97.5% at 0.5 M and 97.3% at 1 M. The silica content of Sanaga sand is therefore acceptable, as it meets Indian and Chinese standards, which require a silica percentage of around 97%.

The mechanical parameters of mortars made from sand extracted from the Sanaga are increasingly similar to those of EN 196-1 standard sand. This observation was confirmed by the rates of change in mechanical strength between local sand and imported EN 196-1 sand, which showed more interesting values when the local sand was treated with 0.5 M. Moreover, according to the Cameroon standard for standardized mortars, these strengths reached the expected threshold.

HCl treatment at 0.5 M of Sanaga sand eliminates efficiently sand defects, enabling it to be used as standardized sand in the building and public works industry.

Author contributions: Conceptualization, JHKT and FN; methodology, JHKT; software, DJT and JSEA; validation, JHKT, WCGK and MMK; formal analysis, DJT and WCGK; investigation, JSEA and JHKT; resources, JSEA and WCGK; data curation, DJT and JHKT; writing—original draft preparation, DJT and JHKT; writing—review and editing, DJT; visualization, DJT; supervision, JHKT; project administration, JHKT. All authors have read and agreed to the published version of the manuscript.

Data availability statement: All data generated or analyzed during this study are included in this article.

Funding: This research received no external funding.

Conflict of interest: The authors declare no conflict of interest.

References

1. Aytekin B, Mardani-Aghabaglou A. Sustainable Materials: A Review of Recycled Concrete Aggregate Utilization as Pavement Material. Transportation Research Record: Journal of the Transportation Research Board. 2021; 2676(3): 468-491. doi: 10.1177/03611981211052026
2. Tam VWY, Soomro M, Evangelista ACJ. A review of recycled aggregate in concrete applications (2000–2017). Construction and Building Materials. 2018; 172: 272-292. doi: 10.1016/j.conbuildmat.2018.03.240
3. Pascal P. Sand, rarer than one thinks. Environmental Development. 2014; 11: 208-218. doi: 10.1016/j.envdev.2014.04.001
4. Dybas C. Sand: A Resource That's Washing Away. Oceanography. 2020; 33(1): 8-10. doi: 10.5670/oceanog.2020.108
5. Sabih G, Tarefder RA, Jamil SM. Optimization of Gradation and Fineness Modulus of Naturally Fine Sands for Improved Performance as Fine Aggregate in Concrete. Procedia Engineering. 2016; 145: 66-73. doi: 10.1016/j.proeng.2016.04.016
6. Tientcheu WH, Ekengoue CM, Lele RF, et al. Socioeconomic impacts of sand harvesting along the Sanaga River in Nkol'Ossananga locality (Yaoundé-Cameroon): a vision toward a mechanized operation for sustainable exploitation. Environnement, Ingénierie & Développement. 2021; 85: 34-39.
7. Elenga RG. Properties of sand used in construction in the Congo and formulation of a local standardized sand. Sciences Appliquées et de l'Ingénieur. 2019; 3(1): 7-13.
8. Debreuil P, Guiscafre J, Nouvelot JF, Olivry JC. The Sanaga river basin (French). OSTORM; 1975.
9. NF P 94-050. Soils: reconnaissance and testing - Determination of water content by weight of materials-Steaming method. (French). AFNOR; 1995.
10. NF P 94-056. Particle size analysis. Dry sieving method after washing (French). AFNOR; 1996.
11. NF P 18-540. Aggregates, definition, specification compliance (French). AFNOR; 1997.
12. NF P 18-598. Sand equivalent (French). AFNOR; 1991.
13. NF EN 1097-3. Tests For Determining the Mechanical and Physical Characteristics of Aggregates-Part 3: Method for Determining Bulk Density and Intergranular Porosity (French). AFNOR; 1998.
14. NF P 94-054. Soils: reconnaissance and testing-Determination of the density of solid particles in soils-Water pycnometer method (French). AFNOR; 1991;
15. EN 196-1. Methods of testing cements-Part 1: Determination of strengths (French). AFNOR; 2006
16. NF EN 12390-3. Tests for hardened concrete-Part 3: compressive strength of the specimens (French). AFNOR; 2012.
17. NF P 94-422. Rocks: Determination of tensile strength-Indirect method-Brazilian test (French). AFNOR; 2001.
18. KoiralaM P, Joshi EBR. Construction sand, Quality and supply management in infrastructure project. International Journal of Advances in Engineering & Scientific Research. 2017; 4: 01-15.
19. Hasdemir S, Tuğrul A, Yilmaz M. Evaluation of alkali reactivity of natural sands. Construction and Building Materials. 2012; 29: 378-385. doi: 10.1016/j.conbuildmat.2011.10.029
20. Pialy P. Study of some clay materials from the Lembo site (Cameroon): mineralogy, sintering behaviour and analysis of elasticity properties (French) [PhD thesis]. Université de Limoges; 2009.
21. Nekous M. Elaboration of silicon from dune sand.Memoire de magister (French). Univ Mohamed BOUDIAF; 2013. p. 100.
22. Dupain R, Lanchon R, Saint-Arronan JC. Aggregates, soils, cements and concretes: Characterization of civil engineering materials using laboratory tests (French). Journal of Sedimentary Petrology. 2009; 27: 3-26.
23. Ben Abdelghani F, Maherezi W, Boutouil M. Geotechnical characterization of marine dredged sediments with a view to their use in road construction (French). Environnement, Ingénierie & Développement. 2014; N°66-mars 2014. doi: 10.4267/dechets-sciences-techniques.269
24. Goltermann P, Johansen V, Palbøl L. Packing of Aggregates: An Alternative Tool to Determine the Optimal Aggregate Mix. ACI Materials Journal. 1997; 94(5). doi: 10.14359/328
25. Makhloufi Z, Bederina M, Bouhicha M, et al. Effect of Mineral Admixtures on Resistance to Sulfuric Acid Solution of Mortars with Quaternary Binders. Physics Procedia. 2014; 55: 329-335. doi: 10.1016/j.phpro.2014.07.048
26. Sujatha T, Kannapiran K, Nagan S. Strength assessment of heat cured geopolymer concrete slender column. Asian Journal of Civil Engineering. 2012; 13: 635-646.

27. ASTM C. Standard Specification for Concrete Aggregates. Available online: https://www.astm.org/d2419-14.html (accessed on 2 March 2024).
28. ASTM. (2002). Standard test methods for sand equivalent value of soils and fine aggregate. Available online: https://www.astm.org/d2419-14.html (accessed on 2 March 2024).
29. EBCS. Ethiopian building codes of standard, EBXCS. EBCS; 2009.
30. ISO. Geotechnical Investigation and Testing-Identification and Classification of Soil-Part 2: Principles for a Classification. Available online: https://www.iso.org/standard/66346.html (accessed on 2 March 2024).
31. Dundulis K, Gadeikis S, Gadeikyté S, et al. Problems of usage of soil classification system for sand soils of Lithuania. In: Modern building materials, structures and techniques, The10th International conference; 19-21 May 2010; Vilnius, Lithuania.
32. Kumar DP, Sashidhar CC. Effect of fineness modulus of manufactured sand on fresh properties of self-compacting concrete. The Indian Concrete Journal. 2018; 92(1): 77-81.
33. Normes NF EN 933-1. Tests for determining the geometric properties of aggregates - Part 1: Determination of grain size - Sieve size analysis (French). AFNOR; 1997.
34. Hasdemir S. Effect of methylene blue test results on concrete compressive strengths. Beton; 2004.
35. Eryurtlu D, Isık M, Öztekin E. Investigation of the effect of sand equivalence test on concrete performance (Turkish). Beton; 2004.
36. Kamga DT, Bishweka BC, Kamdo G, Ngapgue F. Physical characterization of river sands to improve their use in concrete production (French). International Journal of Innovation and Scientific Research. 2016; 25(2): 517-527.
37. Astm C. Standard Test Method for Surface Moisture in Fine Aggregates. Available online: https://www.astm.org/c0070-20.html (accessed on 2 March 2024).
38. Aashto T. Standard method of test for total evaporable moisture content of aggregate by drying. ASTM International; 2000.
39. American Society for Testing Materials. Test method for density, relative density (Specific Gravity) and absorption of coarse aggregate. ASTM C-127; 2001.
40. Aslam F, Zaid O, Althoey F, et al. Evaluating the influence of fly ash and waste glass on the characteristics of coconut fibers reinforced concrete. Structural Concrete. 2022; 24(2): 2440-2459. doi: 10.1002/suco.202200183
41. Monosi S, Sani D, Tittarelli F. Used Foundry Sand in Cement Mortars and Concrete Production. The Open Waste Management Journal. 2010; 3(1): 18-25. doi: 10.2174/1876400201003010018
42. Pancharathi RK, Sangoju B, Chaudhary S, et al. Advances in Sustainable Construction Materials. Springer Singapore; 2020. doi: 10.1007/978-981-15-3361-7
43. Vázquez-Rodriguez FJ, Valadez-Ramos J, Puente-Ornelas R, et al. Nonferrous waste foundry sand and milling fly ash as alternative low mechanical strength materials for construction industry: Effect on mortars at early ages. Revista Română de Materiale Romanian Journal of Materials. 2018; 48 (3):338–345.

Journal of Geography and Cartography 2024, 7(2), 6271.
https://doi.org/10.24294/jgc.v7i2.6271

Article

The essence of soil and soil formation in accordance with soil water regime

Tatyana Romanova[1], Aliaksandr Chervan[2,*], Nadezhda Ivakhnenko[1]

[1] Institute for Soil Science and Agrochemistry of National Academy of Sciences of Belarus, Minsk 220108, Belarus

[2] Belarussian State University, Minsk 220030, Belarus

*** Corresponding author:** Aliaksandr Chervan, ChervanAlex@gmail.com

CITATION

Romanova T, Chervan A, Ivakhnenko N. The essence of soil and soil formation in accordance with soil water regime. Journal of Geography and Cartography. 2024; 7(2): 6271. https://doi.org/10.24294/jgc.v7i2.6271

ARTICLE INFO

Received: 7 May 2024
Accepted: 26 August 2024
Available online: 16 September 2024

Abstract: The obtaining of new data on the transformation of parent materials into soil and on soil as a set of essential properties is provided on the basis of previously conducted fundamental studies of soils formed on loess-like loams in Belarus (15,000 numerical indicators). The study objects are autochthonous soils of uniform granulometric texture. The basic properties without which soils cannot exist are comprehensively considered. Interpolation of factual materials is given, highlighting the essential properties of soils. Soil formation is analyzed as a natural phenomenon depending on the life activity of biota and the water regime. Models for differentiation of the chemical profile and bioenergy potential of soils are presented. The results of the represented study interpret the available materials taking into account publications on the biology and water regime of soils over the past 50 years into three issues: the difference between soil and soil-like bodies; the soil formation as a natural phenomenon of the mobilization of soil biota from the energy of the sun, the atmosphere, and the destruction of minerals in the parent materials; and the essence of soil as a solid phase and as an ecosystem. The novelty of the article study is determined by the consideration of the priority of microorganisms and water regime in soil formation, chemical-analytical identification of types of water regime, and determination of the water regime as a marker of soil genesis.

Keywords: soil formation; essential properties; biota (microbiota); water regime; bioenergy potential

1. Introduction

By the beginning of the 21st century, an opinion about the danger of modern environmental management in general for the life of the Earth's population along with the need to protect nature had been formed in the circles of the scientific community. In the last decades, the issue of nature-like technologies for using biosphere resources, including soils, has been actively discussed [1,2]. The design of such technologies requires an adequate understanding of the nature of soils and prediction of changes in their properties under anthropogenic influence [3,4]. This is evidenced by the attention to soil science problems in the scientific literature [5–8] and journalism [9].

The International Society for Soil Science approved World Soil Day (December 5) under the slogan "Soil is the basis of life," but the definition of "soil" remained in a descriptive version according to Dokuchaev's [10] paradigm. The opinion that there is no single definition of the concept "soil" was expressed by Sokolov [11], and the conclusion that "...the essence of the soil-forming process remains completely unclear" has been made [7]. Chukov and Yakovlev [12] describe the lack of consideration of soil characteristics in Russian land legislation.

The results of soil research obtained in recent years are accumulated but are not combined into general theories [13]. This was noted at International Congresses in Montpellier [14], in Philadelphia (2006), at the congresses of Society soil scientists (2008, 2016, 2020).

Dokuchaev [10] defined soil in 1886 as a special natural-historical body. Gerasimov [15] introduced the concept of elementary soil processes (ESP) into the theory of soil science [15]. About 60 ESP have been described, although there is an opinion that the very concept of ESP is ambiguous and often does not correspond to the definition of "elementary" [13]. Nevertheless, the paradigm "factors-processes-properties" remains the recognized level of scientific achievements of modern soil science.

Soil research in Belarus has intensified in connection with the development of hydro-reclamation since the 1960s of the last century. In its first stages, already in the 1970s, negative consequences along with successes were also discovered, including a decrease in soil fertility in areas adjacent to drainage structures. These changes required special attention to the study of soils of varying degrees and natures of moisture in different parent materials. From 1975 to 1995, a large amount of actual field data was collected. Subsequently, soil science in Belarus developed in the direction of soil geography as detailed (scale 1:2000) mapping, development of research methods, and description of the soil cover structure. From 1995 to 2020, generalizations were compiled and published [16–18]. A fairly complete understanding was obtained not only of the needs of the republic's soils for hydro-reclamation and their changes under the influence of drainage [19,20] but also of the water regime as the most important property of the soil [21].

Numerous characteristics of soil profiles revealed features inherent in the soil as a whole, in itself, and in specific soils, which can be considered, on the one hand, as natural systems (part of the biosphere), on the other—as a solid body phase (part of the soil) with a set of knowable properties. It makes possible to display the soil through an ensemble of essential properties and formulate a detailed general idea of the soil as a system of interconnected nonlinear processes. The synergetic approach most likely clarifies the concept of soil origin [16,17].

In this article, the declarative nature of these first formulations is replaced by reasoning based on the interpretation of previously collected materials [22] concerning the essence of soils. However, the essence of something is not observable in itself and is established on the basis of phenomena (basic properties) without which the object (soil, in this case) can't exist. The totality of such properties constitutes the essence of each soil (soil taxon), determines its genesis, which distinguishes it from a number of its own kind and allows to form a general idea of soil formation. A review of the collected information determined the purpose of this study—to clarify existing ideas about soil and soils as nature components and the basis for the development of technologies for their sustainable use. The original actual field data were used by the authors to obtain new data; the object of study is the pedoecological series—catena, and the subject of study is the properties that determine the essence of soils.

2. Objects and methods

2.1. The study area

The study area is characterized by a high-altitude soil-geobotanical profile (**Figures 1** and **2**), which is representative of the conditions of mixed forests and southern taiga in the humid zone of Eurasia. The site has the form of a transect with length 2.1 km and radius 0.4 km elongated in the latitudinal direction on the southern slope of the Minsk Upland (the central part of the East European border) on cohesive soil-forming parent materials—Valdai moraine with a cover of silty (loess-like) loams. Tectonically, the territory is an element of the Belarusian crystalline massif with Devonian deposits in the form of dolomites and dolomitized limestones. It is overlain by sedimentary deposits of the Quaternary period of the anthropogenic system. They consist of rocks of the Valdai (Sozh) glaciation with a thickness of 60–135 mm covered with loess-like loams. The thickness of the loams at the site decreases from 5 m at higher elevations to 0.8 m in the lower parts of the slopes where the loams are underlain by moraine sands. The relief of the territory is a gently undulating glacial-accumulative plain rising 150–200 m above sea level. The geomorphological appearance is dominated by long, gentle slopes with shallow valley depressions. In some areas, there are short, gentle slopes adjacent to closed depressions with a diameter of 10–20 m and a depth of 0.5–1.0 m. The soil-forming rocks are light silty (loess-like) loams, in places underlain from a depth of 0.5–0.8 m by moraine sands. The climate is mild temperate continental: radial balance 1500–1800 MJ/m^2, precipitation 560–700 mm per year [21].

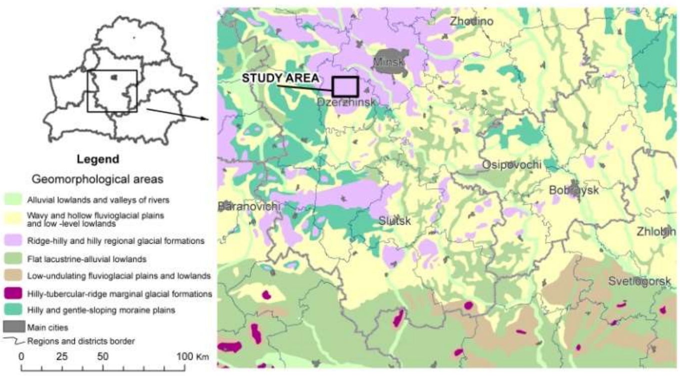

Figure 1. Study area.

According to observations of a weather station 20 km from the test site, the average air temperature for the year is 5.5 degrees, in July 17.6, in January 6.7; sum of temperatures more than 10 degrees 2000–2500, duration of the growing season 190 days. The average annual precipitation is 625 mm, for the warm period 400 mm; moisture coefficient: 1.0–1.1 annual, 1.1–1.2 in spring, 0.7–08 (up to 0.5) in summer. The climate is representative of coniferous-deciduous forests and the southern taiga of the humid zone of Eurasia [22]. Natural vegetation at the test site is represented by oak-spruce and aspen-spruce forests (**Figure 2**).

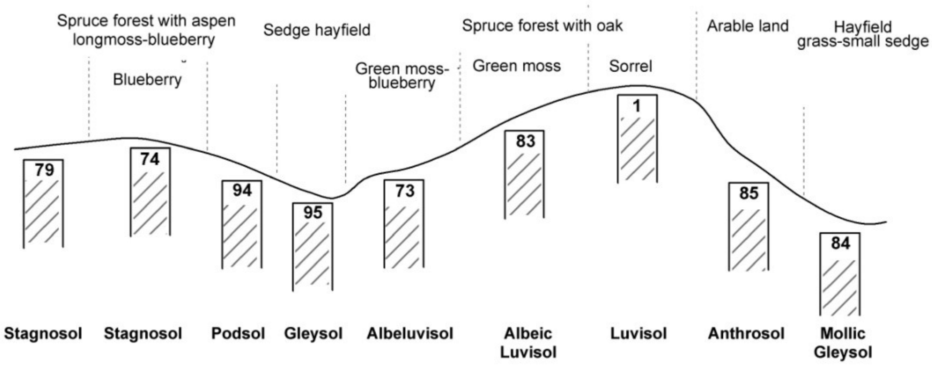

Figure 2. Soil transect.

2.2. The object of the study

The study object is typical soils of Belarus (**Figure 3**) developing on cohesive rocks (loess-like loams)—8 profiles of postlithogenic soils characterized by varying features and degree of moisture (**Figure 2**). The same soils in the World Reference Base for Soil Resources [6] are classified as ones with illuvial-clayey horizons (Bt) and reference soil groups: Albeic Luvisols, Albeluvisols, Anthrosols, Luvisols, Mollic Gleysols, Podsols, and Stagnosols (**Figure 2**). This article further uses the Belarusian nomenclature of soil taxa based on the 1977 USSR Soil Classification. The issues of classification and nomenclature of soils Zonn [8] remain relevant Rozhkov [23]. The experience of constructing a natural classification with determination of soil sites by their properties is presented in [16].

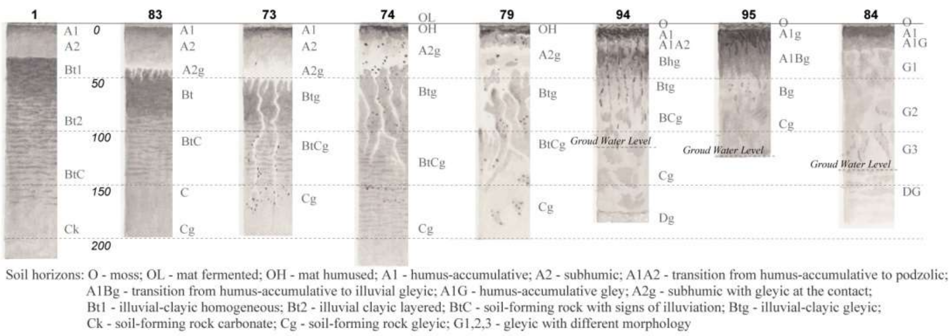

Figure 3. Pedoecological series and morphology of soil profiles of loamy granulometric texture.

2.3. Research methods

The description of all soil characteristics corresponds to national standards and fundamental research in the field of soil science. The methodology is based on the use of the inductive method (representation of the whole through its parts) and the commensurability of the soil taxon with the ecosystem.

Field (natural) studies included descriptions of the location of soil profiles, the botanical structure of ground cover plants, the morphological characteristics of soils with profile sketching, carbonates and gley testing, sampling for general chemical analyses, and determination of physical parameters of water. Samples for all types of analyses were taken from one common sample.

Observations for the dynamics of soil formation were carried out monthly (30 times in total) along the genetic horizons of profiles 83, 73, 74, 94, and 95 (**Figure 2**).

Field humidity was determined by the thermostat-weight method, and the soil temperature and redox potential (Eh) were estimated. The soil samples were taken for content analysis of eight mobile chemical compounds.

In laboratory conditions were determined: granulometric texture (according to the Kachinsky method), gross chemical structure of the total mass of soil and fine-grained soil material, clay minerals in fine soil particles, content of crystalline and amorphous forms of iron, aluminum, and silicon, content of total nitrogen and organic carbon (humus), groups, and fractional structure of humus. Monitoring of monthly changes in field humidity, pH, and Eh content of P_2O_5, Al_2O_3, K_2O, CaO, MgO, FeO, Fe_2O_3, and MnO was carried out with statistical processing and graphical presentation of the results.

The total number of numerical indicators at the research site is about 15000 [22]. Micromorphological descriptions with microelectron photography [18] were carried out for individual soils.

3. Research results

The soil studies results traditionally include descriptions of the environmental conditions of their formation, the profile morphology, and the determined properties. High-altitude soil-geobotanical profile (**Figure 2**) represents the position of each profile in landscape. Field sketches of soil profiles (**Figure 3**) are ranked by moisture degree according to the gradation accepted in Belarus—each subsequent element differs from the previous one by one degree of moisture (catena approach). The catena approach to soil research was used in Belarus in the last century [24] and is currently used abroad [17,25,26].

Soil morphology reveals a certain organization of vertical profiles persisting over time and indicating resistance to entropy accumulation. According to the second law of thermodynamics, this is only possible in an open system with the supply of additional energy from the outside, which confirms the first feature of the soil itself—its systemic energy-dependent nature. **Figure 3** gives an idea of soil diversity replacing detailed descriptions of soil morphology. It allows noting in the profiles of semi-hydromorphic soils (profiles 73, 74, 79) a general lighter color and the presence of vertical “veins” (possibly a trace of permafrost processes of the Valdai period), dark illuvial-humus horizon Bh (profile 94), and thick humus horizon (A1) of hydromorphic soil (profile 95).

3.1. Soil properties

3.1.1. Water-physical

Water-physical (moisture of soils) is usually represented based on information about field humidity. Soil graphs (average values) display the amount of incoming surface water and its movement (distribution) in soil profiles of varying degrees of moisture (**Figure 4**). This is the basis for the identification of types of water regimes, which will be discussed separately below.

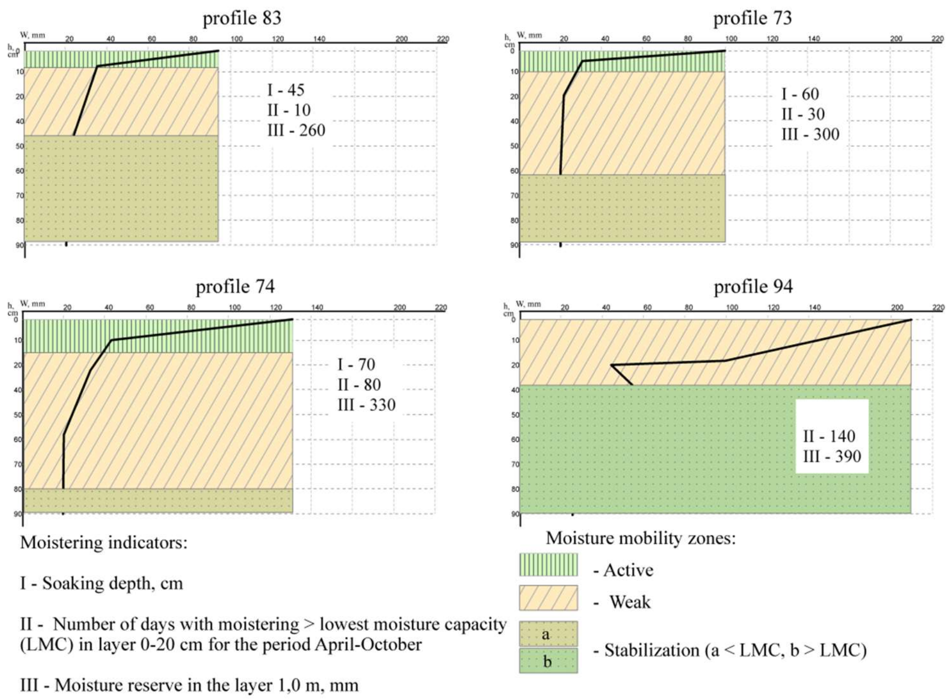

Figure 4. Soil graphs of moistering indicators and mobility zones.

The distribution of moisture over the genetic horizons of three soils with different degrees of moisture (profiles 83, 73, 74) was verified by a statistical (arithmetical mean) method of processing data on the mobility of the previously listed oxides and made it possible to establish reliable depths of wetting (penetration of hydrostatic moisture) into each soil (**Figure 4**).

3.1.2. Soil granulometric texture

Loess-like loams as soil-forming parent materials are widespread in the upland conditions of Belarus. Their originality lies in the predominance (50%–70%) of silt particles (0.05–0.001 mm) with an almost complete absence of large fractions (more than 1.0 mm) and a close to equal (20%–25%) content of fine sand fraction (0.25–0.05 mm) and clay-silt fraction (less than 0.01 mm) as well as coarse silt (0.05–0.01 mm) and clay (less than 0.001 mm)—approximately 10%.

A feature of the granulometric texture of soils developing on loess-like loams is considered to be the textural differentiation of profiles with the accumulation in their middle part of clay (20%–25%) and silt (12%–15%), forming the Bt horizon—illuvial-clayey.

It is known that soil-forming parent materials as a result of physical weathering are crushed to particles with a diameter of about 0.001 mm, but further destruction of these particles to pre-colloidal and colloidal sizes is carried out by microorganisms [2,27–29], revealing the biological origin of the initial part of the soil granulometric texture.

3.1.3. Mineralogical structure

Local loess-like loams have a simple mineralogical structure: quartz 80%–90%, feldspars 10%–15%, accessory minerals—biotite, amphiboles, garnets, etc. ~ 1% [18]. The total mass of soils is dominated by the original ones (quartz, feldspars, micas), and some newly formed minerals are present. The structure of the silty fraction is characterized by the presence of hydromica, kaolinite, chlorite, and fine-grained quartz, as well as newly formed clay (soil) minerals. Moreover, these are clay minerals of the vermiculite group, close to hydromicas in automorphic soils (profiles 1, 83) and montmorillonite group in semi-hydromorphic soils (profiles 73, 74, 79, 94). The connection between the transformation of hydromicas and soil hydromorphism, as well as a progressive increase in transformation up the profile, indicates the soil origin of clay mineral associations. At the same time, it is emphasized that only a small part of clay minerals participates in the biological cycle [30]. According to the majority of researchers starting with Dokuchaev [10], it is recognized the leading role for soil biota and especially for microorganisms in the transformation of minerals due to their ability to selectively absorb elements—biophiles [5]—with the mobilization of solar and atmospheric energy as well as after minerals destruction's energy due to their life activity.

3.1.4. Chemical composition

The chemical composition of the studied soils is characterized by the maximum number of analytical indicators. The most informative of them are used in physical models of chemical differentiation profiles (**Figure 5**) in the form of graphs of the total silt content in the soil-forming material, the total content of bases (CaO and MgO) and sesquioxides (Fe_2O_3 and Al_2O_3) in the total mass of soil and in clay material, as well as indicators of clay decomposition (SiO_2:Al_2O_3) and the content of amorphous iron (**Figure 5**). The presented models are visualized by curves; their origin and combination are the distinctive (diagnostic) characteristics of each soil as a taxon.

A comparison of the vertical distribution of total clay in the parent material (taking into account ignition losses) and in fine-grained soils (marker—the total content of sesquioxides) reveals similarities in the chemical composition of the soil and parent material. The gross composition of silt, on the contrary, clearly reflects the difference between soil and parent material. Thus, in profiles 73, 74, and 83, despite the textural heterogeneity of the profiles, the chemical composition of the silt and the SiO_2:Al_2O_3 indicators in the silt almost do not change across the horizons (**Figure 5**). This fact may indicate intrahorizontal transformations of the chemical composition of clay material without decomposition of minerals and without movement of products or the movement of fine-grained soil material in an unchanged state—lessivage [17], or primary (lithogenic) heterogeneity of the substrate. The soil of profile 94 has obvious signs of mineral decomposition (dashed line SiO_2:Al_2O_3). Soil hydromorphism is manifested in the distribution of amorphous iron along the profiles (**Figure 5**).

Comparing chemical differentiation (**Figure 5**) with graphs of changes in moisture content of the same soils (**Figure 4),** it is easy to notice the similarity of profiles 73, 74, and 83 in the distribution of moisture and sesquioxides. The observed differences between the soils of this group and the soil of profile 94 indicate their different nature. This allows us to conclude that the chemical differentiation profile curves make it possible to differentiate soils based on the test results, regardless of the methods used.

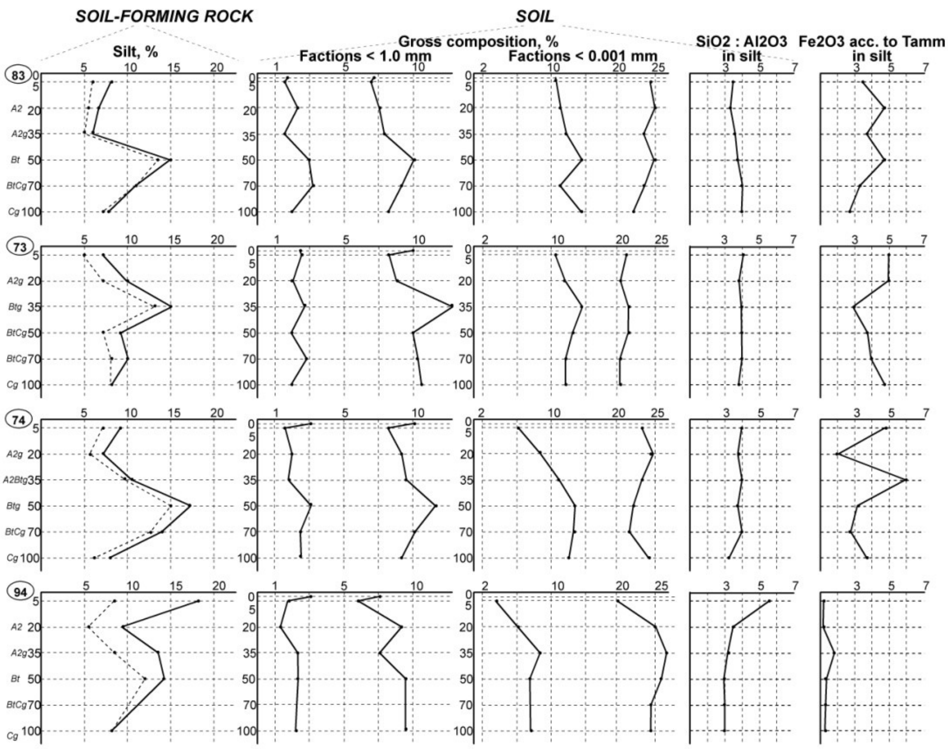

Figure 5. Chemical differentiation of soil profiles.

3.1.5. Organic matter, including humus

Organic matter—including humus—is an integral component of soil as a natural formation. The analytical characteristics of humus in the studied soils are presented in **Table 1**.

Humus content (%) and its reserves in the 0–20 cm layer (t/ha) indicate a correlation with hydromorphism. The relatively high share of humin as the most stable humus component indicates that the humus of the studied soils is characterized by low solubility and a high degree of mineralization. The humus composition ratio (Ch: Cf = 1.0–1.2) is given in **Table 1** and close to the structure of humus in gray forest soils [5]. The share of humic acid carbon in total soil carbon is in the range of 22%–38% (**Table 1**), which corresponds to the natural conditions of the broad-leaved forest zone [31,32]. Both of them indicate a connection between the group structure of humus and zonal climatic conditions [33]. Fractional structure of humic acids (**Table 1**) is determined by the chemistry of the soil-forming materials—fractions associated with sesquioxides (Ch1) predominate, a small proportion of fractions associated with calcium—Ch2, and quite high (with the exception of profiles 94, 95) with soil minerals—Ch3.

The source of humus is biomass (plants, fungi, animals, and microorganisms) accumulated and decomposed by microorganisms with the participation of enzymes [34], which have the ability to deeply transform the "raw material resource". Humus accumulates the energy from the Sun and the Earth initially assimilated by plants and animals, the energy of the atmosphere in the form of moisture entering the soil, and the energy of the destruction of minerals [35]. This fact allows us to consider humus as an indicator of the overall energy supply of the soil. "Green plants together with microorganisms involve solar radiation energy in the process of soil formation", as

D.G. Zvyagintsev writes [29].

Table 1. Analytical characteristics of humus in the studied soils.

Indicators		Soils (№ profile)							
		1	**83**	**73**	**74**	**79**	**94**	**95**	**84**
General humus	Depth A1, cm	4	4	4	5	6	10	21	17
	OSM content, %	5.9	5.5	7.0	13.5	16.2	19.3	19.0	29.2
	Reserves in the layer 0–20 cm, t/ha	31.2	43.0	75.0	105.4		152.3	144.0	239.8
Group humus	Group structure	1.4	1.0	1.0	1.2	n/m	1.0	1.1	1.4
	Humin, %	55.4	44.8	43.6	27.5	32.3	34.7	26.3	33.3
	Ch/Ctotal, %	n/m	22.5	22.4	28.4	n/m	33.0	37.0	38.0
Fractional humus	Ch1 from the sum Ch, %	n/m	52	67	54	n/m	71	59	24
	Ch2 from the sum Ch, %	n/m	2	0	6	n/m	12	12	41
	Ch3 from the sum Ch, %	n/m	46	33	40	n/m	17	29	3

3.1.6. Redox potential

Redox potential characterizes the biological activity of soils through an indicator of the intensity of their chemical and biological state—redox potential—Eh with a range of fluctuations from 180 to 700 mV [21]. Romanova notes [21] that the most important factors influencing redox conditions are temperature, humidity, and biological processes. At the same time, some authors give preference to hydrothermal conditions [36], others—to biological processes [5,37]. Our observations of Eh and biological activity of soils showed that the most noticeable correlation between soil Eh is with the autumn supply of litter and plant residues. In autumn, Eh was determined to be equal to 200 mV, and during spring waterlogging (maximum precipitation)—500 mV [22].

3.1.7. Soil water regime

In our study, special attention is paid to the soil water regime. The foundations of the doctrine of the water regime of soils laid by G.N. Vysotsky developed by Rode [38], who represents the water regime of soils in two aspects: 1) movement or stagnation of moisture in the profile—the type of soil water regime; 2) moisture content in the profile—soil moisture. Types of water regime of soils in the humid zone of the Northern Hemisphere within b. USSR proposed by Rode [29] still serve as a guide used for scientific and practical purposes. The materials collected in Belarus (including those described) made it possible to compile a new (complete) list of types of soil water regime based on monitoring the average long-term moisture supply of arable soils in the country. **Figure 2** demonstrates the role of terrain as a factor in the formation of water regime types, which, in turn, determines the entire diversity of genetic soil types (**Figure 3**). The cause-and-effect relationship between the genesis of soils and the geomorphology of the territory is considered by Dixon [1].

The data in **Table 2** provide generalized information about the water regime of natural soil types in Belarus and illustrate the research results. The following data are presented: 1) a list of types of soil water regime in a new edition (preserving the principle used in the names of A.A. Rode); 2) movement of moisture in the soil profile; 3) soil moisture.

The movement of moisture can be estimated by the severity of chemical differentiation of profiles compatible with the presence or absence of signs of decomposition of soil minerals (**Figure 5**). The direction of movement and the nature of moisture entering the soil can be traced in **Figures 2** and **4**.

Table 2. Types of soil water regime (based on research materials).

Type of water regime	Movement of moisture in the soil profile			Soil moisture			
	Chemical profile differentiation (Figure 5)	**Direction**	**Admission (source)**	**Soaking depth (m)**	**Waterlogging period (days), (Figure 4)**	**Moisture reserve (t/ha)**	**Hydromorphism (№ profiles) (Figure 2)**
Non-flush	Not evident	Vertical	Peliculation (dampening)	0.5	10	260	Automorphic (83)
Stagnant-flush	Not evident (weak)	Lateral	Infiltration and accumulation	0.6–0.8	30–80	300–350	Semi-hydromorphic (73;74)
Flush	Clearly expressed	Vertical	Infiltration and influx	1.3	140	380	Semi-hydromorphic (94)
Effusion	Accumulation at the border of the capillary fringe	Ascending	Evaporation (deduction)	Not determined	Not determined	Not determined	Hydromorphic (84)
Stagnant	Not expressed, absent	Stagnant	Accumulation	Groundwater Level	Not determined	Not determined	Hydromorphic (85)

Soil moisture in Belarus (quantitative assessment) was developed and published in the journal “Soil Science” at the end of the twentieth century. Today it is taken to be the number of days with humidity above the minimum moisture capacity in the 0–20 cm layer for the period April–October. In **Table 2,** soil moisture, moisture depth, and moisture reserves in the meter layer are the result of specific measurements of field moisture (**Figure 4**). The movement of moisture (chemical differentiation of profiles) and moisture content together reflect both general features (the level of hydromorphism and the characteristics of each type of water regime). The list and completeness of the given characteristics of the types of water regime of soils in Belarus suggest their relevance for the entire southern part of the humid zone of Eastern Europe.

Types of soil water regime:

- non-flushing—an attribute of automorphic soils with frontal vertical penetration of gravitational water (wetting) to a depth of half a meter from the day surface without chemical differentiation of profiles and signs of mineral decomposition;
- Stagnant-flushing—characterizes semi-hydromorphic soils with a predominant wetting depth of about one meter with lateral movement and episodic stagnation of intrasoil moisture above the stabilization zone (**Figure 4**) with weak signs of chemical differentiation of profiles and without signs of mineral decomposition;
- flushing—belonging to semi-hydromorphic soils in which capillary suspended

surface moisture occasionally, periodically, or constantly (depending on the degree of moisture) closes with capillary suspended moisture, reaching the level of soil-groundwater. Chemical differentiation of profiles and signs of mineral decomposition are clearly expressed (**Figure 5**);

- effusion (deductive-effusion)—the water regime of semi-hydromorphic soils, diagnosed by the accumulation of sesquioxides and bases at the boundaries of the capillary fringe above the seasonal levels of soil-ground or allochthonous intrasoil waters.
- Stagnant—is formed in hydromorphic soils (silt-gley, peat-bog), which are saturated to full moisture capacity due to the influx of groundwater or the accumulation of surface water.

3.2. Signs of soil formation

The biological component of soil formation except the enzymatic activity and observations of redox potential were not the subject of our research. However, the logic of things in the given descriptions and scientific literature over the past 50 years indicates the dominant role of biota, especially microorganisms, in the transformation of parent materials into soils ([34].

Zvyagintsev et al. [2] believe that "... the transformation of matter and energy by soil in biogeoceonoses is one of the most important functions of soils, determined mainly by the activity of microorganisms and soil invertebrate animals living in the soil". Studies of microflora, enzymes, and nucleic acids in the forests of Belarus [39] indicate a close connection between biological components and soils.

Energy of soil formation. The participation of solar and atmospheric energy—the energy of mineral destruction—in the formation of soils is known [40,41]. In Belarus, the experience of energy characterization of soils formed on loess-like loams was undertaken for four varieties under natural vegetation, also for ten highly cultivated arable varieties [18] and for soils with varying degrees of erosion and salinisation [19,42]. The reserves of total internal energy for all these soils were calculated according to the method developed by Volobuev et al. [35]. Also, it was estimated the energy associated with humus, with the mineral part of the soil, and the energy contained in 1 g and 1 g cm^3 of matter in the 0–50 cm layer.

The energy of soils, according to Fersman [43], is taken into account through the energy of the crystal lattice of chemical elements that make up the soil minerals. It is estimated by the amount of energy required for their complete destruction so that the energy accumulated in soils and taken into account according to Fersman should be estimated quantities inversely proportional.

4. The discussion of the results

4.1. General issues

The original factual material was used by the authors to obtain new data; the object of study is the pedoecological series—catena, and the subject of study is the properties that determine the essence of soils. However, before considering the essence of soil, it is necessary to answer the question of how "soil" differs from a “soil-like body" or “non-soil” [44]. There is an opinion from E.D. Dmitriev [45] that “...the boundaries between “soils” and “non-soils” will always be of a negotiated nature” [44]. Our research has led to the conclusion that the boundary between “soil” and “non-soil” can be the moisture supply. It is the main condition for the existence of a bio-inert system. According to the results of Romanova [17], “soil” according to our data, contains moisture available to plants in a layer of 0–20 cm for at least 5 days during the growing season of an average year in terms of moisture content.

From a philosophical position, “non-soil” (“soil body”) is a phenomenon about which only the fact of its existence is known; “soil” is an object that has a set of observable properties—a specific “natural-historical body”. At the same time, we note that the view of soil as a “natural-historical body of nature” is currently being revised since soil is not a “body” in the full sense of the word—its boundaries except the upper one are not clearly defined. Thus, we suppose “soil” can be defined rather as a fragment of terrain transformed by the action of external factors into a synergistic system with fertility (productive capacity).

4.2. Main (essential) properties of soils

Such properties in the study are properties without which the soil cannot exist. At the same time, the soil profile morphology is the most imagined property determined by the energy of soil formation. The granulometric texture of the soil as a whole is not an essential property since it differs little from the parent material, but in the presence of ultrafine fractions, it has signs of a transition of the substance from inert to bioinert—from parent material to soil.

The mineralogical structure of soil silt is characterized by the new formation of clay (soil) minerals and is the main property that distinguishes soil from parent material. Organic matter (humus) by definition is the essence of soil. In humus, the connection between the exchange of biota and minerals is the dominant feature of soil formation. The chemical composition of the substance of genetic horizons in itself in the form of specific indicators like the granulometric texture is not the main property of the soil, but the chemical differentiation of profiles serves as the basis for models that distinguish soils based on the totality of their properties.

The water regime, which determines the existence and circulation of biota, chemical differentiation of profiles, and genetic diversity of soils, is one of the main, if not the most important, properties—a marker of the genesis, nature, and degree of moisture. The redox potential is a reliable indicator of the role of biota in soil formation.

From the above review, it follows that the essential properties of soils include mineralogical structure, humus content, and water regime. The main agent of soil formation is the living population of the soil, primarily microorganisms, which mobilize biophilic elements contained in minerals using the energy of the sun, the atmosphere, and the energy of the destruction of minerals. The participation of microorganisms in the formation of ultrafine particles and clay minerals allows us to consider these phenomena as one common essential property called the transformation of minerals.

Characterization of the observed properties and identification of the main ones lead to the idea that soil formation is in fact not a process but a natural phenomenon consisting of many individual processes that transform parent materials into soils.

The idea of the essence of the pedosphere was formed on the basis of a generalization of information from a variety of monographs [13,37,45,46] to our own conclusions. As a result, it was concluded that the pedosphere is essentially part of the biosphere with a concentration of microbiota in subaerial conditions.

To the above, it is necessary to add research on soil energy. The information encoded in the energy characteristics of the soil may in the future become the basis of theoretical soil science and the basis for the development of nature-like land use technologies.

Exploring soil, one cannot help but note the duality of the very concept of soil. On the one hand, the soil itself, with its essential properties, acts as an idealized abstraction. On the other hand, it is a specific object with the same essential properties but in different combinations that determine genesis—the only reliable criterion that distinguishes soil from a number of its own kind.

5. Conclusion

The presence of extensive literature and "scientific capital" collected in Belarus, including on the territory of the research area, allows us to expand our understanding of soil as well as soil formation and the pedosphere by identifying their essential properties. This can contribute to the reduction of separately studied soil subsystems into a single soil system [23] that is relevant at least for the wet zone in the form of the following formulations.

The results of this study are an interpretation of the available materials, taking into account publications on the biology and water regime of soils over the past 50 years: 1) the difference between soil and soil-like bodies; 2) soil formation as a natural phenomenon—the mobilization of soil biota from the energy from the sun, the atmosphere, and the destruction of minerals in the original rocks; 3) the essence of the soil a) as a solid phase—a substrate transformed by the transformation of minerals, humus formation, and the water regime; b) as an ecosystem—a fragment of the area, transformed by the action of extraterrestrial and terrestrial factors into a synergistic system with fertility; 4) the essence of the pedosphere is a part of the biosphere with the concentration of microbiota in subaerial conditions.

The essence of soil formation (the transformation of parent material into soil) lies in a natural phenomenon—the mobilization by biota of the energy of the sun, the atmosphere, and the destruction of minerals of the original parent materials. The essence of the soil as a natural system (ecosystem) is the fragment of the territory transformed under the influence of extraterrestrial and terrestrial factors into a synergistic system with fertility (productive ability). The essence of the soil solid phase is that the substrate changed as a result of the transformation of minerals, humus formation, and water regime. The essence of the pedosphere is a part of the biosphere with a concentration of microbiota in subaerial conditions.

The significance of the results obtained in scientific terms lies in the confirmation using specific examples of general ideas about the surrounding world and about soil as a natural system with the decisive role of biota (microbiota) and water regime as a marker of soil genesis in the southern part of the humid zone of Eurasia. For the first time, based on the modules of chemical differentiation of soil profiles, types of water regimes have been identified. The concept of "soil" is considered in the aspect of representing soil as such (in itself) and as a specific object of a) the geobiosphere (natural system-ecosystem) and b) the biolithosphere (substrate modified by microbiota under different types of water regime).

The soil, due to its genesis, characterizes not only the state of the surface layer of the modified parent material but also represents a "solid basis for life" as a complex natural ("bio-inert") system of interaction between alien and terrestrial factors. From the point of view of treating soils as natural resources, an important guideline is the objective diagnosis of the genesis and especially the hydromorphism of soils with the prospect of assessing the bioenergy potential as comprehensive digital information about the diversity, properties, and natural fertility (productive capacity) of soils. Scientific knowledge about the essence of soils is the basis for the development of nature-like technologies for sustainable land use.

Author contributions: Conceptualization, TR and AC; methodology, TR; software, AC; validation, TR, NI; formal analysis, TR; investigation, NI; resources, AC; data curation, TR and AC; writing—original draft preparation, AC and TR; writing—review and editing, AC; visualization, AC; supervision, AC; project administration, TR; funding acquisition, TR. All authors have read and agreed to the published version of the manuscript.

Conflict of interest: The authors declare no conflict of interest.

References

1. Dixon JC. Pedogenesis With Respect to Geomorphology. Treatise on Geomorphology; 2022. pp. 57-77. doi: 10.1016/b978-0-12-818234-5.00162-0
2. Zvyagintsev DG, Bab'eva IP, & Zenova GM. Soil Biology (Russian). Moscow, MSU Publ; 2005
3. Klebanovich NV, Kindeev AL, Sazonov AA, et al. Spatial heterogeneity of soil cover and agrochemical indicators of the Soligorsk region (Russian). Land of Belarus. 2019; 1: 48
4. Andreeva OV, Lobkovsky VA, Kust GS, et al. The Concept of Sustainable Land Management: Modern State, Models and Typology Development. Arid Ecosystems. 2021; 11(1): 1-10. doi: 10.1134/s2079096121010029
5. Dobrovolsky GV, Bab'eva IP, & Bogatyreva DG. Structural and Functional Role of Soils and Soil Biota in the Biosphere (Russian). Moscow, Nauka Publ; 2003
6. Gerasimova MI, Krasilnikov VP, Spiridonova IA, et al. International Soil Classification System for Soil Diagnostics and Legends for Soil Maps (Russian). MSU M. V. Lomonosov Publ.; 2017
7. Kudeyarova AYu. On the Nature and Mechanism of Transformation of Humic Substances: Conceptual and Spatial-Temporal Aspects (Russian). In: Soil-forming processes and spatio-temporal organization of soils. Moscow, Nauka Publ; 2006
8. Zonn SV. Soil Classification Systems and Nomenclature (Russian). Pochvovedenie = Eurasian Soil Science. 1994; 7: 117-126
9. Homburg JA, Brevik EC, Sandor JA. Civilizations and the role of soil, agriculture, and climate change. In: Encyclopedia of Soils in the Environment. Springer International Publishing; 2023. pp. 29-36. doi: 10.1016/b978-0-12-822974-3.00155-5
10. Dokuchaev VV. Oeuvres (Russian). Moscow. 1950; 2
11. Sokolov IA. Theoretical Problems of Genetic Soil Science (Russian). Novosibirsk, Humanitarian Technologies Publ; 2004
12. Chukov SN, & Yakovlev AS. Soil and Land Categories in Modern Legislation of Russia (Russian). Pochvovedeniye = Eurasian Soil Science. 2019; 7: 891-898. doi: 10.1134/ S1064229319070020
13. Korsunov VM, & Krasekha EN. Pedosphere of Land (Russian). Ulan-Ude, BNC CO RAS; 2010

14. Ruellen A. About Scientific Basics of Soil Science. Pochvovedenie = Eurasian Soil Science. 1997; 4: 405-408
15. Gerasimov IP. Elementary Soil Processes as a Basis for Soil Genetic Diagnostics (Russian). Pochvovedenie = Eurasian Soil Science. 1973; 5: 3-19
16. Romanova TA, Berkov VF. Natural classification of soils in Belarus: new approach to soil operation. Proceedings of the National Academy of Sciences of Belarus Agrarian Series. 2019; 57(4): 431-443. doi: 10.29235/1817-7204-2019-57-4-431-443
17. Romanova TA. Diagnostic of Soils of Belarus and Its Classification in System FAO - WRB (Russian). Minsk, IVC Minfin Publ; 2004
18. Sergeenko VT, & Lisisca VD. Clay minerals of the soils of Belarus (Russian). Minsk, Institute of Soil Science and Agrochemistry, IVC Minfin Publ; 2011
19. Chervan AN, Tsybulka NN, & Yatsukhno VM. Methodological approaches and practical application of the results of assessing land/soil degradation in Belarus (Russian). Izvestiya of the Russian Academy of Sciences Geographical series. 2022; 86: 1, 55-68. doi: 10.31857/S2587556622010058
20. Even RJ, Francesca Cotrufo M. The ability of soils to aggregate, more than the state of aggregation, promotes protected soil organic matter formation. Geoderma. 2024; 442: 116760. doi: 10.1016/j.geoderma.2023.116760
21. Romanova TA. Water regime of Soils of Belarus (Russian). Minsk, IVC Minfin Publ; 2015
22. Ivakhnenko NN. Ameliorative Features of Loess-like Loam Soils of Central Belarus (Russian). Minsk; 1988. p. 245
23. Rozhkov VA. Tectological Conception of Classifying and Typology (Russian). In: Sovremennye Problemy Pochvovedeniya = Modern Soil Science Problems. Moscow, Soil Institute V. V. Dokuchaev Publ; 2000. pp. 259-271
24. Blume HP. Genesis and ecology of gley (German). Verhandlungender Komm Hangwasserboeden; 1971. pp. 187-194
25. Bäumler R, Oliver MA, Stockmann U. Overview chapter on factors of soil formation. In: Encyclopedia of Soils in the Environment. Academic Press. doi: 10.1016/b978-0-12-822974-3.00236-6
26. Gerasimova MI, Golovleva YA, Lavrova AM, & Krasilnikov PV. Quantitative assessment of soil diversity at different study scales on the example of the Republic of Karelia (Russian). Bulletin of Moscow University. 2020; 3: 47-52
27. Korneykova M, Kozlova E, Ivashchenko K, et al. Urban soil microbiome: Activity, diversity and functioning. In: Encyclopedia of Soils in the Environment. Academic Press; 2023. pp. 480-493. doi: 10.1016/b978-0-12-822974-3.00266-4
28. Panikov NS. Kinetics of microbial processes: Applications to soil biology. In: Encyclopedia of Soils in the Environment. Elsevier; 2023: 186-218. doi: 10.1016/b978-0-12-822974-3.00259-7
29. Rode AA, & Smirnov VN. Soil Science (Russian). Moscow, Vysshaya shkola Publ; 1972
30. Gradusov BP. Map of Soil-forming and Underlying Rocks of the World, its Genetic-geographical Analysis and Patterns of Soil Formation (Russian). Pochvovedeniye = Eurasian Soil Science. 2000; 2: 180-195
31. Kononova MM. Soil Organic Matter (Russian). Moscow, AS USSR Publ;1963
32. Samec P, Volánek J, Kučera M, et al. Effect of Soil Diversity on Forest Plant Species Abundance: A Case Study from Central-European Highlands. Forests. 2021; 12(5): 534. doi: 10.3390/f12050534
33. Ibáñez JJ, Brevik EC, Cerdà A. Geodiversity and geoheritage: Detecting scientific and geographic biases and gaps through a bibliometric study. Science of The Total Environment. 2019; 659: 1032-1044. doi: 10.1016/j.scitotenv.2018.12.443
34. Shcherbakova TA. Soil Fermentative Activity and Transformation of organic Matter (in Natural and Cultural Phytocenoses (Russian). Minsk: Science and Technics Publ; 1983
35. Volobuev VR. Introduction to the Energy of Soil Formation (Russian). Moscow, Nauka Publ; 1974. p. 128
36. Liu S, Huang Q, Zhang W, et al. Improving soil hydrological simulation under freeze–thaw conditions by considering soil deformation and its impact on soil hydrothermal properties. Journal of Hydrology. 2023; 619: 129336. doi: 10.1016/j.jhydrol.2023.129336
37. Dobrovolsky GV, Karpachevsky LO, Kriksunov EA. Geospheres and pedosphere (Russian). Moscow, GEOS Publ; 2010. p. 190
38. Rode AA. Water Regyme of Soils and Its Types (Russian). Pochvovedenie = Eurasian Soil Science. 1956; 4: 3-23
39. Kirkland M, Atkinson PW, Pearce-Higgins JW, et al. Landscape fires disproportionally affect high conservation value temperate peatlands, meadows, and deciduous forests, but only under low moisture conditions. Science of The Total Environment. 2023; 884: 163849. doi: 10.1016/j.scitotenv.2023.163849
40. Shetty R, Mansouri Bigdeli M, Mooney M. Quantifying foam destruction during conditioning of fine-grained soils. Tunnelling and Underground Space Technology. 2024; 153: 105971. doi: 10.1016/j.tust.2024.105971

41. Xu Z, Tsang DCW. Mineral-mediated stability of organic carbon in soil and relevant interaction mechanisms. Eco-Environment & Health. 2024; 3(1): 59-76. doi: 10.1016/j.eehl.2023.12.003.
42. Zhao B, Chervan A. Spatial distribution of soils by salinization level in Soligorsk district of Belarus. Natural Resources. 2024; 1: 5-12
43. Fersman AE. Geochemistry (Russian). Leningrad, ONTI. 1937; 1: 260
44. Goryachkin SV, Mergelov NS, Targulian VO. Extreme Pedology: Elements of Theory and Methodological Approaches. Eurasian Soil Science. 2019; 52(1): 1-13. doi: 10.1134/s1064229319010046
45. Dmitriev EA. Theoretical and methodological problems of soil science (Russian). Moscow: GEOS Publ; 2001. p. 324
46. Wadoux AMJC, Heuvelink GBM, Lark RM, et al. Ten challenges for the future of pedometrics. Geoderma. 2021; 401: 115155. doi: 10.1016/j.geoderma.2021.115155

Journal of Geography and Cartography 2024, 7(2), 7981.
https://doi.org/10.24294/jgc7981

Article

A remote sensing approach to identify environmental economics considering blue carbon sequestration in Satkhira coastal area, Bangladesh

Raiyan Siddique[1], M. R. Ashikur[2,*], Taspiya Hamid[1], Mohammad Azharul Islam[1]

[1] Department of Oceanography & Hydrography, Bangabandhu Sheikh Mujibur Rahman Maritime University, Dhaka 1216, Bangladesh
[2] Institute of Bay of Bengal & Bangladesh Studies, Bangabandhu Sheikh Mujibur Rahman Maritime University, Dhaka 1216, Bangladesh
*** Corresponding author:** M. R. Ashikur, ro.ibbbs@bsmrmu.edu.bd

CITATION

Siddique R, Ashikur MR, Hamid T, Islam MA. A remote sensing approach to identify environmental economics considering blue carbon sequestration in Satkhira coastal area, Bangladesh. Journal of Geography and Cartography. 2024; 7(2): 7981. https://doi.org/10.24294/jgc7981

ARTICLE INFO

Received: 15 July 2024
Accepted: 22 October 2024
Available online: 8 November 2024

Abstract: The persistence of coastal ecosystems is jeopardized by deforestation, conversion, and climate change, despite their capacity to store more carbon than terrestrial vegetation. The study's objectives were to investigate how spatiotemporal changes impacted blue carbon storage and sequestration in the Satkhira coastal region of Bangladesh over the past three decades and, additionally to assess the monetary consequences of changing blue carbon sequestration. For analyzing the landscape change (LSC) patterns of the last three decades, considering 1992, 2007, and 2022, the LSC transformations were evaluated in the research area. Landsat 5 of 1992 and 2007, and Landsat 8 OLI-TIRS multitemporal satellite images of 2022 were acquired and the Geographical Information System (GIS), Remote Sensing (RS) techniques were applied for spatiotemporal analysis, interpreting and mapping the output. The spatiotemporal dynamics of carbon storage and sequestration of 1992, 2007, and 2022 were evaluated by the InVEST carbon model based on the present research years. The significant finding demonstrated that anthropogenic activity diminished vegetation cover, vegetation land decreased by 7.73% over the last three decades, and agriculture land converted to mariculture. 21.74% of mariculture land increased over the last 30 years, and agriculture land decreased by 12.71%. From 1992 to 2022, this constant LSC transformation significantly changed carbon storage, which went from 11,706.12 Mega gram (Mg) to 9,168.03 Mg. In the past 30 years, 2,538.09 Mg of carbon has been emitted into the atmosphere, with a combined almost 0.86 million USD. The findings may guide policymakers in establishing a coastal management strategy that will be beneficial for carbon storage and sequestration to balance socioeconomic growth and preserve numerous environmental services.

Keywords: remote sensing; geographical information system; InVEST carbon model; blue carbon storage and sequestration; environmental economics

1. Introduction

Carbon is sequestered by coastal ecosystems such as mangroves and seagrass meadows at rates that are substantially greater per unit area in comparison to terrestrial vegetation [1]. Coastal habitats have been identified as having some of the most concentrated quantities of carbon on the planet [2]. Several studies reveal that mangrove ecosystems typically absorb an average of 6 to 8 Mega gram (Mg) of Carbon dioxide (CO_2) per hectare of carbon annually (tons of CO_2 equivalent per hectare) [3]. The carbon sequestration process of an ecosystem absorbs and retains more carbon in biomass, sediments, or water than is released into the atmosphere [4]. Recent research into the function of blue carbon throughout the global carbon cycle indicates that coastal habitats not only encompass enormous above-ground biomass on tropical shorelines but also possess considerably more below-ground carbon storage [5]. Blue carbon, in contrast to green carbon that exists in terrestrial vegetation, endures in ocean sediments for thousands of years [6].

Blue carbon sequestration (BCS) employs the carbon-sequestration competencies of marine creatures and coastal ecosystems to establish carbon sinks. The extraction and processing of blue carbon (BC) could evolve into a financially sustainable industrial endeavor, stipulating the fact that an internationally recognized trading market has been established and a feasible measurement and valuing system for carbon sink services has been placed in established [7]. The efforts intended for restoring and protecting BC also offer the potential to develop market-driven mechanisms that exploit existing frameworks for carbon offsets (also called carbon credits). The commercial viability of BC extraction and processing would be attained through the establishment of a global trading market and the implementation of a proper measurement and pricing mechanism for carbon sink commodities [8].

Coastal habitats are widely regarded as some of the most ecologically and economically crucial regions on Earth [6]. Coastal environments offer a diverse range of amenities and goods [9]. The natural processes and components of ecosystems that contribute to human demands for commodities and amenities are known as ecosystem services [10]. Coastal habitats offer vital ecosystem services due to their variety of ecosystems and organisms that serve a crucial role in preserving the carbon cycle's equilibrium [11]. Bangladesh's coastal and marine ecosystems are integral to the Bay of Bengal (BoB) large marine ecosystems (LMEs), one of 64 LMEs worldwide. A substantial proportion of people living in Bangladesh's coastal region and elsewhere depend on ecosystem services from the coastal and marine ecosystem for their livelihoods and income. The same argument applies to several coastal communities across the globe as well [12]. The Blue Economy (BE) entails a range of commercial activities, goods, services, and investments that hinge on and have an impact on coastal and marine resources [13]. The two primary anthropogenic stresses that coastal ecosystems face worldwide are urbanization and industrialization and these two factors influence the intensity of landscape change (LSC) and have altered the coastal land cover in recent decades [14]. The structure and zonation of the coastal environment have been greatly disturbed by coastal disturbances and changes in LSC [15]. When attempting to comprehend and simulate the transformation in the coastal regions of the planet, LSC modification is considered to be one of the most vital processes. Complex interconnections between human and environmental driving variables are what cause it [16]. BC habitats are threatened by anthropogenic activities such as land conversion for agricultural production and urban growth [17]. The FAO's worldwide forest resources evaluation for 2020 revealed that 113 nations and territories possess mangrove forest lands. From 1990 to 2020, there was a global decline of 1.04 million hectares in the mangrove area [18].

There are a multitude of conventional methods for quantifying stored carbon. The estimation and assessment of spatially explicit services for carbon sequestration potential might vary depending on factors such as meteorological conditions, management applications, ecosystem characteristics, species composition, and local populations. When applied to individual foundational issues, the combination of geographic information systems (GIS) and remote sensing (RS) will produce the most reliable results [19]. A method for tracking the spatiotemporal distribution and condition of coastal ecosystems is RS [20]. Utilizing four carbon pools, the concept of the InVEST Carbon model is used to estimate the current carbon stocks and their potential future growth (aboveground biomass, underground biomass, dead organic matter, and soil carbon) [16]. The InVEST blue carbon model evaluates the fluctuating value of carbon storage and sequestration services provided by coastal ecosystems. It performs this by analyzing the variations in carbon storage over a specific timeframe and contrasting them with various management scenarios.

Ma et al. 2019 have investigated the storage of coastal blue carbon in the Yellow River Delta and its relationship to changes in land cover over the previous four decades in their study article [21]. Aljenaid et al. 2022 have combined GIS and RS data for evaluating the spatiotemporal changes of mangroves in Bahrain over the last 50 years and their relationship with carbon stocks and potential emissions [6].

Climate change is characterized by rising sea levels, increased salinity, and a higher frequency of cyclones making the Satkhira region vulnerable. These environmental stresses and anthropogenic activity put at risk local ecosystems, including the mangrove forests of the Sundarbans, while diminishing the carbon sequestration capacity of these essential blue carbon ecosystems. Despite these challenges, the Satkhira region presents considerable opportunities for blue carbon sequestration. The Sundarbans, recognized as the largest mangrove forest globally, provide significant carbon storage potential. Regional conservation and restoration efforts, supported by government and international organizations, can improve blue carbon sequestration. The increasing global interest in carbon credits offers an economic motivation for the preservation of these ecosystems. Carbon offset programs could fund Satkhira conservation while mitigating climate change and protecting biodiversity.

This study contributes to existing research on blue carbon by examining the environmental economics of BCS rates in the Satkhira coastal area of Bangladesh and specifically reviews earlier studies that mostly focused on data collection and the mapping of blue carbon ecosystems in different nations. In this study, the LSC intensity over the past three decades in the study area using the GIS and RS techniques to better understand the issue. This study's main objectives are to investigate how spatiotemporal changes impact blue carbon storage and sequestration in the research area over the last three decades and evaluate shifting BCS from an economic angle.

2. Materials and methods

2.1. Study area

Satkhira, located in the Southwestern region of Bangladesh, is a constituent of the Khulna division. The Satkhira district has boundaries set by the Jashore district to the North, the Khulna district to the East, the BoB to the South, and India to the West. It is located between latitudes 21°36' North and 22°54′ North and longitude 88°54′ East and 89°20′ East (**Figure 1**). The district has 1440 villages, 2 paurashavas, 7 upazilas, 79 unions, 953 mauzas, 18 wards, and 42 mahallas. Satkhira Sadar, Assasuni, Debhata, Kalaroa, Kaliganj, Shyamnagar, and Tala are the upazilas of the Satkhira district [22]. According to the Bangladesh Meteorological Department (BMD) in 2022, Satkhira's yearly average temperature is 77.0° F (25 °C). May is considered the highest average temperature, at 86.0° F (30 °C). January has the lowest average temperature, at 66.0° F (18.9 °C). In Satkhira, there are 66.5 inches (1689.1 mm) of precipitation on average each year. With 13.9 inches (353.1 mm) of precipitation on average and July is the month with the most precipitation. January has an average of 0.3 inches (7.6 mm) of precipitation, making it the month with the least amount [23]. The important rivers in this region include the Kobadak, Sonai, Kholpatua, Morischap, Raimangal, Hariabhanga, Ichamati, Betrabati, etc. [24].

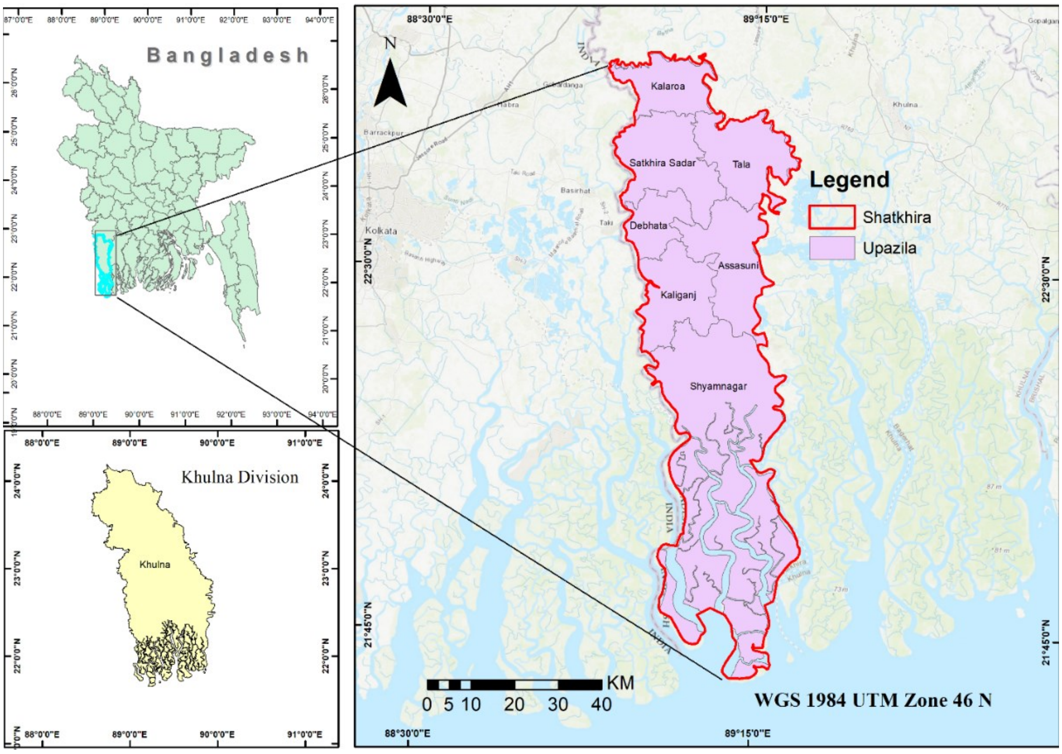

Figure 1. Map shows the location of the study area, index map shows Bangladesh and Khulna division.

2.2. Overview of data and pre-processing

Landsat 4–5 Thematic Mapper (TM) level one image for 1992, 2007 and Landsat 8 OLI/TIRS images for 2022 were acquired from the United States Geological Survey (USGS) for the detection of LSC alteration of the area of interest (AOI). Nine satellite images from the same month of March with a 15-year interval were collected from the USGS. The characteristics and information of the research data are given in **Table 1**.

Table 1. Description of the data used for this study.

Year	Date of Acquisition (yr-mm-dd)	Sensor	Path	Row	Resolution	Cloud Cover
1992	1992-03-08	TM	138	*44/45*	30 m	<10%
2007	2007-03-08	TM	138	*44/45*	30 m	<10%
2022	2022-03-03	OLI_TIRS	138	*44/45*	30 m	<10%

The susceptibility of Landsat sensor-captured images to distortion was influenced by elements such as sensors, solar conditions, atmospheric conditions, and topography.

Preprocessing made a concerted attempt to minimize these effects to the greatest extent possible for a specific application [25]. The satellite images were selected based on several criteria (1) The satellite images must have cloud coverage of less than 10% over the whole research region, or ideally, be completely free of clouds. (2) It is essential to provide access to a continuous sequence of Landsat images over a significant period to optimize the distinction and categorization of diverse land utilization patterns [26]. According to Koppen's climate zone, the Satkhira coastal area was situated in a tropical climate zone [27]. Obtaining completely free cloud data is indicated to be quite challenging. Nevertheless, the data collected for this study only had minimal cloud coverage, amounting to less than 10%. The haze and clouds in satellite images were effectively eliminated using Erdas Imagine software v14.

Due to the absence of homogeneity in the time series of Satellite images, it was necessary to evaluate abrupt changes in the LSC while utilizing multi-temporal satellite images. The noise from surface signals, as well as the absorption and scattering of atmospheric gases and aerosol particles as they passed through the earth's atmosphere and back to the sensor, had an impact on this homogeneity. The satellite images may be accurately interpreted due to atmospheric influences. The atmospheric impact should be removed from the satellite images during pre-processing in order to evaluate change detection [28].

The essential process for transforming image data from many sensors and platforms into a physically significant common radiometric scale was the calculation of at-sensor spectral radiance. Using 32-bit floating-point calculations, pixel values (*Q*) from unprocessed, raw data were changed into absolute spectral radiance units during radiometric calibration. The Equation (1) was carried out to perform the Q_{cal}-to-L_λ conversion for Level 1 products [26, 28–30].

$$L\lambda = \left(\frac{LMAX\lambda - LMIN\lambda}{Qcalmax - Qcalmin}\right)(Qcal - Qcalmin) + LMIN\lambda \tag{1}$$

where;

L_λ = Spectral radiance at the sensor's aperture [W/ (m^2 sr μm)]

Qcal = Quantized calibrated pixel value [DN]

Qcalmin = Minimum quantized calibrated pixel value corresponding to *LMINλ* [DN]

Qcalmax = Maximum quantized calibrated pixel value corresponding to $LMAX_\lambda$ [DN]

$LMIN_\lambda$ = Spectral at-sensor radiance that is scaled to *Qcalmin* [W/(m^2 sr μm)]

$LMAX_\lambda$ = Spectral at-sensor radiance that is scaled to *Qcalmax* [W/(m^2 sr μm)]

By converting the at-sensor spectral radiation to exo-atmospheric TOA reflectance, sometimes referred to as in-band planetary albedo, was achieved scene-to-scene variability. There were three benefits to employing TOA reflectance instead of at-sensor spectral radiance when comparing images from various sensors. The cosine impact of varied solar zenith angles caused by the delay in data collecting is first eliminated. The second was that TOA reflectance made up for variations in exo-atmospheric solar irradiance caused by spectral band discrepancies. Third, the fluctuation in the earth-sun distance between several data-gathering dates was adjusted for using the TOA reflectance. These changes had a big impact on time and space, too.

The acquired value of radiance was converted to top of the atmosphere (TOA) reflectance, which was how the earth's TOA reflectance was calculated from Equation (2) [31].

$$\rho = \frac{\pi L\lambda d^2}{ESUN\lambda . \cos\theta s} \tag{2}$$

where;

ρ = Planetary TOA reflectance for δ [unitless]

π = Mathematical constant equal to~3.14159 [unitless]

$L\lambda$ = Spectral radiance at the sensor's aperture [W/(m^2 sr μm)]

d = Earth–Sun distance [astronomical units]

$ESUN\lambda$ = Mean exo-atmospheric solar irradiance [W/(m^2 μm)]

θs = Solar zenith angle [degrees]

ArcGIS software v10.5 was used to process radiometric calibration, radiometric correction, image cropping, and mapping.

2.3. LSC classification

Multiband raster images with LSC data extracted by classification and image analysis. Autonomously grouping pixels with comparable reflectance ranges into a specific LSC class was the objective of both supervised and unsupervised image classification. Supervised classification, a method directed by the user, entails the selection of training sites to serve as references for categorization. Supervised classification was implemented using a variety of methods, including parallelepiped classification, K-nearest neighbor, minimal distance classification, and others [32].

The commonly used maximum likelihood classification method was applied to the LSC classification in this study using ArcGIS software. The spectral response patterns' variance and covariance were quantitatively evaluated by the maximum likelihood algorithm, and each pixel was then assigned to the class with the greatest likelihood of association [32].

Six LSC categories were selected in total: water body, tide flat, mariculture, built-up area, vegetation, and cultivated land (**Table 2**). For each of the LSC classes, about 50 training samples were gathered for maximum likelihood classification. To estimate the LSC change, multitemporal raster layers were created, and their corresponding data were compared.

Table 2. The classification method for LSC employed in this study.

LSC categories	Description
Built-up Area	Residential; commercial and services; transportation infrastructure; industrial; mixed urban and other urban
Cultivated Land	Agriculture land; paddy field; vegetables; fruits; and other cultivated lands
Water Body	River; canal; pond; Permanent open water; lakes
Mari culture	Shrimp aquaculture; Gher
Vegetation	Mangrove vegetation; homestead vegetation; urban vegetation
Tidal flat	Deposit mud or sand; coastal wetlands

2.4. Accuracy assessment

Three distinct accuracy assessments were conducted to evaluate the quality of the generated LSC map. The error matrix technique was used for the initial approach. The integration of reference data and independent categorization allowed for a clear comprehension of the situation in the field [33]. Accuracy identified the degree to which the created map agreed with the reference categorization. The correctness of a study was frequently assessed using the Kappa coefficient of agreement. Kappa was said to include a correction for "random allocation agreement". By using Equation (3) the Kappa coefficient was calculated [32,34].

$$\text{Kappa coefficient (K)} = \frac{n\sum_{i=1}^{r} x_{ii} - \sum_{i=1}^{r} x_i + x + i}{n^2 - \sum_{i=1}^{r} x_i + x + i} \tag{3}$$

Here;

x_{ii} is the number of observations in row i and column i;

x_i + and $x + i$ are marginal totals for row i and column i respectively;

n is the total number of observations (pixels)

Through the creation of an error matrix; the accuracy of each raster layer was evaluated in the current study. Stratified random sampling was used for the accuracy evaluation. Overall accuracy was calculated by using the Equation (4) [32,34].

$$\text{Overall accuracy} = \frac{\sum_{i=1}^{r} x_{ii}}{x} \tag{4}$$

where x_{ii} is the diagonal elements in the error matrix;

x is the total number of samples in the error matrix; and r is the number of rows in the matrix.

2.5. Blue carbon storages and sequestration utilizing the InVEST carbon model

The quantity of static carbon storage and dynamic sequestration for each cell in the research area was calculated using the InVEST 3.10.2 carbon model. The four carbon pools were examined in this module: soil organic carbon, belowground carbon density, aboveground carbon density, and dead organic matter. The calculation of the carbon storage $C_{m;I;j}$ in a given grid cell (i; j) with land use type "m" achieved by Equation (5) [35].

$$C_{m;I;j} = A \times (Ca_{m;I;j} + Cb_{m;I;j} + Cs_{m;I;j} + Cd_{m;I;j}) \tag{5}$$

In this formula, A is the real area of each grid cell (ha).

$Ca_{m;I;j}$; $Cb_{m;I;j}$; $Cs_{m;I;j}$ $Cd_{m;I;j}$ are the aboveground carbon density, belowground carbon density, soil organic carbon density, and dead organic matter carbon density (i; j), respectively.

Finally, carbon storage "C" and carbon sequestration "S" were calculated by Equations (6) and (7) for the whole case study region [35].

$$C = \sum_{m=1}^{n} c_{m;i;j} \tag{6}$$

$$S = C^{T2} - C^{T1} \tag{7}$$

In Equation (7), C^{T2} and C^{T1} demonstrate static carbon storage in years T2 and T1 (here T2 > T1). The needed data for running the carbon storage model was the LSC map and the biophysical table containing columns of LSC, '*C*_above' '*C*_below' '*C*_soil,' and '*C*_dead' (**Table 3**).

Table 3. Types of LSC and the elements that make up their carbon pools [21,35,36].

LSC Type	C_above (Mg/hm^2)	C_below (Mg/hm^2)	C_soil (Mg/hm^2)	C_dead (Mg/hm^2)
Vegetation	14	7	15	1
Water Body	2	1	10	0
Tidal Flat	6	2	16	1
Mari culture	1	0	12	0
Built-up Area	0	0	8	0
Agriculture Land	4	9	25	1

C_above = Above ground carbon biomass; C_below = Below ground carbon biomass; C_soil = Soil carbon biomass; C_dead = Dead carbon biomass.

The InVEST model, although commonly employed for ecosystem service valuation. The model relies significantly on the quality of input data, which encompasses LSC maps, vegetation characteristics, and various biophysical parameters. Inaccuracies in these inputs can propagate through the model, resulting in potential errors in estimating ecosystem services, such as carbon storage.

2.6. Economic evaluation of blue carbon sequestration

The final step assessed the economic value of BCS in the Satkhira shoreline region. Over 30 years, the LSC in the research region changed, resulting in a modification of the storage of blue carbon. The rate of carbon sequestration was also altered due to the shift in storage. Unfortunately, the Satkhira region did not have any long-term information on the societal costs of land-use change, particularly the removal of mangrove forests and other vegetation. The monetary value of blue carbon across the Satkhira region was calculated based on estimates of the social cost of carbon and the current price of carbon credits. Hence, the economic data about the cost of carbon per mega gram was derived from several sources, including research studies and international organizations, to analyze and assess the economic significance of carbon. The price of carbon at the moment around \$50 per Mg [37]. In this study, the carbon cost was set at \$50 per Mg.

3. Results and discussion

3.1. Spatial and temporal transformation of LSC

The RS technology illustrated the LSC dynamics of the Satkhira shoreline area from 1992 to 2022. The spatial and temporal distribution of LSC patterns considered six classes and these were tidal flat, vegetation, water body, mariculture, agriculture land, and built-up area as shown in **Figure 2**. The percentage of different LSC classes and their percentage of cover change in the years 1992, 2007, and 2022 are presented in **Table 4**. The tidal flat regions have consistently dropped over the years, with a decline from 9.34% in 1992, to 8.2% in 2007, and further down to 6.07% in 2022. Conversely, the vegetation in the study region rose from 33.11% in 1992 to 41.1% in 2007 but declined to 25.39% in 2022. On the other hand, agricultural land areas experienced a significant decrease from 20.92% in 1992 to 4.93% in 2007, followed by a rise in 2022 to 8.21%. Also, build-up areas reduced from 22.29% in 1992 to 17.2% in 2007, followed by a rise in 2022 to 23.65%. Mari culture areas continued their increasing trend from 1992, 2007, and 2022 where it increased from 6.25% to 27.99% respectively. Eventually, there was an absence of discernible alterations in the aquatic systems within the designated research region. The aquatic ecosystem had a 0.61% increase in size during the previous 30 years.

Table 4. Percentile of the LSC categories and percentile change between the study years 1992; 2007; and 2022.

	Percentile (%)			Percentile change		
Class Name	1992	2007	2022	2007–1992	2022–2007	2022–1992
Tidal Flat	9.34	8.20	6.07	−1.14	−2.13	−3.27
Vegetation	33.11	41.10	25.39	7.98	−15.71	−7.73
Water Body	8.08	8.04	8.69	−0.03	0.65	0.61
Mari culture	6.25	20.52	27.99	14.27	7.47	21.74
Agriculture Land	20.92	4.93	8.21	−15.98	3.28	−12.71
Built-up Area	22.29	17.20	23.65	−5.09	6.45	1.36

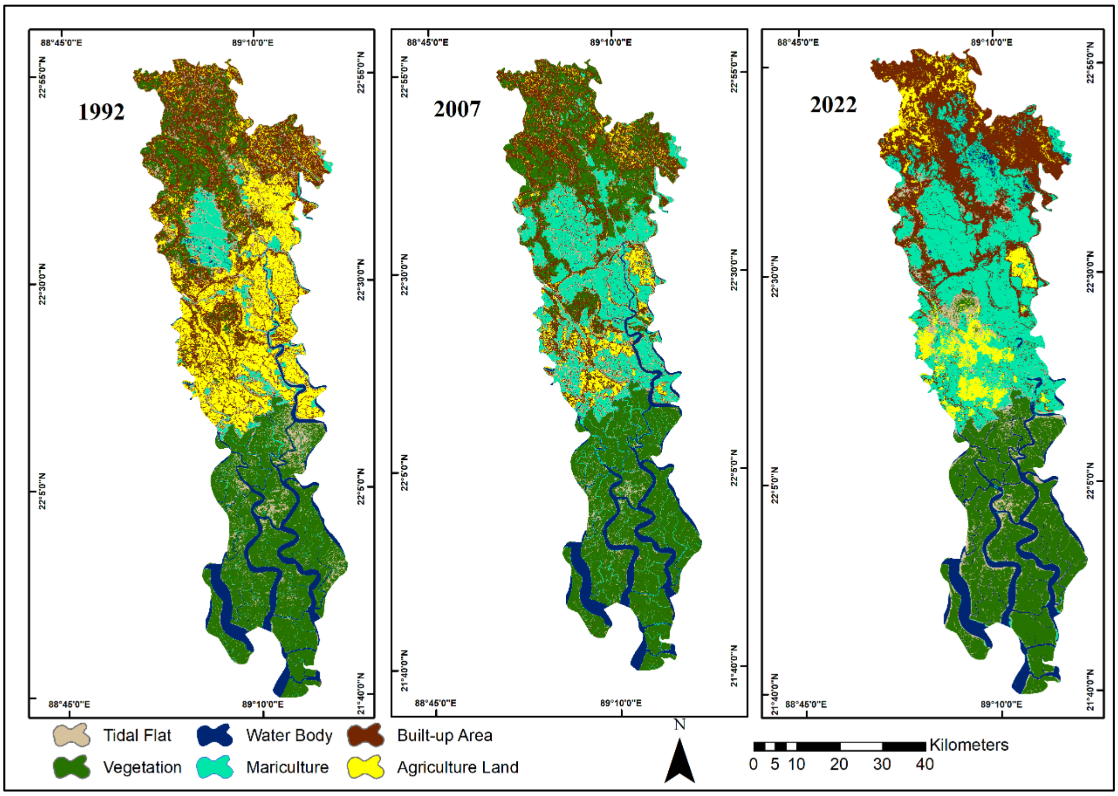

Figure 2. Land cover changes over time in 1992, 2007, and 2022.

Over the past three decades, tidal flats deteriorated by around 4%, with uneven patterns in vegetation cover. The vegetation rose in 2007 as a result of various afforestation efforts, but by 2022 the rapid growth of urbanization, unplanned development, and various socioeconomic activities reduced the vegetation land cover by approximately 8%. The class demonstrated a linear relationship between the years, water bodies did not alter significantly. One of the top nations in the world for shrimp production is Bangladesh. The majority of the coastal population makes a living by raising shrimp. As a result, the area used for mariculture rapidly increased. The research area forecasted a growth of over 22% in this class during the past thirty years. Since the majority of agricultural land was converted to mariculture, the rapid expansion of mariculture land led to the degradation of agricultural land. During the research period, agricultural land declined by about 13%. Additionally, the built-up area grew by about 2%. The main factors related to the increasing development of land use at the expense of deteriorating the vegetation covers can be attributed to urban expansion.

3.2. The estimation of blue carbon storages and sequestration

3.2.1. The changes in carbon pool value

In the research area, significant land cover altered over the past 30 years resulted in a substantial change in CO_2 levels. Four carbon pools were affected by the LSC transition. The spatiotemporal changes of carbon pool value are presented in **Figure 3**. **Table 5** displays the summary of the changes in carbon pool value due to the alteration of LSC in Satkhira between 1992 and 2022. Overall, the carbon pool value changed significantly within the period where carbon below value (BBC), carbon dead value (DOM), and carbon soil value (SOC) reduced in considerable amount with noticeable fluctuation in carbon above value (ABG). ABG showed rising from 1992 to 2007 with a considerable decline in 2022. Over the past 30 years, DOM did not shift that much in the Satkhira coastline region with little change in the CO_2 value. DOM ranged between 1992 and 2022 from 322.92 Mg to 201.87 Mg.

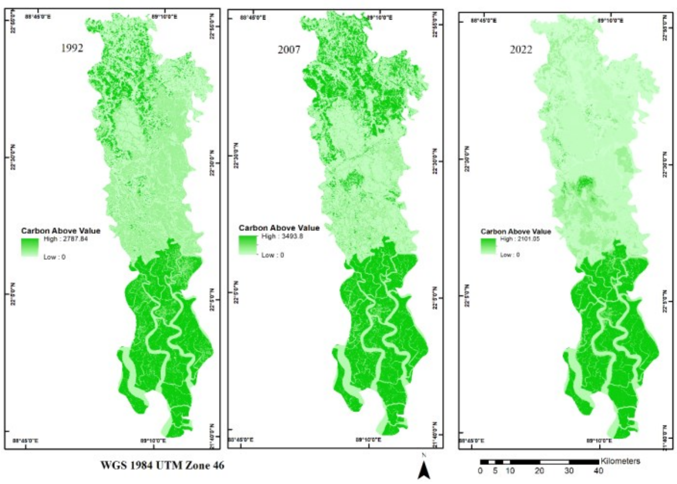

(a)

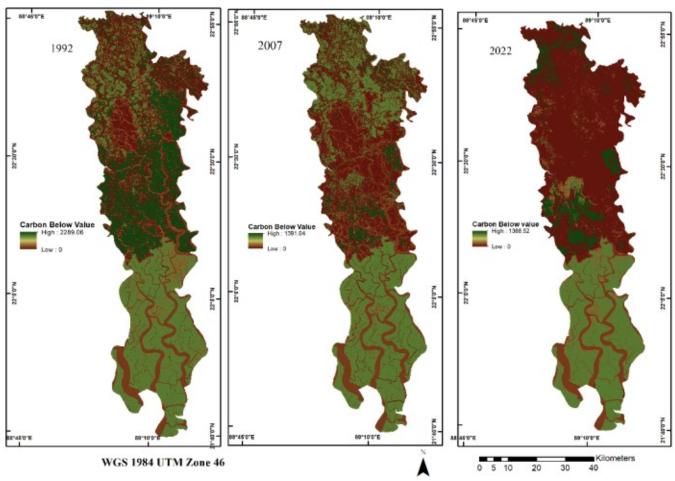

(b)

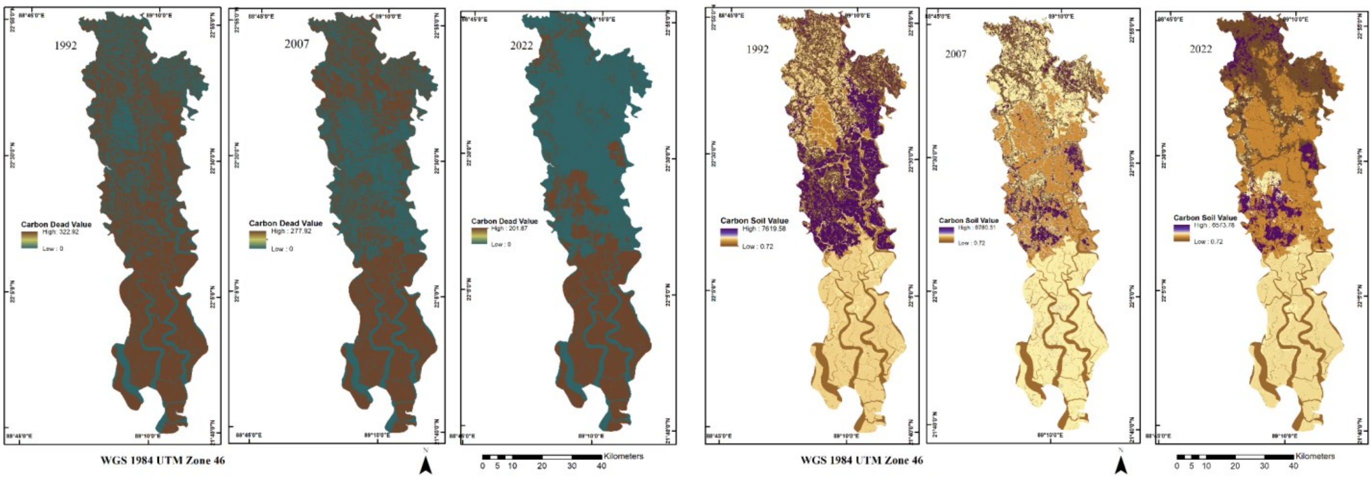

(c) **(d)**

Figure 3. Spatiotemporal changes of carbon pool value. **(a)** ABG, **(b)** BBC, **(c)** DOM, **(d)** SOC.

Table 5. The threshold for the amount of carbon ABG, BBC, DOM, SOC value (Mg) in the soil changed during the study.

CATEGORY	1992	2007	2022
(A) ABG	2787.84	3493.8	2101.05
(B) BBC	2289.06	1388.52	1391.04
(C) DOM	322.92	277.92	201.87
(D) SOC	7619.58	6780.51	6573.78

3.2.2. Calculation of blue carbon storages and sequestration

The spatial distribution of carbon storage variation in the study area is depicted in **Figure 4**. The Satkhira coastline region stored 11706.12 Mg of carbon in total in 1992. The value of the carbon stored was downgraded in 2007, the value of carbon stored in 2007 was 10779.84 Mg. The most concerning outcome was in 2022 when Satkhira's carbon stored capacity was downgraded to the largest amount of 9168 Mg. The highest carbon storage capacity was found in mangrove vegetation and carbon storage was minimal in the built-up area**.** The vegetation contributed the largest amount C for the total value of the ecosystem. Also, it revealed low carbon in water bodies. Thus, the study suggested conserving the mangrove vegetation for sustaining carbon storage.

The second output of this model was the calculation of CS. The values of CS came to negative ranges. The negative values indicated lost carbon; indicated sequestered carbon in Mg per pixel. **Figure 5** depicts the comparison of carbon storage and sequestration in the research area throughout the study period. As carbon storage facilities degraded over the last three decades. CS rates also declined. CS differences between the years were obtained from **Table 6**. It showed that in 2007–1992; CS rates were higher than the difference between 2022–2007 and 2022–1992. **Table 6** shows CS changing with 15-year intervals. Between 2007–1992 CS was found −926.28 Mg. CS rates were found to continuously degrade next 15 years interval which was from 2022 to 2007 –1611.81 Mg carbon was emitted into the atmosphere between this time frame. Overall last 30 years interval from 1992–2022. CS degradation intensity rose at an alarming rate. In this study; it was estimated that CS degraded almost −2538.09 Mg; nearly a 27.68% reduction compared with the previous research year.

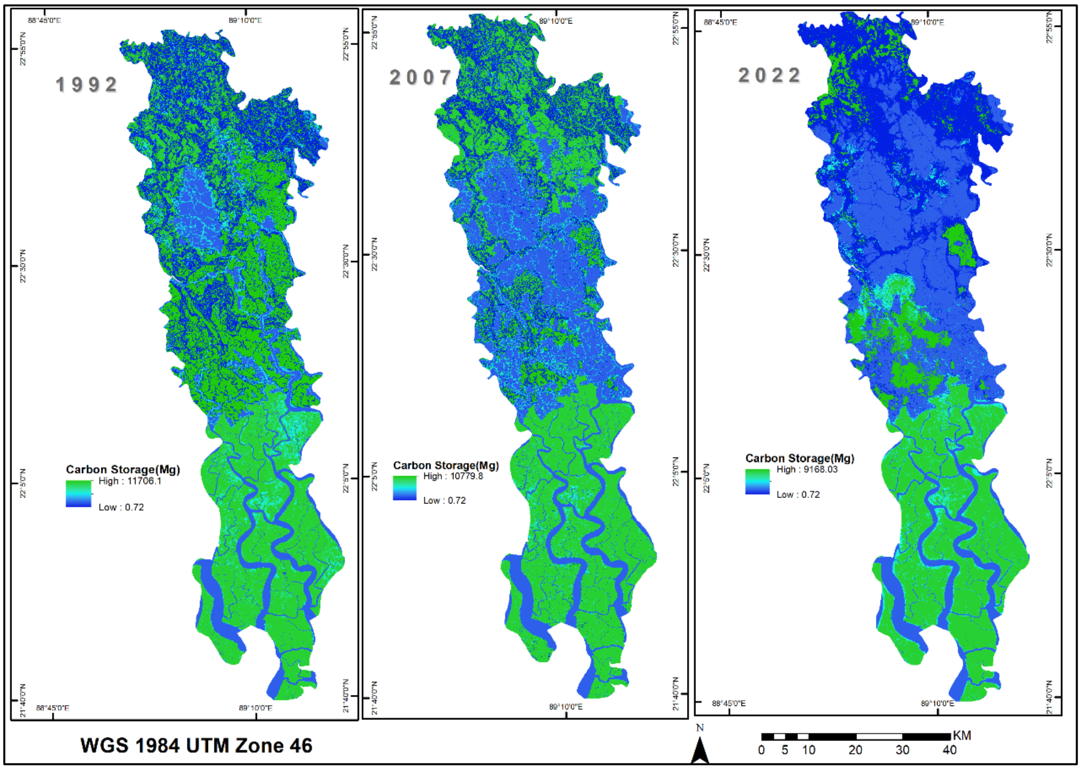

Figure 4. Changes in total carbon storage from 1992, 2007, and 2022, respectively, in the study area.

Table 6. Comparison of carbon sequestration in the different study years.

Category	2007–1992	2022–2007	2022–1992
(a) Carbon sequestration (Mg)	−926.28	−1611.81	−2538.09
(b) Carbon sequestration changes in (%)	−8.59%	−17.58%	−27.68%

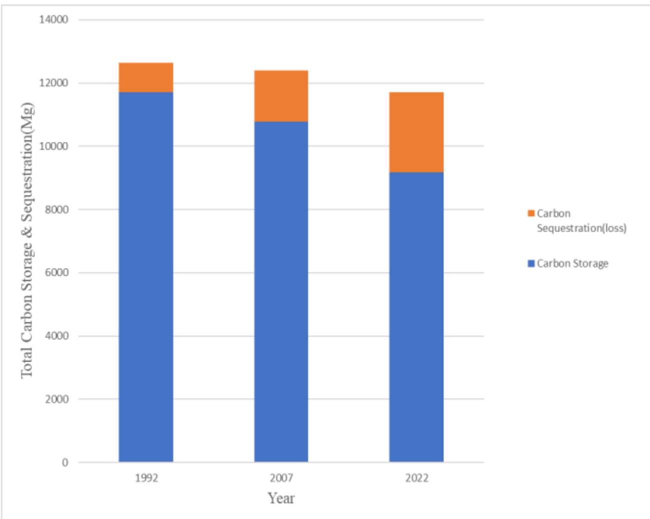

Figure 5. Changes in carbon storage and sequestration comparison chart.

3.3. Economic evaluation of reducing BCS

The outcome of the carbon model was the allocation of economic value for carbon sequestration over several years. The findings of this study indicated that the coastal environment has degraded over the last three decades. The coastal environment deteriorated due to a combination of natural and human activities. As a result, the level of BCS experienced a major decline, while there was a considerable increase in carbon emissions. The blue carbon storage and sequestration calculation section showed that the landscape of the Satkhira district changed very rapidly, approximately 2538.09 Mg of carbon was degraded over the last 30 years, indicating that carbon was not stored but emitted into the atmosphere in the research area. According to **Table 7**, a large amount of carbon was cast into the atmosphere every decade, with a market value of around 0.86 million USD per Mg. During 2007–1992, the carbon emitted into the atmosphere was 926.28 Mg, with a market value of about 0.046 million USD. During 2022–2007, the carbon emitted into the atmosphere was 1611.81 Mg, of which carbon credit was around 0.86 million USD. Due to its low carbon emissions compared to other wealthy countries, which had high carbon emission levels, Bangladesh could continue to profit from carbon trading. The coastal carbon ecosystem was found considerable changes, per the study, changed over the past three decades. The carbon sequestration rate significantly decreased, and a considerable amount of carbon was released into the atmosphere.

Table 7. Economic validation of carbon sequestration during the study year (unit is in million USD).

Category	2007−1992	Carbon Credit	2022−2007	Carbon Credit	2022−1992	Carbon Credit
Carbon Sequestration (Mg)	−926.28	0.046	1611.81	0.80	2538.09	0.86

3.4. Cumulative transformation between LSC and blue carbon dynamics

Integrating land use scenarios and the InVEST model could make it easier to assess the spatial and temporal effects of LSC on carbon storage and sequestration at the landscape scale This study explored the effects and causes of linkage in blue carbon dynamics concerning LSC transformation. From **Table 3**, it was noticed that each LSC class had a different carbon content value. Vegetation had the highest ABG carbon value. As a result, the most abundant ABG stock was found in vegetation areas. According to **Table 4**, vegetation rates increased in 2007. ABG was found to be high in 2007 in comparison with 1992, and 2022 (**Table 5**). So, this changing LSC class area ultimately affected the carbon value. This shifting of LSC caused the alteration of carbon pool value, and these changing pool values affected the carbon storage and sequestration in the research area. **Table 5** shows that SOC changed throughout the study year. This changing SOC value was related to the alteration of agricultural land. Agriculture land could store the highest amount of carbon soil biomass. This study provided information that agricultural land declined quickly in the research area. As a result, it was found that SOC continuously degraded in the Satkhira coastal region. The most alarming alteration of carbon value was seen with the alteration of vegetation land cover. Vegetation had not only the highest ABG value along with agriculture but also the highest BBC carbon value. BBC Carbon value in the Satkhira degraded last three decades because it related to vegetation and agricultural land. From the temporal distribution of these two LSC classes, it was observed that these two LSC classes had a cumulative relation with the carbon pool value, which degraded the SOC value. This study provided a clear overview of blue carbon dynamics and how they are influenced by LSC transformation.

Aljenaid et al. [6] 2022 utilized GIS and RS data to analyze spatiotemporal changes in mangrove habitat. Their findings indicated that Tubli Bay has undergone considerable human activity starting in the 1960s, which ultimately led to the clearing of mangroves. Consequently, the carbon stored in the mangrove environment decreased by 85 from 34, 932 Mg C/ha in 1967 to 5, 112 Mg/ha in 2020. As a result, with an average of 9874.62 Mg CO_2 e yr^{-1} over the previous 53 years, the potential for carbon sequestration grew from 128,200.44 Mg CO_2 e ha^{-1} in 1967 to 18,761.04 Mg CO_2 e ha^{-1} in 2020 [6].

Ma et al. [21] 2019 presented that their study's main purpose was to investigate how land cover changes affect the spatiotemporal dynamics of coastal blue carbon sequestration considering various human-induced and natural driving processes. Their key findings were a 78% loss in shrub and forest cover between 1970 and 2010 and a 1.63×10^6 Mg decline in coastal blue carbon sequestration [21].

3.5. Accuracy assessment

In this study total three accuracy assessments were followed overall accuracy, kappa coefficients, and confusion matrix. Google earth pro was used for validation to assess the accuracy. 40 samples were taken from each LSC class and compared to classified data in the confusion matrix. For study years 1992, 2007, and 2022, the confusion matrix was used to represent producer accuracy and user accuracy, respectively. The Kappa coefficient was adapted to measure the accuracy of classification, which could test all confusion matrix elements based on the minimum requirement. In the accuracy assessment, the identified categories of LSC needed to achieve the minimum requirements, which were at least 0.8. **Table 8** shows the validation for LSC in 1992, 2007, and 2022. Diagonal numbers indicate samples that were successfully categorized for each LSC class. The kappa coefficients for 1992, 2007, and 2022 are 0.84, 0.875, and 0.935, respectively. So, the identified categories of LSC were corrected because they achieved their minimum requirement, which was at least 0.8.

Table 8. Accuracy assessment table for LSC data obtained from Landsat imagery during study years.

Class	TF	V	W	M	A	BU	RT	UA (%)
a. Validation in 1992								
TF	35	2	3	0	0	0	40	87.5
V	0	36	0	0	4	0	40	90
W	2	0	34	4	0	0	40	85
M	0	0	2	34	1	3	40	85
A	0	0	0	3	37	0	40	92.5
BU	0	3	2	0	3	32	40	80
CT	37	41	41	41	45	35	240	

Table 8. (*Continued*).

Class	**TF**	**V**	**W**	**M**	**A**	**BU**	**RT**	**UA (%)**
PA (%)	94.59	87.8	82.93	82.93	82.22	91.43		
OA (%)	86.67%							
Kappa Coefficient(K)	0.84							
b. Validation in 2007								
TF	36	2	2	0	0	0	40	90
V	0	35	0	0	2	3	40	87.5
W	0	0	38	2	0	0	40	95
M	1	0	3	36	0	0	40	90
A	0	0	0	2	37	1	40	92.5
BU	0	5	0	0	2	33	40	82.5
CT	37	42	43	40	41	37	240	
PA (%)	97.23	83.33	88.37	90	90.24	89.19		
OA (%)	89.58							
Kappa coefficient (K)	0.875							
c. Validation in 2022								
TF	38	1	1	0	0	0	40	88.37
V	0	38	0	0	1	1	40	88.37
W	1	0	39	0	0	0	40	97.5
M	1	0	1	38	0	0	40	88.37
A	0	2	0	0	36	2	40	90
BU	0	1	0	0	1	38	40	95
CT	40	42	41	38	38	41	240	
PA (%)	88.37	90.48	95.12	100	94.74	92.68		
OA (%)	94.58							
Kappa coefficient (K)	0.935							

TF = Tidal flat; V = Vegetation; W = Water body; M = Mariculture; A = Agriculture land; BU = Built-up area; RT = Row total; UA = User's accuracy; PA = Producer's accuracy; OA = Overall accuracy.

4. Conclusion

The InVEST carbon model was used to estimate the storage and sequestration of blue carbon using the dynamic shift in LSC data of the Satkhira coastal region of Bangladesh. The findings showed how the fast loss of agricultural land, forest, and tidal flats harmed BCS and storage during the past three decades. This study found that carbon sequestration dropped by 27.68% in 2022 and blue carbon storage reduced from 11706.12 Mg to 9168.03 Mg between 2022 and 1992. Around 2538.09 Mg of carbon were released into the atmosphere in 2022. The total amount of carbon released into the atmosphere from 2022 to 1992 had a market worth of almost 0.86 million dollars (USD). This result gives essential input to policymakers regarding any development activities in the coastal area of Bangladesh. As a result, we have a modified LSC ecosystem that affects the blue carbon ecosystem. The ecological aspect and environmental sustainability must be considered before adopting any development activities, such that strategic position and ease of transit access are not the only important considerations. Our research is anticipated to contribute vital information to understanding the dynamics of blue carbon storage and sequestration as these kinds of studies are being ignored in management and decision-making policy for the future of coastal ecosystems. This research also quantifies the economic value of carbon that is stored or emitted into the atmosphere. Quantifying the economic value of carbon is vital for the restoration of the blue carbon ecosystem. This collection of findings may offer the authorities a dynamic framework for systematic decision-making by considering the spatiotemporal variation in carbon storage and sequestration. This integrated strategy, which might be used to plan and manage the Satkhira coastal ecosystem, considers a variety of factors, including environmental preservation and sustainable development.

Author contributions: Conceptualization, RS and MRA; methodology, MRA; software, MRA; validation, RS and MRA; formal analysis and investigation, RS and MRA; resources, MRA; data curation, RS; writing—original draft preparation, RS; writing—review and editing, MRA, TH and MAI; visualization, TH and MAI; supervision, MRA; project administration, MRA; funding acquisition, MRA. All authors have read and agreed to the published version of the manuscript.

Funding: This research was funded by Bangabandhu Sheikh Mujibur Rahman Maritime University, Bangladesh (BSMRMU) through funding Code- PRMTTC 4829.

Acknowledgments: The authors thank to the US Geological Survey for assisting this research with data sets. The authors would also thank the IBBBS at BSMRMU; Bangladesh for delivering the software and lab assistance.

Conflict of interest: The authors declare no conflict of interest.

References

1. Bertram C; Quaas M; Reusch TBH; Vafeidis AT; Wolff C; Rickels W. The blue carbon wealth of nations. Nat Clim Chang. 2021;11(8):704-709. doi:10.1038/s41558-021-01089-4
2. Bindu G; Rajan P; Jishnu ES; Ajith Joseph K. Carbon stock assessment of mangroves using remote sensing and geographic information system. Egyptian Journal of Remote Sensing and Space Science. 2020;23(1):1-9. doi:10.1016/j.ejrs.2018.04.006
3. Harishma KM; Sandeep S; Sreekumar VB. Biomass and carbon stocks in mangrove ecosystems of Kerala; southwest coast of India. Ecol Process. 2020;9(1). doi:10.1186/s13717-020-00227-8
4. Taillardat P; Friess DA; Lupascu M. Mangrove blue carbon strategies for climate change mitigation are most effective at the national scale. Biol Lett. 2018;14(10). doi:10.1098/rsbl.2018.0251
5. Atchison J. Green and Blue Infrastructure in Darwin; Carbon Economies and the Social and Cultural Dimensions of Valuing Urban Mangroves in Australia. Urban Science. 2019;3(3):86. doi:10.3390/urbansci3030086
6. Aljenaid S; Abido M; Redha GK; et al. Assessing the spatiotemporal changes; associated carbon stock; and potential emissions of mangroves in Bahrain using GIS and remote sensing data. Reg Stud Mar Sci. 2022;52:102282. doi:10.1016/j.rsma.2022.102282
7. Zhao C; Fang C; Gong Y; Lu Z. The economic feasibility of Blue Carbon cooperation in the South China Sea region. Mar Policy. 2020;113(November 2019):103788. doi:10.1016/j.marpol.2019.103788
8. Steven ADL; Vanderklift MA; Bohler-Muller N. A new narrative for the Blue Economy and Blue Carbon. Journal of the Indian Ocean Region. 2019;15(2):123-128. doi:10.1080/19480881.2019.1625215
9. Jiezzelle V; Nesperos C; Mico C; Villanueva M; Garcia JE; Gevaña DT. Assessment of blue carbon stock of mangrove vegetation in Infanta; Quezon; Philippines. Ecosystems and Development Journal. 2021;11(1 and 2):48-60.

10. Carr EW; Shirazi Y; Parsons GR; Hoagland P; Sommerfield CK. Modeling the Economic Value of Blue Carbon in Delaware Estuary Wetlands: Historic Estimates and Future Projections. J Environ Manage. 2018;206:40-50. doi:10.1016/j.jenvman.2017.10.018
11. Sudirman N; Helmi M; Salim HL. Geospatial Modeling of Blue Carbon Ecosystem Coastal Degradation in Jakarta Bay. Indonesian Journal of Oceanography. 2019;1(1):80-92. doi:10.14710/ijoce.v1i1.6266
12. Islam MM; Shamsuddoha M. Coastal and marine conservation strategy for Bangladesh in the context of achieving blue growth and sustainable development goals (SDGs). Environ Sci Policy. 2018;87(12):45-54. doi:10.1016/j.envsci.2018.05.014
13. Whisnant; R. and AReyes. Blue Economy for Business in East Asia: Towards an Integrated Understanding of Blue Economy. Quezon City; Philippines: Partnerships in Environmental Management for the Seas of East Asia (PEMSEA). Published online 2015.
14. Sejati AW; Buchori I; Kurniawati S; Brana YC; Fariha TI. Quantifying the impact of industrialization on blue carbon storage in the coastal area of Metropolitan Semarang; Indonesia. Applied Geography. 2020;124(June):102319. doi:10.1016/j.apgeog.2020.102319
15. Walcker R; Gandois L; Proisy C; et al. Control of "blue carbon" storage by mangrove ageing: Evidence from a 66-year chronosequence in French Guiana. Glob Chang Biol. 2018;24(6):2325-2338. doi:10.1111/gcb.14100
16. Pechanec V; Purkyt J; Benc A; Nwaogu C; Štěrbová L; Cudlín P. Modelling of the carbon sequestration and its prediction under climate change. Ecol Inform. 2018;47(February):50-54. doi:10.1016/j.ecoinf.2017.08.006
17. Moritsch MM; Young M; Carnell P; et al. Estimating blue carbon sequestration under coastal management scenarios. Science of the Total Environment. 2021;777:145962. doi:10.1016/j.scitotenv.2021.145962
18. Pekkarinen A. Global Forest Resources Assessment 2020. Global Forest Resources Assessment 2020. Published online 2020. doi:10.4060/ca8753en
19. Giri RKKV; Mandla VR. Study and evaluation of carbon sequestration using remote sensing and GIS: A review on various techniques. International Journal of Civil Engineering and Technology. 2017;8(4):287-300.
20. Zheng Y; Takeuchi W. Quantitative assessment and driving force analysis of mangrove forest changes in china from 1985 to 2018 by integrating optical and radar imagery. ISPRS Int J Geoinf. 2020;9(9). doi:10.3390/ijgi9090513
21. Ma T; Li X; Bai J; Ding S; Zhou F; Cui B. Four decades' dynamics of coastal blue carbon storage driven by land use/land cover transformation under natural and anthropogenic processes in the Yellow River Delta; China. Science of the Total Environment. 2019;655:741-750. doi:10.1016/j.scitotenv.2018.11.287
22. Mahmud I; Mia AJ; Uddin R; Rahman M; Rahman MH. Assessment on Seasonal Variations in Waterlogging Using Remote Sensing and Gis Techniques in Satkhira District in Bangladesh. Barisal University Journal Part 1. 2017;4(1):67-80.
23. BMD. Temperature Data. Bangladesh Meteorological Department. 2022. https://www.bmd.gov.bd/
24. Islam SkM; Naher N; Roy N; Mahmud MdK; Hossain MdD; Modak S. Agricultural Adaptation Options against Adverse Effect of Climate Change in Shyamnagar Upazila in the Satkhira District; Bangladesh. Asian Journal of Research in Agriculture and Forestry. 2019;2(3):1-12. doi:10.9734/ajraf/2018/46438
25. Young NE; Anderson RS; Chignell SM; Vorster AG; Lawrence R; Evangelista PH. A survival guide to Landsat preprocessing. Ecology. 2017;98(4):920-932. doi:10.1002/ecy.1730
26. Sun Z; Ma R; Wang Y. Using Landsat data to determine land use changes in Datong basin; China. Environmental Geology. 2009;57(8):1825-1837. doi:10.1007/s00254-008-1470-2
27. Mahmud KH; Abid SB; Ahmed R. Development of a Climate Classification Map for Bangladesh Based on Koppen's Climatic Classification. 2018;XXXIX(June).
28. Tan KC; Lim HS; MatJafri MZ; Abdullah K. Landsat data to evaluate urban expansion and determine land use/land cover changes in Penang Island; Malaysia. Environ Earth Sci. 2010;60(7):1509-1521. doi:10.1007/s12665-009-0286-z
29. Ara S; Alif MAUJ; Islam KMA. Impact of Tourism on LSC and LST in a Coastal Island of Bangladesh: A Geospatial Approach on St. Martin's Island of Bay of Bengal. Journal of the Indian Society of Remote Sensing. 2021;49(10):2329-2345. doi:10.1007/s12524-021-01389-4
30. Ashikur MR; Rupom RS; Sazzad MH. A remote sensing approach to ascertain spatial and temporal variations of seawater quality parameters in the coastal area of Bay of Bengal; Bangladesh. Remote Sens Appl. 2021;23:100593. doi:https://doi.org/10.1016/j.rsase.2021.100593

31. Chander G; Markham BL; Helder DL. Summary of current radiometric calibration coefficients for Landsat MSS; TM; ETM+; and EO-1 ALI sensors. Remote Sens Environ. 2009;113(5):893-903. doi:10.1016/j.rse.2009.01.007
32. Alam A; Bhat MS; Maheen M. Using Landsat satellite data for assessing the land use and land cover change in Kashmir valley. GeoJournal. 2020;85(6):1529-1543. doi:10.1007/s10708-019-10037-x
33. Cheema MJM; Bastiaanssen WGM. Land use and land cover classification in the irrigated Indus Basin using growth phenology information from satellite data to support water management analysis. Agric Water Manag. 2010;97(10):1541-1552. doi:10.1016/j.agwat.2010.05.009
34. Olofsson P; Foody GM; Stehman S V.; Woodcock CE. Making better use of accuracy data in land change studies: Estimating accuracy and area and quantifying uncertainty using stratified estimation. Remote Sens Environ. 2013;129:122-131. doi:10.1016/j.rse.2012.10.031
35. Adelisardou F; Zhao W; Chow R; Mederly P; Minkina T; Schou JS. Spatiotemporal change detection of carbon storage and sequestration in an arid ecosystem by integrating Google Earth Engine and InVEST (the Jiroft plain; Iran). International Journal of Environmental Science and Technology. 2022;19(7):5929-5944. doi:10.1007/s13762-021-03676-6
36. Sharp. R; Nelson E; Ennaanay D; et al. InVEST User Guide. National Capital Project. Published online 2015.
37. Rahman MdS; Akter S. Carbon Forestry: Scope and Benefit in Bangladesh. Journal of Forest and Environmental Science. 2013;29(4):249-256. doi:10.7747/jfs.2013.29.4.249

EnPress Publisher

Journal of Geography and Cartography 2024, 7(2), 9185.
https://doi.org/10.24294/jgc9185

Article

Adaptive fuzzy logic for gap filling in UAV orthomosaics: A methodology for accurate geospatial mapping

Neerav Sharma[1,*], Rahul Dev Garg[2], Kavita Sharma[3]

[1] Department of Agriculture and Biological Engineering, Purdue University, IN 47907, USA
[2] Department of Civil Engineering, Indian Institute of Technology Roorkee, Roorkee 247667, India
[3] Department of Botany, Pt. Ravishankar Shukla University Raipur, Raipur 492010, India
*** Corresponding author:** Neerav Sharma, nsharma@ce.iitr.ac.in

CITATION

Sharma N, Garg RD, Sharma K. Adaptive fuzzy logic for gap filling in UAV orthomosaics: A methodology for accurate geospatial mapping. Journal of Geography and Cartography. 2024; 7(2): 9185. https://doi.org/10.24294/jgc9185

ARTICLE INFO

Received: 18 September 2024
Accepted: 20 November 2024
Available online: 28 November 2024

Abstract: Unmanned Aerial Vehicles (UAVs) have gained spotlighted attention in the recent past and has experienced exponential advancements. This research focuses on UAV-based data acquisition and processing to generate highly accurate outputs pertaining to orthomosaic imagery, elevation, surface and terrain models. The study addresses the challenges inherent in the generation and analysis of orthomosaic images, particularly the critical need for correction and enhancement to ensure precise application in fields like detailed mapping and continuous monitoring. To achieve superior image quality and precision, the study applies advanced image processing techniques encompassing Fuzzy Logic and edge-detection techniques. The study emphasizes on the necessity of an approach for countering the loss of information while mapping the UAV deliverables. By offering insights into both the challenges and solutions related to orthomosaic image processing, this research lays the groundwork for future applications that promise to further increase the efficiency and effectiveness of UAV-based methods in geomatics, as well as in broader fields such as engineering and environmental management.

Keywords: UAV; orthomosaic; fuzzy logic; spatial mapping; image enhancement

1. Introduction

The increase in technological trend is glooming globally, allowing the innovations to enhance and advance at a rapid pace daily. Remote Sensing is a technique of gathering information about a phenomenon, or an object without being in physical contact with it [1]. Remote Sensing is such a field which demands constant advancements in the technological aspect to impart efficiency in its concept of accessing the inaccessible areas through non-contact means [2]. Space borne satellites are the prime backbone of remote sensing applications [3]. Despite having larger swaths and high-end sensor on-board, satellites make it harder for carrying out the research in short-area based planning and monitoring applications [4]. This is where the importance of Unmanned Aerial Vehicles (UAVs) become paramount [5]. UAVs are becoming popular day by day and provide extensiveness to almost all remote sensing fields where the field of study is concise and restricted like academic planners, construction sites, architectures, traffic management, transportation applications and urban planners [6,7]. UAVs unlike conventional remote sensing platforms, offers various advantages. Foremost being the temporal resolution as flying the UAV is custom and does not require global coverage followed by high-resolution ROI (Region-of-Interest) specific data acquisition unlike satellite data which acquires global information. Reason being that UAVs offer custom time-frame for dataset acquisition (rather than relying on temporal resolution of satellites) along with high resolution dataset with custom flights and region of interests (ROIs). Furthermore, with recent advances in UAV payload, application-specific sensors like NIR for vegetation, RADAR for urban and Hyperspectral sensors for high-resolution detailed information can be used.

Recent advancements in geospatial mapping have increasingly integrated UAV technologies to enhance accuracy and efficiency in data collection. However, challenges such as gaps, voids, and distortions in orthomosaic imagery remain significant hurdles. Various studies have proposed methods for improving orthomosaic quality through image processing techniques. For instance, Ye et al. [8] highlighted the importance of feature matching and multiple flight datasets in reducing distortion in UAV-generated orthomosaics. Meanwhile, Nguyen et al. [9] explored the use of fuzzy logic and edge-detection techniques for image enhancement, particularly in identifying and correcting faulty pixels in remote sensing imagery. Similarly, a study by Singh et al. [10] emphasized the potential of adaptive fuzzy logic approaches in automating pixel interpolation for gap filling, leading to sharper and more precise geospatial outputs. This was further escalated to water-based feature mosaicking which acts as a robust lay-work for pixel-based and image processing applications for orthomosaic imageries [11]. Furthermore, addition of multi-spectral sensor imparts effectiveness as an extra layer of information strengthens robustness into the entire platform of processing the UAV deliverables [12]. The theoretical advancements are necessary for providing georeferencing to the entire schema of accurate orthomosaic [13]. These studies collectively underline the importance of integrating adaptive image processing techniques with advanced pixel-based approach to address the common issues faced in UAV orthomosaic generation, paving the way for more accurate geospatial mapping applications. Furthermore, one of the paramount approaches of advanced image processing refers to Fuzzy logic technique which focuses on decision-making through rule-based heuristic approach, therefore, a pivotal pillar for such applications.

The primary objective of this research is to develop an adaptive fuzzy logic-based methodology for gap filling and enhancing UAV orthomosaics, addressing common issues such as distortions, voids, and mismatched features in traditional orthomosaic generation processes. This approach advances beyond conventional methods by incorporating fuzzy logic, gradient analysis, and interpolation techniques to dynamically adjust pixel values, providing more precise, high-resolution geospatial outputs. By achieving distortion-free and sharp orthomosaics, this method significantly improves accuracy in geospatial mapping, making it an attractive tool for researchers involved in environmental monitoring, resource management, and precision surveying. Its adaptability across different datasets and conditions further enhances its applicability, providing researchers with a robust, automated solution to produce reliable orthomosaics for a wide range of geospatial applications.

2. Material and method

2.1. Study area

The study area for the research is the Civil Engineering Department building, Indian Institute of Technology (IIT) Roorkee [29° 51' 46.998" N, 77° 53' 56.3928" E], [UTM Zone 43, Easting: 780,045.452 m, Northing: 3,307,140.529 m]. IIT Roorkee, formerly University of Roorkee and Thomason College of Civil Engineering, is a public technical and research university established in 1847 being considered as one of the oldest technical institutes located in Roorkee, district of Haridwar, Uttarakhand.

2.2. UAV and camera

The UAV utilized in this study is the Aibotix X6, a hexacopter classified as a rotary-wing UAV. The Aibotix X6, as part of the rotary-wing category, offers the advantage of vertical take-off and landing, making the acquisition process flexible. It can incorporate a payload up to 2.4 kg and comes with a Coming Home (CH) functionality. In the cases where pilot is unable to hover the UAV or the battery goes down to a cautious limit, this skill-set assists the pilot to bring the vehicle and land it safely to avoid any damage to the UAV, pilot or the environment where the flight is being held on. Sony Alpha 6000 E-mount RGB optical digital SLR camera is used with Advanced Photo System-type C (APS-C) sensor. It has 24.3 megapixel with capturing capability up to 24 fps. It also consists of inbuilt Wi-Fi and NFC control with JPEG and RAW data capturing provisions. The Aibotix UAV and the Camera sensor can be seen in **Figures 1a** and **1b**.

(a) **(b)**

Figure 1. UAV Components used **(a)** Aibotix hexacopter type UAV; **(b)** Sony optical camera.

2.3. Methodological schema

2.3.1. Acquisition of UAV data

UAV-based data acquisition is a common phenomenon these days due to the exponential surge in UAV-based remote sensing. However, as the process of acquisition like flight planning, payload deployment, area delineation and flight execution are quite common, the paramount part comes in the attributes of flight planning. With respect to Indian context, areas where UAVs can be flied are restricted and therefore, selection of site for data acquisition is a vitally important part. The attributes to be configured while planning a flight therefore acts as the backbone for efficiency of any UAV flight. The configuration used in this study comprised the following attributes as portrayed in **Table 1**.

Table 1. UAV Characteristics.

Attribute		Specification
Altitude	:	70 m
Front Overlap	:	75%
Side Overlap	:	65%
Flight Speed (Between waypoints)	:	3.5 m/s
GPS and Mode of Flying	:	RTK and Manual Fly

Figure 2 shows the acquisition of UAV data in schematic sketch followed by the schematics of UAV flight in **Figure 3**.

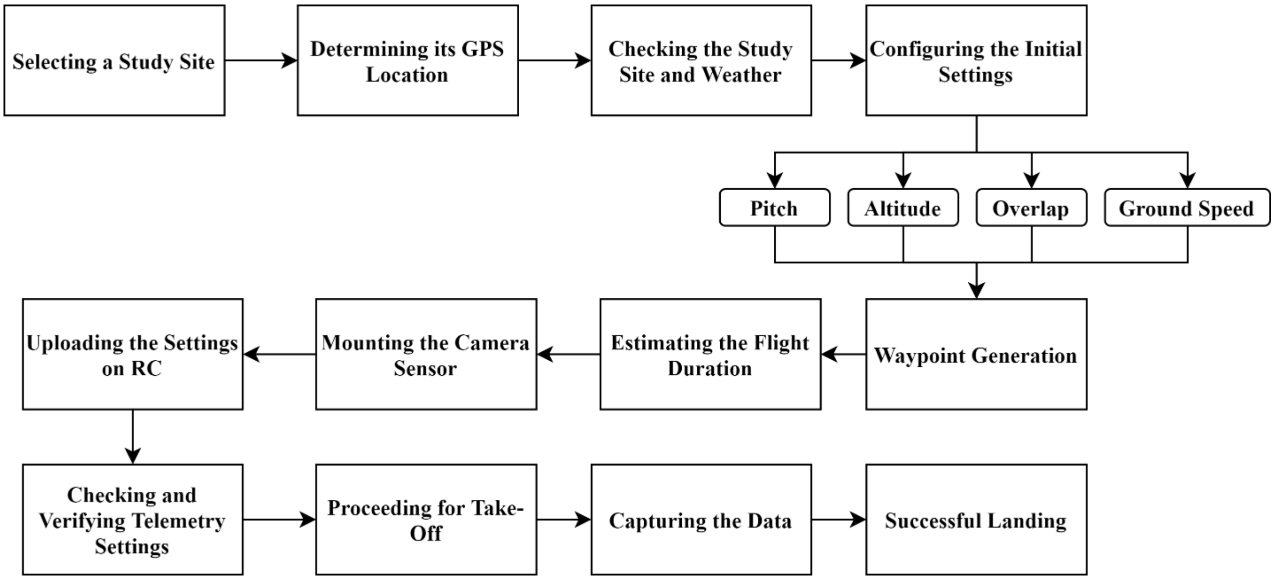

Figure 2. Acquisition of UAV data.

Figure 3. Flight of UAV in the study area for data acquisition.

2.3.2. Generation of Orthomosaic from the point cloud data

The paramount deliverable of the majority of UAV applications is the Orthomosaic image. The mosaicked image refers to the cumulative stitching of the aligned photographs captured in the most initial stage [14]. This image may contain error, and in fact, it has been witnessed by many types of research that geometric distortion is quite prominent in the mosaicked image [15]. Orthomosaic image is the final product of mosaicked image after the successful completion of geometric correction to eliminate the distortions and errors [16]. It is shown in **Figure 4**.

Figure 4. Process for generating the orthomosaic image.

2.3.3. Enhancement of orthomosaic image through fuzzy logic techniques

Fuzzy logic works through the definition of input variables as well as the membership functions and in this case, the input variables pertain to the attributes of pixels surrounding the void/gap areas in the orthomosaic image. There exist a plethora of platforms ranging from python to MATLAB for the processing domain and in this research, MATLAB was chosen as the software platform. Reason being the flexibility of MATLAB functions to tweak the pixels of the orthomosaic image and seamless integration between image and pixel-information. The initial generation of orthomosaic, textured mesh, tie-points and point clouds originate from Pix4D and then the orthomosaic generated is integrated with MATLAB environment. The initial step is the measuring of pixel intensity gradient. This assesses the change in values of the pixel's intensity around the void/gap. In simpler words, this identifies whether the neighboring pixels contain smooth or sharp transitions.

$$Grad.(x,y) = \sqrt{\left(\frac{\delta I}{\delta x}\right)^2 + \left(\frac{\delta I}{\delta y}\right)^2} \tag{1}$$

where $Grad.(x,y)$ signifies the gradient at pixel locations (x,y).

The next step involves the estimation of spatial distance from the known pixels D_s. This assists in measuring the distance of the void/gap pixels from the neighboring valid pixels (correct and accurate pixels). To portray the execution process, the pixels closer to the valid areas are more likely to be interpolated based on their nearby values.

$$D_s(x,y) = \sqrt{\left(x - x_p\right)^2 + \left(y - y_p\right)^2} \tag{2}$$

where x_p and y_p are the pixel location coordinates of the valid pixels nearest to the void/gap pixels.

Intensity Variance ($I.V.$) is the variance in intensity between the valid neighboring pixels indicating whether the void is within a homogeneous area (corresponding to Low variance) or near an edge *viz.* complex feature (corresponding to High variance).

$$I.V. = \frac{1}{N}\sum_{i=1}^{N}(I_i - \bar{I})^2 \tag{3}$$

where $\bar{I}$ denotes the mean intensity of the neighboring pixels and I_i corresponds to the individual intensities. Once the gradient, spatial distance and the intensity variance of the pixels are available, fuzzy membership functions are the primitive corresponding steps for each of the input variables. These functions categorize the input variables into different fuzzy sets, like High, Medium and Low.

For Gradient (*G*):

Low: Indicates smooth transitions, often in homogeneous regions.

Medium: Moderate changes in intensity, possibly near objects or boundaries.

High: Sharp changes in intensity, indicating edges or complex textures.

For Distance (*D*):

Close: Pixels are close to known valid pixels.

Medium: Moderate distance from valid pixels.

Far: Pixels are far from valid pixels, making interpolation harder.

For Variance (*V*):

Low: Indicates homogeneous regions where interpolation will be smoother.

Medium: Moderate variation between neighboring pixels.

High: Large differences between pixels, indicating edges or object boundaries.

The membership functions can be represented using a triangular function shown in Equation (4) below where a and b are the parameters that defines the range of the low set and in the similar manner, they can be defined for medium and high sets.

$$\mu_{Low}(x) = \begin{cases} 0, x < a \\ \frac{x-a}{b-a}, a \le x \le b \\ 1, x > b \end{cases} \tag{4}$$

3. Results and discussion

The tie points are generated once the images are aligned correctly. Tie-points depend upon the overlap in general and in this research, the forward and side overlap are set to 75% and 65% respectively. These points signify the density of the information and features available. The denser the tie-points would be, denser would be the point cloud which promises high efficiency in the resultant orthomosaic. Additionally, the utilization of the point clouds can be visualized in the analysis of evapotranspiration models which opens up new emerging fields of research using UAVs [17]. The orthomosaic image, shown in **Figure 5** even though contains voids and gaps but, unlike the dense point clouds and 3D mesh, it does not show redundant information which is not the point or object of interest. The utilization of orthomosaic imagery is of utmost essentiality but it is equally essential to maintain its homogeneity and uniformity throughout generation [18–20].

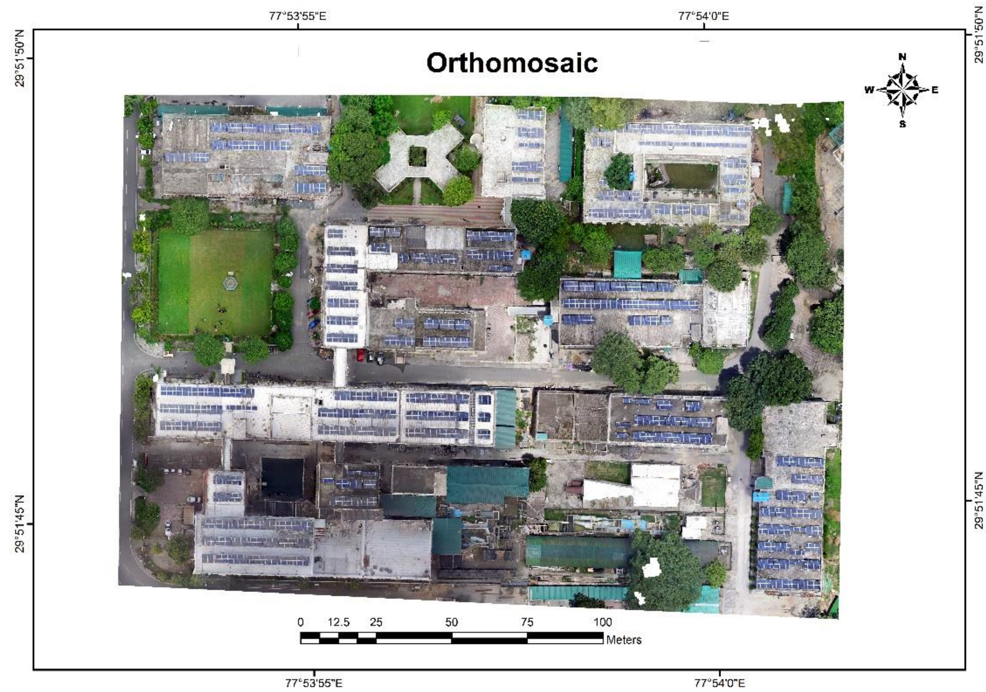

Figure 5. Orthomosaic generated initially consisting of errors and dead pixels.

It can be clearly seen from **Figure 5**, the initially generated orthomosaic image contains gaps and voids in the form of null pixels. These faulty pixels contain features and the necessary information about the area mapped by the UAV. The necessity of eradicating these faulty pixels is of highest priority and obtaining the enhanced fault-free image is utmost desirable. The faulty pixels (voids) arise due to multiple reasons. The primary reason pertains to irregular feature resolving process during the data processing comprising either water-based or tree-based features (prevalence of greenery characteristics) [21]. Secondary reasons could include faulty instruments or poor resolution of data acquisition. Once the ortho is itself not precise, the output extractions of elevation and other topographic models wouldn't be precise as well and in turn, imparting inefficiencies in the entire workflow of the spatial mapping [22].

The fuzzy logic approach employed in this study leverages gradient analysis, membership functions, and fuzzy rules to enhance the quality of the orthomosaic image. The gradient function helped identify areas with abrupt changes in pixel intensity, which often signify edges or faulty regions [23]. These gradients were then categorized using membership functions, which classify pixel characteristics into fuzzy sets such as "low quality," "medium quality," and "high quality." By utilizing these classifications, fuzzy rules were applied to determine the necessary corrections. For instance, if a pixel was identified as having a high gradient but low intensity, the fuzzy rule might dictate an enhancement by interpolating values from surrounding pixels [24]. This rule-based system enabled the dynamic correction of faulty or distorted pixels, filling in gaps and ensuring smoother transitions between image features. The combination of gradient detection, fuzzy logic, and membership-driven pixel adjustments provided a robust framework for rectifying and refining the orthomosaic, ultimately resulting in an enhanced, more accurate image for precise mapping and monitoring applications [25].

The process involves execution of gradient and evaluation of the spatial distance of valid and invalid pixels using Equations (1) and (2) shown in the methodological section. Once done, these primitively baselines a robust foundation for membership function estimation and correspondingly, the respective fuzzification functions. **Figure 6** shows the sample detection of voids/gaps in the orthomosaic image. Furthermore, through the estimation of membership function and corresponding fuzzification, the interpolation and/or rectification is done accordingly. The aforementioned process generates a voidless image *viz.* the rectified orthomosaic image as shown in **Figure 7**.

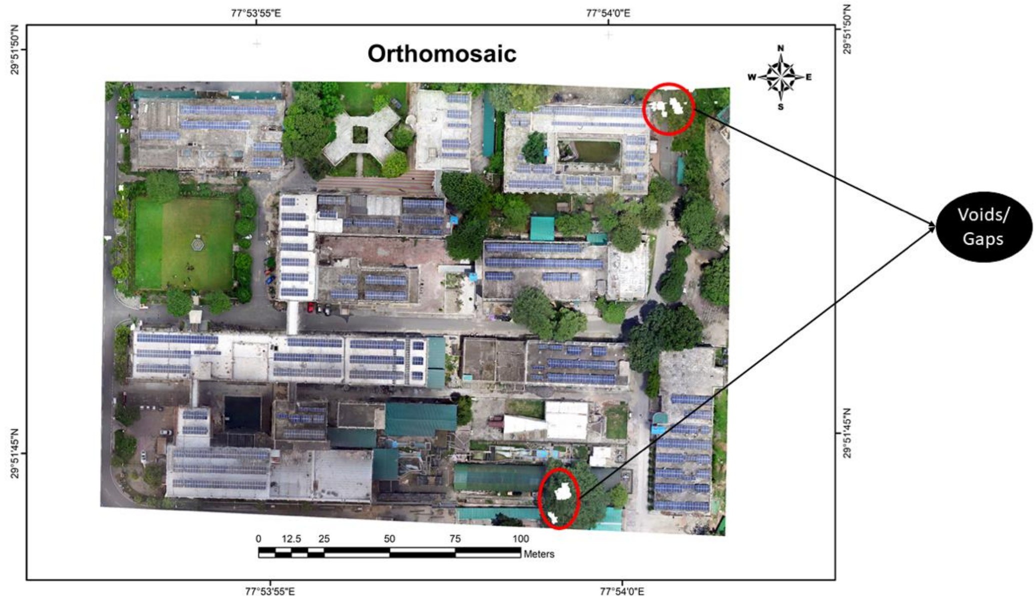

Figure 6. The null pixels or voids detected.

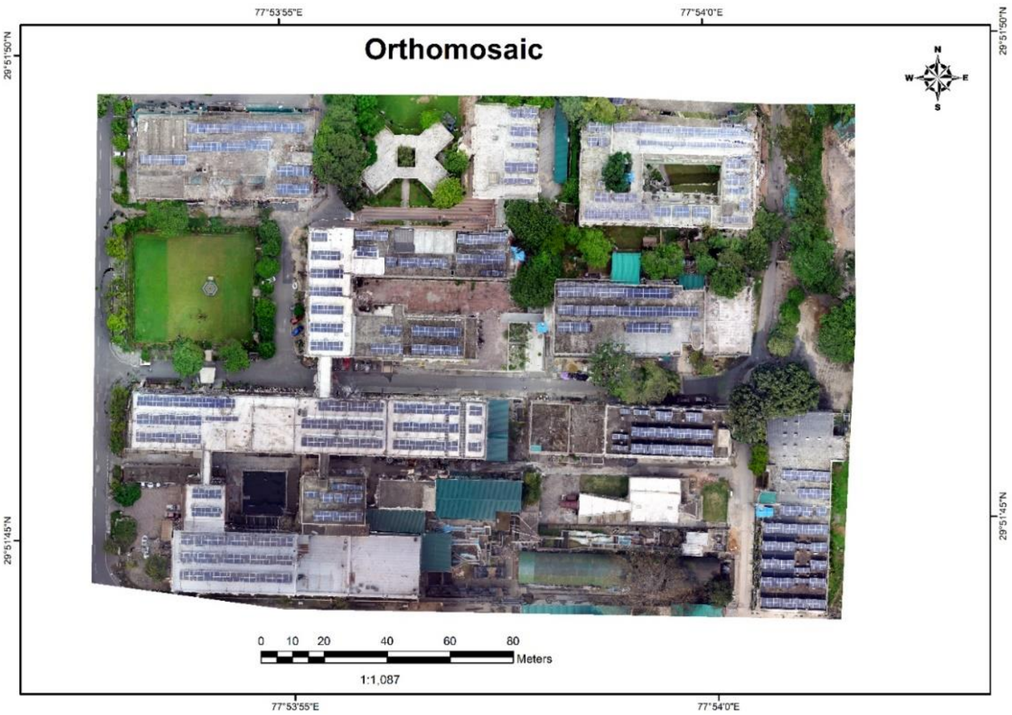

Figure 7. Enhanced orthomosaic image.

Correspondingly, the enhanced orthomosaic free of voids/gaps acts as a strong baseline for computing digital elevation models, digital surface models and digital terrain models [26–28]. They are presented in **Figure 8**.

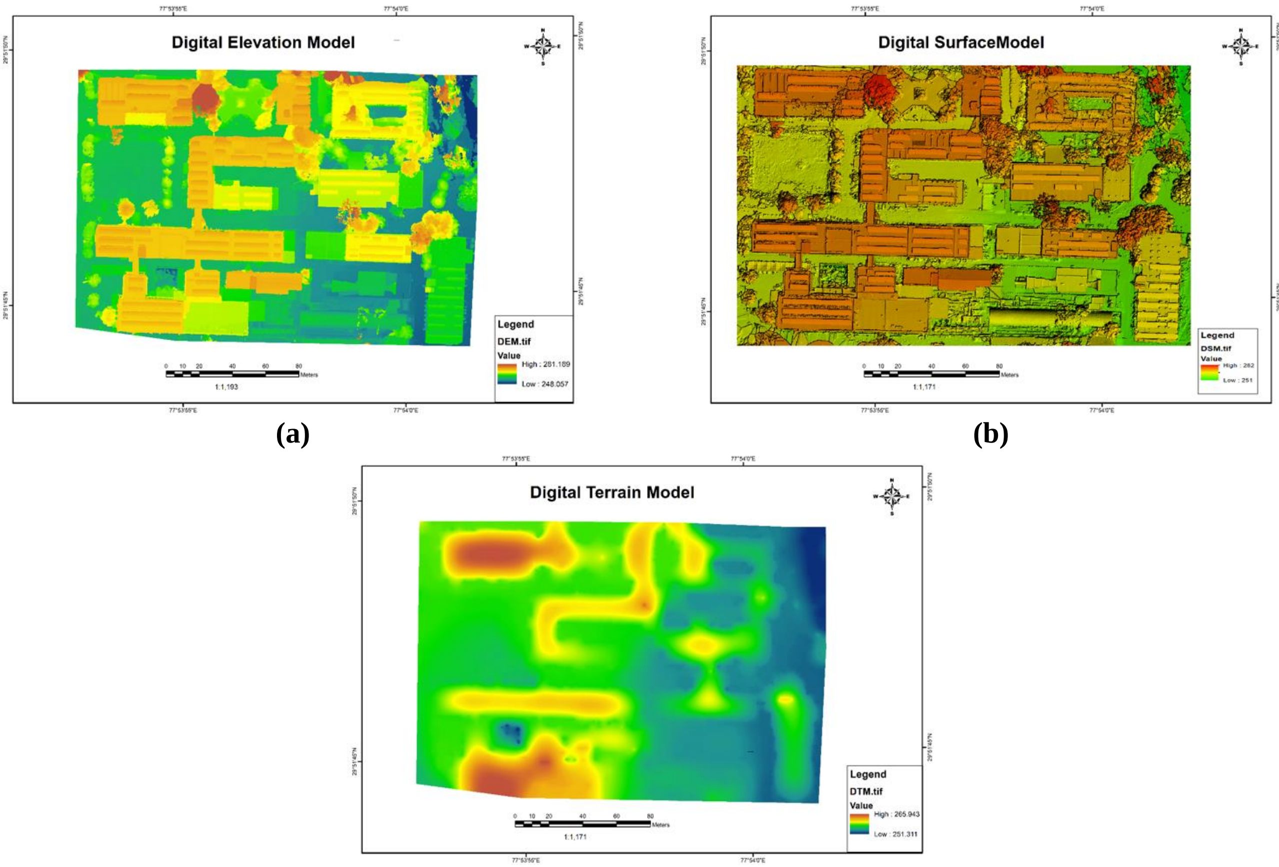

(a) **(b)**

(c)

Figure 8. Advanced models based on enhanced orthomosaic. **(a)** DEM; **(b)** DSM; **(c)** DTM.

4. Conclusion and future scope

In recent times, UAV-based data acquisition has become the preferred method due to its ability to capture high-resolution images with precise points of interest. Key deliverables in geomatics, such as point clouds, 3D meshes, and orthomosaics, serve as the foundation for generating Digital Elevation Models (DEM), Digital Surface Models (DSM), and Digital Terrain Models (DTM). However, challenges arise during the generation of point clouds and orthomosaics due to voids and gaps caused by incorrect feature matching, leading to distortions that compromise the accuracy of the outputs. This issue can be mitigated, though not entirely eliminated, by incorporating multiple flight datasets to improve feature matching and produce distortion-free outputs.

Orthomosaic generation is crucial for a wide range of applications, including environmental assessment, resource management, and sustainable utilization. This research focuses on generating orthomosaic imagery and enhancing it using fuzzy logic and morphological image processing techniques. The application of fuzzy logic is pivotal in modern research, and the integration of morphological techniques enhances the overall system's efficiency. The study involves creating the orthomosaic image, followed by its enhancement using fuzzy logic rules. Histogram equalization and edge-detection-based dilation methods are applied to identify and correct faulty or missing pixels within the orthomosaic. Additionally, interpolation techniques are used for further image enhancement, resulting in a sharp, clear orthomosaic free from pixel errors. In conclusion, the combined use of fuzzy logic, morphological techniques, and interpolation not only improves the quality of orthomosaic images but also offers a robust framework for addressing image distortions, contributing to more accurate and reliable outputs in geomatics applications.

The field of mapping and related applications require such enhanced form of orthomosaic images to carry out urban-planning, strategy making, rural studies, cropland monitoring and also the advanced application like post-disaster assessment. The edge-detected images can be utilized for fragmenting the numerous entities present in the orthomosaic like roads, structures, vegetation, water bodies, parking areas, residential areas, etc. The future of UAV-based technology is very bright and it serves as the most efficient tool for sensing any entity remotely. Traffic analysis and precision agriculture are the two most prominent applications and constant researches are spotlighted in these domains with emphasized and amplified magnitude involving AI and IoT approaches.

Author contributions: Conceptualization, NS and RDG; methodology, NS; software, RDG; validation, NS, RDG and KS; formal analysis, KS; investigation, NS; resources, RDG; data curation, NS; writing—original draft preparation, NS; writing—review and editing, RDG and KS; visualization, NS; supervision, RDG and KS; project administration, RDG and KS; funding acquisition, RDG. All authors have read and agreed to the published version of the manuscript.

Conflict of interest: The authors declare no conflict of interest.

References

1. Hodam H, Rienow A, Jürgens C. Bringing Earth Observation to Schools with Digital Integrated Learning Environments. Remote Sensing. 2020; 12(3): 345. doi: 10.3390/rs12030345
2. Ye X, Zhang L, & Wu Y. Improving UAV orthomosaics by feature matching and multiple flight datasets. Journal of Photogrammetry and Remote Sensing. 2019; 149: 101–115. doi: 10.1016/j.isprsjprs.2019.01.003
3. Zhu Z. Science of Landsat Analysis Ready Data. Remote Sensing. 2019; 11(18): 2166. doi: 10.3390/rs11182166
4. Egorov A, Roy D, Zhang H, et al. Landsat 4, 5 and 7 (1982 to 2017) Analysis Ready Data (ARD) Observation Coverage over the Conterminous United States and Implications for Terrestrial Monitoring. Remote Sensing. 2019; 11(4): 447. doi: 10.3390/rs11040447
5. Nex F. UAV-g 2015 - Unmanned Aerial Vehicles in Geomatics. The Photogrammetric Record. 2015; 30(150): 250–250.
6. Shakhatreh H, Sawalmeh AH, Al-Fuqaha A, et al. Unmanned Aerial Vehicles (UAVs): A Survey on Civil Applications and Key Research Challenges. IEEE Access. 2019; 7: 48572–48634. doi: 10.1109/access.2019.2909530
7. Restas A. Drone Applications for Supporting Disaster Management. World Journal of Engineering and Technology. 2015; 03(03): 316–321. doi: 10.4236/wjet.2015.33c047
8. Ye J, Zhang C, Lei H, et al. Secure UAV-to-UAV Systems with Spatially Random UAVs. IEEE Wireless Communications Letters. 2019; 8(2): 564–567. doi: 10.1109/lwc.2018.2879842
9. Nguyen T, Pham D, & Tran H. Fuzzy logic and edge-detection techniques for remote sensing image enhancement. Remote Sensing. 2021; 13(5): 1129.
10. Singh A, Sharma P, & Kumar V. Adaptive fuzzy logic approaches for pixel interpolation in UAV orthomosaics. International Journal of Remote Sensing. 2022; 43(10): 2525–2540.

11. Román A, Heredia S, Windle AE, et al. Enhancing Georeferencing and Mosaicking Techniques over Water Surfaces with High-Resolution Unmanned Aerial Vehicle (UAV) Imagery. Remote Sensing. 2024; 16(2): 290. doi: 10.3390/rs16020290
12. Román A, Tovar-Sánchez A, Gauci A, et al. Water-Quality Monitoring with a UAV-Mounted Multispectral Camera in Coastal Waters. Remote Sensing. 2022; 15(1): 237. doi: 10.3390/rs15010237
13. Essel B, Bolger M, McDonald J, et al. Developing a theoretical assessment method for an assisted direct georeferencing approach to improve accuracy when mapping over water: the concept, potential and limitations. The International Archives of the Photogrammetry, Remote Sensing and Spatial Information Sciences. 2023; XLVIII-1/W1-2023: 139–144. doi: 10.5194/isprs-archives-xlviii-1-w1-2023-139-2023
14. Seifert E, Seifert S, Vogt H, et al. Influence of Drone Altitude, Image Overlap, and Optical Sensor Resolution on Multi-View Reconstruction of Forest Images. Remote Sensing. 2019; 11(10): 1252. doi: 10.3390/rs11101252
15. Xiang R, Sun M, Jiang C, et al. A method of fast mosaic for massive UAV images. Jackson TJ, Chen JM, Gong P, Liang S, eds. Land Surface Remote Sensing II. 2014; 9260: 92603W. doi: 10.1117/12.2069201
16. Cui J hui, Wei R xuan, Liu Z cheng, et al. UAV Motion Strategies in Uncertain Dynamic Environments: A Path Planning Method Based on Q-Learning Strategy. Applied Sciences. 2018; 8(11): 2169. doi: 10.3390/app8112169
17. Aboutalebi M, Torres-Rua AF, McKee M, et al. Incorporation of Unmanned Aerial Vehicle (UAV) Point Cloud Products into Remote Sensing Evapotranspiration Models. Remote Sensing. 2019; 12(1): 50. doi: 10.3390/rs12010050
18. Fritz A, Kattenborn T, & Koch B. UAV-based photogrammetric point clouds – tree stem mapping in open stands in comparison to terrestrial laser scanner point clouds. International Archives of the Photogrammetry, Remote Sensing and Spatial Information Sciences. 2013; XL-1/W2: 141–146. doi: 10.5194/isprsarchives-XL-1-W2-141-2013
19. Rhee S, Kim T. Dense 3d point cloud generation from UAV images from image matching and global optimazation. ISPRS - International Archives of the Photogrammetry, Remote Sensing and Spatial Information Sciences. 2016; XLI-B1: 1005–1009. doi: 10.5194/isprsarchives-xli-b1-1005-2016
20. Malihi S, Valadan Zoej MJ, Hahn M. Large-Scale Accurate Reconstruction of Buildings Employing Point Clouds Generated from UAV Imagery. Remote Sensing. 2018; 10(7): 1148. doi: 10.3390/rs10071148
21. Zhang J, Xu S, Zhao Y, et al. Aerial orthoimage generation for UAV remote sensing: Review. Information Fusion. 2023; 89: 91–120. doi: 10.1016/j.inffus.2022.08.007
22. Sangjan W, McGee RJ, Sankaran S. Optimization of UAV-Based Imaging and Image Processing Orthomosaic and Point Cloud Approaches for Estimating Biomass in a Forage Crop. Remote Sensing. 2022; 14(10): 2396. doi: 10.3390/rs14102396
23. Mayathevar K, Veluchamy M, Subramani B. Fuzzy color histogram equalization with weighted distribution for image enhancement. Optik. 2020; 216: 164927. doi: 10.1016/j.ijleo.2020.164927
24. Abbasi N, Khan MF, Khan E, et al. Fuzzy histogram equalization of hazy images: a concept using a type-2-guided type-1 fuzzy membership function. Granular Computing. 2022; 8(4): 731–745. doi: 10.1007/s41066-022-00351-0
25. Ludwig M, M. Runge C, Friess N, et al. Quality Assessment of Photogrammetric Methods—A Workflow for Reproducible UAS Orthomosaics. Remote Sensing. 2020; 12(22): 3831. doi: 10.3390/rs12223831
26. Forlani G, Dall'Asta E, Diotri F, et al. Quality Assessment of DSMs Produced from UAV Flights Georeferenced with On-Board RTK Positioning. Remote Sensing. 2018; 10(2): 311. doi: 10.3390/rs10020311
27. Sammartano G, Spanò A. DEM Generation based on UAV Photogrammetry Data in Critical Areas. Proceedings of the 2nd International Conference on Geographical Information Systems Theory, Applications and Management. Published online 2016: 92–98. doi: 10.5220/0005918400920098
28. Escobar Villanueva JR, Iglesias Martínez L, Pérez Montiel JI. DEM Generation from Fixed-Wing UAV Imaging and LiDAR-Derived Ground Control Points for Flood Estimations. Sensors. 2019; 19(14): 3205. doi: 10.3390/s19143205

Journal of Geography and Cartography 2024, 7(2), 9091.
https://doi.org/10.24294/jgc9091

Article

Assessing flood risk and vegetation dynamics: Implications for sustainable land management in Fars province

Amir Maleki[1], Alireza Naseri[2], Mohammadreza Yari[3], Faraz Estelaji[4], Rahim Zahedi[5,*], Seyyedeh Fatemeh Hosseini[6]

[1] Department of Civil, Water and Environmental Engineering, Shahid Beheshti University, Tehran 1971733861, Iran

[2] Department of Transportation and Highway Engineering, Faculty of Civil and Environment Engineering, Amirkabir University of Technology, Tehran 1971733861, Iran

[3] Department of Construction Engineering, Faculty of Civil Engineering, Iran University of Science and Technology, Tehran 1971733861, Iran

[4] Department of Construction Engineering and Management, Faculty of Civil Engineering, Khajeh Nasir Toosi University, Tehran 1971733861, Iran

[5] Department of Renewable Energy and Environmental Engineering, University of Tehran, Tehran 1971733861, Iran

[6] Department of Geography and rural planning, Faculty of Urban Planning, Azad University, Science and Research Branch, Tehran 1971733861, Iran

*** Corresponding author:** Rahim Zahedi, rahimzahedi@ut.ac.ir

CITATION

Maleki A, Naseri A, Yari M, et al. Assessing flood risk and vegetation dynamics: Implications for sustainable land management in Fars province. Journal of Geography and Cartography. 2024; 7(2): 9091. https://doi.org/10.24294/jgc9091

ARTICLE INFO

Received: 12 September 2024
Accepted: 12 November 2024
Available online: 30 November 2024

Abstract: The design of effective flood risk mitigation strategies and their subsequent implementation is crucial for sustainable development in mountain areas. The assessment of the dynamic evolution of flood risk is the pillar of any subsequent planning process that is targeted at a reduction of the expected adverse consequences of the hazard impact. This study focuses on riverbed cities, aiming to analyze flood occurrences and their influencing factors. Through an extensive literature review, five key criteria commonly associated with flood events were identified: slope height, distance from rivers, topographic index, and runoff height. Utilizing the network analysis process within Super Decision software, these factors were weighted, and a final flood risk map was generated using the simple weighted sum method. 75% of the data was used for training, and 25% of it was used for testing. Additionally, vegetation changes were assessed using Landsat imagery from 2000 and 2022 and the normalized difference vegetation index (NDVI). The focus of this research is Qirokarzin city as a case study of riverbed cities, situated in Fars province, with Qir city serving as its central hub. Key rivers in Qirokarzin city include the Qara Aghaj River, traversing the plain from north to south; the primary Mubarak Abad River, originating from the east; and the Dutulghaz River, which enters the eastern part of the plain from the southwest of Qir, contributing to plain nourishment during flood events. The innovation of this paper is that along with the objective to produce a reliable delineation of hazard zones, a functional distinction between the loading and the response system (LS and RS, respectively) is made. Results indicate the topographic index as the most influential criterion, delineating Qirokarzin city into five flood risk zones: very low, low, moderate, high, and very high. Notably, a substantial portion of Qirokarzin city (1849.8 square kilometers, 8.54% of the area) falls within high- to very-high flood risk zones. Weighting analysis reveals that the topographic humidity index and runoff height are the most influential criteria, with weights of 0.27 and 0.229, respectively. Conversely, the height criterion carries the least weight at 0.122. Notably, 46.7% of the study area exhibits high flood intensity, potentially attributed to variations in elevation and runoff height. Flood potential findings show that the middle class covers 32.3%, indicating moderate flood risk due to changes in elevation and runoff height. The low-level risk is observed sporadically from the east to the west of the study area, comprising 12.4%. Analysis of vegetation changes revealed a significant decline in forest and pasture cover despite agricultural and horticultural development, exacerbating flood susceptibility.

Keywords: geographic information systems (GIS); flood risk analysis; network analysis process (NAP); weighted simple sum (WSS) method; sustainable development

1. Introduction

Flooding, inherently a natural phenomenon, often yields positive outcomes; however, its manifestation in urban environments entails devastating consequences, including property destruction and threats to human health. The escalation of population density, coupled with inadequate land use planning, deforestation, and the proliferation of impermeable surfaces, has impeded water infiltration in watersheds and accelerated downstream flow, exacerbating the frequency, intensity, and abruptness of urban floods, thereby affecting a growing number of individuals [1]. Spatial analysis offers a potent tool for examining dispersal patterns, enabling the establishment of logical relationships between human population distribution and environmental resources. Corrective measures for environmental risks and degraded lands hinge upon effective spatial planning [2]. Notably, recent years have witnessed extensive research endeavors both domestically and internationally, focusing on the assessment of flood risk sensitivity.

The analysis of floods in the United States, approached from a geomorphological standpoint and utilizing geographic information systems alongside a hierarchical analysis model, underscores the significant role played by geomorphological factors in flood occurrence within the region. Urban areas often employ impermeable surfaces as part of infrastructure development to augment runoff during heavy rainfall and flood events, consequently heightening flood susceptibility due to land use changes associated with urbanization [3]. A study spanning four years and employing a high-resolution monitoring network across eight catchments in southern England, encompassing both rural and urban locales, revealed discernible hydrological response disparities between the two settings. Notably, differences in runoff volume and flood response times were observed, with urbanization-induced alterations diverging from rural patterns [4]. Furthermore, soil moisture did not significantly impact runoff dynamics in urban areas, suggesting that spatial measurements of urbanization alone are sufficient predictors of flood occurrence in urban basins. The confluence of changes in rainfall patterns and land use further exacerbates urban areas' vulnerability to heavy rainfall and subsequent flooding [5]. In Egbaro state and Anambra state, topography and human alterations to riverbeds emerge as pivotal factors influencing flood risk. Flood risk assessment conducted in Bang Rakam, Thailand, utilizing a hierarchical analysis process (fuzzy) and incorporating eight flood risk assessment criteria (including distance from drainage networks, drainage density, water flow accumulation height, land slope, and average annual rainfall) revealed high flood risk concentrations near drainage networks with elevated ratings [6]. Notably, water flow accumulation height, water infiltration in soil, distance from drainage networks, medium drainage density, and basin land slope emerged as the most influential factors contributing to flood risk escalation in the region.

The vulnerability assessment of floods in Anambra, Nigeria, employing the network analysis process model, reveals a significant susceptibility of the state to flooding, with 73% of its total area classified as having medium to very high vulnerability [7]. A study conducted in Bangladesh utilized Sentinel 1 and 2 satellite imagery to classify land use and assess flood-induced damage, revealing that approximately 23.98% of agricultural lands in Bangladesh have been adversely affected by recent floods. Zoning of flood risk potential within the Mardagh Chai catchment area, employing the network analysis process model, identifies slope and runoff height as the most critical factors, with weights of 0.3 and 0.28, respectively [8]. Conversely, lithology emerged as the least influential factor. Flood risk within this basin is contingent upon its physical characteristics [9]. In the West Islamabad catchment and its sub-basins, flood risk zoning utilizing the network analysis process model reveals that approximately 46% of the catchment area is deemed highly unsuitable. The West Islamabad catchment exhibits high flood capacity [10]. A flood vulnerability map for the Neka watershed of Sari city, utilizing a novel combined method of Bayesian theory and hierarchical analysis, identified areas of heightened flood sensitivity, particularly in the northern and northwestern regions characterized by dense human settlements and sparse vegetation cover. Flood zoning in Sari city, employing fuzzy analysis, indicates that the central and southern areas face the highest flood risk, with 12.24% of the mapped area falling into the very high-risk zone and 5.37% into the very low-risk zone [11]. Proposals to mitigate flood risk include retrofitting buildings along riverbanks to minimize flood damage. Qasimi et al. [12] aimed to assess landslide susceptibility in the Badakhshan province of Afghanistan, an area highly susceptible to landslides due to its complex topography and geological conditions. Koralay and Kara [13] chose the Söğütlü stream watershed in the Eastern Black Sea Region of Turkey as the study area to create a flood risk map using the Analytical Hierarchy Process and Weighted Overlay tools in ArcGIS.

In a separate study conducted in the Gomnabchai catchment area of Azerbaijan province, ten factors influencing flooding were identified using the network analysis process model. Results indicate that rainfall, land use, lithology, and slope are the most pivotal factors contributing to flood formation in the region [14]. Similarly, an investigation into the Qasimlu watershed in West Azarbaijan province, utilizing the network analysis process model, highlighted rainfall, distance from the river, and vegetation density as the primary influencing factors in flood occurrence. Notably, 22.82% of the study area was classified as having high to very high flood susceptibility [15]. Flood risk zoning of the Qatourchai watershed, employing a multi-criteria decision-making approach through the network analysis process and weighted linear combination model, revealed areas with a high potential for flooding, predominantly concentrated in the lower reaches of the basin. Waterways ranked 3 and 4 were identified as flood-prone zones, directing floodwaters downstream [16]. A spatial correlation analysis of vegetation cover changes and runoff height within the Gorganrood catchment area demonstrated that cities such as Agh Qola, Siminshahr, and Gomish Tepe, along with the Gorganrood River, are situated at high runoff elevations. Moreover, a significant negative spatial correlation (78%) between runoff height and vegetation density was observed, indicating a decline in forest and pasture cover from 1990 to 2021 [17]. Flood zoning of the Qarasu River in Golestan province, employing the analytic network process (ANP) method, identified topography, surface type, and vegetation as the principal factors influencing flooding in the region [18].

As a result of the literature, an increase in the likelihood and adverse impacts of flood events is expected. Therefore, concentrated action is needed at the regional level to avoid severe impacts on human life and property. In order to have an effective tool available for information on flood risk, as well as a valuable basis for priority setting and further technical, financial, and political decisions regarding flood risk mitigation and management, it is necessary to establish flood risk maps that show the potential adverse consequences associated with different flood scenarios.

Riverbed cities have a historical record of recurrent floods, spanning various periods. These inundations resulted in human casualties, agricultural land damage, disruption of transportation routes, and destruction of urban infrastructure, including buildings and gardens. The flood of 2018 in Qirokarzin city, for instance, incurred significant financial losses amounting to $4,826,151. Given this context, the present research endeavors to identify the primary criteria governing flood occurrences in Qirokarzin city, with a particular focus on exploring the relationship between floodplain distribution and changes in vegetation cover. The main innovation of this paper is that, along with the objective to produce a reliable delineation of hazard zones, a functional distinction between the loading and the response system (LS and RS, respectively) is made.

2. Methodology

2.1. Case study

The focus of this research is Qirokarzin city as a case study of riverbed cities, situated in Fars province, with Qir city serving as its central hub. Geographically, Qirokarzin city spans from longitude 52 degrees 6 minutes to longitude 53 degrees 13 minutes east and latitude 28 degrees 32 minutes to latitude 28 degrees 54 minutes north (**Figure 1**) [19]. The city covers an area of 339,547 hectares, with an elevation of 750 meters above sea level. Over eleven years, the average annual rainfall in the region amounts to 319.6 mm, with the highest rainfall occurring in February (86.6 mm) and the lowest in June (0 mm). The average highest and lowest temperatures are recorded in July (34.1 degrees Celsius) and January (12.4 degrees Celsius), respectively. According to Dumarten's classification, the study area falls within a dry climate zone [20]. Elevations range from a maximum of 2187 meters in the north to a minimum of 314 meters in the south and central regions of the city. Notably, key rivers in Qirokarzin city include the Qara Aghaj River, traversing the plain from north to south; the primary Mubarak Abad River, originating from the east; and the Dutulghaz River, which enters the eastern part of the plain from the southwest of Qir, contributing to plain nourishment during flood events. The construction of the Bitumen Reservoir Dam in the northeast of Qir city, situated on the Qara-Aghaj River, is a notable feature of the area's hydrological infrastructure [21]. From a soil science perspective, the predominant soil type across much of the study area is classified as antisol. Land use analysis reveals that approximately 15,370 hectares are designated as second-grade pastures, while third-grade pastures cover about 216,553 hectares [22]. Agricultural lands occupy an estimated area of 44,861 hectares. Additionally, approximately 59,505 hectares of Qirokarzin city's area are forested, with the remaining land use comprising rocky terrain devoid of vegetation, as well as areas designated for urban and village boundaries, transportation routes, water bodies, and miscellaneous uses. **Figure 2** shows a photo of the flood in the area.

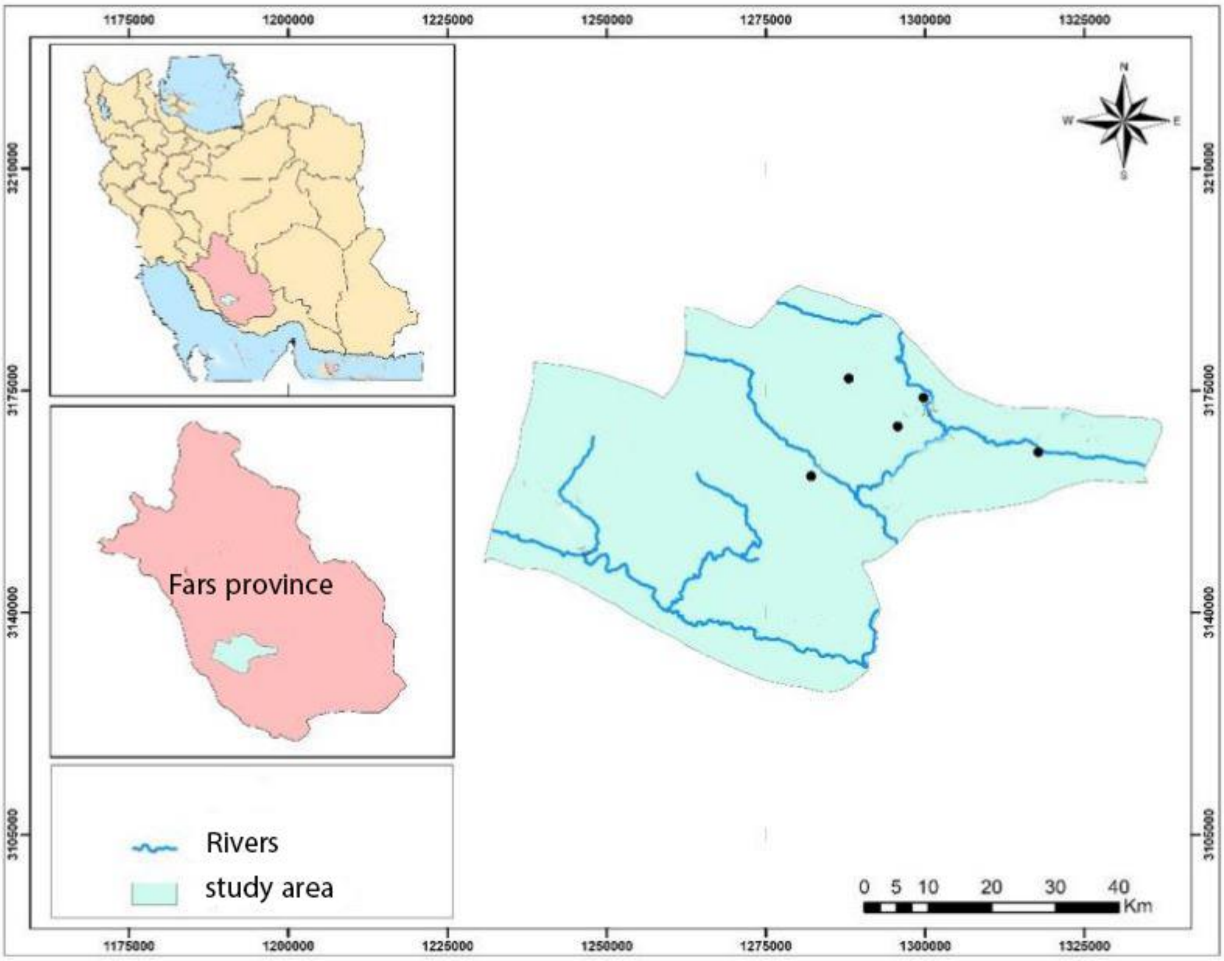

Figure 1. Location of Qirokarzin city in Fars province.

Figure 2. Qirokarzin city's flood photo.

2.2. Vegetation difference index

The analysis of vegetation changes reveals notable shifts in the normalized vegetation difference index values between 2000 and 2021 across the study area (**Figures 3** and **4**). The increase in these index values indicates a proliferation of vegetation, primarily driven by agricultural and horticultural expansion, particularly along the Hengam and Qara-Aghaj rivers, as well as in the vicinity of Mubarak Abad, Imam Shahr, and Qir cities. However, this expansion of agricultural activities has come at the expense of natural vegetation, leading to the conversion of low-density forests into pastures and the degradation of once robust pastures into weaker ones with minimal coverage. Consequently, the diminishing forest and pasture vegetation have resulted in reduced water infiltration and increased runoff, exacerbating the risk of flooding in the area. Furthermore, the expansion of agricultural lands along riverbanks has left them susceptible to flooding during periods of heavy rainfall. Moreover, the absence of vegetation on agricultural lands for certain parts of the year renders them more susceptible to erosion compared to forest and pasture lands. This heightened erosion leads to soil fertility depletion and loss of vegetation cover.

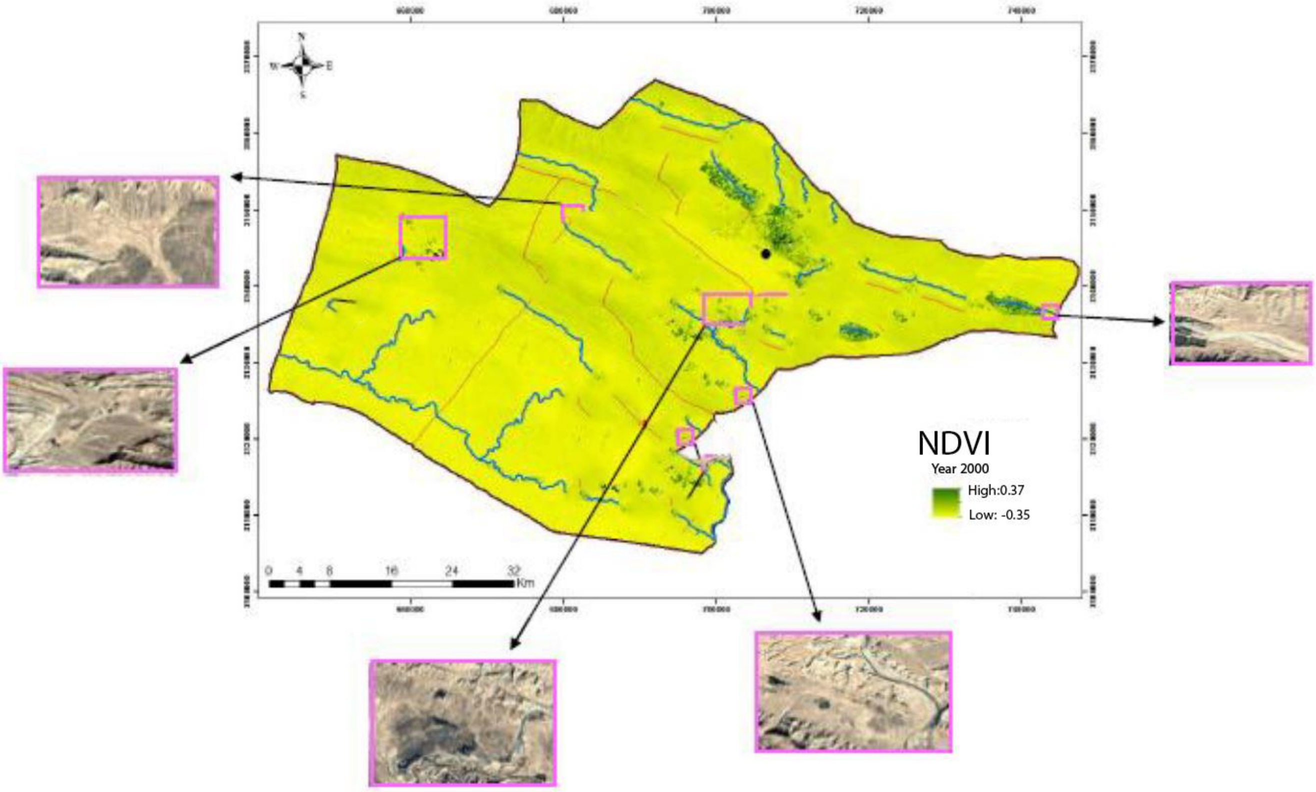

Figure 3. The normalized vegetation difference index in the year 2000.

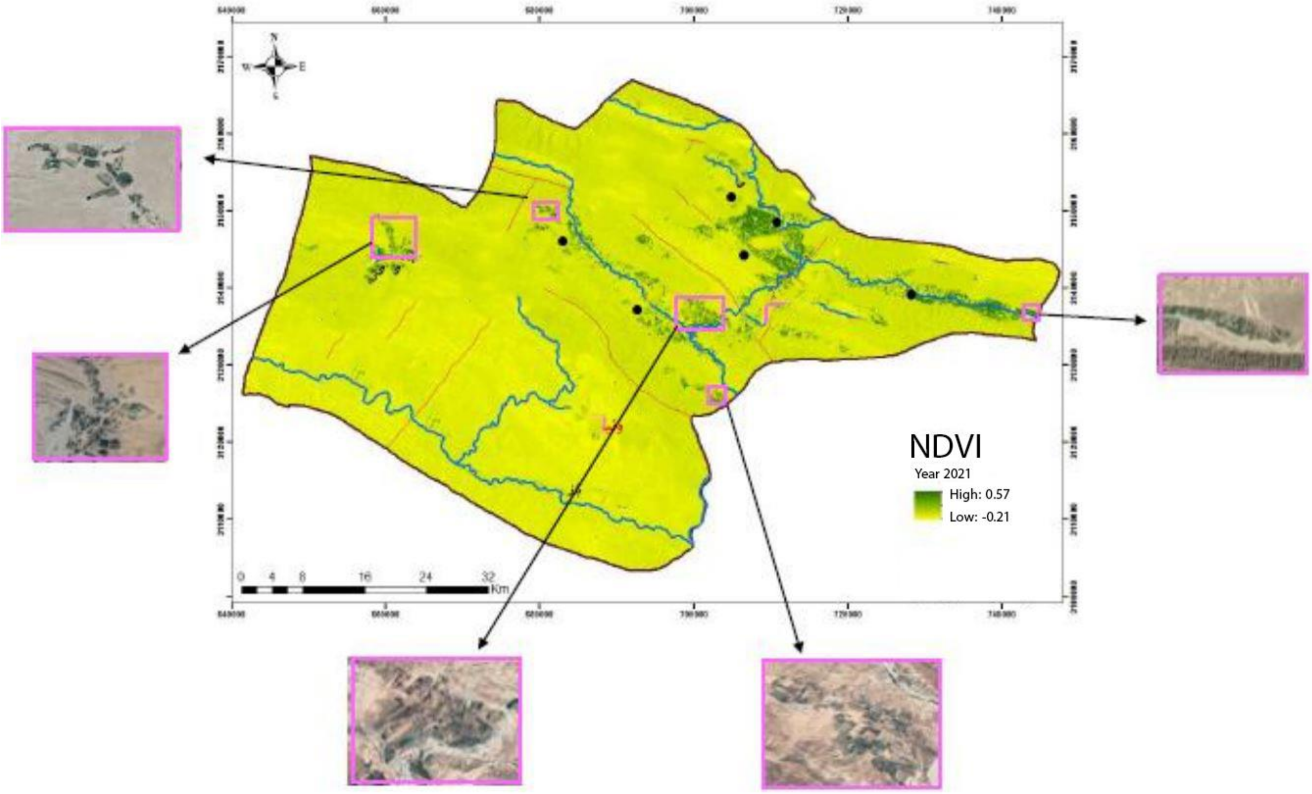

Figure 4. The normalized vegetation difference index in the year 2021.

To facilitate flood zoning in Qirokarzin city, the following approach was undertaken: Initially, a comprehensive review of literature alongside field visits was conducted to identify key factors influencing flood occurrences in the study area. Subsequently, a multi-criteria decision model was employed, integrating both primary and secondary data sources. The primary dataset included a digital elevation model (DEM) with a resolution of 101 meters, derived from topographic data with a scale of 1: 25,000. Additionally, slope data, obtained from the DEM, and a fundamental geological map with a scale of 1:100,000 were incorporated into the analysis. Furthermore, average rainfall data spanning a 30-year period and a map delineating soil hydrological groups were utilized to enhance flood zoning accuracy. In order to assess vegetation status and estimate changes over a 21-year timeframe, Landsat 8 and Landsat 7 satellite images from the years 2000 and 2021 were employed. The normalized difference vegetation index (NDVI) was utilized to analyze vegetation dynamics within Qirokarzin city, providing valuable insights into vegetation trends and alterations over the specified period.

The normalized difference vegetation index (NDVI) is a widely utilized indicator in vegetation change monitoring. It is calculated using Equation (1) [23].

$$\mathrm{NDVI} = \frac{\mathrm{NIR} - \mathrm{RED}}{\mathrm{NIR} + \mathrm{RED}} \tag{1}$$

In this context, NIR represents the spectral reflectance of the near-infrared band, while RED signifies the spectral reflectance of the red band. The normalized difference vegetation index (NDVI) ranges from −1 to +1. For green vegetation, the normalized plant difference index typically falls within the range of approximately 0.1

to 0.8, indicating greenness and high plant density. Thus, this index serves as an effective indicator for assessing plant growth and distribution. Following the preparation of Landsat imagery for the study area, vegetation quantity and density were extracted within the ArcGIS software environment.

2.3. Network analysis process model

The network analysis process model stands out as a prominent and practical decision-making tool, emphasizing the interdependence among criteria. Initially proposed by Chemweno et al. [24] in 2015, this model provides a structured framework for decision-making and problem evaluation. It delineates a network of connections between elements across different clusters, encompassing both external dependencies and internal connections within a cluster. Essentially, the network analysis process model elucidates the interrelationships among components, facilitating a comprehensive understanding of complex systems. One of the key advantages of the network analysis process model is its applicability to both qualitative and quantitative scenarios, offering a versatile approach to addressing various issues and challenges [25]. By employing this model, it becomes feasible to overcome interconnected issues and optimize decision-making processes. Given the significance of flood control and mitigation, understanding the factors influencing floods is paramount for effective planning and management. Prior knowledge of these factors enables proactive measures to be implemented, enhancing flood control efforts and minimizing potential damages. The process of executing the network analysis process model typically involves the following steps:

The process of executing the network analysis process model typically involves the following steps [26]:

(1) Building the analysis model:

- Identify criteria influencing the final decision and establish connections between them to form a network structure.
- Develop pairwise comparison matrices to evaluate the impact of criteria and sub-criteria, considering higher levels of the network and internal communication.
- Calculate the weight vector W using Equation (2), where λ_{max} represents the largest eigenvalue of matrix A. The compatibility index (CI) of the criteria weight is utilized to determine the degree of compatibility of comparisons, as calculated by Equation (3). If CI is less than 0.1, the comparisons are deemed acceptable.

$$AW = \lambda_{max} W \tag{2}$$

$$CI = \frac{\lambda_{max} - n}{n - 1} \tag{3}$$

(2) Forming the primary supermatrix.

(3) Forming the weighted supermatrix:

- Utilize the Super Decision software to calculate the dependencies and generate the weighted supermatrix.

(4) Calculation of the general weighted vector of the limit of the supermatrix:

- Ensure convergence of the weighted supermatrix to its limit power, where the elements of the convergent matrix and its row values are equal.

In this study, maps and information layers for each element were prepared using ArcGIS software. Subsequently, the final coefficients obtained from the network analysis process were applied to each layer. Finally, the simple weight sum method was employed to generate the final map.

The topographic index represents the degree of flow accumulation at any point within a catchment area, indicating the tendency of water to move downhill under the influence of gravity. In Equation (4), A is the specific catchment area, measured in square meters per meter, and β is the slope of the pixel, measured in degrees.

$$TWI = \ln \left(\frac{A_s}{\tan \beta}\right) \tag{4}$$

Topography serves as a crucial factor influencing the spatial distribution of saturated areas and driving changes in hydrological conditions within a watershed. It significantly impacts soil moisture distribution, with underground water flow often closely following surface topography [27]. The topographic moisture index is a valuable tool for assessing moisture conditions at the watershed scale, influenced by flow direction and cumulative flow [28]. Flow direction dictates the transfer of water from one cell to another, while flow accumulation describes the concentration of runoff from various elevation points, guided by the slope and shape of the terrain [29]. Consequently, areas with abundant waterways in the catchment area exhibit high levels of accumulation. The topographic moisture index assigns numerical values to landscapes, with lower values indicating dry cells and higher values signifying wet cells [30]. Threshold values are determined through classification methods, incorporating local knowledge of basin characteristics and observations of local responses to heavy precipitation and surface runoff. These criteria are applied to the output raster, facilitating comprehensive analysis of water flow dynamics on the Earth's surface.

The American Soil Conservation Organization's rainfall-runoff model, established subsequent to Sherman's 1949 studies on rainfall-runoff relationships, is a commonly utilized method in hydrology. This model aims to generate a single hydrograph representing the correlation between rainfall and runoff [31]. To determine the volume of rainfall converted into runoff, it is imperative to ascertain the rainfall depth within the study area. Runoff volume is directly proportional to flood magnitude; as runoff depth increases, the likelihood of flooding escalates, whereas a reduction in runoff depth corresponds to a decreased flood risk. Equation (5) is employed to compute the maximum potential for rainfall retention in centimeters [32].

$$S = \frac{2500}{\mathrm{CN} - 254} \tag{5}$$

The calculation of Curve Number (CN) involves factors such as soil hydrological groups, land productivity, hydrological conditions of the land, and previous soil moisture status of the region. CN values range from zero to 100, with zero indicating no runoff production [33]. As the CN value increases, the runoff volume also increases. At a CN value of 100, all rainfall is converted into runoff [34]. Ultimately, the height of runoff in the study area can be determined based on layers representing the maximum rainfall retention potential of the land and the thirty-year average rainfall of Qirokarzin, using Equation (6).

$$Q = \frac{(P - 0.2S)^2}{P + 0.8S} \tag{6}$$

Q is the runoff height in millimeters.

P is the average annual precipitation in millimeters.

S is the maximum potential of land precipitation retention.

The proposed procedural map is shown in **Figure 5**. The first step (sub-procedure A) in the proposed procedural roadmap consists of determining consistent flood hazard and risk scenarios. The specific aims are to obtain a spatially explicit representation of the frequency and magnitude (intensity) for each of the underlying hazard scenarios and to quantify the associated consequences in terms of losses with respect to values exposed, and thus risk. The main result is the so-called risk reference prospect, which serves as a basis for a performance comparison between possible risk mitigation alternatives. In this paper, emphasis is put on the computational aspects needed to derive flood risk.

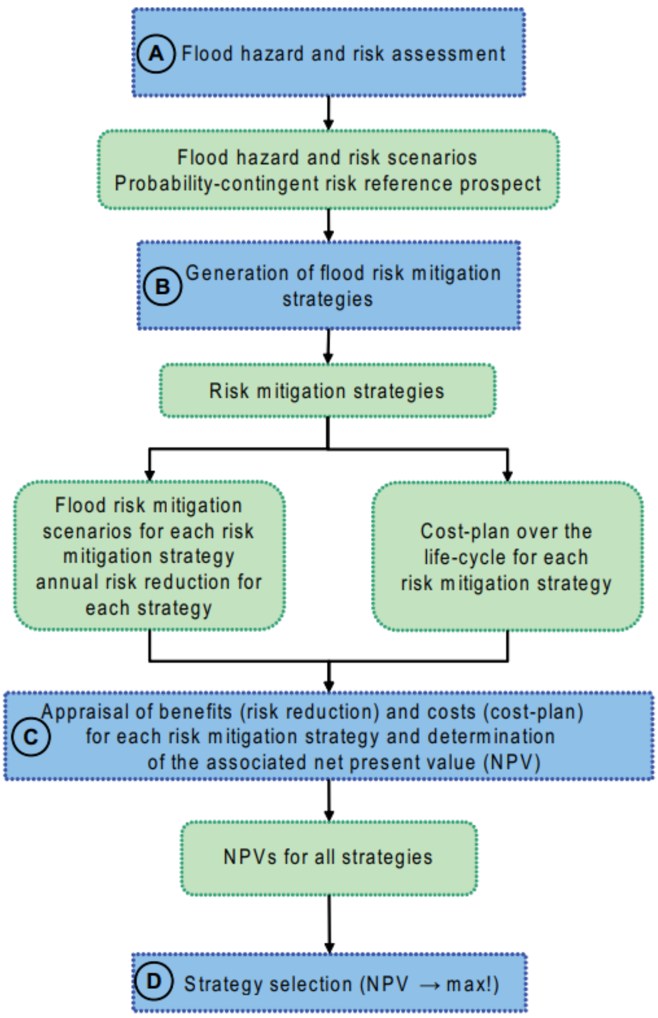

Figure 5. Procedural roadmap for a comprehensive risk mitigation project assessment.

3. Results and discussion

In analyzing the spatial distribution of flooding and vegetation changes in Qirokarzin city, maps depicting criteria such as slope height, distance from the river, topographic moisture index, and runoff height were generated. The results of the benchmark map are presented below:

3.1. Slope height

Altitude significantly influences various environmental factors such as rainfall patterns, evaporation rates, temperature, hydrology, runoff, soil conditions, and vegetation. There exists an inverse relationship between altitude and flooding, with higher elevations associated with reduced flood risk. The slope height criterion map illustrates that as elevation increases, the likelihood of flooding decreases, whereas flooding probability rises with decreasing elevation. Qir, Imam Shahr, Mubarak Abad, and Afzer are situated at lower altitudes, posing a higher risk of flooding. Notably, major rivers in the study area, including the Baz River, Hengama, Tang Kish, and Qara Aghaj, flow through these low-lying areas, contributing to their elevated flood risk.

Overall, the analysis of slope height provides valuable insights into flood vulnerability across Qirokarzin city, highlighting areas at heightened risk due to their lower elevations and proximity to major water bodies. **Figure 6** illustrates the standard slope map within the city, aiding in visualizing the terrain characteristics and their impact on flood susceptibility.

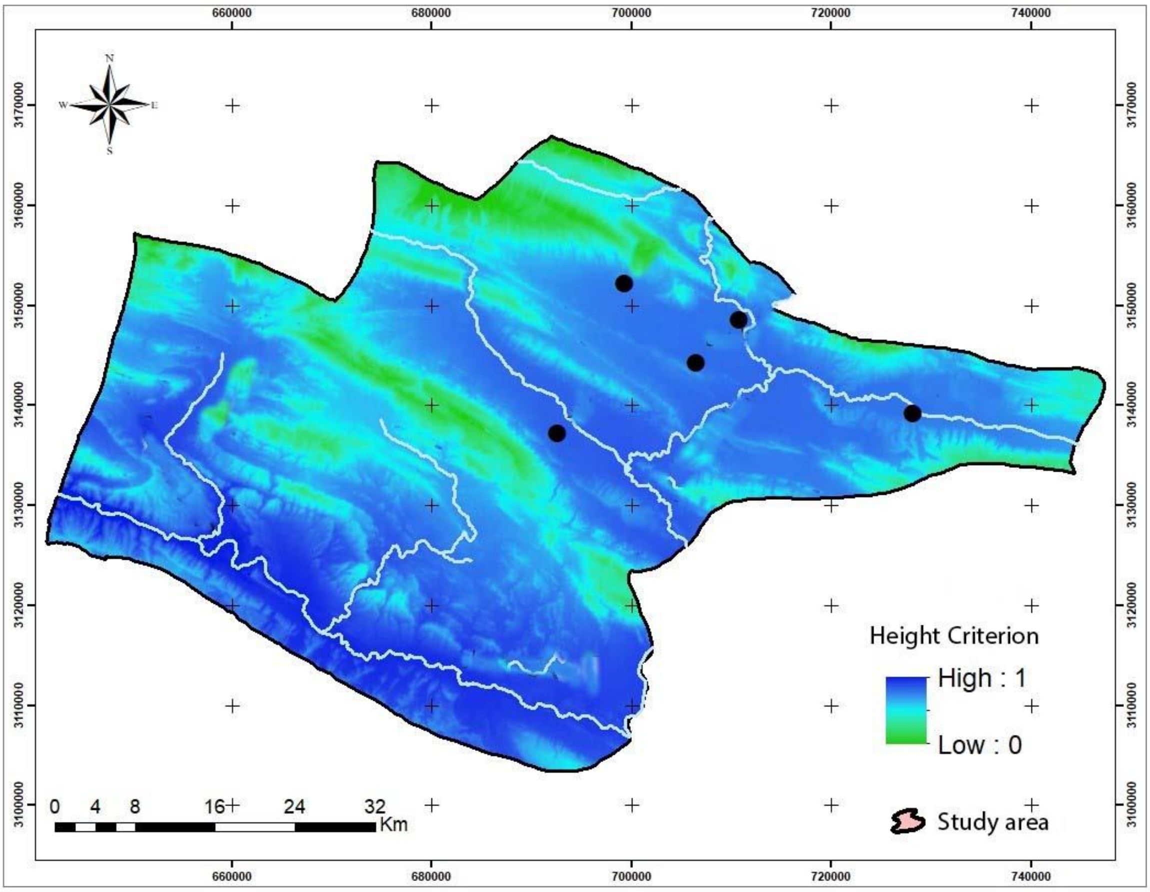

Figure 6. The standard slope height map.

3.2. Slope

The slope criterion exhibits an inverse relationship with the likelihood of flooding. Areas with higher slopes tend to experience decreased flood probabilities, whereas those with lower slopes are at higher risk of flooding. A standard map of slope within the study area was prepared to visualize this relationship (**Figure 7**). Analysis indicates that cities such as Qir, Imam Shahr, Mubarak Abad, and Afzer are situated in regions with low slopes, indicating a higher flood risk. Notably, major rivers, including Baz, Hengama, Tang Kish, and Qara-Aghaj, are located in areas with the lowest slope, correlating with the highest probability of flooding.

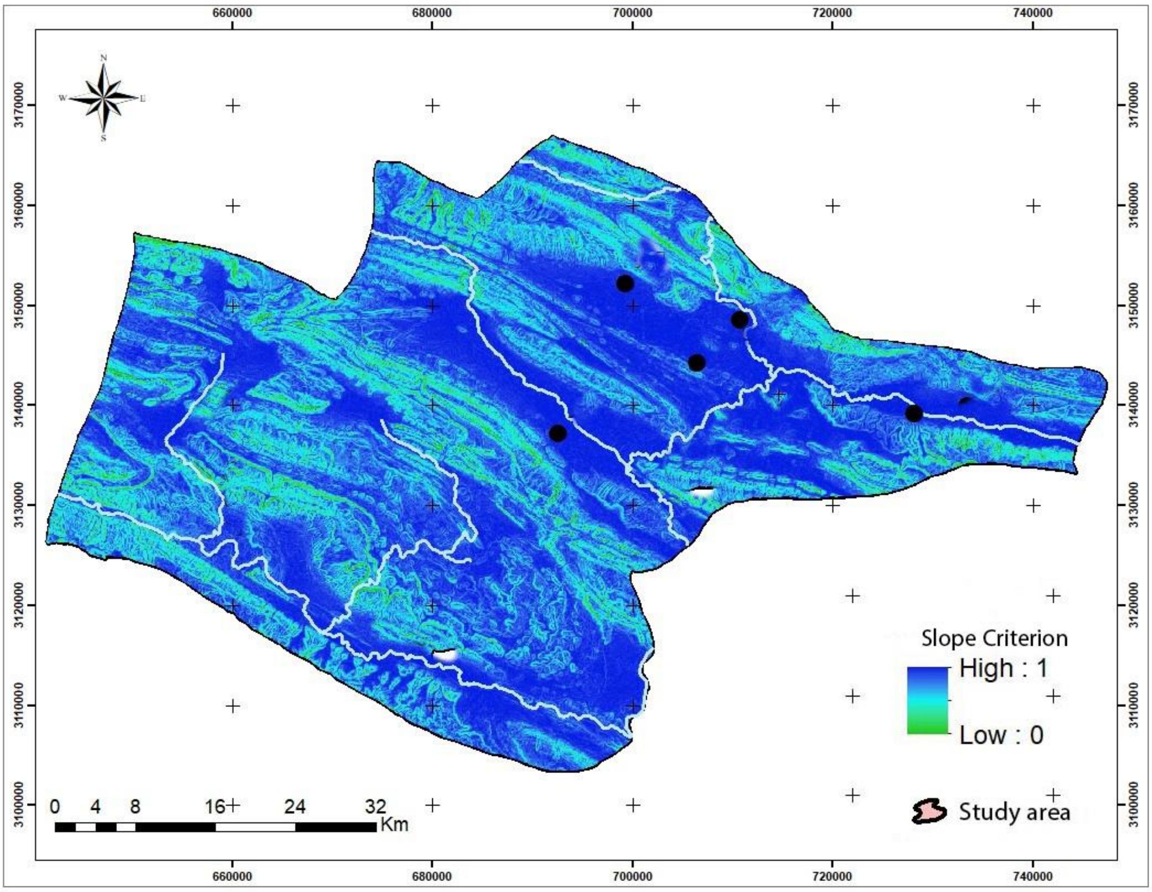

Figure 7. Standard map of slope criterion.

3.3. Distance from river

Flooding occurs when rainwater exceeds the soil and vegetation's absorption capacity, and the natural river channel cannot accommodate the runoff. Higher values on the distance from the river map signify a greater flood probability closer to the riverbed, while flood probability decreases with distance from the riverbed. Hence, the distance from the river criterion directly influences flood probability. Analysis reveals that cities like Qir, Imamshahr, Mubarakabad, and Afzer are at risk of flooding due to their proximity to the main riverbed (**Figure 8**). Additionally, the main rivers Baz, Hengama, Tang Kish, and Qara-Aghaj exhibit the highest probability of flooding within their beds.

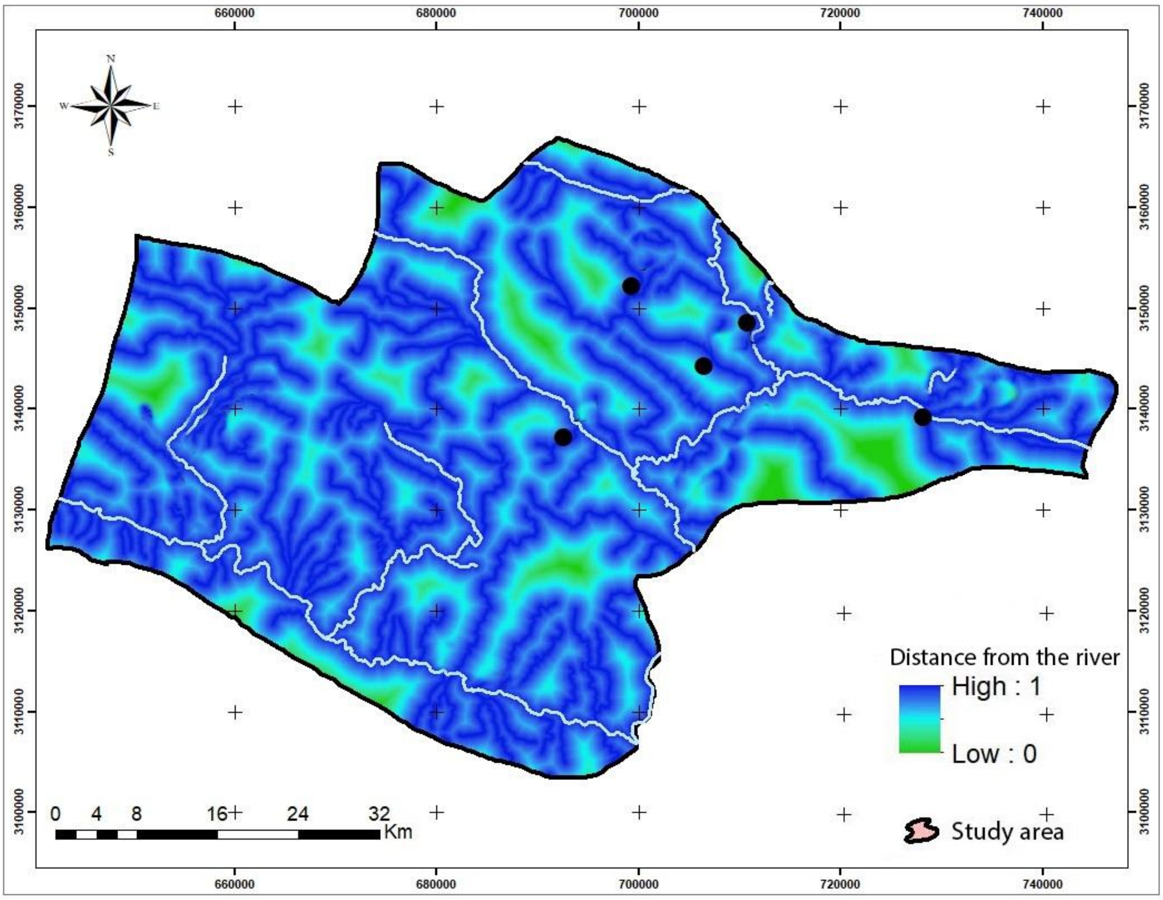

Figure 8. map of distance from the river criterion.

3.4. Topographic moisture index

The topographic moisture index is directly related to floods. Analysis of the topographic moisture index within the study area reveals significant insights into flood susceptibility. In valleys and depressions, where the index reaches its highest value of one, there is increased flow accumulation and soil moisture. Conversely, in ridge areas characterized by low flow accumulation and dry soil conditions, the index attains its lowest value of zero (**Figure 9**). This spatial distribution of the topographic moisture index provides valuable information about areas prone to flooding, with higher values indicating elevated flood risk due to increased flow and soil moisture. Conversely, lower values indicate reduced flood risk associated with drier soil conditions and limited flow accumulation.

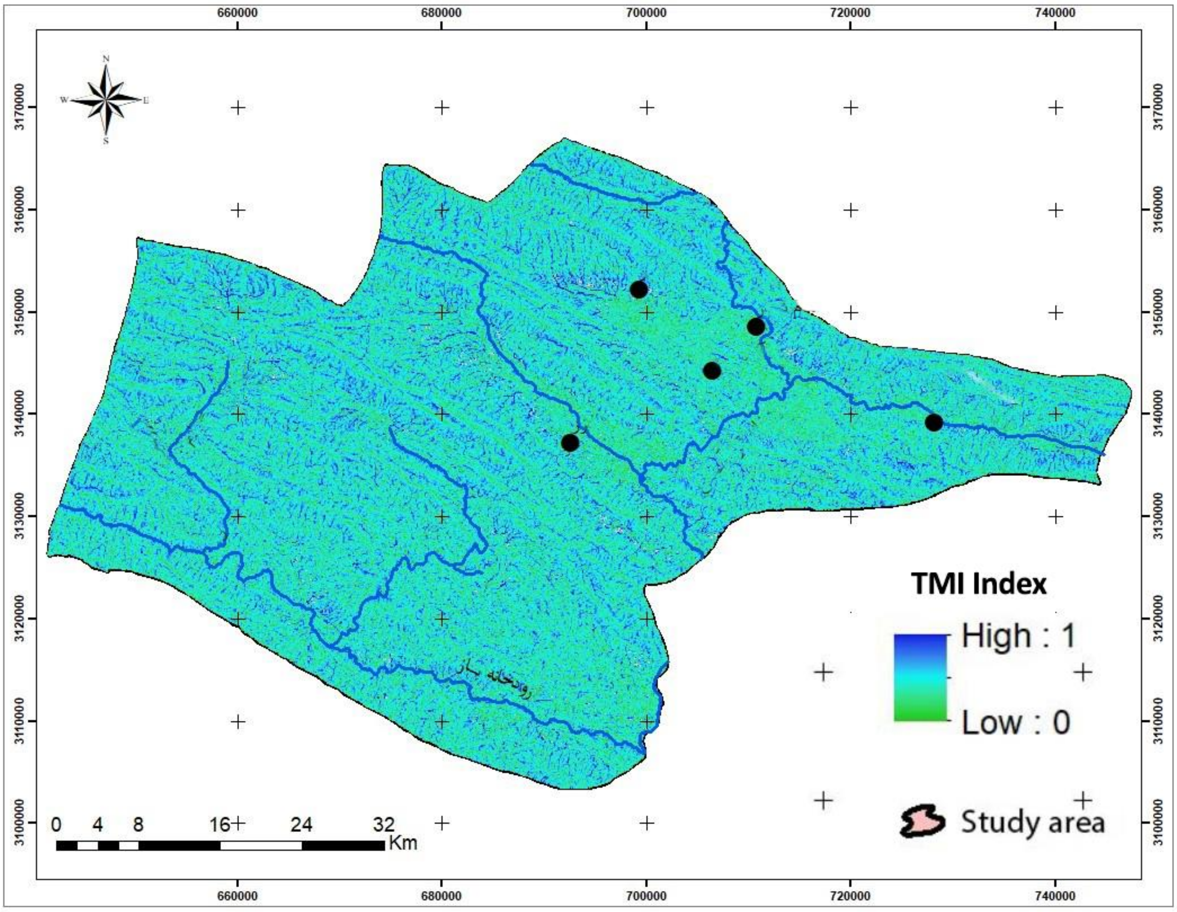

Figure 9. Topographic Moisture Index map.

3.5. Runoff height

The analysis of runoff height provides crucial insights into flood vulnerability within the study area. Observations reveal that the maximum runoff height is concentrated at the headwaters of rivers, denoted by a value of 1 with Imam Shahr located in this region (**Figure 10**). In these areas, soil infiltration is high, leading to minimal runoff production. Conversely, green areas indicate locations where all rainfall is absorbed into the soil, resulting in no runoff. Furthermore, within the riverbeds of major rivers such as Roodkhane Baz, Hengam, and Qara Aghaj, the runoff height reaches its highest calculated value, indicating the highest probability of flooding in these areas. As distance from the main rivers increases, the probability of flooding decreases. Notably, the Tang Kish River exhibits lower runoff height compared to other major rivers, suggesting a relatively lower flood risk in its vicinity.

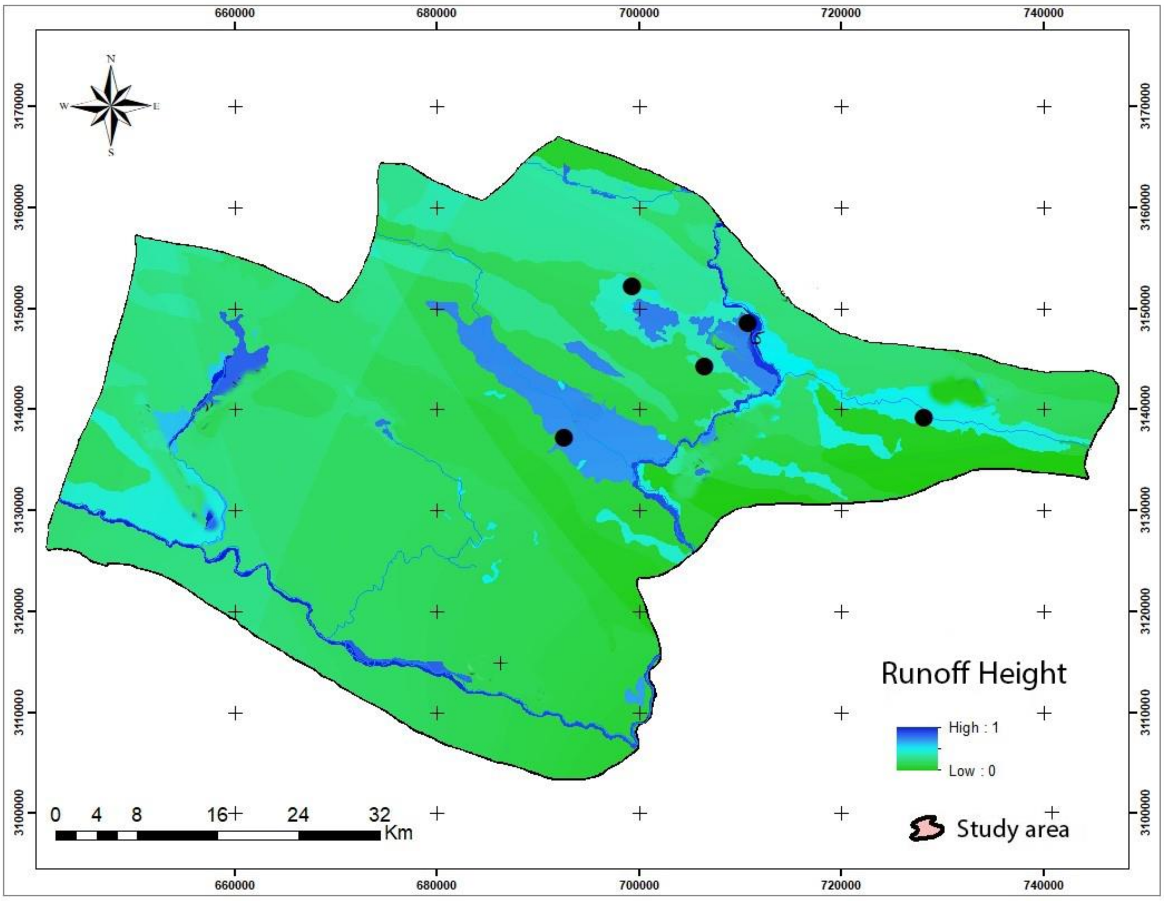

Figure 10. Runoff height map.

3.6. Weighting criteria

The analysis reveals the weighting of criteria within Qirokarzin city, with the topographic moisture index criterion holding the highest weight of 0.27 and the height criterion having the lowest weight of 0.122. Additionally, the distance from the Shib River and the height of the runoff in the study area hold weights of 0.183, 0.196, and 0.229, respectively. The weight of each criterion affecting the flood occurrence is shown in **Table 1**.

Table 1. Weight of each criterion affecting the flood occurrence.

	Criteria	Weight
1	Slope Height	0.122
2	Slope	0.196
3	Distance from the River	0.183
4	Topographic Moisture Index	0.270
5	Runoff Height	0.229

3.7. Flood potential analysis

The risk of flooding within the study area is categorized into five levels: very low, low, medium, high, and very high (**Figure 11**). **Table 2** provides details on the area and percentage of each flood occurrence class. Notably, five primary areas, along with several sub-areas, exhibit a very high flood risk. These areas are predominantly situated in the central, southern, northeastern, and northwestern regions of the study area. Cities such as Imam Shahr and Afzer face a high risk of flooding, particularly along major rivers like Baz, Hengam, Qara Aghaj, and parts of the Tang Kish riverbed. The distribution of strata with a high probability of flooding is scattered throughout the study area. Qir, Karzin, and Mubarak Abad are located within high flood risk zones, with a significant portion of the Tang Kish riverbed also facing high flood risk. This class encompasses the largest area, covering 157,730.1 hectares (46.7 percent) of the study area. Furthermore, the middle class covers an area of 108,946.1 hectares (32.3 percent), indicating moderate flood risk due to changes in elevation and runoff height. The low-level risk is observed sporadically from the east to the west of the study area, comprising 41,746.7 hectares (12.4 percent). Finally, very low-risk areas are minimal and primarily located in the eastern and northern regions of the study area, where increased elevation and slope contribute to reduced flood probability.

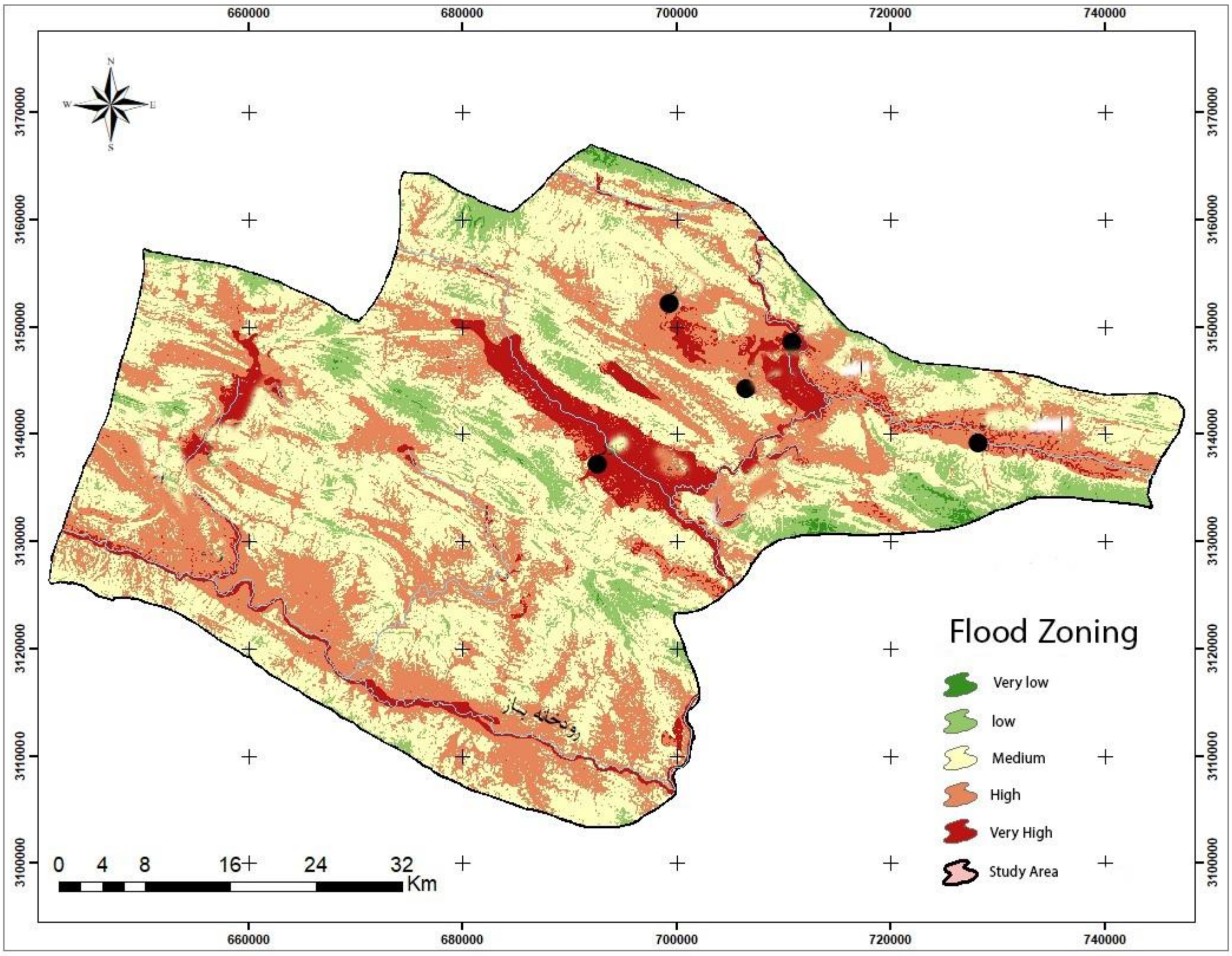

Figure 11. Flood zoning map.

The spatial distribution results reveal that areas with high and very high flood risk are dispersed across three sections of the study area characterized by low altitude and slope. During heavy rainfall events, the adjacent elevations to these areas play a critical role in generating runoff and peak discharge. Additionally, the geological composition of the study area, dating back to the late third and fourth geological periods, contributes to a very low infiltration rate, often leading to hazardous floods. Moreover, the presence of gravel and stones in floodwaters enhances their force, resulting in greater erosion of riverbeds and channel banks and even causing significant damage to houses located nearby.

Table 2. Area and percentage of flood risk.

Flood Risk	Area (hectares)	Percentage
Very Low	1933.6	0.5
Low	41,746.7	12.4
Medium	108,946.1	32.3
High	157,730.1	46.7
Very High	27,230.7	8.1

3.8. Vegetation changes analysis

In areas lacking vegetation, heavy rainfall events result in significant water flow down mountain slopes, often culminating in hazardous floods. The presence of soil erosion, sediment-laden water, and debris such as sand, rubble, and stones increases the force of floodwaters, causing severe erosion of riverbeds and channel banks and even the destruction of nearby houses. Overall, the analysis underscores the intricate relationship between vegetation dynamics, land use changes, soil erosion, and flood risk, highlighting the urgent need for sustainable land management practices to mitigate the adverse impacts of flooding in the study area.

The findings of this study echo those of previous research on the spatial correlation between vegetation changes and runoff height, as evidenced in the Gorgan River catchment. A study on this catchment revealed a 78% spatial correlation between vegetation and runoff height, indicating a negative relationship between these variables [35]. Similarly, in our study area, human-induced land use changes, such as deforestation, pasture degradation, and agricultural expansion, have contributed to reduced vegetation cover and increased runoff height. Comparing the distribution of flooding and vegetation changes over the study period highlights the prevalence of agricultural areas in high flood-risk zones. Emphasizing the importance of vegetation density and sustainable land use practices, previous research on the Shiraz dry river basin underscores the role of preserving natural land cover in mitigating floods. Alterations in land use upstream have been shown to decrease flood delay times by 50%, elevating flood risks. Moreover, our research aligns with studies utilizing hierarchical analysis models to assess flood risk. For instance, a study employing lithological precipitation, drainage density, land slope, and land use criteria identified high and very high flood-risk zones, predominantly situated in upstream areas. Similarly, satellite imagery analysis of Qirokarzin revealed dense vegetation in agricultural lands, consistent with our vegetation change findings.

4. Conclusion

Floods pose a significant threat in the world, including Iran, where historical records and observations underscore the recurring nature of this hazard. Vegetation dynamics play a pivotal role in influencing flood patterns, influenced by a myriad of factors. This study investigates flood risk in Qirokarzin city in relation to vegetation changes, identifying five critical criteria: height, slope, distance from the river, topographic humidity, and runoff height. Weighting analysis reveals that the topographic humidity index and runoff height are the most influential criteria, with weights of 0.27 and 0.229, respectively. Conversely, the height criterion carries the least weight at 0.122. Notably, 46.7% of the study area exhibits high flood intensity, potentially attributed to variations in elevation and runoff height. The presence of the bitumen reservoir dam in a flood-prone area raises concerns regarding overflow risks during peak periods, warranting further research into flood risk management strategies.

Analysis of vegetation changes from 2000 to 2022 indicates a significant expansion of agriculture. Despite the rise in the normalized difference vegetation index (NDVI), flood intensity remains unabated. Spatial analysis reveals a weak correlation (Pearson coefficient: 0.320) between flood intensity and NDVI changes, emphasizing the primacy of upstream land management practices over vegetation improvements in flood mitigation efforts. The findings underscore the imperative of proactive watershed management, focusing on soil conservation, runoff infiltration, and flood control in upstream areas. Redirecting management efforts towards protection, soil conservation, and enhanced runoff infiltration can yield more sustainable flood mitigation outcomes. Further research into flood risk dynamics and vegetation changes is warranted to inform evidence-based flood management strategies in Qirokarzin city and similar regions.

Investigations into rural-urban settlements indicate over 70% vulnerability to floods in developed areas, emphasizing the need for management measures. These include vegetation preservation in upstream areas, maintaining safe distances from riverbeds during urbanization, watershed management to extend flood concentration times, and public awareness initiatives to promote nature-friendly practices and sustainable land use patterns. By integrating these findings into flood risk management strategies, there’s potential to reduce vulnerability and enhance resilience to flooding in Qirokarzin city and similar regions. Analysis of the alike areas morphology, channel confinement, and the analysis of present land use maps, as well as exploratory investigation to anticipate future land demands and land use change, can be conducted in future studies.

Author contributions: Conceptualization, AM and RZ; methodology, AN; software, MY; validation, FE, SFH and AM; formal analysis, RZ; investigation, AM; resources, AN; data curation, MY; writing—original draft preparation, FE; writing—review and editing, SFH; visualization, AM; supervision, RZ; project administration, AN; funding acquisition, MY. All authors have read and agreed to the published version of the manuscript.

Conflict of interest: The authors declare no conflict of interest.

References

1. Few R, Matthies F. Flood hazards and health: responding to present and future risks. Taylor & Francis; 2013.

2. Melo-Merino SM, Reyes-Bonilla H, Lira-Noriega A. Ecological niche models and species distribution models in marine environments: A literature review and spatial analysis of evidence. Ecological Modelling. 2020; 415: 108837. doi: 10.1016/j.ecolmodel.2019.108837
3. Guria R, Mishra M, Dutta S, et al. Remote sensing, GIS, and analytic hierarchy process-based delineation and sustainable management of potential groundwater zones: a case study of Jhargram district, West Bengal, India. Environmental Monitoring and Assessment. 2023; 196(1). doi: 10.1007/s10661-023-12205-6
4. Sauquet E, Shanafield M, Hammond JC, et al. Classification and trends in intermittent river flow regimes in Australia, northwestern Europe and USA: A global perspective. Journal of Hydrology. 2021; 597: 126170. doi: 10.1016/j.jhydrol.2021.126170
5. Oudin L, Salavati B, Furusho-Percot C, et al. Hydrological impacts of urbanization at the catchment scale. Journal of Hydrology. 2018; 559: 774–786. doi: 10.1016/j.jhydrol.2018.02.064
6. Yousefi H, Moradi S, Zahedi R, et al. Developed analytic hierarchy process and multi criteria decision support system for wind farm site selection using GIS: A regional-scale application with environmental responsibility. Energy Conversion and Management: X. 2024; 22: 100594. doi: 10.1016/j.ecmx.2024.100594
7. Chukwuma EC, Okonkwo CC, Ojediran JO, et al. A GIS based flood vulnerability modelling of Anambra State using an integrated IVFRN-DEMATEL-ANP model. Heliyon. 2021; 7(9): e08048. doi: 10.1016/j.heliyon.2021.e08048
8. Zahedi R, Sadeghitabar E, Khazaee M, et al. Potentiometry of wind, solar and geothermal energy resources and their future perspectives in Iran. Environment, Development and Sustainability. 2024. doi: 10.1007/s10668-024-04633-2
9. Ghanbarpour MR, Saravi MM, Salimi S. Floodplain Inundation Analysis Combined with Contingent Valuation: Implications for Sustainable Flood Risk Management. Water Resources Management. 2014; 28(9): 2491–2505. doi: 10.1007/s11269-014-0622-2
10. Johnston R, Smakhtin V. Hydrological Modeling of Large river Basins: How Much is Enough? Water Resources Management. 2014; 28(10): 2695–2730. doi: 10.1007/s11269-014-0637-8
11. Tien Bui D, Khosravi K, Shahabi H, et al. Flood Spatial Modeling in Northern Iran Using Remote Sensing and GIS: A Comparison between Evidential Belief Functions and Its Ensemble with a Multivariate Logistic Regression Model. Remote Sensing. 2019; 11(13): 1589. doi: 10.3390/rs11131589
12. Qasimi AB, Isazade V, Enayat E, et al. Landslide susceptibility mapping in Badakhshan province, Afghanistan: a comparative study of machine learning algorithms. Geocarto International. 2023; 38(1). doi: 10.1080/10106049.2023.2248082
13. Koralay N, Kara Ö. Assessment of flood risk in Söğütlü stream watershed of Trabzon province in Turkey using geographic information systems and analytic hierarchy process approach. Natural Hazards. 2024; 120(11): 9977–10000. doi: 10.1007/s11069-024-06594-1
14. Estelaji F, Moniri N, Yari MH, et al. Earthquake, flood and resilience management through spatial planning, decision and information system. Future Technology. 2024; 3(2): 11–21. doi: 10.55670/fpll.futech.3.2.2
15. Khah MV, Zahedi R, Mousavi MS, et al. Forecasting renewable energy utilization by Iran's water and wastewater industries. Utilities Policy. 2023; 82: 101546. doi: 10.1016/j.jup.2023.101546
16. Mehrzad K, Rahim Z, Reza F, et al. Potential assessment of renewable energy resources and their power plant capacities in Iran. Global Journal of Ecology. 2022; 7(2): 060–071. doi: 10.17352/gje.000062
17. Goodarzi MR, Niknam ARR, Sabaghzadeh M. Rainfall-runoff modeling using GIS: A case study of Gorganrood Watershed, Iran. Water Resource Modeling and Computational Technologies. 2022; 165–181. doi: 10.1016/b978-0-323-91910-4.00011-x
18. Taherizadeh M, Niknam A, Nguyen-Huy T, et al. Flash flood-risk areas zoning using integration of decision-making trial and evaluation laboratory, GIS-based analytic network process and satellite-derived information. Natural Hazards. 2023; 118(3): 2309–2335. doi: 10.1007/s11069-023-06089-5
19. Estelaji F, Aghajari AA, Zahedi R. Flood zoning and developing strategies to increase resilience against floods with a crisis management approach. Asian Review of Environmental and Earth Sciences. 2023; 10(1): 14–27. doi: 10.20448/arees.v10i1.4439
20. Estelaji F, Naseri A, Keshavarzzadeh M, et al. Potential measurement and spatial priorities determination for gas station construction using WLC and GIS. Future Technology. 2023; 2(4): 24–32. doi: 10.55670/fpll.futech.2.4.3

21. Estelaji F, Naseri A, Zahedi R. Evaluation of the Performance of Vital Services in Urban Crisis Management. Advances in Environmental and Engineering Research. 2022; 03(04): 1–19. doi: 10.21926/aeer.2204057
22. Mirzavand H, Aslani A, Zahedi R. Environmental impact and damage assessment of the natural gas pipeline: Case study of Iran. Process Safety and Environmental Protection. 2022; 164: 794–806. doi: 10.1016/j.psep.2022.06.042
23. Pettorelli N. The normalized difference vegetation index. Oxford University Press; 2013.
24. Chemweno P, Pintelon L, Van Horenbeek A, et al. Development of a risk assessment selection methodology for asset maintenance decision making: An analytic network process (ANP) approach. International Journal of Production Economics. 2015; 170: 663–676. doi: 10.1016/j.ijpe.2015.03.017
25. Dwyer L, Gill A, Seetaram N, et al. Handbook of research methods in tourism: Quantitative and qualitative approaches. Edward Elgar Publishing; 2012.
26. Teng J, Jakeman AJ, Vaze J, et al. Flood inundation modelling: A review of methods, recent advances and uncertainty analysis. Environmental Modelling & Software. 2017; 90: 201–216. doi: 10.1016/j.envsoft.2017.01.006
27. Liu S, Wang Y, An Z, et al. Watershed spatial heterogeneity of soil saturated hydraulic conductivity as affected by landscape unit in the critical zone. CATENA. 2021; 203: 105322. doi: 10.1016/j.catena.2021.105322
28. Ghorbani M, Ghaderi N, Estelaji F, et al. Evaluating Surface Water Collection Infrastructure for Management of Urban Flood Risk: Integrating HEC-RAS with GIS in Overland Flow Modeling and Flood Hazard Zone Mapping within the Kan River Watershed of Tehran. AGU24. https://agu.confex.com/agu/agu24/prelim.cgi/Paper/1594722
29. Murphy PNC, Ogilvie J, Arp P. Topographic modelling of soil moisture conditions: a comparison and verification of two models. European Journal of Soil Science. 2009; 60(1): 94–109. doi: 10.1111/j.1365-2389.2008.01094.x
30. Estelaji F, Zahedi R, Gitifar A, et al. Integrating HEC-RAS, GIS, and LISREL for assessing and enhancing urban building resilience against flood threats: Comprehensive model and analysis. Heliyon. 2024; 10(20): e39463. doi: 10.1016/j.heliyon.2024.e39463
31. Mishra SK, Singh VP. Soil Conservation Service Curve Number (SCS-CN) Methodology. Springer Netherlands; 2003.
32. Young AF, Papini JA. How can scenarios on flood disaster risk support urban response? A case study in Campinas Metropolitan Area (São Paulo, Brazil). Sustainable Cities and Society. 2020; 61: 102253. doi: 10.1016/j.scs.2020.102253
33. Huang M, Gallichand J, Dong C, et al. Use of soil moisture data and curve number method for estimating runoff in the Loess Plateau of China. Hydrological Processes. 2006; 21(11): 1471–1481. doi: 10.1002/hyp.6312
34. Daly C, Halbleib M, Smith JI, et al. Physiographically sensitive mapping of climatological temperature and precipitation across the conterminous United States. International Journal of Climatology. 2008; 28(15): 2031–2064. doi: 10.1002/joc.1688
35. Hu C, Wright AL, Lian G. Estimating the Spatial Distribution of Soil Properties Using Environmental Variables at a Catchment Scale in the Loess Hilly Area, China. International Journal of Environmental Research and Public Health. 2019; 16(3): 491. doi: 10.3390/ijerph16030491

Journal of Geography and Cartography 2024, 7(2), 9639.
https://doi.org/10.24294/jgc9639

Article

Impact of extreme rainfall events on soil erosion in downstream Parnaíba River Basin, Brazilian Cerrado

Wellynne Carla de Sousa Barbosa[1,*], Antonio José Teixeira Guerra[1], Iracilde Maria de Moura Fé Lima[2]

[1] Federal University of Rio de Janeiro, Rio de Janeiro 21941-909, Brazil
[2] Federal University of Piauí, Teresina 64049-550, Brazil
*** Corresponding author:** Wellynne Carla de Sousa Barbosa, wellynnekarla@gmail.com

CITATION

Barbosa WCdS, Guerra AJT, Lima IMdMF. Impact of extreme rainfall events on soil erosion in downstream Parnaíba River Basin, Brazilian Cerrado. Journal of Geography and Cartography. 2024; 7(2): 9639. https://doi.org/10.24294/jgc9639

ARTICLE INFO

Received: 15 October 2024
Accepted: 19 November 2024
Available online: 10 December 2024

Abstract: This study investigates the impact of extreme rainfall events on soil erosion in the downstream Parnaíba River Basin, located in the Brazilian Cerrado. The analysis focused on rainfall erosivity (*R* factor) and soil erodibility (*K* factor) as key indicators. The average erosivity in the region was 9051 MJ mm $h^{-1}ha^{-1}year^{-1}$, with a variation between 7943 and 10,081 MJ mm $h^{-1}ha^{-1}year^{-1}$, suggesting a high erosive potential, mainly in the rainiest months, from December to April. The soils of the studied area, mainly Ultisols and Chernosols, present high to very high erodibility, with *K* factor values ranging from 0.025 to 0.050 t h MJ^{-1} mm^{-1}. Furthermore, fieldwork revealed areas, near highways, with apparently fragile soils, as well as rills and gullies, identified through photographs taken during fieldwork. These locations, due to the combination of high erosivity and susceptible soils, were considered prone to the occurrence of erosion processes, representing an additional risk to local infrastructure. The spatialization of *R* and *K* factors, along with field observations, showed that much of the area is at high risk of erosion and landslides, particularly in regions with greater topographic variability and proximity to water bodies. These results provide a basis for the development of mitigation strategies, being important for the effective prevention of landslides.

Keywords: soil erosion; rainfall erosivity; soil erodibility; extreme rainfall events; Brazilian Cerrado

1. Introduction

Soil erosion, intensified by extreme rainfall events, represents one of the greatest environmental challenges in vulnerable regions of Brazil, particularly in the Cerrado. The Parnaíba River Basin, located in this region, is severely affected by erosive processes, which worsen during periods of heavy rainfall, leading to significant soil loss and posing risks to local infrastructure [1–6].

The Universal Soil Loss Equation (USLE) and its revised version (RUSLE) are widely used to estimate soil erosion by combining data on natural factors and human activities. These models, integrated with Geographic Information Systems (GIS) and Remote Sensing technologies, allow for mapping and quantifying soil loss in different regions.

Given the vast extent of the Parnaíba River Basin, the application of the Revised Universal Soil Loss Equation (RUSLE) was particularly suited for this study, as it enables large-scale soil erosion assessments at the watershed level, where direct erosion plot management would be financially unfeasible. This approach is especially valuable in expansive regions like the Cerrado, where varied soil types and challenging terrain impact erosion dynamics [6].

Fieldwork was also conducted to support the model, with strategically collected soil samples across the study area, enhancing the accuracy of the soil erodibility factor (*K*) in the RUSLE model and validating the remote sensing data used. This methodology integrates GIS with empirical data to create a more comprehensive assessment of erosion susceptibility, essential for effective land management and conservation efforts tailored to the Cerrado's unique environmental conditions.

In the study by Dang and Sun [7], USLE was used to evaluate erosion in the Loess Plateau, China. Among the factors analyzed by RUSLE, the *R* Factor, which measures rainfall erosivity, and the *K* Factor, which reflects soil erodibility, stand out. These factors are key to understanding vulnerability to erosive processes and are the central focus of this study.

Studies on rainfall erosivity developed in Brazil highlight some rainfall erosivity indices (EI30) in MJ mm ha^{-1} h^{-1} yr^{-1}: for Lavras (MG), around 6843; for Mococa (SP), 7747; in Paraná State for 32 locations, a range from 5275 to 12,559; for Goiânia, Goiás State, 8355; for Sete Lagoas, Minas Gerais State, 5835; for Lajes, Santa Catarina State, 5790; and for Manaus, Amazonas State, a high value of around 14,129. The author notes that the range for erosivity in Brazil is between 3116 and 20,035 MJ mm ha^{-1} h^{-1} yr^{-1} [8].

Soil erodibility refers to the susceptibility of soil to water erosion. It is an intrinsic attribute of each soil and is fundamental for predicting soil loss and planning land use. Among the soil attributes that, in an integrated manner, affect erodibility are water permeability, water storage capacity, texture (especially silt content), cohesion, structure type and degree, organic carbon, Fe and Al oxide contents, and clay mineral type [9–13].

The relationship between rainfall erosivity and soil erodibility is crucial for understanding the dynamics of erosion. Rainfall erosivity not only varies according to precipitation intensity and duration, but is also related to the spatial and temporal distribution of extreme rainfall, which in turn is influenced by climate change [14–16]. In contexts where improper soil management and deforestation prevail, vulnerability to erosion increases, intensifying the adverse impacts of intense rainfall events [2,11]

Field observations revealed areas near highways with seemingly fragile soils, as well as the formation of rills and gullies, which are indicative of linear erosion and landslide risk. The combination of high erosivity and susceptible soils makes these areas particularly vulnerable [1,11,17]. Additionally, areas with greater topographic variability and proximity to water bodies are more prone to erosive processes, reflecting the importance of physical context and land use in intensifying erosion [3,18–20].

This study aims at analyzing the impact of extreme rainfall events on soil erosion in the Lower Parnaíba River Basin, in the Brazilian Cerrado, using the *K* (soil erodibility) and *R* (rainfall erosivity) factors from RUSLE (Revised Universal Soil Loss Equation). The research integrates Geographic Information Systems (GIS) data and field observations, focusing on these factors. The investigation seeks to identify areas susceptible to erosion, with particular attention to the urban gully in Miguel Alves Municipality, and to provide a foundation for developing mitigation strategies.

2. Materials and methods

2.1. Study area

The area of the downstream Parnaíba River in Piauí State is a strip of land that lies parallel to the Parnaíba River. It begins in Teresina City and stretches to the confluence of the Sub-basin of the Longá River in Buriti dos Lopes Municipality.

This area covers a strip of land that extends from the city of Teresina to the river's mouth in the Atlantic Ocean. However, considering the dynamic differences between the coastal and continental zones, a new spatial delimitation was defined. This delimitation includes only the sub-basins located on the continental perimeter of the region, resulting in an area of approximately 6075.48 km^2. The area lies between the geodetic coordinates 5°1′20.06″ S/42°50′43.95″ W and 3°7′41.42″ S/41°55′32.98″ W, as shown in **Figure 1** [1,21].

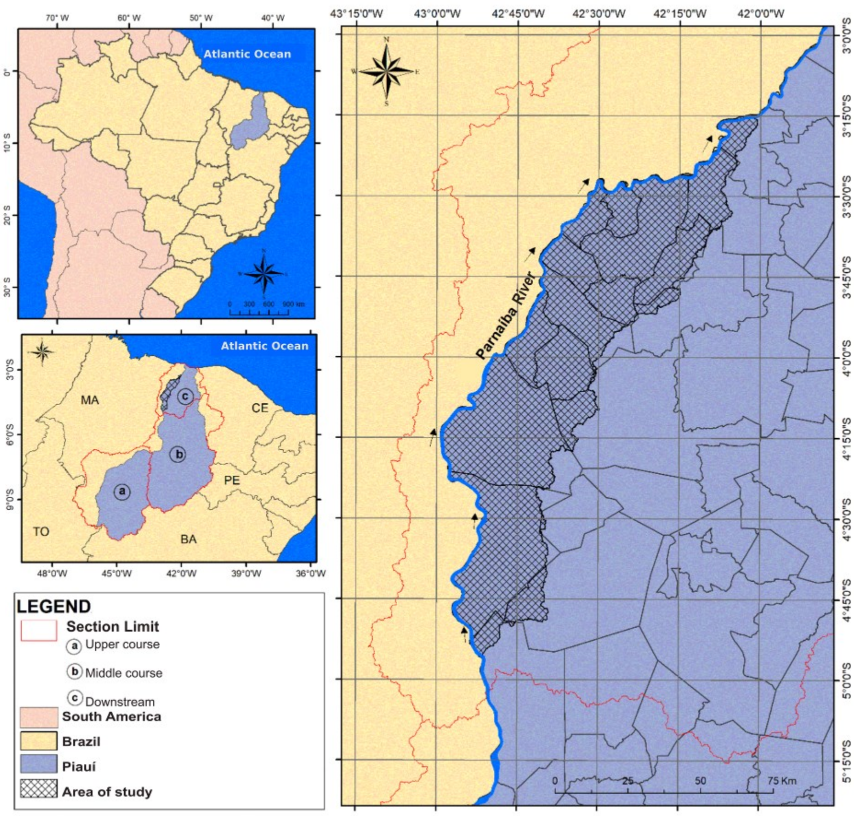

Figure 1. Multiscale view of the Parnaíba River watershed location in the northwest of Piauí State-Brazil.

The dataset for this study was sourced from the United States Geological Survey (USGS). Precipitation data, initially compiled in 2020, were later updated through the HidroWeb platform, which is part of the National Water Resources Information System administered by the National Water Agency (ANA) [22].

The evaluation of soil erosion focused on the *K* factor (soil erodibility) and the R factor (rainfall erosivity) from the Revised Universal Soil Loss Equation (RUSLE), which were critical in determining erosion risk across the study area:

a) Drainage data were obtained from ANA's digital cartographic database [23].

b) The vector cartographic base of soils, in shapefile format, was obtained from the INDE-National Spatial Data Infrastructure website, with the original scale of 1:250,000, and associated with the soil profile information contained in the exploratory soil survey of Piauí State.

c) Erosivity was calculated based on the collection of monthly and annual rainfall data from the Brazilian Rain Atlas (1:5,000,000 scale) between 1977 and 2006 and updated through ANA's HidroWeb tool, corresponding to basin 3−Atlantic, North, and Northeast.

d) Rainfall data from rain gauge stations were obtained from previous studies [22,24], including the Brazilian Rain Atlas. For this study, data from eight stations were used.

2.2. Calculation of RUSLE factors

The *R* (rainfall erosivity) and *K* (soil erodibility) factors were calculated according to the appropriate equations, taking into account the influence of extreme rainfall events on soil erosion in the Baixo Parnaíba basin.

2.3. Soil erodibility (*K* factor)

The *K* factor represents soil erodibility, which is a measure of the soil's susceptibility to erosion under the influence of water. Erodibility is defined by the soil's resistance to dispersive forces, splashing, abrasion, and the transport of soil particles by water, as well as by considering infiltration rate, permeability, and water retention capacity in the soil [2,25,26].

The *K* value can be determined through laboratory methods or empirical estimates, using tables that correlate soil characteristics with *K* values. Despite the limitations in obtaining the *K* factor, various researchers have developed experiments to make this factor applicable to different types of Brazilian soils [4,27–29]. In this research, we opted to adopt the soil erodibility factors available in the literature, considering the soil classes of the Parnaíba River Basin.

The *K* factor data were sourced from the work of Aquino and Oliveira [28], which provided a comprehensive approach to calculating the weighted average soil erodibility for associations in Piauí State. This method involved selecting representative soil profiles by comparing soil descriptions with those outlined in previous studies [30].

Erodibility for each profile was computed based on its specific characteristics and contribution to the soil associations. The *K* values were then averaged arithmetically for each soil type, and a weighted average was calculated, factoring in the proportion of each soil within the association. The erodibility classes were subsequently adapted from the classification system proposed in a previous study [26], as presented in **Table 1**.

Table 1. Soil erodibility (*K*) factor classification [26].

Classification of Soils Based on Erodibility Factor (*K*)	
Propensity to erodibility	(ton.ha.h/ha. MJ.mm)
Very low	< 0.009
Low	0.009–0.015
Medium	0.015–0.30
High	0.30–0.045
Very high	0.045–0.060
Extremely high	> 0.060

2.4. Rainfall erosivity factor (*R* factor)

The *R* factor represents rainfall erosivity, which is a measure of the erosive potential of precipitation in a specific area. Erosivity depends on the characteristics of rainfall, and the *R* factor can be calculated using historical precipitation data, considering the energy and impact of rainfall events. The calculation methodology typically involves the following steps:

a) Collection of precipitation data

Precipitation data were gathered from meteorological stations in the Baixo Parnaíba basin region. These values were estimated based on approximately 30 years of precipitation history, which was used to identify cyclical rainfall patterns [22,31]. According to some authors, around 80% of soil loss is influenced by this factor [32].

b) Calculation of erosivity

To calculate the *R* factor (erosivity), the equation (E2) of Wischmeier and Smith [31] was used, adapted to Brazilian natural conditions [25]

$$R = \sum_{i=1}^{12} \quad 67.355\left(\frac{r_i^2}{P}\right)^{0.85} \tag{1}$$

In the equation, *R* represents rainfall erosivity (MJ mm h^{-1} ha^{-1} $year^{-1}$), *r* is the average monthly total precipitation (mm), and *P* corresponds to the average annual total precipitation (mm). These values were obtained from rainfall data collected from meteorological stations. Rainfall erosivity was then calculated for each station, and the data were interpolated using the Inverse Distance Weighted (IDW) method from the ArcGIS Spatial Analyst Tools.

2.5. Validation

Considering the vast area studied (6075.48 km^2) and the scarcity of erosion plots across the region, a careful approach was adopted in the selection and use of available data. Establishing experimental erosion plots in the lower Parnaíba River basin would be logistically difficult and impractical.

Therefore, alternative validation approaches were used in place of direct experimental data. These included comparisons with field observations and historical data, assessments of internal consistency, cross-referencing with findings from previous studies, and analysis of the sensitivity of results to changes in model parameters.

3. Results and discussion

The results indicated that the impact of extreme rainfall events is greatly intensified by the physical characteristics of the soil in the watershed of the Parnaíba River. The combination of high erosivity and highly erodible soils creates a favorable scenario for the formation of gullies and rills, especially in areas under human interventions.

3.1. Rainfall erosivity (factor *R*) and erosion risk

Erosivity-*R*

The rainfall erosivity analysis for the Parnaíba River watershed revealed an average value of 9051.52 MJ mm h^{-1} ha^{-1} $year^{-1}$, with a standard deviation of 148.33, highlighting the significant erosive potential in the region. These results are consistent with those reported for the Longá River basin, a tributary of the Parnaíba, where critical values ranged from 8865 to 9540 MJ mm h^{-1} ha^{-1} $year^{-1}$ [5]. Specifically, in the downstream area of the Parnaíba River, the R factor ranged from 7943.46 to 10,081.61 MJ mm h^{-1} ha^{-1} $year^{-1}$, with erosivity intensity classified from medium to very strong, as shown in **Table 2**.

Table 2. Interpretation of rainfall erosivity.

Range (MJ mm h^{-1} ha^{-1} $year^{-1}$)	Interpretation of Erosivity
$R < 6000$	Very weak
$6000 > R < 7500$	Weak
$7500 > R < 8500$	Average
$8500 > R < 9000$	Strong
$R > 9000$	Very Strong

Source: Adapted from Morais and Silva [5].

The spatial distribution map of the *R* factor, shown in **Figure 2**, illustrates the significant spatial variability of rainfall. Data linked to individual rainfall measurements monitored by both automatic and conventional stations in Piauí State [22] emphasize that the highest annual rainfall volumes in the state are concentrated in the northern and northwestern regions, where values exceed 1500 mm.

From February to August are the rainiest months, supporting the high *R* values found in this research. In the study area, precipitation values ranged approximately from 1279 to 1710 mm [3].

Similar to studies conducted in other arid and semi-arid regions [16] in northwest Somalia, rainfall erosivity strongly influences soil erosion risk. In Somalia, areas with lower annual rainfall showed low erosivity, while those with moderate rainfall exhibited moderate erosivity. This contrast with the more humid Parnaíba basin emphasizes how local rainfall patterns shape erosion risks, underscoring the need for region-specific monitoring and soil conservation strategies.

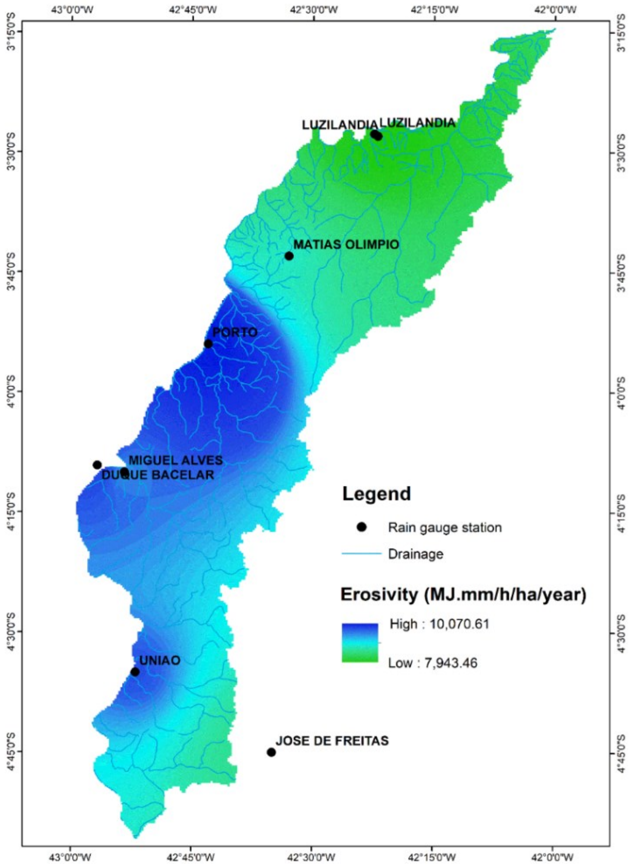

Figure 2. Map illustrating the distribution of rainfall erosivity (*R*).

The analysis of monthly rainfall variations at the rain gauge stations in the study area reveals distinct seasonal trends, as illustrated in **Figure 3**. The dry season, occurring from July to November, is characterized by reduced rainfall, while the wet season, spanning from January to March, experiences significantly higher precipitation levels. This seasonal pattern is vital for identifying periods of increased vulnerability to erosion [2,3,33] During the dry season, the lack of rainfall diminishes the soil's ability to absorb runoff, contributing to soil compaction and degradation. Consequently, when the rains return, the soil becomes more susceptible to erosion.

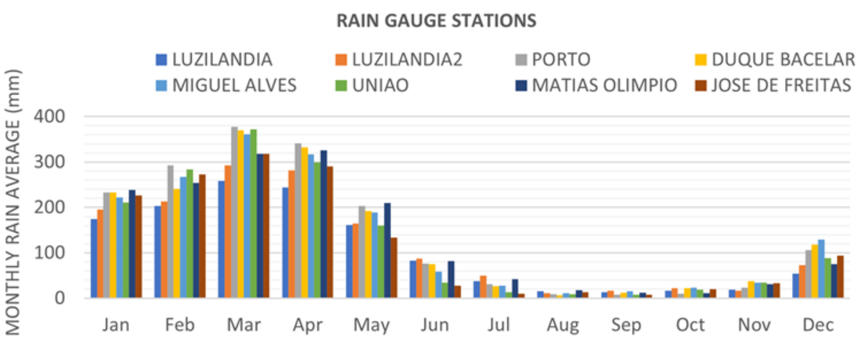

Figure 3. Monthly variation of precipitation from the rain gauge stations in the study area [3].

Figure 4 shows a strong correlation between erosivity (factor *R*) and average annual precipitation, with both parameters closely aligned and relatively stable throughout the year despite monthly fluctuations. This relationship is crucial for assessing erosion risk and developing effective soil erosion prevention strategies.

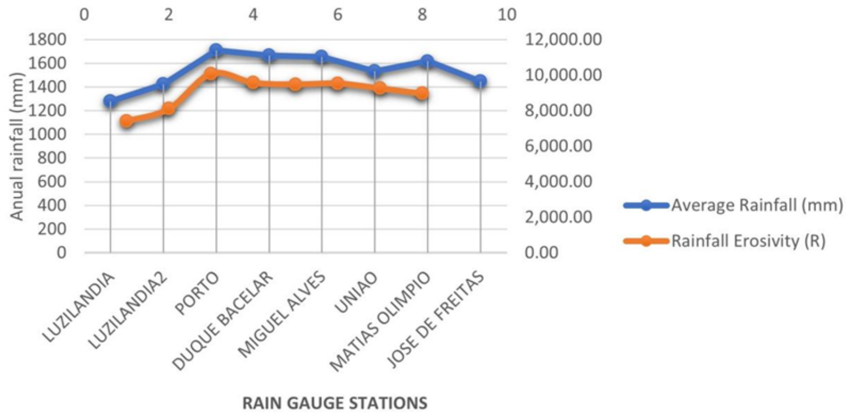

Figure 4. Relationship between erosivity (factor *R*) and average annual precipitation [3].

3.2. Soil erodibility (factor *K*)

The soils in the region, primarily characterized as Argissols and Chernozem, exhibited high erodibility. The most vulnerable areas were identified in regions where the soils are sandier and less cohesive. The combination of these characteristics with the high erosivity of rainfall intensified erosive processes, leading to the formation of features such as ravines and gullies.

The combination of rainfall with high erosivity and fragile, unprotected soils promotes the onset of erosive processes. **Table 3** presents the soil classes found in the area of the Diffuse Basins of Baixo Parnaíba, along with their erodibility values, associated with the extent occupied by each class within the basin.

Table 3. Soil classification based on the soil erodibility factor (*K*) in the study area, northwest Piauí, Brazilian Cerrado.

Soil Unit	Soil Taxonomy	Erodibility Classes	Area (ha)	Area (%)	K Factor ton.ha.h/ha. MJ.mm
A1	ENTISOLS (FLUVENTS)	Medium	38,805.56	5.97%	0.028
A4		High			0.032
BV1	MOLLISOLS	Very high	16,559.63	2.55%	0.05
LA10	OXISOLS	Medium	74,811.94	11.50%	0.025
LA11		Medium			0.028
LA13		Medium			0.028
LA5		High			0.035
LA8		High			0.037
LA9		High			0.035

Table 3. (*Continued*).

Soil Unit	Soil Taxonomy	Erodibility Classes	Area (ha)	Area (%)	K Factor ton.ha.h/ha. MJ.mm
PE10	ALFISOLS	High	49,729.27	7.65%	0.031
PE11		High			0.036
PE9		Very high			0.043
PL3	ULTISOLS	High	25,019.50	3.85%	0.039
PT1	ULTISOLS (PLINTHICS)	Medium	108,837.6	16.73%	0.027
PT12		Very high			0.047
PT3		High			0.038
PT9		High			0.037
PV10	ULTISOLS	High	269,956.7	41.51%	0.031
PV11		High			0.039
PV12		High			0.036
PV13		High			0.037
PV14		Medium			0.03
PV20		Very high			0.042
R1	ENTISOLS (LITHICS)	High	43,476.21	6.68%	0.041
R2					
*	WATER	*	23,011.33	3.54%	*
*	ISLAND	*	2104.23	0.03%	*
Total			650,418.13	100%	*

Source: Organized by the Authors; based on Mannigel et al. [26], Aquino and Oliveira [28], Jacomine and Paulo Klinger Tito Jacomine [30]; (*) no value assigned.

The spatialization of factor *K* can be visualized in **Figure 5**. The soil erodibility values (factor *K*) ranged from 0.025 to 0.050 t h MJ^{-1} mm^{-1}, with a predominance of medium to very high erodibility, according to studies conducted in the region [28].

The Alfisols class comprises 7.65% of the total area, accounting for 49,729.27 hectares. This class shows notable variability in erodibility, with high *K* factor values ranging from 0.031 to 0.036 t h MJ^{-1} mm^{-1} and instances of very high erodibility reaching up to 0.043 t h MJ^{-1} mm^{-1}. These soils are predominantly found in relatively flat to undulating terrains, with slopes between 3% and 20%, which makes them particularly susceptible to erosive processes.

In contrast, the study area does not contain soils classified with low erodibility. The medium erodibility class presents the lowest *K* factor values, with Entisols (Fluvents) showing a *K* factor of 0.028 t h MJ^{-1} mm^{-1} and occupying 5.97% of the area. Other soil classes with very high erodibility include Mollisols, covering 2.55% of the area with a K factor of 0.050.

Another notable soil class is the Oxisols, accounting for 11.50% of the area. These soils exhibit *K* factor values ranging from 0.025 to 0.035 t h MJ^{-1} mm^{-1}. The topography of the area characterized by wide, gentle hills, dissected plateaus, and degraded flat surfaces, directly influences the erosive processes affecting these soils.

Overall, while Alfisols are prominent, they are part of a broader spectrum of soil erodibility in the region, including significant contributions from Ultisols with *K* factor values reaching up to 0.047 t h MJ^{-1} mm^{-1} and occupying 41.51% of the area.

This diverse soil composition underscores the varying susceptibility to erosion throughout the study area.

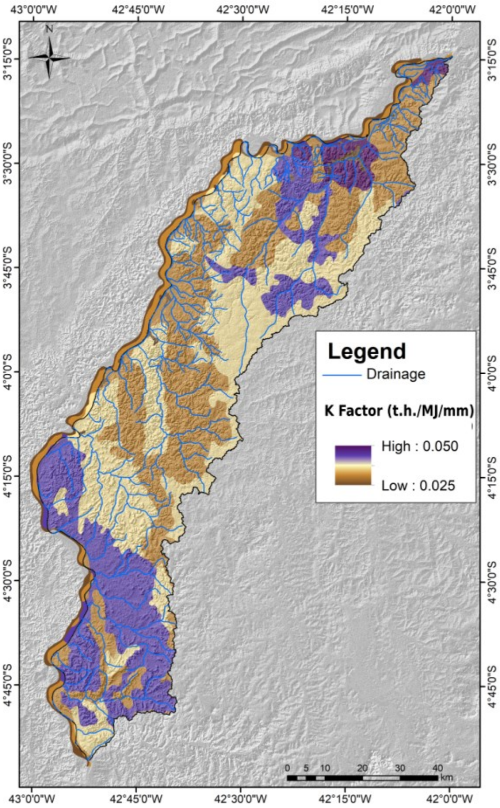

Figure 5. Spatialization of factor *K*.

As shown in **Figure 5** and **Table 3**, there is a predominance of *K* values classified as high and very high erodibility in the study area. This is consistent with previous studies [28] that concluded that about 94.4% of the soils in Piauí State have high or very high erodibility.

Granulometric analyses were carried out to determine the soil textural classes, and although the number of samples analyzed was limited, this analysis is crucial for accurately characterizing the soils in the region. **Figure 6** illustrates the variations in coarse sand, fine sand, silt, and clay fractions across eight strategically selected sites within the study area, offering a detailed insight into the soil textures.

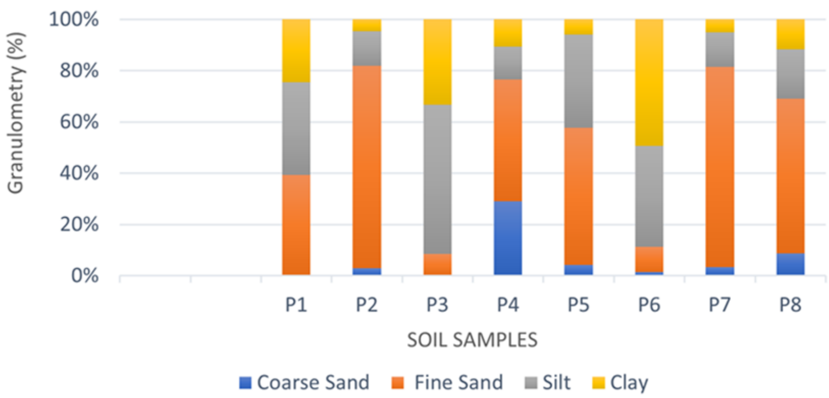

Figure 6. Variation of soil particles in the study area [3].

Erosive features

After analyzing the soil erodibility factors (*K*) and rainfall erosivity (*R*), it is observed that the conditions conducive to erosive processes manifest in various erosive features in the study area. These features, commonly associated with the combined action of rainfall events, vegetation clearing, topographical characteristics, and improper land use, are widely distributed in both urban and rural areas.

Figure 7 illustrates some of these erosive features. In rural areas of the União Municipality, the presence of a gully (**Figure 7A**) reflects the impacts of erosion, reinforcing the need for appropriate conservation practices.

The gully (**Figure 7B**), located in the urban periphery of the municipality of Miguel Alves, was triggered by the natural dynamics of the environment; however, factors such as deforestation, soil compaction, and improper land use may have intensified its development. Additionally, the consequences of improper land use can be observed in features such as rill erosion (**Figure 7C**), generated by the construction of highways in the municipality of União, highlighting soil vulnerability when exposed to human intervention without adequate containment measures.

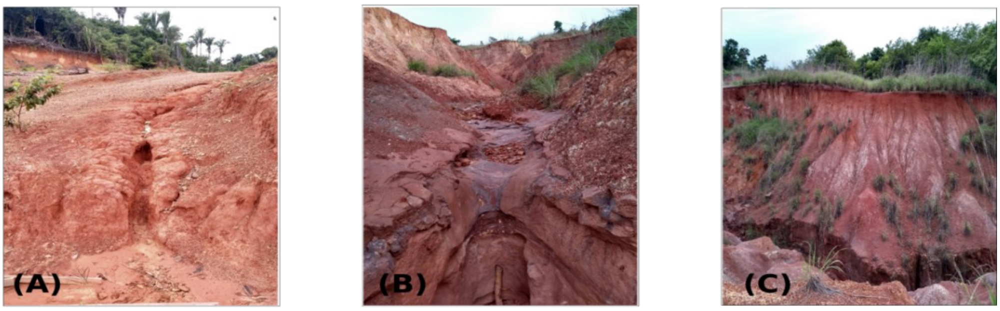

Figure 7. Erosive features found in the study area: **(A)** rills located in the municipality of União; **(B)** gully located in the municipality of Miguel Alves; **(C)** rills located in the municipality of União.

The analysis of the urban gully in Miguel Alves Municipality demonstrated an accelerated growth of 21.85% between 2007 and 2017, a direct result of the combination of erosive rains and erodible soils [34]. The advancement of the gully poses a risk to local infrastructure, especially highways and adjacent urban areas.

The lack of adequate erosion control measures has contributed to this rapid expansion, and the climatic conditions forecasted for the coming years suggest that, without intervention, the gully will continue to expand [35]. In **Figure 8**, it is possible to see the area of growth of the gully.

Figure 8. Area of growth of the gully [34].

4. Conclusion

The study demonstrates that the downstream Parnaíba River Basin presents a high risk of erosion due to the combination of climatic and pedological factors. The erosivity of rainfall, concentrated in the months of highest precipitation, acts as a catalyst for erosive processes, especially in areas with highly erodible soils. The expansion of the gully in Miguel Alves Municipality exemplifies the potential risks that extreme rainfall can bring, particularly when combined with vulnerable soils and the absence of mitigation measures.

The results obtained provide important insights for formulating soil management policies and implementing conservation techniques to mitigate erosion in the Lower Parnaíba Basin. It is essential that erosion control measures, such as revegetation and surface runoff management, be adopted to prevent the worsening of erosion problems and protect both infrastructure and the local environment.

Author contributions: Conceptualization, WCdSB; AJTG and IMdMFL; methodology, WCdSB, AJTG and IMdMFL; validation, WCdSB; formal analysis, WCdSB; investigation, WCdSB, AJTG and IMdMFL; resources, WCdSB, AJTG and IMdMFL; data curation, WCdSB; writing—original draft preparation, WCdSB; writing—review and editing, WCdSB and AJTG; visualization, WCdSB; supervision, AJTG and IMdMFL; funding acquisition, WCdSB. All authors have read and agreed to the published version of the manuscript.

Conflict of interest: The authors declare no conflict of interest.

References

1. Abreu LP, Mutti PR, Lima KC. Spatial and temporal variability of precipitation in the Parnaíba River basin, Northeast Brazil (Portuguese). Revista Brasileira de Meio Ambiente; 2019.
2. Guerra AJT, Fullen MA, Jorg MCO, et al. Slope Processes, Mass Movement and Soil Erosion: A Review. Pedosphere. 2017; 27 (1), 27-41. doi: 10.1016/S1002-0160(17)60294-7

3. Barbosa WCS, Guerra AJT, Valladares GS. Soil Erosion Modeling Using the Revised Universal Soil Loss Equation and a Geographic Information System in a Watershed in the Northeastern Brazilian Cerrado. Geosciences. 2024; 14(3): 78. doi: 10.3390/geosciences14030078
4. Morais RCS, Sales MCL. Estimating the natural soil erosion potential of the Alto Gurguéia watershed, Piauí-Brazil, using a Geographic Information System. (Portuguese). Caderno de Geografia; 2017.
5. Morais RCS, Silva AJO. Estimating the Natural Potential for Soil Erosion in the Longá River Basin, Piauí, Brazil. (Portuguese). Revista Geotemas; 2020.
6. Alves WS, Martins AP, Morais WA, et al. USLE modelling of soil loss in a Brazilian cerrado catchment. Remote Sensing Applications: Society and Environment. 2022; 27: 100788. doi: 10.1016/j.rsase.2022.100788
7. Dang X, Sun Y. Estimation of soil erosion in loess plateau based on geographic information system. Journal of Geography and Cartography. 2021; 5(1): 1. doi: 10.24294/jgc.v5i1.1410
8. Silva AMD, Silva MLN, Curi N, et al. Rainfall erosivity and erodibility of Cambissolo and Latossolo in the Lavras region, southern Minas Gerais. (Portuguese). Revista Brasileira de Ciência do Solo. 2009; 33(6): 1811-1820. doi: 10.1590/s0100-06832009000600029
9. Bonilla CA, Johnson OI. Soil erodibility mapping and its correlation with soil properties in Central Chile. Geoderma. 2012; 189-190: 116-123. doi: 10.1016/j.geoderma.2012.05.005
10. Guerra AJT, Fullen MA, Bezerra JFR, Jorge MCO. Gully Erosion and Land Degradation in Brazil: A Case Study from São Luís Municipality, Maranhão State. Cingapura: Springer Singapore; 2018.
11. Favis-Mortlock D. Erosion by Water: Accelerated. Managing Soils and Terrestrial Systems; 2020.
12. Barbosa WCS, Lima IMMF, Guerra AJT. Study of soil erosion in a gully located in the municipality of Miguel Alves-Piauí/Brazil, based on soil density and porosity parameters. (Portuguese). In: Pereira R, Cachada A, Rodríguez-Seijo A, et al. (editors). Solos e Desenvolvimento Sustentável: Desafios e Soluções, 1st ed. Porto: GreenUPorto-Centro de Investigação em Produção Agroalimentar Sustentável, U.Porto Press; 2021.
13. Delgado D, Sadaoui M, Ludwig W, et al. Depth of the pedological profile as a conditioning factor of soil erodibility (Rusle K-Factor) in Ecuadorian basins. Environmental Earth Sciences. 2023; 82(12). doi: 10.1007/s12665-023-10944-w
14. Freires EV, Silva Neto CÂ, Silva MT, et al. Mapping the erosivity and erodibility of the humid slope of the Uruburetama Massif and its surroundings as a subsidy to environmental planning. (Portuguese). Revista de Geociências do Nordeste. 2023; 9(2): 21-40. doi: 10.21680/2447-3359.2023v9n2id30719
15. Andriyani I, Indarto I, Soekarno S, et al. Analysis of rainfall erosivity factor (R) on prediction of erosion yield using USLE and RUSLE Model's; A case study in Mayang Watershed, Jember Regency, Indonesia. Sains Tanah-Journal of Soil Science and Agroclimatology. 2024; 21(1): 64. doi: 10.20961/stjssa.v21i1.63641
16. Nur AH, Ahmed AH, Mohamed AA,et al. Geospatial Assessment of Aridity and Erosivity Indices in Northwest Somalia Using The CORINE Model. Journal of Environmental and Science Education. 2024.
17. Fullen MA, Catt JA. Soil Management: Problems and Solutions. Edward Arnold, Londres; 2004.
18. Moisa MB, Dejene IN, Merga BB, et al. Soil loss estimation and prioritization using geographic information systems and the RUSLE model: a case study of the Anger River sub-basin, Western Ethiopia. Journal of Water and Climate Change. 2022; 13(3): 1170-1184. doi: 10.2166/wcc.2022.433
19. Amraoui M, Bouabidi L, El Amrani M, et al. Land Use Dynamics And Soil Conservation Strategies In The El Kssiba Region, Atlas Mountains Of Morocco. The Journal "Agriculture and Forestry". 2024; 70(3). doi: 10.17707/agricultforest.70.3.01
20. Ennaji N, Ouakhir H, Abahrour M, et al. Impact of watershed management practices on vegetation, land use changes, and soil erosion in River Basins of the Atlas, Morocco. Notulae Botanicae Horti Agrobotanici Cluj-Napoca. 2024; 52(1): 13567. doi: 10.15835/nbha52113567
21. MMA, Ministério do Meio Ambiente. Parnaíba Hydrographic Region Booklet. (Portuguese). Secretaria de Recursos Hídricos-Brasília: MMA; 2006.
22. Nascimento JRS, Marcuzzo FFN, Pinto EJA. Maps of annual and monthly rainfall distribution and pluviogram of the Parnaíba river basin. (Portuguese). ABRH; 2020.
23. HidroWeb. Historical rainfall series. (Portuguese). Available online: https://www.snirh.gov.br/hidroweb/ (accessed on 12 July 2023).
24. Pinto EJA, Azambuja, AD, Farias JAM, et al. Rainfall atlas of Brazil: monthly isopleths, quarterly isopleths, annual isopleths, driest months, wettest months, driest quarters, wettest quarters. (Portuguese). Brasília: CPRM; 2011.

25. Bertone J, Lombardi Neto F. Soil Conservation (Portuguese). Icone Editora Ltda: São Paulo; 2014.
26. Mannigel AR, E Carvalho MDP, Moreti D, et al. Erodibility factor and soil loss tolerance in the State of São Paulo. (Portuguese). Acta Scientiarum Agronomy. 2008; 24: 1335. doi: 10.4025/actasciagron.v24i0.2374
27. Albuquerque AW, M. Filho G, Santos JR, et al. Determination of universal soil loss equation factors in Sumé, PB. (Portuguese). Revista Brasileira de Engenharia Agrícola e Ambiental. 2005; 9(2): 153-160. doi: 10.1590/s1415-43662005000200001
28. Aquino CMS, Oliveira JGB. Estimating the erodibility factor (k) of soil associations in the state of Piauí described in Jacomine (Portuguese). Revista Geotemas; 2017.
29. Farinasso M, Carvalho Júnior OA, Guimarães RF, et al. Qualitative Evaluation of the Potential for Laminar Erosion in Large Areas by Means of the EUPS Universal Soil Loss Equation Using New GIS Methodologies for Calculating its Factors in the Alto Parnaíba PI-MA Region. (Portuguese). Revista Brasileira de Geomorfologia. 2006; 7(2). doi: 10.20502/rbg.v7i2.80
30. Jacomine PKT, Paulo Klinger Tito Jacomine, C. Exploratory and reconnaissance survey of soils in the state of Piauí. (Portuguese). Embrapa Solos; 1986.
31. Wischmeier WH, Smith DD. Predicting Rainfall Erosion Losses: A Guide to Conservation Planning. Department of Agriculture, Science and Education Administration. 1978.
32. Renard KG, Freimund JR. Using monthly precipitation data to estimate the R-factor in the revised USLE. Journal of Hydrology. 1994.
33. Loureiro HAS, Guerra AJT. Landscapes of Geomorphology: Themes and Concepts of the 21st Century. (Portuguese). Rio de Janeiro: Bertrand Brasil; 2022.
34. Barbosa WCS, Lima IMMF, Guerra AJT. Multivariate analysis of the urban gully located in the southern portion of the Lower Parnaíba River basin. (Portuguese). William Morris Davis- Revista de Geomorfologia; 2021.
35. Tesfaye G, Bekele D, Eshetu M, et al. Gully Erosion Risk Assessment Using a GIS-Based Bivariate Statistical Models and Machine Learning in the Dodota Alem Watershed, Ethiopia. American Journal of Environmental Science and Engineering. 2024; 8(3): 49-64. doi: 10.11648/j.ajese.20240803.11

Journal of Geography and Cartography 2024, 7(2), 10193.
https://doi.org/10.24294/jgc10193

Article

Application of geophysical methods in subsurface mapping and mineral exploration: Adiyaman-Besni region, Türkiye

Cihan Yalçın[1,*], **Ali Karan**[2]

[1] Department of Exploration, GMK Energy, Aydın 09010, Türkiye
[2] MESED Madencilik Inşaat ltd. Şti, Mersin 33000, Türkiye
*** Corresponding author:** Cihan Yalçın, cihan.yalcin@sanayi.gov.tr

CITATION

Yalçın C, Karan A. Application of geophysical methods in subsurface mapping and mineral exploration: Adiyaman-Besni region, Türkiye. Journal of Geography and Cartography. 2024; 7(2): 10193. https://doi.org/10.24294/jgc10193

ARTICLE INFO

Received: 8 November 2024
Accepted: 4 December 2024
Available online: 13 December 2024

Abstract: The present study aimed to delineate subsurface features and identify prospective metallic mineral deposits in the Adıyaman-Besni area, situated within the Southeastern Anatolian Thrust Belt of Turkey. This region, characterized by ophiolitic mélanges and volcanic massive sulfide (VMS) deposits in its geological framework, possesses significant mineralization potential, encompassing copper, lead, and various other sulfide minerals. Utilizing the combined methodologies of Induced Polarization (IP) and Electrical Resistivity Tomography (ERT), a comprehensive electrical mapping of the subsurface structures was conducted, revealing that mineralized zones had low resistivity and high chargeability. The findings indicate that the combined use of IP and ERT techniques yields excellent precision in accurately delineating the features of sulfide mineralization and the peripheries of mineral deposits. This study offers fundamental data for the economic assessment of prospective mineral deposits in the Adıyaman-Besni region and underscores the benefits of IP and ERT techniques in subsurface mapping and mineralization delineation investigations. The mineralized zone has low resistivity (< 50 ohm-m) and strong chargeability (> 30 ms), according to geophysical tests. It also offers a methodological framework for subsequent mineral exploration research in analogous geological formations.

Keywords: subsurface mapping; induced polarization; electrical resistivity tomography; metallic mineralization; Adıyaman-Besni

1. Introduction

The Adıyaman-Besni region, situated in southeastern Turkey, possesses significant potential for metallic mineral resources. The geological framework, particularly the ophiolitic mélanges in the area, provides a conducive environment to produce metallic mineral deposits, including copper, lead, and zinc [1,2]. The investigation and mapping of metallic mineral resources have become increasingly precise and effective due to advancements in contemporary geophysical techniques. Geophysical techniques, including Induced Polarization (IP) and Electrical Resistivity Tomography (ERT), have proven useful for subterranean imaging of metallic minerals [3,4].

Subsurface mapping is crucial, particularly for the search for metallic minerals. IP and ERT techniques yield a comprehensive representation by utilizing the electrical characteristics of subterranean formations and mineral deposits. The IP approach demonstrates excellent efficiency, particularly in regions with sulfide mineralization, and produces anomalies based on the polarization characteristics of metallic minerals [5,6]. The ERT method is essential for ascertaining the depth, width, and extent of mineral deposits by delineating the electrical resistivity distribution of subterranean formations. The integration of these methodologies facilitates a more accurate definition of metallic ore deposit limits [7,8].

Currently, the application of integrated geophysical techniques in subsurface mapping and mineral prospecting is well acknowledged in scholarly literature. Yalçın and Canlı [5] performed comprehensive research employing IP and ERT techniques to identify Pb-Zn deposits in the Sudöşeği region of Turkey. The research indicated that low resistivity and elevated chargeability values are crucial for Pb-Zn mineralization, and the combined application of both methods ensures excellent precision [5]. In a study by Andi et al. [6] in Sumatra, IP and ERT techniques were effectively utilized to ascertain the distribution of gold mineralization in the subsurface [6].

Cyprus-type volcanogenic massive sulphide (VMS) deposits and ophiolitic complexes in Turkey facilitate the production of metallic mineral deposits, particularly in areas like Adıyaman-Besni. The Adıyaman-Besni region is situated on the Southeastern Anatolian Thrust Belt and is notable for its sulphide mineralization concentrated in geological formations like the Koçali Complex [1]. A comprehensive examination of copper and other metallic minerals in the region by geophysical methods is essential for the effective and secure extraction of prospective mineral resources. The Adıyaman-Besni region possesses significant potential for subterranean resources. The geological structure of the region offers favorable environments, especially for the formation of metallic mineral deposits. This study intends to delineate and examine the metallic mineral resources in the region comprehensively by Electrical Resistivity Tomography (ERT) and Induced Polarisation (IP) techniques. These technologies offer efficient instruments for detecting mineralized zones using the electrical characteristics of subterranean formations.

The present study intends to delineate prospective metallic mineral deposits in the Adıyaman-Besni area utilizing IP and ERT methodologies. The geophysical data gathered throughout the investigation offers a comprehensive analysis to ascertain the position, depth, and extent of the mineral deposits inside the ophiolitic mélange in the region. The results will enhance the economic and geological assessment of metallic mineral reserves in the area.

2. Materials and methods

The research was conducted in the Adıyaman-Besni area, situated in the Southeastern Anatolia Region of Turkey. The study area encompasses roughly 5 km^2 and is situated in a location characterized by the prominent exposure of the Koçali Ophiolite Complex. The study region is situated between 37°39′ N latitude and 41°75′ E longitude, signifying a geographical location where ophiolitic rocks are recognized to have metallic mineral resources.

Geophysical measurements were conducted along 23 profiles within the research area. The profiles’ positions and orientations were strategically established to encompass the whole study region. The geological map and mineralization potential of the region constituted the foundation for the assessment of the ERT and IP data. A more compact profile architecture was designed in regions with significant mineralization potential. The geographical coordinates of the profiles utilized in the study region are shown in **Table 1**, enabling the analysis of geophysical data in connection to subsurface structures. The region contains a geological structure that is both topographically complicated and appropriate for metallic mineral deposits.

2.1. Geological background

The Adıyaman-Besni region is situated within the Southeastern Anatolian Thrust Belt of Turkey and contains Cyprus-type volcano massive sulfide (VMS) deposits along this belt. The primary geological units in the region comprise intricate formations, including the Upper Cretaceous ophiolitic mélange, Koçali Complex, and Gölbaşı Formation [1,9]. **Figure 1** illustrates that these geological units contain strata abundant in metallic mineralization, highlighting their significance as regions with copper, lead, and zinc deposits [10,11].

The ophiolitic mélange in the region predominantly consists of ultramafic and mafic rocks, typically located in zones of significant tectonic activity. **Figure 1** illustrates that mineralization zones within the ophiolitic mélange signify regions enriched in metallic minerals [3]. These formations were elevated to the surface by intricate tectonic processes and provide considerable potential for mineralization [6].

The Koçali Complex is a significant geological unit where mineralization processes in the area are focused. This complex contains formations composed of basaltic and gabbroic rocks, along with veins exhibiting sulfide mineralization. Research indicates that these mineralizations encompass significant minerals, including iron sulfide (pyrite), copper sulfide (chalcopyrite), and zinc sulfide (sphalerite) [12,13]. These formations are essential for groundwater circulation and mineralization processes.

The Adıyaman-Besni region, influenced by the Southeastern Anatolian Thrust Belt, has experienced alterations in the chemical composition and mineral content of its rocks due to high pressure and temperature conditions resulting from continental collision. This scenario has established an optimal environment for sulfide mineralization, and comprehending the geological structure is crucial for the efficacy of mineral exploration studies.

The metallic mineral reserves in Adıyaman province are intricately linked to the region's geological structure. Mineralization in the study area is predominantly associated with the diabase and quartz veins within the Koçali Ophiolite Complex. The Koçali Ophiolite Complex comprises tectonites, cumulates, a plate dyke complex, pillow lavas, and deep-sea deposits [14]. These formations were influenced by hydrothermal activities that created an advantageous environment for the circulation and deposition of metallic minerals.

Diabase veins and dykes in the region (ophiolitic mélange) are crucial for mineralization, serving as conduits for hydrothermal fluids and containing sulfide minerals like pyrite, chalcopyrite, and sphalerite. Quartz veins are also significant, containing copper, lead, and zinc due to hydrothermal alteration processes. Fault and fracture systems direct the circulation and accumulation of metallic minerals, controlling the localization of sulfide mineralization, particularly in the ophiolitic complex. The low resistivity and high chargeability values associated with these structures strongly support the presence of metallic mineral deposits.

2.2. Geophysical study

Geophysical measurements were conducted along 23 profiles in the Adıyaman-Besni region. Each profile is 410 m in length and was conducted using the dipole-dipole measuring technique. Forty-two electrodes were utilized in the profiles, with an electrode spacing of 10 m and a profile spacing of 50 m. The AGI (Advanced Geosciences Inc.) SuperSting R8 instrument utilized in these measurements efficiently gathered both resistivity (ERT) and Induced Polarization (IP) data. The acquired data were reviewed in EartImager 2D software to build 2D cross-sections and then examined in accordance with the geological structures.

This study employed Induced Polarization (IP) and Electrical Resistivity Tomography (ERT) techniques to delineate probable metallic mineral deposits in the Adıyaman-Besni region. These techniques utilize the electrical characteristics of subterranean formations to ascertain the depth, thickness, and extent of mineral deposits [4,8]. Mineralized zones were identified based on low resistivity (< 50 ohm-m) and high chargeability (> 30 ms). Resistivity values varied from 15 to 30 ohm-m, with chargeability exceeding 30 ms in mineral-rich locations.

ERT and IP measurements were conducted at several places during the fieldwork. **Figure 1** delineates the ophiolitic mélange and mineralization zones within the research area. ERT measurements identified mineralized zones by analyzing the resistivity distribution of subsurface structures, whereas IP measurements supplied data to ascertain mineral density based on chargeability attributes. **Figures 2** and **3** illustrate the configuration of the equipment utilized during the fieldwork and the data collection procedure.

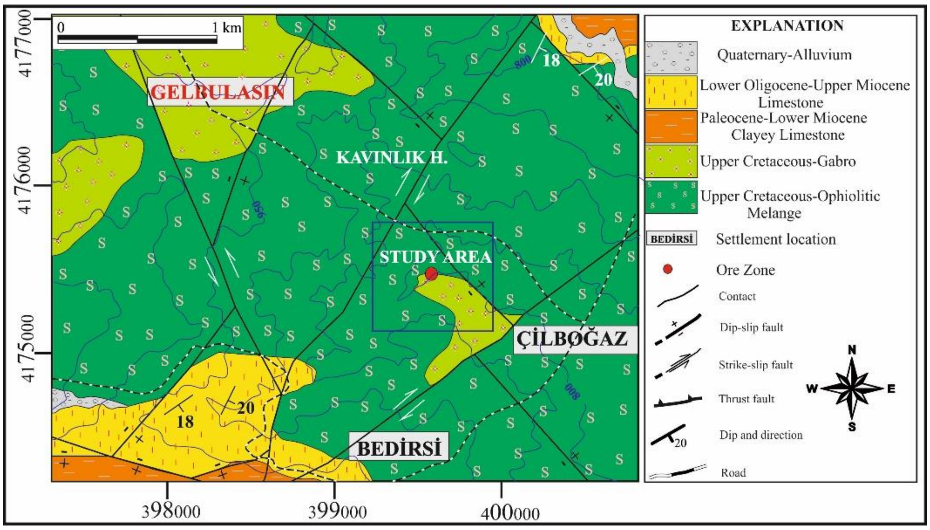

Figure 1. Geological map of the study area (modified from [14]).

Figure 2. General view of the study area and ore zone.

Installation of geophysical equipment and identification of measurement spots utilized during field research in the Adıyaman-Besni region.

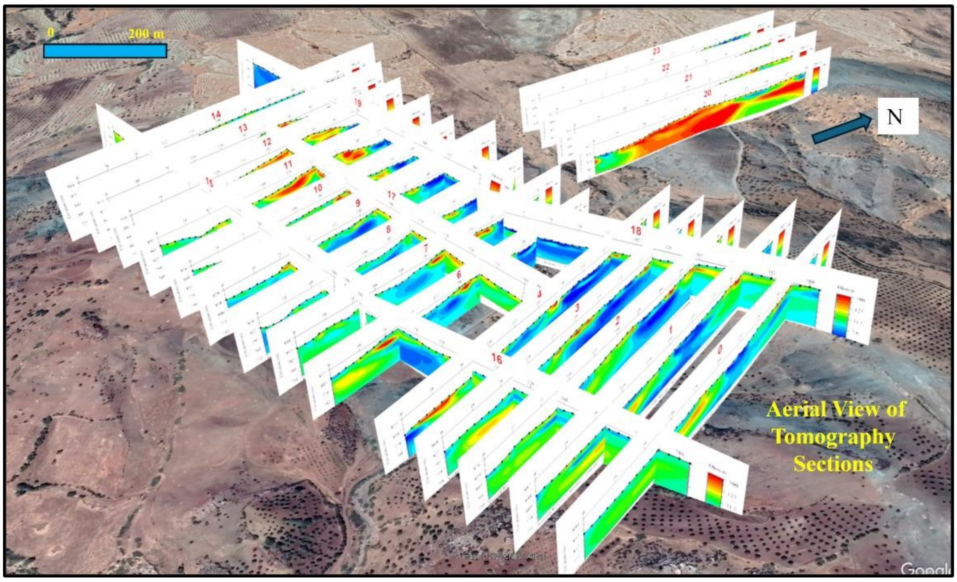

Figure 3. Profiles of Induced Polarization (IP) and Electrical Resistivity Tomography (ERT) measurements in the Adıyaman-Besni region.

The gathered IP and ERT data were analyzed utilizing a unique inverse solution algorithm, resulting in 2D cross-sections for each profile. These cross-sections illustrate the distribution, depths, and widths of subterranean metallic mineral deposits. The results were evaluated by examining the mineralization zones depicted in **Figure 1** [15,16].

ERT data facilitates the comprehension of the structural attributes of mineral deposits by measuring the electrical resistivity of subterranean formations, whereas IP data is employed to identify sulfide mineralization. The data are represented in 2D cross-sections in **Figures 4** and **5**, where elevated chargeability and diminished resistivity values designate mineralization zones [7,17].

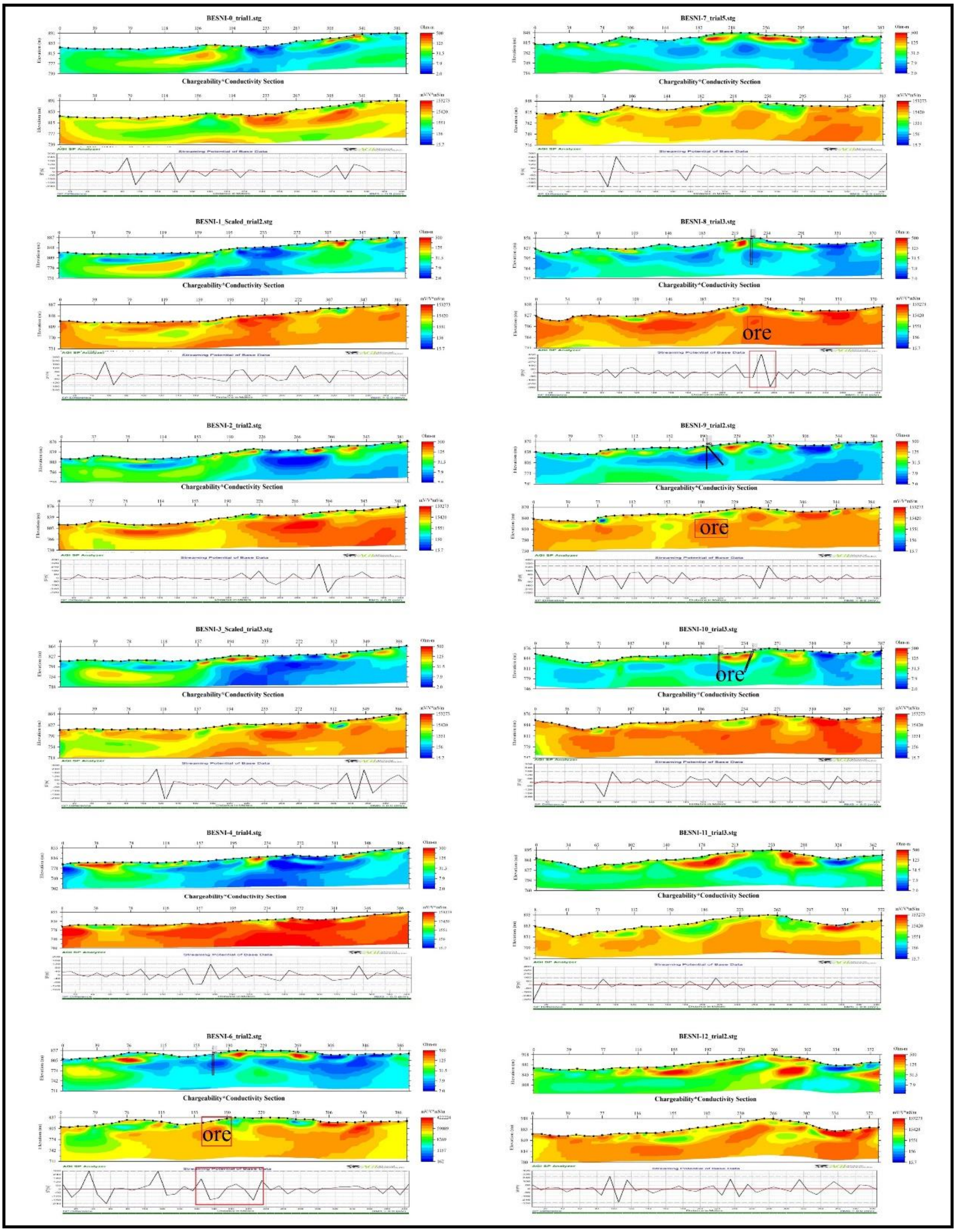

Figure 4. Two-dimensional cross-sectional image derived from Induced Polarization and Electrical Resistivity Tomography data in the Adıyaman-Besni region.

The illustration depicts low resistivity and high chargeability anomalies, signifying metallic and sulphide mineralization, specifically copper and lead, together with distinct structural characteristics.

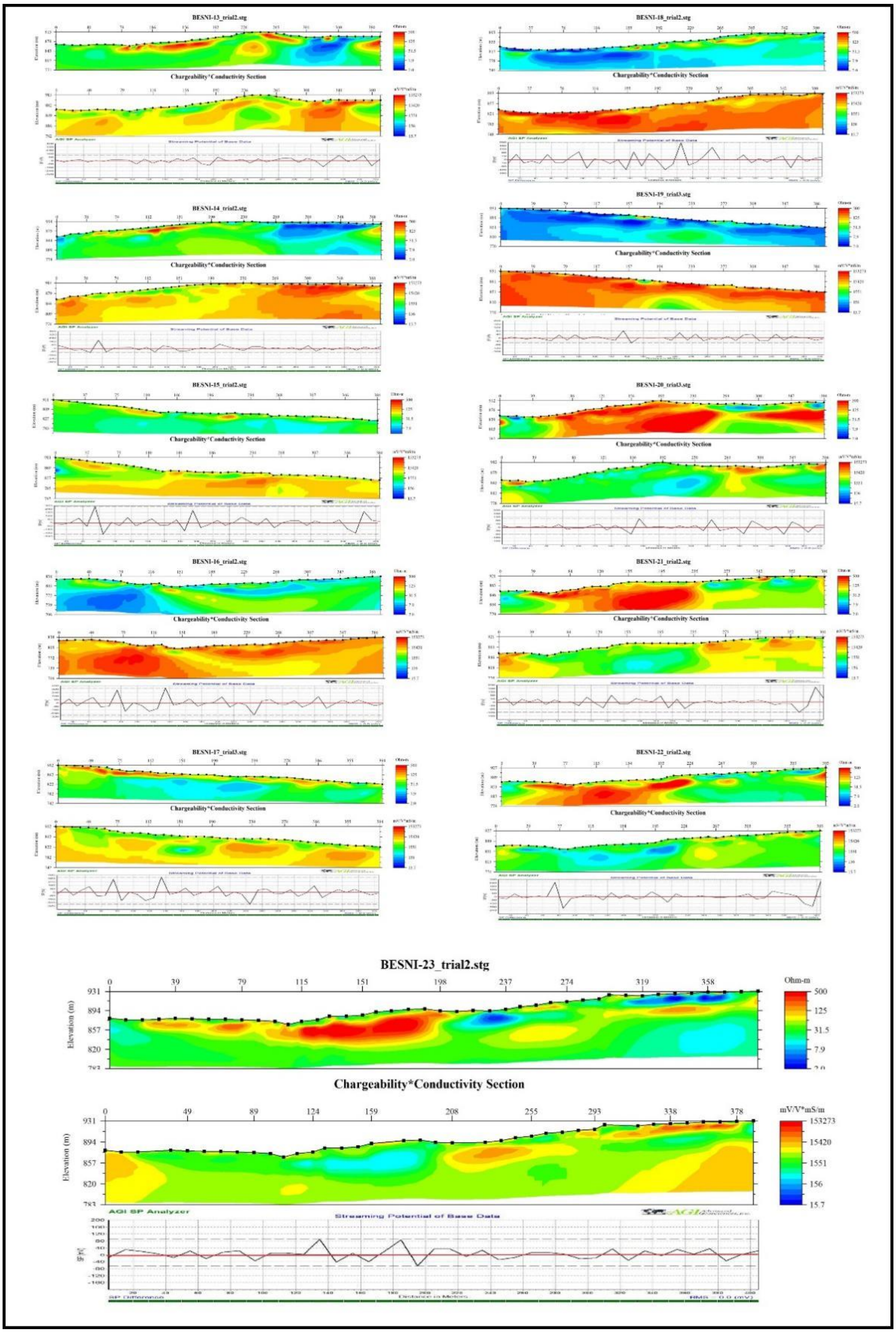

Figure 5. Two-dimensional cross-sectional image derived from Induced Polarization and Electrical Resistivity Tomography data in the Adıyaman-Besni region.

The integration of IP and ERT techniques offers considerable benefits, particularly in identifying sulphide-rich mineral resources like copper and lead. The combined application of these technologies yields more comprehensive and dependable information regarding subterranean structures and enhances the precision of mineral exploration in the Adıyaman-Besni area.

This study encompassed geophysical data across 23 profiles utilizing resistivity, Induced Polarization, and spontaneous potential techniques. The lines measured 410 m in length and utilized an AGI brand 8-channel equipment. EartImager 2D software facilitated resistivity and Induced Polarization measurements, whilst SPAnalyzer software assessed self-potential measurements. The data was examined as two-dimensional subsurface sections and modeled in three dimensions to yield a comprehensive mapping of the geological features in the area.

Table 1 presents the initial and final coordinates of the measurement profiles. These coordinates indicate the positioning and measurement configuration of each profile. The examination of the measurements involved optimizing the ground contact resistance of each electrode to reduce the Root mean square (RMS) error values. This led to enhanced data accuracy. All measurements were analyzed with EartImager 2D software, and the precision and dependability of the results were meticulously assessed.

Table 1. Profile coordinate chart.

Profile	Beginning/End	Latitude	Longitude
Profile 0	1. Electrode	37 399777 E	4175843 N
	42. Electrode	37 399618 E	4176202 N
Profile 1	1. Electrode	37 399728 E	4175831 N
	42. Electrode	37 399571 E	4176190 N
Profile 2	1. Electrode	37 399681 E	4175810 N
	42. Electrode	37 399527 E	4176164 N
Profile 3	1. Electrode	37 399632 E	4175800 N
	42. Electrode	37 399480 E	4176149 N
Profile 4	1. Electrode	37 399584 E	4175780 N
	42. Electrode	37 399426 E	4176140 N
Profile 6	1. Electrode	37 399491 E	4175743 N
	42. Electrode	37 399337 E	4176087 N
Profile 7	1. Electrode	37 399444 E	4175724 N
	42. Electrode	37 399289 E	4176075 N
Profile 8	1. Electrode	37 399397 E	4175700 N
	42. Electrode	37 399247 E	4176041 N
Profile 9	1. Electrode	37 399352 E	4175680 N
	42. Electrode	37 399194 E	4176033 N
Profile 10	1. Electrode	37 399309 E	4175653 N
	42. Electrode	37 399160 E	4175984 N
Profile 11	1. Electrode	37 399263 E	4175633 N
	42. Electrode	37 399110 E	4175966 N
Profile 12	1. Electrode	37 399215 E	4175615 N
	42. Electrode	37 399079 E	4175950 N
Profile 13	1. Electrode	37 399167 E	4175597 N
	42. Electrode	37 399027 E	4175943 N

Table 1. (*Continued*).

Profile	Beginning/End	Latitude	Longitude
Profile 14	1. Electrode	37 399123 E	4175573 N
	42. Electrode	37 398975 E	4175934 N
Profile 15	1. Electrode	37 399024 E	4175621 N
	42. Electrode	37 399376 E	4175782 N
Profile 16	1. Electrode	37 399410 E	4175805 N
	42. Electrode	37 399767 E	4175946 N
Profile 17	1. Electrode	37 399121 E	4175801 K
	42. Electrode	37 399451 E	4175962 N
Profile 18	1. Electrode	37 399316 E	4176011 N
	42. Electrode	37 399670 E	4176165 N
Profile 19	1. Electrode	37 398912 E	4175821 N
	42. Electrode	37 399263 E	4176001 N
Profile 20	1. Electrode	37 399217 E	4176202 N
	42. Electrode	37 399215 E	4176568 N
Profile 21	1. Electrode	37 399166 E	4176202 N
	42. Electrode	37 399159 E	4176587 N
Profile 22	1. Electrode	37 399116 E	4176198 N
	42. Electrode	37 399113 E	4176585 N
Profile 23	1. Electrode	37 399064 E	4176205 N
	42. Electrode	37 399060 E	4176588 N

IP data can signify the presence of sulfide minerals (e.g., pyrite, chalcopyrite), particularly when chargeability levels are elevated. However, this technique alone is not sufficient to unambiguously identify mineral species. The acquired data serves as an effective instrument for pinpointing regions of metallic mineral concentration; however, geochemical investigations are necessary for the accurate identification of mineral kinds. The correlation between mineralization and specific lithological units indicates a potentially elevated sulfide concentration in these regions.

Resistivity measurements were evaluated to ascertain the existence of mineralized zones. Metallic minerals were recognized for their low resistivity values attributable to their strong conductivity. The mineralized zones observed in the study typically exhibit values between 2 ohm-m and 31.5 ohm-m.

IP data is essential for identifying the existence of sulfide minerals. Chargeability values of 30 ms were observed in regions with significant mineralization. These values were important in delineating the limits of mineralized zones based on geological data.

Self-potential (SP) measurements used as an adjunct tool to detect structural alterations and non-mineralized regions. In particular, SP data supplied supportive information for the identification of fractures and fault zones in the subsurface.

3. Results

Results from ERT and IP measurements in the Adıyaman-Besni area elucidate the distribution and depth configuration of metallic mineralization in the region. **Figures 4** and **5** depict 2D cross sections that illustrate the subsurface electrical characteristics of the mineral deposits in the area, indicating regions of low resistivity and high chargeability. These characteristics are crucial for identifying metallic deposits that signify sulfide mineralization. The zones were identified by their low resistivity (usually between 15 ohm-m and 31.5 ohm-m) and high chargeability (greater than 30 ms). These values agree with sulfide-rich mineralization.

Uncertainty analysis was conducted throughout the modeling of ERT and IP data, and the precision of all models was assessed using Root Mean Square (RMS) error rates. All RMS values were maintained below 5% in the study of 23 profiles. Especially in the profiles where mineralized zones were discovered, RMS error rates were computed as follows: Profile 6: 3.8%, Profile 8: 4.2%, Profile 10: 4.0%, Profile 10: 4.0%. These values demonstrate the reliability of the modeling procedures and confirm that the data provide an accurate depiction of subsurface structures. The minimal error rates facilitated a more accurate determination of the borders of mineralized zones in the subsurface.

The computed tomography sections depicted in **Figures 4** and **5** reveal specific regions that exhibit abnormalities characterized by elevated chargeability and reduced resistance. The anomalies are scattered throughout the ophiolitic mélange, with metallic mineral occurrences situated according to the prevailing geological structure. The acquired data indicate that mineralization in the region is predominantly oriented in a specific direction from the surface to the depths [3]. **Figure 5** delineates the limits of the mineralized zones with precision. Elevated resistivity values (> 30 ms) derived from IP measurements signify areas of significant sulfide mineralization. The zones, along with low resistivity values (< 50 ohm-m), strongly indicate the possible occurrence of sulfide mineralization in the study area.

An in-depth investigation of the data indicated that the mineral deposits in the region typically display low resistivity and high chargeability traits, which are directly associated with the structural properties of the ophiolitic mélange in the area. Furthermore, these mineralization zones are delineated on the surface, as evidenced by the images captured in the field shown in **Figure 3**, and the correlation between the geophysical data and surface observations is noteworthy.

The geophysical measurement findings revealed mineralized zones in the studied area. On the sixth profile, a mineralized zone was discovered at a depth of around 80 m in the area beneath electrode 19. Mineralization was discovered on the eighth profile at a depth of around 80 m below electrode 27. At a depth of 80 m–100 m along the 9th profile, two distinct mineralized zones, one angled 60° N and the other vertical, were discovered between electrodes 21 and 22. Similarly, on profile 10, a vertical mineralized zone was detected below electrode 23 at a depth of 80 m–100 m, and another mineralized zone was identified below electrode 27 at a depth of 80 m–100 m, orientated 70° S.

These mineralized zones are often linked to the diabase and quartz veins of the Koçali Ophiolite Complex. The geophysical findings are compatible with geological investigations in the area and provide valuable information about the position and depth of the mineralization. These discoveries in the research region serve as the foundation for recommended drilling locations, allowing for a thorough analysis of prospective metallic mineral resources.

4. Discussion

The present study meticulously mapped metallic mineral deposits in the Adıyaman-Besni region utilizing Induced Polarization (IP) and Electrical Resistivity Tomography (ERT) techniques. The results indicated that sulphide mineralization in the region is localized in zones of low resistivity and high chargeability. The findings reveal notable similarities and some discrepancies when juxtaposed with analogous geological features in Turkey and other worldwide studies. The results corroborate the occurrence of low-resistivity (15 ohm-m–30 ohm-m) and high-chargeability zones (> 30 ms), which are indicative of sulfide mineralization. These anomalies are consistent with the geological environment and anticipated properties of metallic mineral deposits.

4.1. Comparison with studies in Türkiye

Cyprus-type volcanic massive sulphide (VMS) deposits in Turkey are linked to ophiolitic complexes, especially along the Southeastern Anatolian Thrust Belt [10]. Yalçın and Canlı [5] employed IP and ERT techniques to examine Pb-Zn deposits in the Sudöşeği and Küre areas, demonstrating that low resistivity and high chargeability anomalies are characteristic of these deposits. Likewise, mineralization in the Adıyaman-Besni area is correlated with ophiolitic mélange, aligning with other VMS deposits in Turkey.

The research of Akyıldız and Yıldırım [1] provided a detailed analysis of the metallic mineral deposits in the Koçali complex, revealing that their geological properties are analogous to other mineralizations in Southeastern Anatolia. The identification of metallic mineral deposits in intricate formations like the Koçali Complex is enhanced with the application of IP and ERT techniques. The results of this investigation enhance the precision of the findings by demonstrating geological commonalities and analogous anomalies with other places, including the Koçali Complex and Sudöşeği.

4.2. Comparison with global research

Research investigations worldwide demonstrate that IP and ERT technologies are efficiently employed in the exploration of metallic mineral resources. Al-Fares et al. [3] employed IP and ERT techniques to identify metallic mineral deposits in ophiolitic complexes in the Middle East, demonstrating that elevated chargeability and diminished resistivity values indicate the presence of metallic sulfide minerals. This study aligns with the findings in the Adıyaman-Besni region and validates that IP and ERT methods are universally applicable for identifying mineral deposits in ophiolitic mélange.

A research by Shirazy et al. [2] on copper deposits in Iran demonstrated that anomaly data acquired by IP and ERT methods serve as optimal markers for identifying sulfide mineralization. This study aligns with the findings in the Adıyaman-Besni region and corroborates that IP and ERT methods yield excellent precision in ascertaining the depth, width, and density of metallic mineral deposits.

4.3. Effectiveness of IP and ERT techniques in various geological contexts

The IP and ERT technologies have been effectively utilized in mineral discovery across various geological environments globally, not solely restricted to ophiolitic complexes. Su et al. [15] shown in China that regions with low resistivity and high chargeability, found by IP and ERT approaches, serve as significant markers of metallic mineralization. This work is significant for identifying analogous geophysical signatures across diverse geological contexts, in contrast to the mineralization observed in the Adıyaman-Besni region.

Furthermore, the gold exploration research by Liu et al. [17] in the Sumatra region of Indonesia utilized high-resolution data from the combined application of IP and ERT technologies, facilitating precise mapping of metallic mineral resources. The findings of this study align with mineral exploration research in the Adıyaman-Besni region, demonstrating that IP and ERT technologies yield comprehensive insights into subsurface structures.

4.4. Comparability and divergences with other research in Turkey and globally

Comparable research in Turkey and globally demonstrates that IP and ERT methodologies are efficacious instruments for the exploration of metallic mineral resources. Nonetheless, owing to the distinctive geological attributes of each region, certain disparities have also been noted. In the study conducted by Al Hakim et al. [18] on gold mineralization in Indonesia, low sulfidation epithermal gold deposits display a distinct geophysical signature compared to VMS deposits in Turkey. The disparity arises from the mineralogical diversity of subsurface structures, indicating that the efficacy of IP and ERT approaches may change according to mineral kinds.

The alignment of findings in the Adıyaman-Besni region with other VMS deposits in Turkey and elsewhere enhances the credibility of this study and reinforces the overall validity of the results. Moreover, the combined use of IP and ERT methodologies establishes a framework for forthcoming research in Turkey and other nations. The integration of these methodologies with precise data gathering, inverse solution algorithms, and comprehensive analysis enhances the accuracy of mineral exploration studies [16].

The results of the Adıyaman-Besni investigation largely correspond with Martínez et al. [19], who utilized IP and ERT techniques to delineate galena-rich veins in southwestern Spain. The investigation successfully identified low-resistivity and high-chargeability zones, which corresponded with areas of significant mineralization, akin to our findings in Adıyaman, where probable sulfide mineralizations had comparable geophysical signatures [19]. Yalçın and Canlı [20] in Yahyalı, Turkey, illustrated the effectiveness of IP and resistivity methods in evaluating carbonate-hosted Pb-Zn deposits, emphasizing the role of geophysical surveys in elucidating the geometry and extent of mineralization, even in intricate geological environments. Moreover, Yalçın et al. [21] illustrated the efficacy of these techniques in the Kavşut region, where integrated Induced Polarization and resistivity investigations effectively identified Cu-Pb-Zn polymetallic deposits linked to fractured and karstic formations in carbonate settings. Our research in Adıyaman corroborates these findings by affirming the effectiveness of IP and ERT methodologies for comprehensive subsurface mapping, especially in orogenic and structurally intricate environments prevalent in southeastern Turkey and elsewhere [20,21].

The geophysical data collected throughout the investigation gave valuable insights into the location and geological context of possible metallic mineral deposits in the area. Low resistivity and high chargeability values highlighted significant mineralization zones, which were then connected with structural aspects of the Koçali Ophiolite Complex. Mineralized zones were found to have low resistivity (< 50 ohm-m) and high chargeability (> 30 ms) values, indicating sulphide mineralization.

Mineralization in the studied area was found to be primarily associated with diabase and quartz veins. This is compatible with the geophysical results, which show low resistivity and high chargeability values. In particular, the link between the mineralized zones discovered along profiles 9 and 10 and geological units gives strong indication that these areas represent possible mineralization zones.

The IP cross sections illustrated in **Figure 5** were useful in delineating the limits of the mineralized zones within the study area. The simultaneous occurrence of elevated chargeability (> 30 ms) and low resistivity (< 50 ohm-m) data suggests the possible existence of sulfide mineralization. The data provide essential insights into the depth, width, and strike extent of the mineralized zones.

Nevertheless, IP data merely indicate the presence of metallic minerals. While elevated chargeability readings may correlate with sulfide minerals such as pyrite and chalcopyrite, geochemical investigation is essential to ascertain the specific kind of these minerals. In the study, IP data served as an effective instrument to ascertain the overarching properties of mineralization; nevertheless, a definitive classification of mineral kinds was not established.

The findings in the Adıyaman-Besni region align with analogous geological structures and mineral deposits in Turkey and globally, indicating that IP and ERT methods serve as effective tools for identifying metallic mineralization. This study's methodologies offer a comprehensive delineation of prospective metallic mineral deposits in the Adıyaman-Besni region, serving as a reference for future extensive geophysical investigations.

5. Conclusion

This study seeks to examine the prospective metallic mineral deposits in the Adıyaman-Besni region by geophysical methods and provides a comprehensive mapping of the subsurface structure utilizing Induced Polarization (IP) and Electrical

Resistivity Tomography (ERT) techniques. The findings indicate that mineralization in the region is localized in zones of low resistivity and high chargeability, signifying the existence of sulfide mineralization and metallic minerals.

The study assessed the distribution and density of metallic minerals, including copper and lead deposits, particularly inside the ophiolitic mélange. Comparisons with other VMS deposits in Turkey, including Sudöşeği and Küre, validate the findings in the Adıyaman-Besni region and demonstrate the efficacy of IP and ERT technologies in exploring such deposits. Moreover, when juxtaposed with other global investigations, these methodologies have demonstrated considerable precision in delineating the borders and depth configurations of mineral deposits.

The findings of this study indicate that the synergistic application of IP and ERT methodologies provides a significant benefit in the comprehensive mapping of metallic mineral deposits. The technologies utilized in the Adıyaman-Besni region offer a geophysical comprehension of the subsurface structure and the requisite information for the economic extraction of metallic mineral deposits in the area. The research establishes a systematic framework for forthcoming geophysical explorations in other areas with prospective mineral resources, including Adıyaman-Besni.

Future research should incorporate supplementary geophysical techniques, such as Magnetotellurics (MT), to examine deeper structures. The incorporation of sophisticated approaches will enhance the accuracy and thoroughness of the evaluation of existing mineral resources and provide a more dependable assessment of the metallic mineral potential in the Adıyaman-Besni region.

Author contributions: Conceptualization, CY and AK; methodology, CY; software, CY; validation, CY, and AK; formal analysis, CY; investigation, AK; resources, AK; data curation, CY; writing—original draft preparation, CY; writing—review and editing, CY; visualization, CY; supervision, CY; project administration, CY; funding acquisition, AK. All authors have read and agreed to the published version of the manuscript.

Acknowledgments: We express my gratitude to MESED MADENCİLİK İNŞAAT LTD. ŞTİ. Staffs.

Conflict of interest: The authors declare no conflict of interest.

References

1. Yıldırım A, Akyıldız A. The geology, geochemistry, and genetical features of the Ormanbaşı copper deposit in the Koçali complex, Adıyaman. J. Earth. Sci. 2014; 25(4): 45–59. doi: 10.1016/j.jesc.2014.07.011
2. Shirazy F, Alipour A, Mirjafari SA. The origin of vein-type copper-lead-zinc mineralization in the Central Iran Ophiolite Complex. Geochem Explore. 2022; 135(3): 201–215. doi: 10.1016/j.gexplo.2022.04.007
3. Al-Fares F, Hashim M, Salih A. Characterization of metallic mineralization using integrated IP and ERT techniques in ophiolitic complexes of the Middle East. Int. J. Geosci. 2023; 14(7): 77–88. doi: 10.4236/ijg.2023.147007
4. Pellicer X, Gibson DA. Application of resistivity and IP methods for sulfide mineral exploration: A review of techniques and case studies. Prog. Geophys. 2011; 56(2): 187–202. doi: 10.1016/j.pgeoph.2011.04.014
5. Yalçın C, Canlı H. Detection of Pb-Zn mineralization using IP and ERT methods in Sudöşeği, Turkey. Geol. Surv. J. 2024; 29(1): 32–44. doi: 10.1016/j.geosj.2024.01.005

6. Andi A, Sudirjo A, Puspita D. Application of IP and ERT in gold mineralization mapping: A Sumatra case study. J. Gold. Explor. 2024; 18(2): 51–63. doi: 10.1080/14680303.2024.115237
7. Sanusi A, Hassan Z, Noor M. Identifying mineralization zones using IP and ERT in West Africa. Afr. J. Geophys. Res. 2024; 11(2): 61–74. doi: 10.1080/00378909.2024.090678
8. Farias L, Godoy R, Sánchez A. Mineral deposit boundary definition using IP and ERT: Insights from South American case studies. South Am. Min. J. 2023; 27(1): 42–54. doi: 10.1080/00349909.2023.112987
9. Haritha B. Application of magnetic and IP methods for identifying subsurface copper mineralization. Geosci. Tech. J. 2023; 31(7): 543–557. doi: 10.1016/j.gstj.2023.03.015
10. Görhan O, Yıldız K. Metallic mineral deposits and structural analysis in the Southeastern Anatolian Thrust Belt. Turk. Geol. Rev. 2023; 13(4): 289–308. doi: 10.1080/12345678.2023.101112
11. Al-Hameedawi AH, Thabit R. Integration of geophysical and geochemical methods for copper exploration in Turkey. J. Min. Explor. 2017; 25(3): 88–99. doi: 10.1080/1876827.2017.101234
12. Loke MH, Barker R. 3D resistivity and IP inversion: An advanced methodology for mineral exploration. Geophys. Methods. 2021; 48(6): 563–575. doi: 10.1029/rgm2021.01.048
13. Shirazy F, Taheri S, Akbari E. IP and ERT data inversion techniques for complex mineral deposits in Iran. J. Inverse. Prob. 2022; 18(4): 270–285. doi: 10.1007/s12518-022-02456
14. MTA. Geology map M39 C1 1/25.000 in scale. MTA; 2020.
15. Su W, Liu C, Zhang H. Sulfide mineral exploration using geophysical imaging techniques in complex terrains of China. Geophys. Res. J. 2024; 29(5): 95–110. doi: 10.1016/j.grj.2024.04.003
16. Gurin Y, Vlasov A, Kochergin A. Advanced IP and ERT imaging techniques for subsurface mineral identification. J. Min. Sci. 2023; 59(3): 98–105. doi: 10.1007/s12517-023-11645
17. Liu X, Prasetyo D, Nasution R. High-resolution mineral mapping using IP and ERT for gold exploration in Sumatra, Indonesia. Geophys. Explor. 2024; 31(8): 115–128. doi: 10.1016/j.geophys.2024.02.022
18. Al Hakim H, Setiawan M, Triyana Y. Epithermal gold deposits mapping in Indonesia using integrated geophysical approaches. Miner. Explor. Rev. 2024; 12(3): 120–135. doi: 10.1016/j.mer.2024.04.008
19. Martínez J, Ruíz A, Delgado C. Exploring galena-rich veins using IP and ERT methods in southwestern Spain. J. Appl. Geophys. 2019; 92: 101–112. doi: 10.1016/j.jappgeo.2019.03.002
20. Yalçın C, Canlı H. Exploration of the carbonate-hosted Pb-Zn deposit via using IP/Resistivity and ground penetrating radar (GPR) methods in Yahyalı (Kayseri-Türkiye). Advanced Engineering Science. 2023; 3: 125–136.
21. Yalçın C, Canlı H, Haznedaroğlu K, Akbulut F. Exploration of the Cu-Pb-Zn deposit via using IP/Resistivity methods in Kavşut (Göksun-Kahramanmaraş). Advanced Engineering Science. 2023; 3: 151–163.

Journal of Geography and Cartography 2024, 7(2), 9183.
https://doi.org/10.24294/jgc9183

Article

Assessing drought risk conditions through SPI and NDVI indices in Oued Kert watershed

Zahar Elkheir Alioua*, Abdelhamid Mezrhab, Mohammed Laaboudi, Ali Achebour, Wadii Snaibi, Mohammed Sahil, Said Elyagoubi, Mohammed Melhaoui

Geographic Information Technologies and Space Management (ETIGGE), Communication, Education, Digital Usage and Creativity Lab, Faculty of Letters and Human Sciences, Mohamed First University, Oujda 60000, Morocco
*** Corresponding author:** Alioua Zahar Elkheir, zaharelkheir.alioua.d24@ump.ac.ma

CITATION

Alioua ZE, Mezrhab A, Laaboudi M, et al. Assessing drought risk conditions through SPI and NDVI indices in Oued Kert watershed. Journal of Geography and Cartography. 2024; 7(2): 9183. https://doi.org/10.24294/jgc9183

ARTICLE INFO

Received: 18 September 2024
Accepted: 7 November 2024
Available online: 23 December 2024

Abstract: The Oued Kert watershed in Morocco is essential for local biodiversity and agriculture, yet it faces significant challenges due to meteorological drought. This research addresses an urgent issue by aiming to understand the impacts of drought on vegetation, which is crucial for food security and water resource management. Despite previous studies on drought, there are significant gaps, including a lack of specific analyses on the seasonal effects of drought on vegetation in this under-researched region, as well as insufficient use of appropriate analytical tools to evaluate these relationships. We utilized the Standardized Precipitation Index (SPI) and the Normalized Difference Vegetation Index (NDVI) to analyze the relationship between precipitation and vegetation health. Our results reveal a very strong correlation between SPI and NDVI in spring (98%) and summer (97%), while correlations in winter and autumn are weaker (66% and 55%). These findings can guide policymakers in developing appropriate strategies and contribute to crop planning and land management. Furthermore, this study could serve as a foundation for awareness and education initiatives on the sustainable management of water and land resources, thereby enhancing the resilience of local ecosystems in the face of environmental challenges.

Keywords: meteorological drought; Normalized Difference Vegetation Index (NDVI); Oued Kert watershed; Standardized Precipitation Index (SPI)

1. Introduction

Meteorological drought is characterized by a significant decrease in precipitation compared to the historical average, thus affecting the normal functioning of local ecosystems and the growth of living organisms [1]. This gradual phenomenon develops over an extended period and its impacts are diffuse, slowly spreading through the environment, affecting many countries around the world, particularly those located in arid or semi-arid regions like Morocco.

Oued Kert watershed is notably impacted by this phenomenon due to its vulnerability to climate fluctuations and its socio-economic importance to local populations. This region has experienced significant climate variations over the decades, exacerbated by the effects of climate change. Rising temperatures and changes in precipitation patterns have intensified arid conditions, making water resource management even more critical.

In the 1990s, several studies were conducted to examine the links between water access and development. These studies include those carried out by organizations such as the World Water Council, the Global Water Partnership, the World Panel on Water Infrastructure Financing, and during the Third World Water Forum in Kyoto [2–5].

The conclusions of these studies highlighted a marked sensitivity to changes in hydrological regimes, an increase in water resource scarcity, and emphasized the threats to water availability and management [6].

The primary aim of this study is to evaluate drought risk conditions in the Oued Kert watershed using the Standardized Precipitation Index (SPI) and the Normalized Difference Vegetation Index (NDVI). We selected these two indicators due to their complementary ability to provide insights into hydrological conditions and vegetation health. In particular, the study of the correlation between precipitation patterns and vegetation dynamics throughout the seasons highlights the influence of climatic variability on vegetation. The SPI allows us to analyze precipitation variations and detect periods of drought, while the NDVI assesses the health and coverage of vegetation. By correlating these two indices, we aim to illustrate how climatic variations affect the response of vegetation in the region. These indices are particularly relevant for several reasons:

(1) Identification of dry and wet episodes: These tools enable the rapid detection of climatic condition variations, which is essential for proactive management of water resources and ecosystems.
(2) Analysis of spatial and temporal variations: The indices provide a dynamic perspective, allowing for the evaluation of how drought and humidity evolve over time and vary across regions, thus offering crucial information for environmental planning.
(3) Interpretation of ecological dynamics: By linking climatic data to vegetation health, these indices facilitate the understanding of the complex interactions between climate, vegetation, and other ecosystem components, which is fundamental for ecological research.
(4) Support for decision-making: The results derived from these indices can guide policies for natural resource management, enabling decision-makers to formulate appropriate strategies to address the impacts of drought.
(5) Awareness-raising tools: By providing visual and quantitative data, these indices help raise awareness among communities and stakeholders about environmental issues, thus fostering a collective approach to resource management.

Furthermore, this study examines the relationships between these indices and their relevance in interpreting landscape dynamics, thereby enhancing our understanding of the impacts of meteorological drought and enabling the development of sustainable solutions.

2. Geographical context of the study

Study area

Oued Kert watershed, located in the northeast of Morocco, west of the Nador province, is characterized by particularly distinct natural boundaries. To the north, it is bordered by the foothills of the Middle Atlas, where the mountainous reliefs of Jbel Tistoutine form a clear natural frontier. Despite this clear delimitation by mountainous formations, the basin, covering an area of 520 km^2, is enclosed, which increases its vulnerability to climatic fluctuations. This enclosed topography directly influences the hydrological regime of the basin, exacerbating the effects of drought and highlighting the importance of careful water resource management for local communities. It also offers protection against climatic influences from the north. To the south, the watershed is bordered by semi-arid plains that extend toward the Sahara (**Figure 1**). These areas present a flatter topography and lower precipitation, contrasting with the northern mountains, which are characterized by diverse vegetation, including dense forests, lush pastures, and grassy plains.

To the east, the basin is bordered by a series of ridges and steep valleys, including the mountain ranges of the eastern Rif, which form a natural barrier separating the region from the surrounding territories. These geographical formations direct rainwater and streams toward the Oued Kert, playing a crucial role in regulating the hydraulic basin. They influence the collection and concentration of surface waters, contributing to the nourishment of Oued Kert and the management of water resources in the region. To the west, the watershed is bordered by other mountainous reliefs, notably the Temsamane massif, which acts as a natural barrier against western influences. This geographical configuration helps preserve the basin ecosystem.

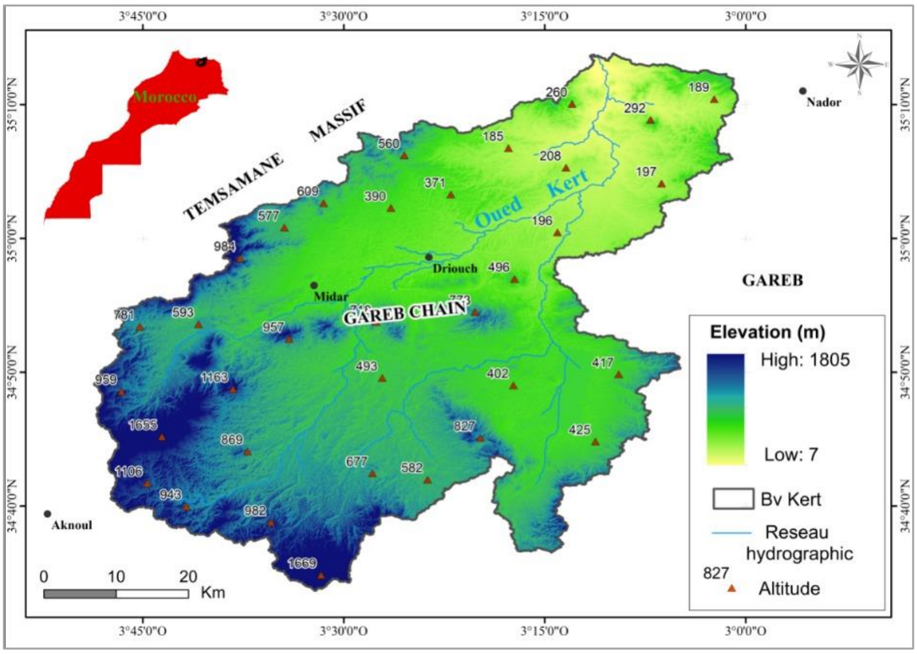

Figure 1. Map of the topography of Oued Kert basin.

3. Climate and hydrological dynamics

3.1. Precipitation patterns and trends

Temporal fluctuations in precipitation are closely linked to the seasonal characteristics of the climate, including parameters such as temperatures and precipitation that vary regularly with the seasons summer, autumn, winter, and spring as well as geographical factors such as altitude, latitude, and land cover [7]. During the twentieth century, the climate observed across Morocco has shown trends toward increasing temperatures and decreasing precipitation [7].

Since the 1970 s, there has been a substantial decrease in precipitation accompanied by a significant rise in temperatures. **Figure 2** illustrates the variation in average precipitation ranging from 216 mm to 450 mm.

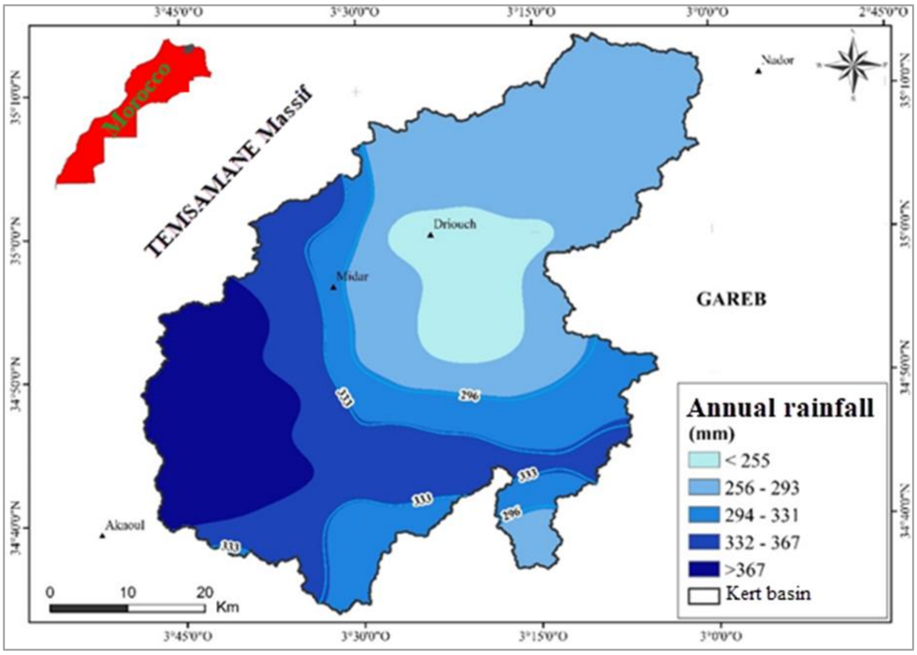

Figure 2. Map of the average annual precipitation using the isohyets method in Oued Kert basin from 1981 to 2022.

3.2. Hydrological processes and water resource management

When examining the issues related to water resources, it is essential to focus on the key unit of hydrological processes: the basin. A basin represents both a topographically delineated area by watershed lines and a zone of precipitation reception [8], with surface flow converging towards an outlet [8]. Indeed, the basin acts as a collector, capturing precipitation and converting it into flow towards an outlet, with water losses influenced by climatic conditions and the physical characteristics of the basin [9].

Temperature and precipitation variations play a crucial role in the hydrological cycle in the Mediterranean, a continuous process of water movement through the atmosphere, on the Earth's surface, and in the subsurface. This cycle includes processes such as evaporation of water from land and water surfaces, cloud formation through condensation, precipitation as rain or snow, and the return of water to the Earth's surface through soil infiltration and runoff into rivers and lakes [7], affecting various aspects such as soil moisture, runoff, streamflow, and lake levels [6,9,10]. Morocco, characterized by an arid to semi-arid climate, faces growing challenges in water resource management due to their limited availability and complex exploitation. These resources are heavily influenced by highly variable precipitation both in time and space [11–13]. The hydrology of Oued Kert basin is of paramount importance due to its crucial role in water resource management, environmental conservation, and support for the region's socio-economic activities. Oued Kert basin includes various water sources such as precipitation, permanent and temporary rivers, springs, wells, and water reservoirs. The availability of these resources varies according to seasons and climatic conditions, directly affecting agricultural, industrial, and domestic practices in the region.

4. Data and methods

Drought events exhibit variations in terms of intensity, duration, and spatial extent. Their assessment is generally based on comparing an index with a predefined critical norm [1]. To understand droughts, researchers adopt various approaches, including:

- Traditional approaches: These use simple statistical tests applied to climatic or hydrological time series.
- Satellite-based approaches: These utilize data collected by satellite sensors and processed using remote sensing tools.
- Combined approaches: These integrate traditional data with satellite data for a more comprehensive and accurate assessment.

4.1. CHIRPS data

Precipitation data play a crucial role in assessing and monitoring drought in Oued Kert basin. Among the widely used data sources is CHIRPS [14], which provides precipitation estimates by combining rain gauge observations with satellite data. This dataset of annual precipitation covers the period from 1981 to 2022. Calibration of CHIRPS data with precipitation measurements from 28 national stations has allowed to use these data for this study area to calculate the Standardized Precipitation Index (SPI) on both a seasonal and annual basis.

4.2. Satellite data

Satellite data play a crucial role in assessing vegetation at the basin scale. Among the satellite tools used is the Moderate-Resolution Imaging Spectroradiometer (MODIS 6.0, Terra and AQUA), which provides detailed information on vegetation. One widely used index for evaluating vegetation health is the Normalized Difference Vegetation Index (NDVI). The MODIS products utilized have a 16-day temporal resolution and a spatial resolution of 500 meters. These data enable the monitoring of changes in vegetation distribution and abundance in Oued Kert basin. The MODIS (Moderate Resolution Imaging Spectroradiometer) satellite scenes, available through the NTCDF (NASA's Distributed Active Archive Center), are essential tools for calculating the Normalized Difference Vegetation Index (NDVI) for the period from 1981 to 2022. These data provide detailed images of the Earth's surface, allowing for the assessment of vegetation health and coverage on a global scale. With their ability to capture information across different wavelengths, MODIS images offer valuable insights into seasonal and interannual variations in ecosystems. Users can access and download these data by visiting the NTCDF website [15]. Analyzing NDVI from these satellite scenes enhances our understanding of climate change impacts and environmental dynamics. While satellite images offer significant advantages, such as broad spatial coverage and the ability to monitor large areas over time, they also have notable limitations. One major issue is the resolution; many satellite images may not capture fine-scale features, making them less effective for localized studies. Additionally, atmospheric interference can affect data quality, resulting in inaccuracies due to clouds, haze, or varying lighting conditions. The temporal resolution is another constraint, as some satellites do not provide frequent updates, which can be problematic for tracking rapidly changing phenomena. Furthermore, satellite data often requires calibration and validation with ground-based measurements to ensure accuracy, and such data may not always be available or reliable. Lastly, certain variables, such as soil moisture or specific vegetation types, may not be directly measurable from space, limiting the applicability of satellite data for specific research questions.

4.3. Methods

This work is based on a methodology suited for evaluating drought in Oued Kert basin, incorporating the use of the Standardized Precipitation Index (SPI) and the Normalized Difference Vegetation Index (NDVI). This approach allows for the quantification and monitoring of precipitation anomalies relative to a reference period, supported by CHIRPS data. CHIRPS data are used to generate spatial precipitation maps with a spatial resolution of 5 km, as schematically illustrated in **Figure 3**. In our study, we utilized various equipment and software tools to analyze precipitation anomalies and vegetation dynamics. Below are the details of the key components used: OriginPro: Is a powerful data analysis and graphing software widely used in scientific research. It offers advanced statistical analysis capabilities and extensive graphing options, enabling users to create high-quality visual representations of their data. OriginPro facilitates the manipulation of large datasets, supports various file formats, and provides a user-friendly interface for performing complex analyses. In our study, we employed OriginPro for statistical analyses and visualization of the Standardized Precipitation Index (SPI) and the Normalized Difference Vegetation Index (NDVI). Standardized Precipitation Index (SPI): is a statistical index used to quantify precipitation anomalies relative to a reference period. It helps in identifying drought conditions by assessing precipitation deficits over various time scales. In our study, we used SPI to monitor and analyze precipitation trends using CHIRPS data. Normalized Difference Vegetation Index (NDVI): is a widely used remote sensing index that assesses vegetation health and density. It is calculated using satellite imagery, allowing for the monitoring of vegetation cover over time. In our research, NDVI was calculated using MODIS data to analyze vegetation responses to precipitation variations. CHIRPS (Climate Hazards Group InfraRed Precipitation with Station Data): is a high-resolution precipitation dataset that combines satellite data with ground station observations. It provides spatial precipitation maps with a resolution of 5 km, which were essential for our analysis of precipitation anomalies in conjunction with the SPI. By combining these tools and datasets, we were able to effectively quantify and monitor precipitation anomalies and vegetation dynamics, contributing to a comprehensive understanding of the study area.

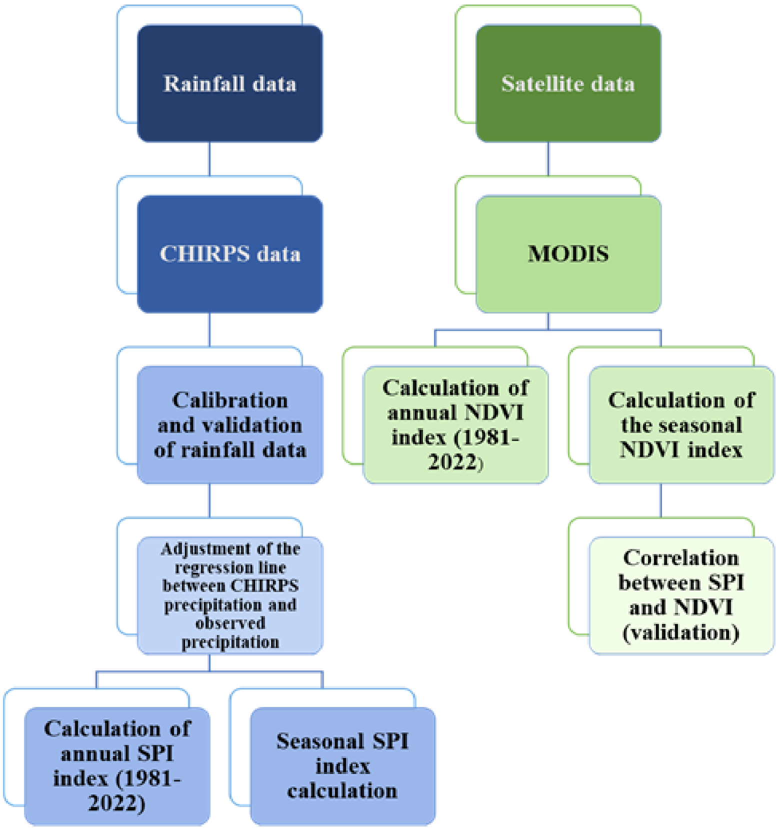

Figure 3. General framework flowchart of the adopted methodology.

4.4. Calculation and mapping methodology for SPI

The Standardized Precipitation Index (SPI) is a statistical indicator based on the probability of precipitation for a given period. It offers advantages in terms of statistical consistency and can describe the impacts of drought both in the short and long term across various time scales [16]. In the short term (1 to 6 months), it provides information on weather conditions and soil moisture, which is useful for agriculture. In the long term (6 to 24 months), it provides insights into groundwater levels, streamflow, and stored water volumes. Additionally, the SPI can provide early warnings of drought and help assess its severity [17]. In our study, we specifically used the SPI on an annual scale. We chose this scale for several reasons. First, the annual SPI allows us to assess precipitation conditions over a sufficiently long period to capture long-term trends and seasonal variations while providing a stable view of climatic anomalies. This approach is particularly relevant for analyzing impacts such as droughts or excess rainfall, which often manifest over extended periods.

Regarding the use of 24- or 48-month scales, we deemed them unnecessary in our context. Longer scales can sometimes mask important fluctuations that may be revealed through annual analysis. By using the annual SPI, we could better focus on the climatic effects relevant to our study.

The SPI at different time scales expresses the variability of precipitation in relation to long-term averages. Specifically, the annual SPI measures precipitation over a full year, providing insights into long-term trends and overall water availability. It smooths out seasonal variations, allowing us to assess how the year compares to historical norms. This is particularly useful for evaluating the impact of precipitation anomalies on water resources, agriculture, and climate trends.

In contrast, the seasonal SPI focuses on specific seasons (e.g., winter, spring, summer, autumn) and captures variations in precipitation during these critical periods. The seasonal SPI helps identify patterns that may affect agriculture, hydrology, and ecosystem health, as certain crops and water systems are more sensitive to precipitation during specific times of the year.

The mathematical formula for SPI, established by McKee et al. in 1993 [18], is as follows:

$$PI = \frac{(\mathrm{Pi} - \mathrm{Pm})}{\sigma} \tag{1}$$

Pi: Precipitation for year iii;

Pm: Average precipitation;

σ: Standard deviation or standard deviation.

Using severity thresholds defined by the standard deviation method, Aghrab [19] developed a new classification of the Standardized Precipitation Index (SPI), known as the corrected SPI (SPIc), specifically for the Sais region [20]. This revised classification (see **Table 1**) appears particularly well-suited to the Moroccan climate, and especially to the Oriental region [21,22].

We utilized monthly precipitation data to calculate the Standardized Precipitation Index (SPI) for both annual and seasonal time scales. By analyzing these monthly precipitation records, we were able to assess the variability and trends in precipitation patterns over time. The SPI, which quantifies the deviation of precipitation from the mean, allows us to classify the severity of wet or dry periods, providing valuable insights into drought conditions and hydrological changes. This method not only enhances our understanding of precipitation dynamics but also aids in water resource management and agricultural planning by highlighting critical periods of moisture availability.

Table 1. Classification of drought severity according to the corrected SPI compared to the classification proposed by Mckee et al. [18].

Class	Classification	Threshold according to SPI	Threshold according to SPI_C
Extremely humid	More than 2.0	pi > pm + 2o	More than 2.0
Very humid	1.5 to 1.99	Pm + o < pi < pm +2o	1 to 1.99
Moderately humid	1.0 to 1.49	Ls < pi < pm + o	0.31 to 0.99
Near normal	−0.99 to 0.99	Li < pi < Ls	−0.30 to 0.30
Moderately dry	−1.0 to −1.49	Pm − o < pi < Li	−0.31 to −0.99
Severely dry	−1.5 to −1.99	Pm − 2o < pi < Pm − o	−1 to −1.99
Extremely dry	Less than −2.0	pi < Pm − 2o	Less than −2.0

4.5. Remote sensing approach: The NDVI

Vegetation indicators are essential quantitative measures of vegetation cover status, crucial for monitoring its dynamics and detecting signals of water stress or drought. Various indices such as the Enhanced Vegetation Index (EVI), the Vegetation

Condition Index (VCI), and the Vegetation Health Index (VHI) are available for drought assessment. In the context of this study, the Normalized Difference Vegetation Index (NDVI) has been opted for due to its prominence and recognized effectiveness in analyzing drought conditions. The NDVI is widely acknowledged for providing relevant information in this regard. Utilizing satellite data allows for precise mapping of daily solar irradiance levels, thus facilitating early detection of water stress manifestations within vegetation cover. The NDVI assesses vegetation biomass by considering its phenological phases and offers insights into seasonal and annual fluctuations in vegetation density, influenced by various climatic parameters such as moisture and atmospheric conditions, as highlighted by Franchomme [23]. This study classified vegetation cover into four consecutive categories, adopted from Layelmam and Mimouni et al. [21,24], as illustrated in **Table 2**.

Table 2. Classification of vegetation cover according to the NDVI index [24].

Class	NDVI Value
Degraded	Less than 0.15
Near normal	0.15 to 0.30
Good	0.30 to 0.45
Very good	More than 0.45

5. Results and interpretations

This section presents the results of the meteorological drought monitoring by displaying maps of the Standardized Precipitation Index (SPI), aiming to highlight the influence of precipitation anomalies on vegetation growth.

5.1. Calibration of CHIRPS data

The results of the regression analysis between satellite-derived precipitation data and measurements from 28 national stations revealed a coefficient of determination (R^2) of 0.89, indicating a strong correlation between the two data sets (**Figure 4**). This regression equation was applied to calibrate CHIRPS satellite data at the pixel level over a period of forty-one years, from 1981 to 2022. In other words, this procedure is a method for adjusting satellite precipitation values based on direct observations, allowing for accurate correction of satellite data relative to ground measurements.

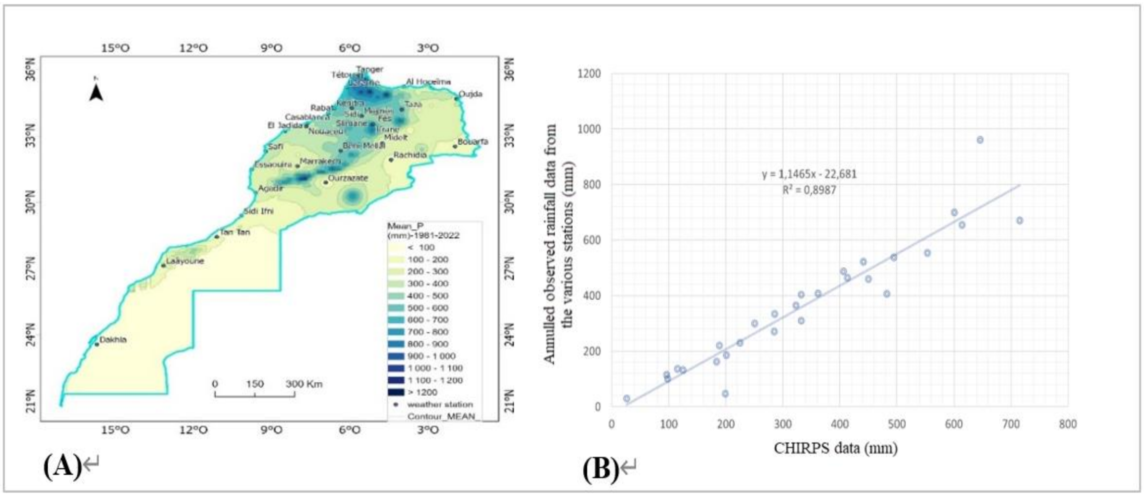

Figure 4. National precipitation map and correlation diagram: **(A)** National average precipitation for the period 1981-2022; **(B)** Correlation between precipitation recorded by national meteorological stations and precipitation estimated from CHIRPS images.

The fundamental value of this method lies in its ability to enhance the accuracy and reliability of satellite-derived precipitation data. This approach is particularly relevant in regions where ground observations are limited or unreliable, as is the case in this study area, because it helps address gaps in meteorological data, thereby improving the quality of information available for planning and decision-making processes.

5.2. Frequency and intensity of droughts in Oued Kert Basin

According to the results obtained, over the study period from 1981 to 2022, the following observations were noted:

(1) Two extremes: in 1983, the driest year (with SPI = −1.5), and in 2010, the year with the most extreme moisture (with SPI = 3.7);

(2) An alternation between dry and wet periods, with the longest non-dry period recorded between 2006 and 2013 (**Figure 5**). Due to its standardization, the SPI has the advantage of allowing comparison of drought conditions over different time periods [24]. Comparative analysis of seasonal SPI indices highlights the seasonal characteristics of precipitation as well as the associated drought conditions.

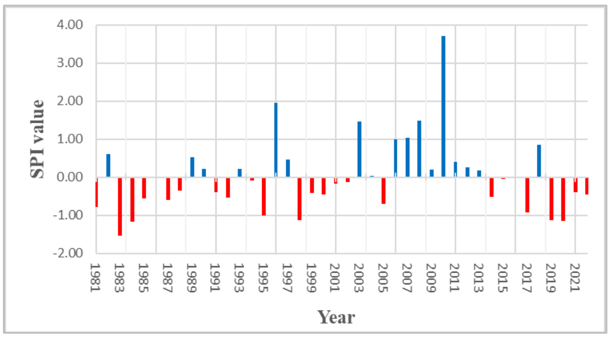

Figure 5. Annual values of the standardized precipitation index (SPI) in Oued Kert Basin (1981–2022).

5.3. SPI maps derived from CHIRPS data

Monitoring meteorological drought relies on a rigorous analysis of various indicators, which are determined from multiple climatic parameters. Due to the inherent complexity in objectively quantifying the characteristics of drought, such as its duration, intensity, and spatial extent, significant efforts have been made to develop techniques for monitoring, characterizing, and analyzing drought. These efforts have led to the creation of several specific indices and indicators designed to better understand this critical climatic phenomenon. CHIRPS precipitation data consist of satellite estimates corrected by integrating ground-based meteorological station observations. They are represented as raster images in time series available from 1981 to the present [14]. These CHIRPS data are presented as spatial precipitation maps with a spatial resolution of 5 km.

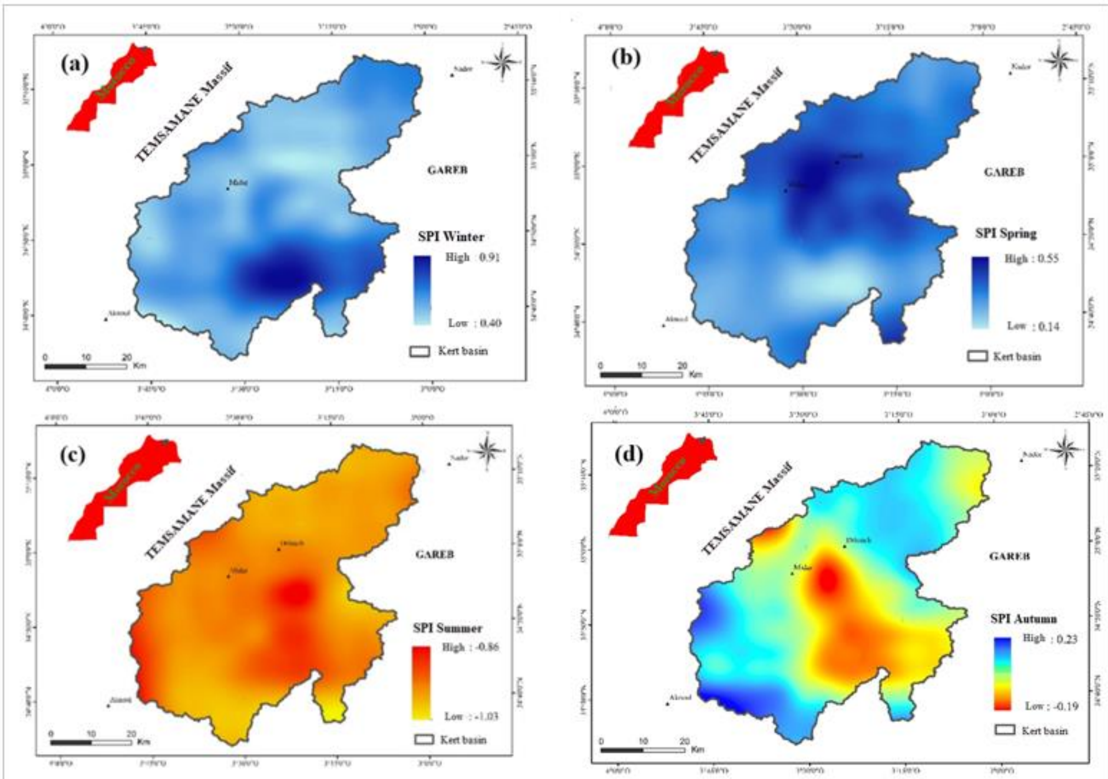

Figure 6. Seasonal SPI maps derived from average seasonal CHIRPS data (1981–2022). **(a)** Winter SPI; **(b)** Spring SPI; **(c)** Summer SPI**; (d)** Autumn SPI.

The expected results of this study, based on the calculation of the seasonal SPI index from seasonal average CHIRPS data (1981–2022) in Oued Kert basin, reveal significant observations. Specifically, the SPI index for the winter period ranges from 0.40 to 0.91 (**Figure 6a**). These values indicate a period characterized by moderate moisture, suggesting relatively favorable precipitation conditions in the studied basin. Spring presents a period of moderate moisture, reflecting spring precipitation amounts that are greater than those received during summer and less than those received during winter (**Figure 6b**). In contrast, in Oued Kert basin, the SPI index for the summer period, representing the dry season, shows values of −0.86 and −1.03 (**Figure 6c**). The summer season in Oued Kert basin is characterized by dry weather conditions due to a significant reduction in precipitation. In the context of Oued Kert basin, the analysis of the autumn SPI index (**Figure 6d**) reveals that the basin experiences conditions close to normal during autumn, which can be explained by precipitation amounts equal to or near the autumnal average.

5.4. Spatial distribution of NDVI in Oued Kert Basin

The results of mapping the Normalized Difference Vegetation Index (NDVI) reveal considerable diversity in the matrices, both temporally and spatially. The fluctuations observed in the studied seasonal series highlight a variety in land cover and land use characteristics. The spatial distribution of the NDVI shows that during the spring season, vegetation conditions were better compared to other seasons (**Figure 7**). During this phase, non-degraded vegetation covered areas characterized by dense and diverse plant cover, supporting a variety of plant species. Non-degraded areas in Oued Kert basin are often associated with specific topographic features, such as fertile soils and adequate water availability. These conditions promote the development and maintenance of natural vegetation, leading to the formation of healthy and resilient ecosystems. Some areas exhibit vegetation degradation throughout all seasons, which may be attributed to construction activities.

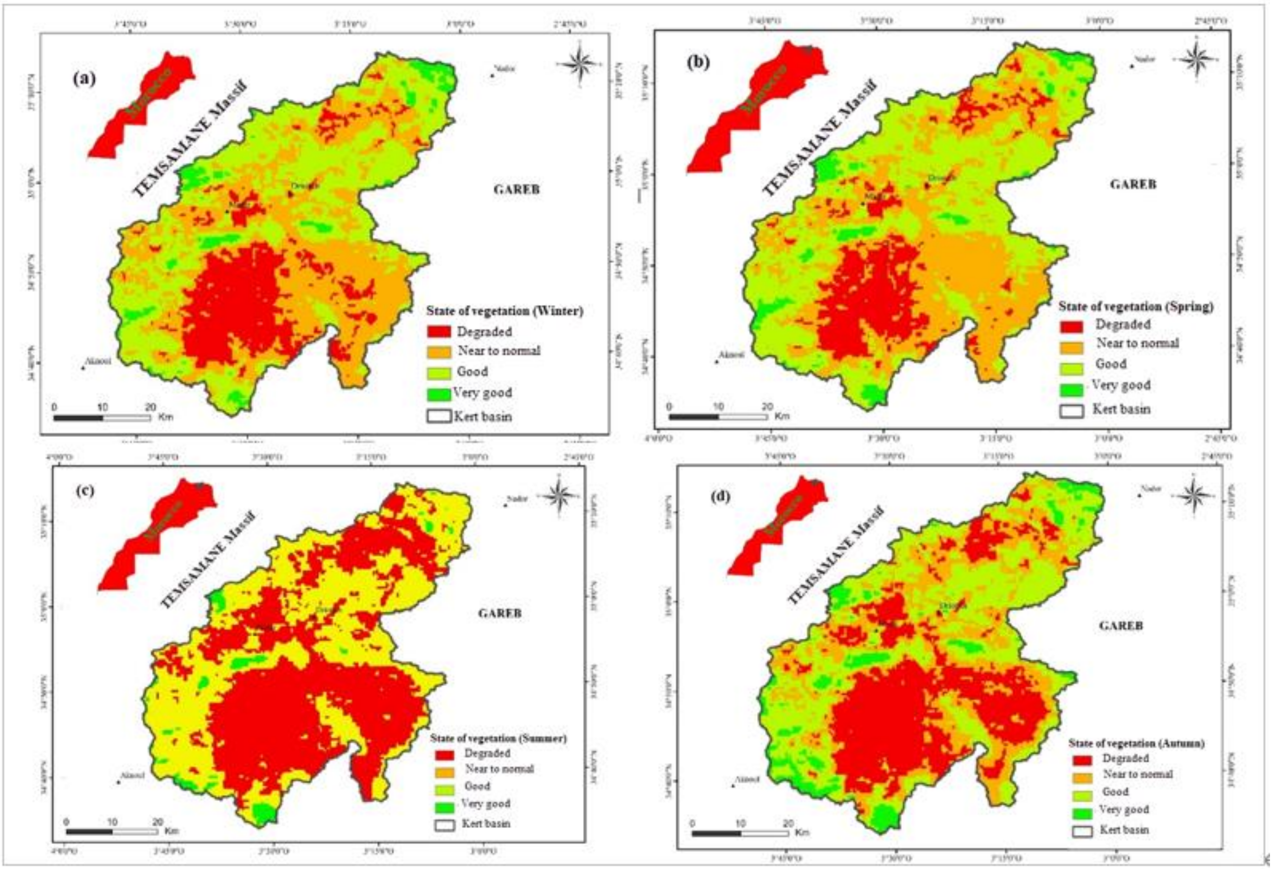

Figure 7. Maps of drought classes according to the seasonal normalized difference vegetation index (NDVI) in Oued Kert Basin **(a)** Vegetation condition (Winter); **(b)** Vegetation condition (Spring); **(c)** Vegetation condition (Summer); **(d)** Vegetation condition (Autumn)).

Spring vegetation cover is greater than that of other seasons. This situation results from the precipitation received during the winter semester and the accelerated physiological activity of plants during the spring season. During wet periods, farmers in Oued Kert basin are encouraged to practice plowing, even beyond the traditional soil preparation phase for major crops, due to increased precipitation. However, this practice exacerbates the vulnerability of the area.

5.5. Correlation between seasonal SPI and NDVI

The study of the correlation between precipitation patterns and vegetation dynamics throughout the seasons highlights the influence of climatic variability on vegetation. An analysis of the relationship between the Normalized Difference Vegetation Index (NDVI) during the winter season and the Standardized Precipitation Index (SPI) for the same period reveals a correlation coefficient (R^2) of 0.66. This result underscores a significant correlation between vegetation vigor and drought conditions during winter (**Figure 8**). These findings emphasize the importance of closely monitoring winter climatic conditions and their impact on pasture availability in grazing areas.

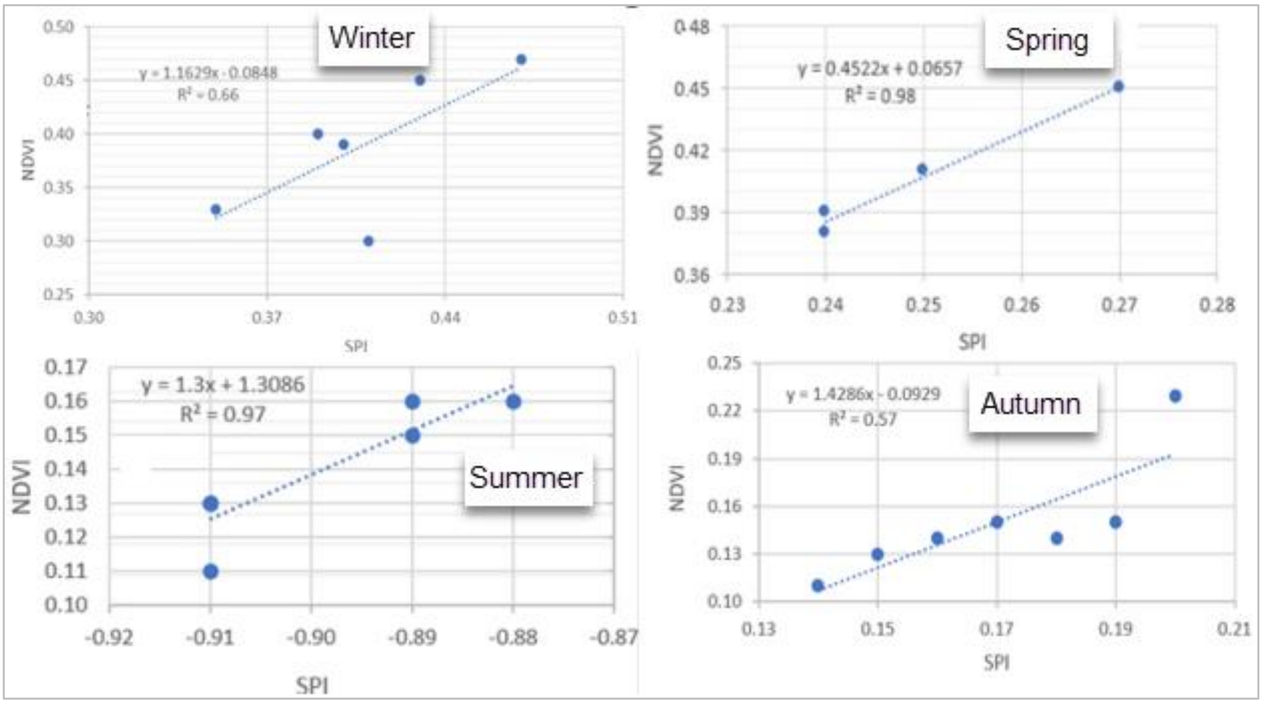

Figure 8. Correlation diagram between seasonal NDVI and SPI in Oued Kert Basin.

During the spring season, precipitation plays a crucial role in vegetation growth and development. Adequate precipitation levels can promote optimal plant growth, while prolonged drought can lead to reduced vegetation biomass. Thus, significant variations in the SPI can translate into similar variations in the NDVI, resulting in a strong correlation between the two.

The NDVI is sensitive to rapid changes in weather conditions, especially during active growing seasons like spring. Vegetation responds quickly to changes in hydrological conditions, which is reflected in the NDVI. Consequently, when precipitation varies considerably, the NDVI may exhibit similar fluctuations, leading to a high correlation of $R^2 = 0.98$ with the SPI.

A high correlation between the NDVI and SPI for the spring season indicates a strong association between precipitation and vegetation vigor during this active growth period, reflecting the vegetation's sensitive response to weather conditions.

During the autumn season, the interactions between vegetation and weather conditions are often more complex due to the transition between active growth and dormancy seasons. Precipitation may impact vegetation vigor, but other factors such as temperature, day length, and soil conditions may also play a role. This complexity can reduce the strength of the correlation between NDVI and SPI. The results show a moderate correlation, R^2 of 0.57, between the Normalized Difference Vegetation Index (NDVI) and the Standardized Precipitation Index (SPI) for the autumn season, which is due to the complexity of environmental interactions, delayed effects of precipitation on vegetation, and local and regional variability in environmental conditions.

6. Discussion

Numerous studies have shown that the Normalized Difference Vegetation Index (NDVI) is frequently correlated with the Standardized Precipitation Index (SPI), reflecting the influence of precipitation on plant health. For example, research indicates that during droughts, NDVI decreases align with negative SPI values, highlighting vegetation's direct response to water availability. This approach has notable advantages, such as utilizing satellite data for large-scale assessments and easily integrating climatic and ecological information. However, it also has drawbacks; factors like temperature, soil conditions, and land management can significantly affect vegetation health beyond just precipitation. Thus, while the NDVI-SPI correlation is valuable for understanding drought impacts, a comprehensive analysis must consider additional variables.

Further explored this relationship in the upper Noteć catchment area in central Poland [25], demonstrating that NDVI effectively indicates variations in vegetation health during droughts. Their findings underscore the importance of remote sensing in climate monitoring and reveal a significant correlation between NDVI values and SPI-identified drought episodes. This research contributes to the growing literature advocating for the combined use of these indices to enhance natural resource management amid climate change challenges.

The approach that analyzes the relationship between the Standardized Precipitation Index (SPI) and the Normalized Difference Vegetation Index (NDVI) offers several significant advantages. Firstly, it enables large-scale assessments through the use of satellite data, providing an overview of vegetation health and drought conditions. The NDVI, as a sensitive indicator, reacts quickly to variations in plant health, facilitating the monitoring of drought impacts [26]. Additionally, this method promotes the integration of climatic and ecological data, enriching multidisciplinary analyses and allowing for continuous monitoring of environmental conditions over extended periods.

However, this approach also has its drawbacks. Local variability can affect the results, as factors such as soil quality and agricultural practices may nuance data interpretation. Furthermore, vegetation health is influenced by multiple elements, including temperature and soil moisture, which complicates the analysis. The timing of the data presents another challenge, as NDVI measurements may not always align with drought periods, making it difficult to establish clear relationships. Moreover, the accuracy of satellite data can vary due to atmospheric factors like cloud cover. Lastly, it is essential to note that a correlation between NDVI and SPI does not necessarily imply a causal relationship, which can lead to misinterpretations.

In summary, while the association between SPI and NDVI provides valuable insights into understanding drought impacts on vegetation, it is crucial to consider the various advantages and disadvantages to achieve a comprehensive and accurate analysis.

7. Conclusion

The anticipated results of this study have highlighted a statistically significant correlation between the two selected indices on a seasonal scale. This can be attributed to the immediate response of photosynthetic activity to precipitation. The choice of the Standardized Precipitation Index (SPI) for monitoring drought from precipitation data offers several advantages. During this study, the index was calculated for Oued Kert basin over a period extending from 1981 to 2022.

Monitoring vegetation cover changes using satellite-derived indicators provides insights into vegetation response to precipitation fluctuations and facilitates the comparison of its current state on a seasonal level. Additionally, a thorough analysis of these indicators on a seasonal scale allows for the identification of times when anomalies in crop development occur due to climatic variations. This information is crucial for agricultural managers, enabling them to implement appropriate corrective measures to ensure optimal plant growth.

Author contributions: Conceptualization, ZEA, AM and ML; methodology, ZEA, AA and WS; software, ZEA, WS and SE; validation, ZEA, AM and MM; formal analysis, ZEA; writing—original draft preparation, ZEA; writing—review and editing, ZEA, AM and ML; visualization, ZEA, AA, MS, WS, SE and MM; supervision, AM. All authors have read and agreed to the published version of the manuscript.

Conflict of interest: The authors declare no conflict of interest.

References

1. Observatoire du Sahara et du Sahel. Towards a Maghreb drought early warning system. Observatoire du Sahara et du Sahel; 2013.
2. The World Bank. Governance and Development. The World Bank; 1992.
3. Boubaker HB. Assessment of existing national drought early warning systems (French). Report. Collection Synthèse, numéro 4. Cadre du projet SMAS; 2006.
4. Beltrando G. Climates - Processes, variability and risks (French). Available online: https://www.dunod.com/histoire-geographie-et-sciences-politiques/climats-processus-variabilite-et-risques (accessed on 2 August 2024).
5. UNESCO. International Glossary of Hydrology. Organisation météorologique mondiale; 2012.
6. IPCC. Synthesis Report: Climate Change 2014. In: Pachauri RK, Meyer LA (editors). IPCC; 2014.

7. Mounir K. Analysis and modeling of the impact of climate change on water resources in the Ouergha watershed (Morocco). Sidi Mohamed ben Abdellah University, Morocco; 2024.
8. Roche M. French dictionary of surface hydrology (French). Available online: https://horizon.documentation.ird.fr/exl-doc/pleins_textes/divers21-02/26812.pdf (accessed on 2 August 2024).
9. Roche M. Hydrologie de surface. Available online: https://www.pseau.org/outils/ouvrages/ird_hydrologie_de_surface_marcel_roche_1963.pdf (accessed on 2 August 2024).
10. Food and Agricultrue Organazition of the United Nations. Climate change and water resources in the Mediterranean region. Food and Agricultrue Organazition of the United Nations; 2010.
11. De Girolamo AM, Barca E, Leone M, et al. Impact of long-term climate change on flow regime in a Mediterranean basin. Journal of Hydrology: Regional Studies. 2022; 41: 101061. doi: 10.1016/j.ejrh.2022.101061
12. Riad S. Typology and hydrological analysis of surface waters in representative Moroccan watersheds. Semantic Sch.; 2003.
13. El Orfi T, El Ghachi M, and Lebaut S. Comparison of satellite precipitation data (French). In: Proceedings of the Colloque de l’Association Internationale de Climatologie: Changement Climatique Et Territoires; 2020; Rennes, France.
14. Funk CC, Peterson PJ, Landsfeld MF, et al. A quasi-global precipitation time series for drought monitoring. Data Series. Published online 2014. doi: 10.3133/ds832
15. United States Geological Survey. Available online: https://lpdaac.usgs.gov/data/ (accessed on 10 May 2024).
16. Buishand TA. Some methods for testing the homogeneity of rainfall records. Journal of Hydrology. 1982; 58(1–2): 11–27. doi: 10.1016/0022-1694(82)90066-X
17. Nieves A, Contreras J, Pacheco J, et al. Assessment of drought time-frequency relationships with local atmospheric-land conditions and large-scale climatic factors in a tropical Andean basin. Remote Sensing Applications: Society and Environment. 2022; 26: 100760. doi: 10.1016/j.rsase.2022.100760
18. McKee T, Doesen N, and Kleist J. The relationship of drought frequency and duration to time scales. In: Proceedings of the Eighth Conference on Applied Climatology; 1993; California.
19. Aghrab. A methodology for characterizing a region’s climate and drought (French). Editions Le Manuscrit; 2005. p. 51.
20. Aghrab. Study of drought in Morocco: Essay (French). Available online: https://www.abebooks.fr/9782748146486/Etude-s%C3%A9cheresse-Maroc-Types-impacts-2748146484/plp (accessed on 10 May 2024).
21. Mimouni J. Climate and drought. In: Proceedings of the Conférence donnée aux étudiants du master complémentaire de développement, Université de Liège; 2012; Belgique.
22. Melhaoui M, Mezrhab A, and Mimouni J. Assessment and mapping of meteorological drought in the eastern highlands of Morocco (Pdpeo project area). Rev Microbiol Ind San Environn. 2018; 12(1): 22.
23. Franchomme M. Remote sensing monitoring of changes in vegetation cover in the Mediterranean coastal zone of Tunisia [Master thesis]. Université des Sciences et Technologies de Lille; 2002.
24. Layelmam M. Calcul des indicateurs de sécheresse à partir des images NOAA/AVHRR. Published online 2008. doi: 10.13140/2.1.4680.8966
25. Kubiak-Wójcicka K, Pilarska A, Kamiński D. Meteorological drought in the upper Noteć catchment area (Central Poland) in the light of NDVI and SPI indicators. Applied Water Science. 2024; 14(8). doi: 10.1007/s13201-024-02215-1
26. Boulariah and Longobardi A. Assessing the Relationship Between the Standardized Precipitation Evapotranspiration Index (SPEI) and the Normalized Difference Vegetation Index (NDVI) During 1985–2020 in a Mediterranean Area. In: Ksibi M, Sousa A, Hentati O, et al. (editors). Recent Advances in Environmental Science from the Euro-Mediterranean and Surrounding Regions (4th Edition). Cham: Springer Nature Switzerland; 2024. pp. 881–883.

Journal of Geography and Cartography 2024, 7(2), 6909.
https://doi.org/10.24294/jgc.v7i2.6909

Review

Spectroscopic techniques for detecting naturally occurring radioactive nuclides in geology and water: A comprehensive review and health implications

Mohamed H. Fathy[1,*], Farha Shaban[1], Thowayba M. Fawzy[1], Dat Viet Nguyen[2], Ahmed M. Eldosouky[1]

[1] Geology Department, Faculty of Science, Suez University, Suez 43221, Egypt
[2] University of Science, Vietnam National University, Hanoi 334, Vietnam
*** Corresponding author:** Mohamed H. Fathy, Mohamed.HeFaK@sci.suezuni.edu.eg

CITATION

Fathy MH, Shaban F, Fawzy TM, et al. Spectroscopic techniques for detecting naturally occurring radioactive nuclides in geology and water: A comprehensive review and health implications. Journal of Geography and Cartography. 2024; 7(2): 6909.
https://doi.org/10.24294/jgc.v7i2.6909

ARTICLE INFO

Received: 5 June 2024
Accepted: 24 June 2024
Available online: 11 July 2024

Abstract: Naturally occurring radionuclides can be categorized into two main groups: primordial and cosmogenic, based on their origin. Primordial radionuclides stem from the Earth's crust, occurring either individually or as part of decay chains. Conversely, cosmogenic radionuclides originate from extraterrestrial sources such as space, the sun, and nuclear reactions involving cosmic radiation and the Earth's atmosphere. Gamma-ray spectrometry is a widely employed method in Earth sciences for detecting naturally occurring radioactive materials (NORM). Its applications vary from environmental radiation monitoring to mining exploration, with a predominant focus on quantifying the content of uranium (U), thorium (Th), and potassium (K) in rocks and soils. These elements also serve as tracers in non-radioactive processes linked to NORM paragenesis. Furthermore, the heat generated by radioactive decay within rocks plays a pivotal role in deciphering the Earth's thermal history and interpreting data concerning continental heat flux in geophysical investigations. This paper provides a concise overview of current analytical and measuring techniques, with an emphasis on state-of-the-art mass spectrometric procedures and decay measurements. Earth scientists constantly seek information on the chemical composition of rocks, sediments, minerals, and fluids to comprehend the vast array of geological and geochemical processes. The historical precedence of geochemists in pioneering novel analytical techniques, often preceding their commercial availability, underscores the significance of such advancements. Geochemical analysis has long relied on atomic spectrometric techniques, such as X-ray fluorescence spectrometry (XRFS), renowned for its precision in analyzing solid materials, particularly major and trace elements in geological samples. XRFS proves invaluable in determining the major constituents of silicate and other rock types. This review elucidates the historical development and methodology of these techniques while showcasing their common applications in various geoscience research endeavors. Ultimately, this review aims to furnish readers with a comprehensive understanding of the fundamental concepts and potential applications of XRF, HPGes, and related technologies in geosciences. Lastly, future research directions and challenges confronting these technologies are briefly discussed.

Keywords: radioactivity; radionuclides; HPGe detector; NaI(Tl) detector; LSC detector

1. Introduction

Cosmic beams and naturally radioactive components make up the natural radiation environment. A parcel of the materials is primordial, cosmogenic, and naturally occurring due to the radioactive change of compounds delivered by these forms. Their physical characteristics and changes over time are related to their radiological significance [1]. The primordial radionuclides are inferred from the outside of the crust and may exist alone or as a portion of a decay chain. Illustrations of decay series components that are as often as possible found in gamma-spectroscopic perceptions are the uranium series' 224Ac and 214Bi; of the radionuclides that occur independently, 40K is the most common in natural estimations. On the other hand, the source of cosmogenic radionuclides is found in space, the sun, and atomic reactions, including cosmic radiation and the earth's atmosphere. Through air blending or precipitation, radionuclides are brought down to the Earth's surface. These radionuclides incorporate 7Be and 14C as illustrations [2].

Due to their possibly disastrous impacts on wellbeing, naturally occurring primordial radionuclides and the ionizing radiations they go with in encompassing natural compartments are of incredible concern [3–8]. Radiation introduction can lead to a number of health issues, including lung cancer, bone variations from the NORM (naturally occurring radioactive material), renal failure, and kidney breakdown. Primordial radionuclide dispersion in different natural fragments (such as sediment, soil, sand, dust, and water) is frequently impacted by local geomorphological, geological, climatic, and geochemical highlights as well as weathering process(es) [9]. Norms in soil or sediment are regularly connected to exposure to outside radiation, be that as it may, vaporous 222Rn inward breath ought to not be ignored. The primary source of natural radiation is radon, a naturally occurring gas that comes from rock and soil. People breathe in and consume radioactive materials on a daily basis from food, water, and the air. Radiation exposure can come from both external and internal sources. When a radionuclide is breathed, swallowed, or enters the bloodstream in any other way (by injection, for example, or through wounds), internal exposure to ionizing radiation takes place. Internal exposure ends when the radionuclide leaves the body on its own (via excreta, for example) or as a consequence of a therapeutic intervention [10].

Water exposure to radionuclides can happen in a variety of ways, but since surrounding water sources contain low amounts of primordial Norms, the impacts appear to be irrelevant [11]. Not at all like water, radionuclides are shown in street dust and cannot be ignored. Street dust exposures to ionizing radiation from Norms are not constrained to outside pathways (that disregard 222Rn absorption), such as soil or sediment. Breathing in street dust and its related Norms can enter the respiratory system [12]. Ordinarily related to better dust frameworks (diameter < 2 μm), Norms have the capacity to move over longer distances and pose posture wellbeing dangers to individuals due to their ability to enter the respiratory system [3,4]. There has been a critical resurgence in thinking about natural radioactivity in recent years. One clarification for this is the common rise in significance and request of nuclear science, of which this field is a portion.

The consideration of the characteristics and events of thorium, the parent of most known natural radionuclides, has been provoked by its practical significance as a source of raw materials for nuclear energy. Furthermore, it has been found that natural radioactivity is a phenomenon with far greater changeability and hereditary incidence than previously thought. Numerous earth researchers have utilized nuclear technologies in their investigations since the well-established and, as of late, found geological results of radioactivity's presence in the natural world. Radionuclides that naturally emerge and have lives extending from billions of a long time to less than a diminutive can give experiences into a wide range of occasions, from cosmic history to micrometeorology. In any case, nature has appeared to be a valuable research facility accomplice for nuclear researchers, having the capacity to quicken particles to energies well past their claim capabilities and having the foreknowledge to start tests for them millions of years ago [13].

There are changing degrees of radioactivity in all rocks and soils. The 40K, 232Th, and 238U naturally occurring radioisotopes are the most predominant on Earth's surface. It is apparent from watching different inquiries about radioisotope concentrations in diverse sorts of rocks that this is same sort of rock [14–17] ordinarily shows a wide range of concentration values. However, certain patterns can be observed. For instance, felsic igneous rocks ordinarily have higher levels than sedimentary rocks. The rate at which people absorb outside gamma doses from the environment is impacted by the radioactivity of rocks. As a result, it's critical to gauge the radioactivity of rocks and comprehend how radioisotope dynamics influence the environment, human health, and development techniques.

The present review is concerned mainly with material published with references to a few prior works that are relevant to later advancements. The number of publications in this range is expanding quickly each year. In this research, we will center on the modern applications of radioactivity and spectrometry and highlight the case studies, their methods, and how they were done. These applications will be in distinctive areas, but the primary center will be in the geology field. In the next sections, we will show the applications in conversation, starting with their methodology.

2. Methodology

Nuclear radiation detectors became fundamental gadgets when radioactive sources were utilized in different spaces like health physics, industry, energy, and environmental applications. This is since radiation poses a health hazard [18]. The gadget that changes radiation energy into an electrical signal is called a detector. It is the radiation escalated that is created at the instrument's output after being digitally processed. In spite of the fact that these detectors work on different speculations, they eventually show the radiation output. a variety of radiation detectors for X-rays, UV, visible, and infrared light [19]. In this section, we will discuss a few of the most commonly utilized methods and detectors, and how they work, and their principles.

2.1. High purity germanium detector

A non-destructive method for evaluating the radioactive concentration of man-made and natural radionuclides in the environment is gamma-ray spectrometry utilizing germanium detectors. The earlier information on the full-energy peak efficiency at each photon energy for a certain measuring geometry is vital in order to determine the activity for each radionuclide. Hence, in order to continue, an efficiency calibration must be performed previously, utilizing a standard radioactive source that has the same shape, density, and chemical composition as the sample being examined. Nevertheless, these necessities are regularly not taken care of. It too proposes the issue that each sample configuration requires an efficiency calibration [20].

The number of photons discharged from the source and absorbed by the detector is the most pivotal step in estimations performed with a gamma-ray spectrometer. The capacity of a detector to absolutely and reliably detect and measure gamma radiation discharged by a radioactive source is known as detector efficiency. Different efficiency sorts, including intrinsic, photopeak, relative, and absolute efficiencies, are fundamental to precisely detecting and measuring gamma-ray radiation transmitted from radioactive sources [21].

Early in the 1980s, high purity germanium (HPGe) detectors were made available. They are planned to detect excited nucleus energies with more penetration power than can be measured with conventional junction and surface barrier detectors [22]. Liquid nitrogen is utilized to chill them in order to stop breakdowns and minimize electrical spillage. When compared to other sorts of radiation detectors, high purity germanium (HPGe) detectors can clearly perceive close-by energy peaks and give sufficient data to reliably and precisely recognize radionuclides from their gamma-ray radiation [23].

Semiconductors, or bunch four elements in the periodic table, are utilized to make the HPGe detectors. Three band gaps are shown in semiconductor materials: the valence band, the forbidden band, and the conduction band. The conduction band is empty, and the valence band is filled at the absolute temperature. Energized electrons go from the valence band into the conduction band, where they shape an empty zone known as a “hole”. When an electric field is present, current is delivered by the movement of the electrons and holes in the valence and conduction bands. There are the same number of holes and electrons in a pure semiconductor. A semiconductor’s band gap sets up the greatest number of energy carriers per signal. Germanium has a band gap energy of generally 0.6 eV, compared to 1.1 eV for silicon [24].

Through the deliberate presentation of impurities from group three or bunch five elements, a process known as “doping,” the conducting properties of these materials can be conveniently altered. The material is an N-type semiconductor if the impurities are group V elements since more electrons are given to the system. In any case, the material is alluded to as a P-type semiconductor if the impurities are from group three elements since fewer electrons are contributed to the system [25]. The P-N junction in the material was made by the two sorts of semiconductors. At this minute, the electrons and holes will clear past one another to deliver an electrical pulse. When an ionizing adiation ionizes a semiconductor material, the charges are straightforwardly collected by the high purity germanium (HPGe) detectors. Charge carriers, or electron-hole pairs, are made when a photon is interatomic with its substance. There will be an electron hole pair created inside the depletion layer as a result of an external particle entering the depletion layer (between the P-N junction). When an external particle enters the depletion layer, it essentially collides with the atoms and molecules in that region and transfers energy. The electrons in the valance band of that specific depletion layer will then absorb that energy and jump to the conduction band when that happens. These carriers are at that point cleared over one another and collected at the electrodes. The charge is closely related to the incident gamma photon’s energy [23].

In modern gamma-ray spectroscopy, HPGe detectors have widespread application owing to their outstanding output efficiency and fine energy resolution. The distance between the source and detector, calibrator dimensions, shielding thickness, and incoming gamma ray energy all impact the HPGe detector's absolute efficiency, as recent studies have shown [26].

2.1.1. Parts of HPGe

Germanium is not liked by many detectors due to the need to cool them to liquid nitrogen temperatures. This is caused by the fact that the element has a relatively narrow band gap, which requires cooling so as to reduce the thermal generation of charge carriers to an acceptable level. Inadequate cooling of these devices causes noise from leakage currents that affects detector energy resolution. It should be noted that germanium's bandgap is extremely small (Egap = 0.67 eV). When it is cooled down to −195.8 ℃ (the temperature of liquid nitrogen), the excitations of valence electrons decrease, thereby allowing only gamma-rays interactions to provide an electron with enough energy to cross this gap into the conduction band. For this reason, most HPGe detectors are fitted with cryostats, while their crystals are enclosed in an evacuated metal holder known as the detector.

To avoid low-energy photon attenuation, the detector holder and endcap are made thin. The holder is ordinarily constructed from aluminum with a thickness of about 1 mm. The end cap is equally made of aluminum, analogously. The HPGe crystal is in the holder, and it is in direct thermal contact with a cold finger, which is a metallic rod. The transfer of heat from the assembly to the nitrogen container is facilitated by this cold finger. In general, the cryostat is made up of a vacuum metal canister, cold fingers, and a Dewar flask for the liquid nitrogen cryogenics system.

The germanium detector preamplifier is typically part of the cryostat itself. In order to minimize the total capacitance, the preamplifier is placed in close proximity to both detectors and is also cold-shielded. The cryostat has a vacuum enclosure that ends at the Dewar, containing liquid nitrogen, into which the cold finger extends. The Ge cryostat must be kept at a very low temperature, so it is immersed in liquid nitrogen. The liquid nitrogen remains at −195.8 ℃ because its gradual boiling releases nitrogen gas, thereby keeping the system insulated from thermal energy. Depending on their size and configuration, vacuum flasks can retain their contents for hours or weeks.

One major inconvenience of using liquid nitrogen for cooling is the time it takes the detector reach operational temperature. Another is that we can't let it warm up when in use. However, unlike HPGe detectors, which need to be kept at room temperature all the time they are not being used, Ge(Li) crystals should never be allowed to warm up, as this would cause lithium within them to drift out and damage the crystal, thus permanently break the detector.

There are advanced commercial systems nowadays that can use various modern cooling methods, like a pulse tube cooler and others, besides liquid nitrogen cooling. This new cooling system only requires electricity to work, and no LN2 is needed (**Figure 1**), making it a better option as it is more convenient and efficient.

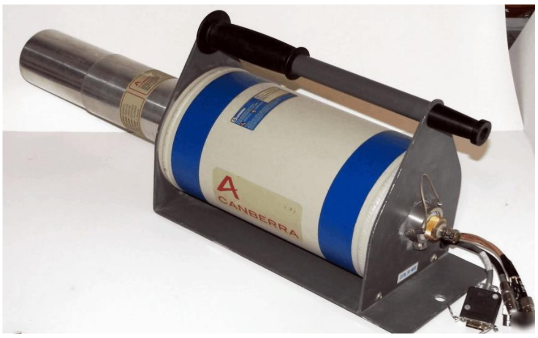

Figure 1. HPGe detector with LN2 cryostat [27].

2.1.2. Principle of operation

When ionizing radiation enters the germanium crystal of the detector, it interacts with the semiconductor material. A powerful photon passing through the detector triggers the ionization of atoms in the semiconductor, leading to the generation of pairs of electrons and holes. The number of electron-hole pairs produced is linked to the energy of the radiation interacting with the semiconductor. As a result, many electrons move from the valence band to the conduction band, creating a number of holes in the valence band.

Germanium, because of its property to maintain a sensitive layer measuring in centimeters, can fully capture high-energy photons (up to a few MeV). When subjected to a field, both electrons and holes move toward the electrodes, resulting in the creation of a signal, in an external circuit. The pulse of this signal contains details, about the power of the radiation exposure. Additionally, the rate at which these signals occur over a period of time gives us clues about the strength of the radiation.

In all cases, a photon emits part of its energy along the path and may be completely absorbed. When a 1 MeV photon is completely absorbed, it gives rise to about 3×10^5 electron-hole pairs. Compared with the total number of free carriers in an intrinsic semiconductor of 1 cm^3, this figure is rather small.

Thermal excitation, which is dominant in germanium-based detectors operating at room temperature, is not the only factor that causes ionization of the semiconductor atoms when particles pass through the detector. Dopants, impurities, and lattice irregularities are responsible for this phenomenon, and it depends largely on the *E*gap (energy gap) of the material, which for germanium is quite small (*E*gap = 0.67 eV) (**Figure 2**). Therefore, thermal excitation produces noise in detectors, and thus active cooling has to be applied to some kinds of semiconductors, such as germanium.

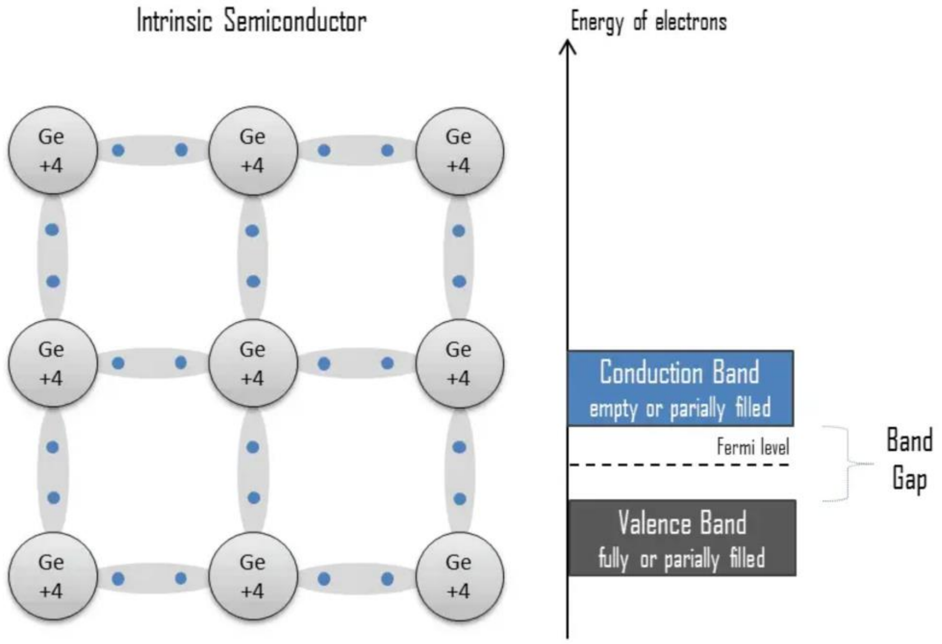

Figure 2. The influence of Egap on thermal excitation [27].

It deserves keeping in mind that a 1 cm^3 example of pure germanium at 20 ℃ consists of about 42 × 10^{22} atoms in addition to approximately 2.5 × 10^{13} complimentary electrons together with 2.5 × 10^{13} openings that are constantly produced from thermal power. Subsequently, the signal-to-noise proportion (S/N) is influenced [27].

2.1.3. Efficiency calibration

Using HPGe detectors, an efficiency calibration technique has been devised to assess the radioactivity of volume samples. The samples must be measured using the same measuring parameters as those used to calibrate the device in order to get accurate results [28].

A set of photopeak efficiencies over the energy region of interest, or a detection efficiency curve, must be known ahead of time in order to use the method. In addition to the detection technology, the sample shape and sample matrix with varying ambient sample densities and heights affect the detection efficiency curve. Since mass attenuation coefficients (μm) in environmental samples vary only little between samples, sample chemical composition variability is not a significant issue. Monte-Carlo calculations [29,30] can be used to estimate this effect or modeling [31]. Matrices increased [32]. In this instance, it is possible to experimentally determine and fit an efficiency curve for a wide range of matrices and energies. In order to achieve this goal, the standards' composition should as nearly resemble the samples' density, attenuation factors, and activity concentrations as feasible [33,34].

In order to reduce the deviation in the measured activity, the calibration standard source needs to have physical dimensions, a chemical composition, and a density similar to the samples that will be tested. In terms of geometry, if the container has the same dimensions and all of the samples and the standard source's heights are similar, the variance can be nearly eliminated.

2.1.4. Quality control

"In-house procedures" might be used to prepare the standards. This can be achieved by uniformly adding certified and traceable radionuclide solutions into inactive matrices that have the same density and composition as the material that needs to be tested. Like any other analysis method, γ-ray spectrometry requires standard samples to obtain the most precise experimental efficiency calibration in order to perform a quantitative analysis. However, if many configurations (e.g., different γ-ray detectors, geometries, densities, and sample shapes) are present, it can be time-consuming [35].

In order to calculate the activity of the various radionuclides contained in a sample, radioactive sources were prepared from two different standards, such as mixed standard QCY40, which contained 210Pb, 241Am, 109Cd, and 57Co, and standard QCY48, which contained 241Am, 109Cd, 57Co, 139Ce, 113Sn, 85Sr, 137Cs, 88Y, and 60Co. In terms of the measurement setups, we are pouring a certain volume of radioactive solution into a bottle that is partially filled with soil in order to prepare aqueous sources. The bottle is then consistently filled to the same height. Once the homogeneous soil has been added to the bottle until it reaches the required volume (weight or height), the bottles were sealed hermetically with a screw cap at the end.

2.1.5. Energy measurement

We measure the soil by itself in the same vial since it contains some naturally occurring radioactivity. By comparing the activity of the bottles with standard solution sources, the natural radioactivity of the soil was calibrated. At ZSR, gamma-ray data is analyzed using the GW program. The net count rate in the full-energy peak is then divided by the decay corrected gamma-ray emission rate of the standard source to determine the absolute detector efficiency at that energy [36].

2.2. Thallium activated sodium iodide detector NaI(Tl)

The NaI(Tl) scintillation detectors are one of the most commonly used detector systems used to measure gamma-ray detection (**Figure 3**). This can be explained by their low cost compared to HPGe detectors, high stability against thermal events and weather conditions (namely because they do not need additional cooling devices), etc. Furthermore, our NaI(Tl) scintillation detectors show huge detection efficiency [37].

The NaI(Tl) detector provides valuable benefits to users by allowing a variety of gamma spectroscopy studies to be performed at room temperature. This feature proves to be very beneficial for researchers. Additionally, the use of NaI(Tl) detectors with large surface areas effectively reduces the time required for measurements [38–40]. Unlike HPGe detectors, NaI(Tl) detectors offer the advantage of high absorption efficiency due to the presence of thallium (Z = 81) in their structure. This results in a high photo peak/Compton ratio.

Then again, HPGe detectors are known for their higher resolution capabilities [41] In the detection of gamma rays utilizing a NaI(Tl) detector, the physical interactions between the gamma rays and the crystal of the detector are well caught on, counting the photoelectric effect, Compton scattering, and pair production. To successfully measure gamma rays with a NaI(Tl) detector, it is fundamental to get parameters such as reaction work, energy resolution, and their relationship with experimental setup conditions like geometry, gamma ray energies, and source distance from the detector. Whereas experimental methods can give a few of this data, they are constrained by experimental conditions.

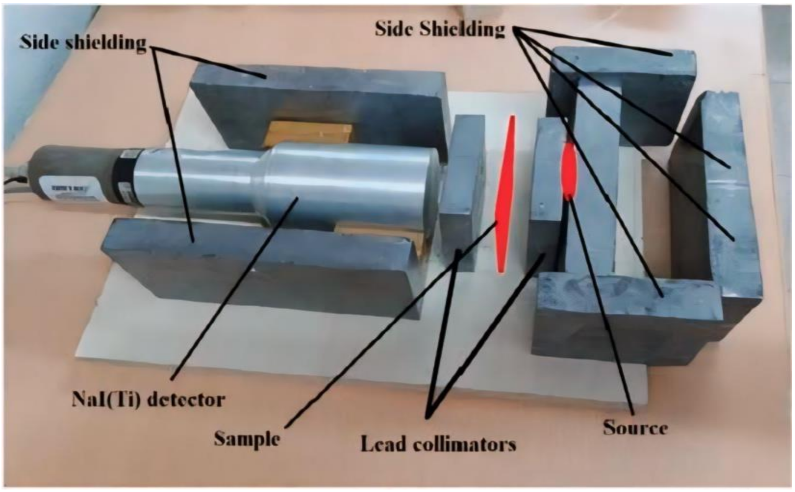

Figure 3. NaI(Tl) detector and its components [48].

Instead, Monte Carlo simulations, including the FLUKA simulation tool, provide the capability to gain a huge range of parameters without energy or setup obstacles. FLUKA is a flexible tool for calculating particle transport and interactions with matter, with programs ranging from accelerator shielding to detector design, dosimetry, and more.

FLUKA sticks out from other Monte Carlo applications because of its dual capability to function in both biased and absolutely analog modes, allowing for the prediction of fluctuations, signal coincidences, and uncommon events at the same time as presenting a variety of statistical techniques to investigate attenuations over many orders of magnitude [42,43].

Many publications have used FLUKA and many other Monte Carlo codes for research purposes. Among these publications, a notable part focuses on modeling the 3"×3" NaI(Tl) scintillation detector [44–48] some of which relate to the measurements performed for this specific target [47] and some of them are linked to the use of radiation doses [48].

The energy resolution of the 3" × 3" NaI(Tl) detector at about 49 keV turned out to be 7.4% for 662 keV gamma rays. This is close to the typical energy resolution reported for a NaI(Tl) detector detecting 662 keV gamma rays emitted from a 137Cs source. The resolution values of cylindrical detectors of this type are typically between 7.0% and 8.5%, and these values can be easily achieved with commercially available detectors [48].

The performance ranges from 186.1 to 2614 keV, showing two distinct regions, indicating variation in detector performance behavior due to attenuation and absorption processes. At lower photon energies, the absolute efficiency of the detector continues to increase as the attenuation of the radioactive source is significantly reduced. The observed gamma energy peak depends on detector and source characteristics. Beyond a few hundred keV, the performance gradually decreases. In the case of the NaI(Tl) detector, the absolute detection efficiency cannot be expressed as a single value. Detection efficiency is highly dependent on factors such as gamma-ray energy, source location, activity, and the shape and composition of the source detector system, all of which are contextual variables [49].

Most of the time, standard spectra obtained using at least three concrete pads enriched in K, U, and Th are used to calibrate portable gamma-ray spectrometers for use in natural radioactivity measurements. A background is represented by a pad free of radioactivity [50,51]. Typically, these pads have an area of at least 2 m^2 and a thickness of 0.5 m [52]. A more affordable and practically impractical approach was used in place of designing an ideal pad with a single radionuclide within and a flawlessly homogenous distribution of radioisotopes across its volume. The detector's performance is ascertained through two calibration stages. The process that allowed the obtained spectrum to be understood as a function of the energy connected to the decay events is known as energy calibration. This depends on how much radioactive element content there is in the system being studied. Finding the parameters that connected the count rate under a photopeak to the radionuclide's soil radioactivity concentration (BqKg-1) and air dose rate was the second step in the calibration process.

2.2.1. Energy calibration

Weighing reference materials from the International Atomic Energy Agency (IAEA) such as RGU, RGK, and RGTh in petri dishes allowed for the energy calibration of the detector. To illustrate the non-uniform dispersion of the radionuclide in the surroundings, standard materials were placed in petri dishes. The detector, which stood 140 mm tall, was positioned directly above the setup. This was permitted because the goal was to collect only the naturally occurring radioactivity that resulted from the low-gamma-emitting radionuclides found in the soil. The spectrum analysis technique used was the Window Analysis Method (WAM). This technique just takes the spectrum's region of interest into account [50]. Therefore, the single peak released by 40K at 1460 keV was studied to determine the concentration of potassium. Uranium, 238U, was found at 1765 keV from 214Bi, while Thorium, 232Th, was found by 208Tl's gamma rays at 2614 keV. Following a predetermined 300 s [53], the channels of the various photopeaks that corresponded to the gamma energies were recognized when a spectrum was captured. The software's calibration option was chosen, and each peak of interest's gamma energies were inserted against its channel number to complete the calibration process. The software consequently created a relationship between the gamma energy and the channel number. To acquire count rates owing to each radionuclide under its reference peak, the regions of interest (ROI) were carefully established around these photo peaks. Using the conversion parameters, these count rates were translated to radionuclide soil activity concentration.

2.2.2. Efficiency calibration

We can only infer the distribution of energy depositions in the detector's active volume from the pulse height distribution that was previously acquired from the detector and MCA. Efficiency calibration connecting the number of recorded counts in the detector to the ground deposition activity level is necessary for a radionuclide-specific measurement of the activity [54]. According to Beck et al. [55], the soil radioactivity concentration of the radionuclide causing the peak is correlated with the number of counts per second, acquired under a photopeak due to a specific gamma energy.

2.3. Liquid scintillation counting (LSC) technique

Ernest Rutherford used luminescence to detect α particles, making it one of the first techniques to measure radioactivity. Initially, the human eye could detect pulses of light. However, the advent of sensitive photodetectors, such as photomultiplier tubes (PMTs), paved the way for the development of scintillation counters. In 1950 [56,57], two independent groups reported that organic solutions could be used to detect β particles, leading to the advent of liquid scintillation. The first commercial clock was produced by Packard Instruments in 1953, and since then, many complex data processing techniques have been incorporated into LSC clocks following the invention of the microprocessor. Commercial production of LSC counters peaked around 1975, but there was then a steady decline due to the emergence of alternative non-radioactive monitoring techniques for biological purposes. At the same time, there was growing interest in LSC techniques in the field of radionuclide measurement, especially after the publication in 1979 of two quantitative LSC measurement methods: the triple coincidence ratio (TDCR) [58] and the CIEMAT/NIST method in 1982 [59]. Currently, the main focus of the commercial LSC market lies on providing low activity measurements and developing liquid scintillators with reduced toxicity levels.

2.3.1. Liquid scintillators composition

A liquid scintillator is capable of changing a portion of the energy from ionizing radiation into light. It is basically composed of scintillator molecules that are dissolved in an organic solvent. In order to tailor the liquid scintillation cocktail for particular applications, extra components such as a secondary solvent, secondary scintillator, surfactant, extractant, and quencher are added (**Figure 4**). The composition of the liquid scintillation cocktail ought to facilitate efficient transfer of energy between the solvent and scintillator solute while also allowing for the coexistence of the aqueous radioactive solution with the organic solvent. Be that as it may, these requirements can now and then clash, making the improvement of an ideal liquid scintillator cocktail a matter of compromise.

The solvent plays a vital role in the cocktail as it absorbs the energy radiated by charged particles from the radionuclide and transfers this energy to the fluorescent molecules. Aromatic organic molecules are commonly utilized as liquid scintillator solvents. Whereas benzene and toluene were already utilized, less poisonous solvents like xylene or pseudocumene are presently favored. In recent years, a new generation of aromatic solvents, such as di-isopropyl naphthalene (Din), phenyl xylyl ethane (PXE), and dodecylbenzene (DB), have been developed. These solvents offer reduced toxicity and higher flash points, although they may show lower stability and production consistency. It is vital to note that these new solvents are mixtures of different products and isomers, and the producer cannot ensure that the composition of products sold under the same commercial title will stay unaltered. Solvents have lower toxicity and higher flash points but may have lower stability and consistent production. The new solvents are mixtures of various products and isomers, so the producer cannot guarantee the composition remains unchanged for products sold under the same name.

The primary scintillator, displayed in concentrations extending from 5 g/L to 10 g/L of solvent, is responsible for converting the excitation energy of the solvent molecules into light. Commonly utilized primary scintillators include 1,5-diphenyloxazole (PPO), p-terphenyl (TP), 2-phenyl-5-(4-diphenyl)-1,3,4-oxadiazole (PBD), and (2-(4-t-butylphenyl)-5-(4-biphenyl)-1,3,4-oxadiazole (butyl-PBD). However, other fluorescent molecules, such as laser dyes, can also be utilized in this part.

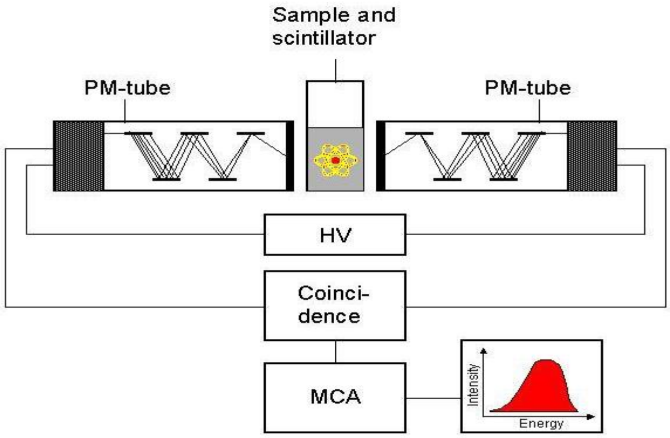

Figure 1. LCS detector and its components [60].

The secondary scintillator is utilized in LS cocktails to adjust the scintillator emission range to match the greatest sensitivity of the photocathodes of PMT. It is ordinarily shown in a mass concentration of roughly 0.5 g/L of solvent. The scintillators utilized for this reason include 1,4-di-(2-(5-phenyloxazolyl)) benzene (POPOP), p-bis-(o-methyl styryl) benzene (bis-MSB), or 1,4-di-(2-(4-methyl-5-phenyloxazolyl)) benzene (DM-POPOP).

In LS cocktails that are water-miscible, the addition of a surfactant is necessary to guarantee the miscibility of the radioactive aqueous sample with the primary solvent-solute system. The surfactants are ordinarily shown in amounts up to 30% by weight. To upgrade detection efficiency, non-ionic aromatic surfactants with great energy propagation properties are favored. One such surfactant is iso-octyl phenoxy-poly ethoxy ethanol (Triton X-100®). On the other hand, a polar molecule that allows the coexistence of organic and aqueous phases inside a constrained volume range can be utilized as a substitution for surfactants. Whereas ethanol was previously utilized for this reason, phenoxyethanol is presently favored due to its energy transfer properties, which help limit the reduction of scintillator light yield caused by the addition of the surfactant.

Certain LS cocktails contain extractant molecules in molar concentrations of roughly 10^{-2} mol/L. These extractants facilitate the liquid-liquid extraction of the radionuclide from the aqueous phase into the scintillator organic phase. Organic extractants such as di-2-ethylhexylphosphoric acid (HDEHP) or tri-n-octyl phosphine (TOPO) are commonly utilized. These extractants not only enhance the stability of the scintillator but also improve the detection efficiency for particular elements.

In some LS cocktails, a secondary solvent is presented in mass concentrations of up to 200 g/L to improve the differentiation between electron and alpha particle responses. Aromatic molecules with long half-life triplet states, such as naphthalene or naphthalene compounds, are regularly utilized for this purpose.

If wanted, a chemical quencher can be added to LSC cocktails to decrease the scintillation efficiency.

2.3.2. Transfer of energy in the scintillator

Radionuclide decay radiation traverses the liquid scintillator and primarily interacts with the solvent molecules. The interaction between radiation and matter generates incident electrons or secondary electrons, which in turn excite or ionize the solvent molecules. In any case, a critical portion of the incident energy is dissipated as heat.

Approximately 10% of the energy is transferred to excited singlet and triplet molecular states. Singlets rapidly return to their ground state S1 through de-excitation, whereas triplets lose their energy through internal change and cannot directly transmit light. All things considered, bimolecular triplet-triplet reactions can deliver singlet states, enabling light emission. The extents of excitation and ionization depend on the stopping power and energy of the incident particle, with alpha particles causing more ionizations compared to electrons. Both ionization and excitation can result in fluorescence, but triplet production is more prominent in ionization.

The energy migrates from one solvent molecule to another within a sub-nanosecond timeframe until it is either trapped by a solute molecule or scattered as heat. These energy transfer processes happen without radiation. Fluorescence occurs when excited singlet states of the solute experience radiative de-excitation. The decay time constants for fluorescence are typically a few nanoseconds.

On the other hand, light production through de-excitation of triplet states, known as phosphorescence, is less likely as it requires triplet-triplet bimolecular reactions. Consequently, the decay time for phosphorescent emission is longer.

The spectrum of emitted photons is particular to the fluorescent solute and solvent species. If a secondary solute is shown, the energy transfer to it happens through radiation [61].

2.3.3. The CIEMAT/NIST method

The CIEMAT/NIST method is exemplified in **Figure 5**, where the initial step involves calculating the efficiency of a system with two PMTs in coincidence according to Peng and Li [62] with P (E, λ) and $R = 2$. This calculation must be carried out for both the nuclide under investigation and a tracer nuclide, typically 3H. By introducing the free parameter $M = \lambda$, a connection between the counting efficiencies of the two radionuclides is established, allowing for the determination of the counting efficiency of the nuclide under study, $\varepsilon_{\text{nuclide}}$, in relation to the counting efficiency of the tracer, $\varepsilon_{\text{tracer}}$. This relationship is known as the 'efficiency curve'. Subsequently, the calibration curve, which represents the counting efficiency of the tracer, $\varepsilon_{\text{tracer}}$, as a function of the quenching indicator, QIP, is determined. This process involves preparing a series of approximately ten vials, each containing a scintillation cocktail and a known quantity of a tritium activity standard solution. Starting from the second sample, increasing amounts of a quenching agent are added to reduce the counting efficiency. Since the activities of the tritium samples are already known, the measured net counting rates provide the counting efficiencies ε_{tracer}. Furthermore, the quenching indicator QIP is automatically measured for each sample using an external standard source integrated into the counter system.

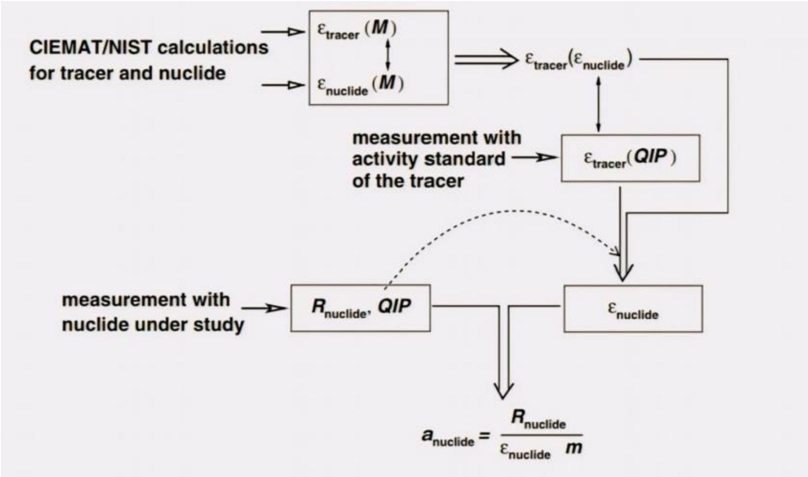

Figure 5. Illustration of the CIEMAT/NIST method [61].

R denotes the measured counting rate, *M* is the free parameter, QIP is the quench Indicating parameter, ε is the counting efficiency, $a_{nuclide}$ is the solution activity concentration and *m* is the mass of solution in an LSC sample.

In conclusion, a sample series is meticulously prepared using a solution of the nuclide being investigated. It is imperative that the sample composition and measuring geometry closely resemble those used in the calibration measurements. The counting rate and the quenching indicator QIP of the sample series are then accurately measured.

The QIP indicator enables the determination of the tracer efficiency from the calibration curve. Once the tracer efficiency is known, the nuclide efficiency can be determined using the efficiency curve. Consequently, all necessary information is available for calculating the activities of the samples and the activity concentration of the solution.

2.3.4. Quality control

Periodic global checks of the LS counter are essential, especially after significant changes in the counter. While the IEC 1304 standard provides guidance for conducting these checks [61], it is important to note that the document contains outdated information. Therefore, it is recommended to adhere to the principles outlined in the standard rather than strictly following the outdated details. Various checks, such as repeatability, reproducibility, fidelity, and linearity, should be performed using reference LS sources. Typically, pure organic 3H or 14C labeled scintillators enclosed in flame-sealed ampoules are used as reference sources. Although IEC 1304 suggests replacing these reference sources every five years, practical experience indicates that they can remain stable for decades if stored at a moderate temperature (below 20 ℃) in a dark environment. The linearity of the counter's performance can be assessed by employing a series of reference LS sources that exhibit progressively higher levels of activity. This particular test enables the identification of the operational range within which the counting rate remains accurate, while also providing a means to rectify any counting bias that may occur beyond this range.

2.2.5. Calculation of energy spectra

The determination of the counting efficiencies necessitates the calculation of the energy spectrum that is transferred to the liquid scintillator, denoted as *S€*. This energy spectrum is normalized.

$$\int_0^{E\text{max}} S(E)\mathrm{d}E = 1$$

This range encompasses electrons that originate either from the decay of the initial isotope or from rearrangement processes occurring in the shell of the daughter atom. Furthermore, photons resulting from the decay process can transfer energy to electrons through Compton scattering and the photoelectric effect. If the energy of the photon exceeds 1.022 MeV, it can also generate an electron-positron pair.

3. Case studies

In this section, we will discuss case studies where they used the methodologies mentioned before and how they used them in their experimental work in their research.

3.1. Intercomparison NaI(Tl) and HPGe spectrometry to studies of natural radioactivity on geological samples

A case study by Hung et al. [63].

3.1.1. Experimental setup

The NaI(Tl) detector’s scintillation crystal is a cylindrical shape measuring 7.62 cm × 7.62 cm and is made by Canberra, Inc., USA. This detector is connected to an Osprey™ tube, which serves as a modern, all-in-one multi-channel analyzer (MCA) tube base designed to facilitate scintillation spectrometry [64].

Table 1. Parameters of the HPGe detector [63].

Main parameters	**Geometrical parameters**	**Value**
Relative efficiency		35%
Energy resolution (FWHM) at 1332 KeV (Co60)		2 KeV
Peak-to-Compton ratio (Co60)		66:1
Geometrical parameters of the detector	Window thickness (mm)	1.5
	Crystal-window distance (mm)	5
	Crystal dead layer thickness (outer) (mm)	0.46
	Crystal dead layer thickness (inner) (µm)	0.3
	Crystal length (mm)	50.1
	Crystal diameter (mm)	62.2
	Crystal hole depth (mm)	23
	Crystal hole diameter (mm)	7.5
	Side cap thickness (mm)	1.5
	Side cap diameter (external) (mm)	76.2

This integrated module comprises a high-voltage power supply (HVPS), a preamplifier, and a comprehensive digital MCA. It is operable through a single cable connecting the Osprey™ to the control and information acquisition systems. The HPGe detector, given by Canberra, Inc., USA, is developed with a p-type high-purity germanium material (**Table 1**).

The concentration of 238U was determined by analyzing the activities of 226Ra (186.2 keV), 214Pb (241.9 keV, 295.2 keV, and 351.9 keV), and 214Bi (609.3 keV, 1120.3 keV, 1764.5 keV, and 2204.2 keV). On the other hand, the concentration of 232Th was calculated based on the activities of 212Pb (238.6 keV), 208Tl (583.2 keV, and 2614.5 keV), and 228Ac (338.3 keV, and 911.1 keV). The activity of 40K was determined directly from the gamma line at 1460.8 keV. The analysis of gamma rays' spectra and information processing were carried out utilizing Geniee 2K software, which was also utilized for the show and processing of spectra from both detectors. The acquisition time for background, reference, and samples was set at 86,400 s each. Peak identification and resolution of overlapping peaks were performed utilizing Colegram software [65].

3.1.2. Reference sample

The NaI(Tl) detector's efficiency was experimentally calibrated using three reference samples from the International Atomic Energy Agency [66]: RGK-1, RGTh-1, and RGU-1. These samples have mass activities of 14,000 ± 400 Bq/kg, 3250 ± 90 Bq/kg, and 4940 ± 30 Bq/kg, respectively. Moreover, the RGU-1 source was utilized to establish the standard curve of efficiency for the HPGe detector. This calibration was conducted inside the energy range of 46.5 keV to 2204.2 keV, particularly focusing on 210Pb (46.5 keV), 234Th (63.3 keV), 226Ra, 214Pb, and 214Bi (in equilibrium with its parent 238U with a mass activity of 4940 ± 30Bq/kg) for the evaluation of 238U.

In our analysis, we encountered a sample that emits gamma transitions of 186.2 keV and 185.7 keV, compared to 226Ra and 235U, respectively. By examining the count rate in the 186 keV region, we can apply a correction factor of 0.5709 to precisely determine the value of 226Ra and get an extra result for 235U [67]. The ACORES software is utilized to fit the experimental efficiency curves to a log-log polynomial [68] (see **Figure 6**).

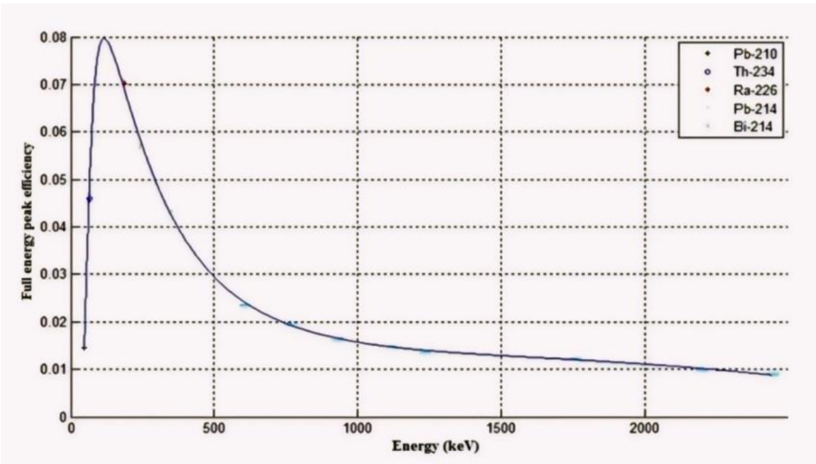

Figure 6. Experimental full energy peak efficiency calibration curve for volume source [63].

3.1.3. Sample data.

The Southern Geological Mapping Division collected the samples from a location in Vietnam's environment. Each area yielded more than 200 g of material, which was carefully collected and ground into dust. In this way, the samples underwent sieving and were set in cylindrical containers. These containers were, at that point, sealed off in the laboratory for a minimum of 30 days. This duration is significant to prevent any radon from escaping and to avoid any potential disequilibrium issues between 226Ra and its corresponding progenies (**Table 2**) [63].

Table 2. The information of the standard and the samples [64].

Sample	Mass (g)	Density (g/cm^3)
RGK-1	135	1.62
RGU-1	130	1.55
RGTh-1	119	1.42
S1	140	1.68
S2	116	1.39
S3	132	1.57
S4	136	1.63
S5	132	1.57

The cylindrical container, which housed both the standard and sample sources, had particular qualities. These included an external diameter of 75 mm, a wall thickness of 2 mm, and a bottom thickness of 2 mm. Besides, the container was filled to a height of 20 mm [63].

3.1.4. Results

The background and sample of both detectors **Figure 7a,b** were compared.

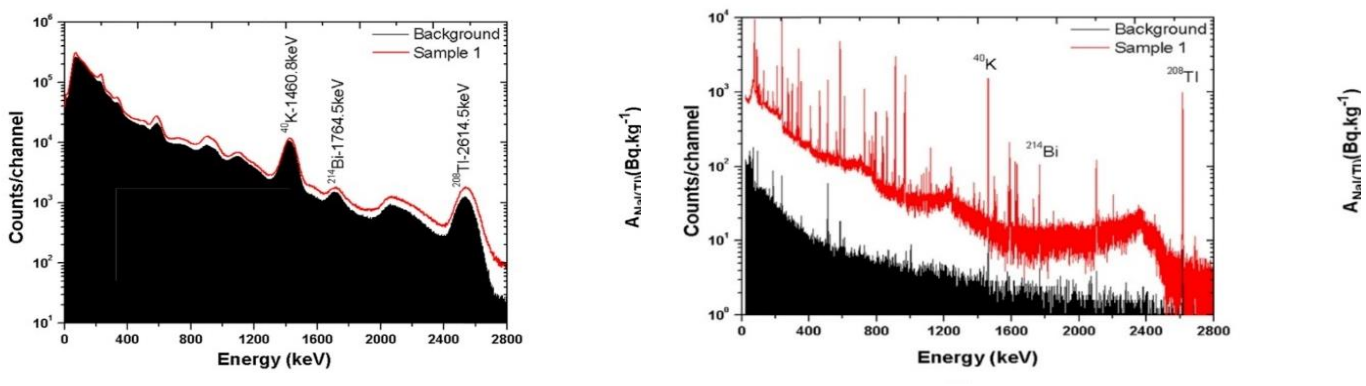

(a) **(b)**

Figure 7. Sample 1 and background spectra resulting from 86,400 s acquisition time; **(a)** for NaI(Tl); **(b)** for HPGe detectors respectively [63].

At first, the efficiency of the NaI(Tl) detector was experimentally calibrated using the kit standard to determine the activities of radionuclides in the sample. At the same time, the HPGe detector in the laboratory was utilized to measure the activities of the radionuclides in the sample. In accordance with Equation (1) [63], the mass activity of radionuclide for each peak with energy *E* was calculated based on the net peak area, *Np€*, the relevant photon emission intensity, *I€*, the efficiency, *ε€* for the calibration conditions, acquisition live time (s), dry mass (kg), and the product of different correction coefficients such as coincidence summing, radioactive half-life.

$$A_i = \frac{NP(Ei)}{\varepsilon P(Ei) \times I(Ei) \times t \times m} \times IICi \quad (1)$$

The results, along with their corresponding combined standard uncertainties [69], are displayed in this study. The relative uncertainties mentioned in this paper are based on the combined standard uncertainties (k = 1). The computation of these uncertainties includes factors such as peak area, interpolation efficiency derived from a function, and the intensity of photon emission that is relevant to the analysis. To assess the performance of the estimation procedure for the samples, both detectors were utilized. The evaluation followed the approach utilized by the International Atomic Energy Agency (IAEA) in recent intercomparison exercises and proficiency tests [70].

The *U*-score is decided by utilizing the data obtained from the Nal(T) detector, the HPGe detector, and a standard deviation, as outlined in the subsequent formula:

$$U_{\text{score}} = \frac{A(\text{HPGe}) - A(\text{NaI(Tl)})}{0.1 \times A(\text{HPGe})}$$

The performance assessment of the Nal(TI) detector is considered satisfactory if the U_{score} is equal to or greater than 2. It is considered questionable if the *U*-score is greater than 2 but less than 3, and it is considered unsatisfactory if the *U*-score is equal to or greater than 3. The *A*(HpGe) represents the activity concentration value gotten from the HPGe detector, while the *A*(NaI(Tl)) represents the activity concentration result detailed by the NaI(TI) detector. The relative bias (RB) is calculated using the following equation:

$$RB = 100 \times \frac{|A(\text{HPGe}) - A(\text{NaI(Tl)})|}{A(\text{HPGe})}$$

Accuracy assessment: the findings are deemed satisfactory if:

$$\left|A(\text{HPGe}) - A\big(\text{NaI(Tl)}\big)\right| \leq 2.58 \times \sqrt{U_{\text{HPGe}}^2 + U_{\text{NaI(Tl)}}^2}$$

The standard uncertainties $U_{\text{NaI(Tl)}}$ and U_{HPGe}, along with a parameter of 2.58, are utilized to evaluate the probability of a result passing a test at a 99% confidence level.

The calculation of precision (*P*) assessment requires adherence to the prescribed formula:

$$P = 100\% \times \sqrt{\left(\frac{U_{\text{HPGe}}}{A_{\text{HPGe}}}\right)^2 + (\frac{U_{\text{NaI(Tl)}}}{A_{\text{NaI(Tl)}}})^2}$$

The NaI(Tl) detector results are regarded as satisfactory for precision when the specified condition is met:

$$P \leq \text{LAP}$$

In this investigation, we set the LAP (limit of acceptable precision) and MAB (maximum acceptable bias) at roughly 10% for each radionuclide. To accomplish the designation of “acceptable,” the result must demonstrate satisfactory levels of accuracy and precision. If either precision or accuracy is regarded as “not acceptable,” the RB is compared to the MAB. If RB < MAB, the result is labeled as a “warning”; on the other hand, if RB > MAB, the result is classified as “not acceptable.” The maximum deviation of the *U*-score is 0.52 for the radionuclides present in the samples, indicating that the values obtained from both the Nal(TI) and HPGe detectors meet the *U*-score criteria. Besides, there is a solid agreement in relative bias when utilizing both detectors.

The findings are illustrated in **Figure 8a–c**, which shows the relative activities of 238U, 232Th, and 40K, respectively. **Table 3** outlines the mass activities of the samples, with a maximum relative deviation of roughly 5% for both detectors, except for radionuclide 238U in sample (S2). Following the proficiency test protocol for assessing accuracy and precision, all radionuclides passed the evaluation. Consequently, the overall performance of the analytical determinations in the proficiency test meets the criteria for acceptability, with all results considered "acceptable" for the radionuclides present in the samples [63].

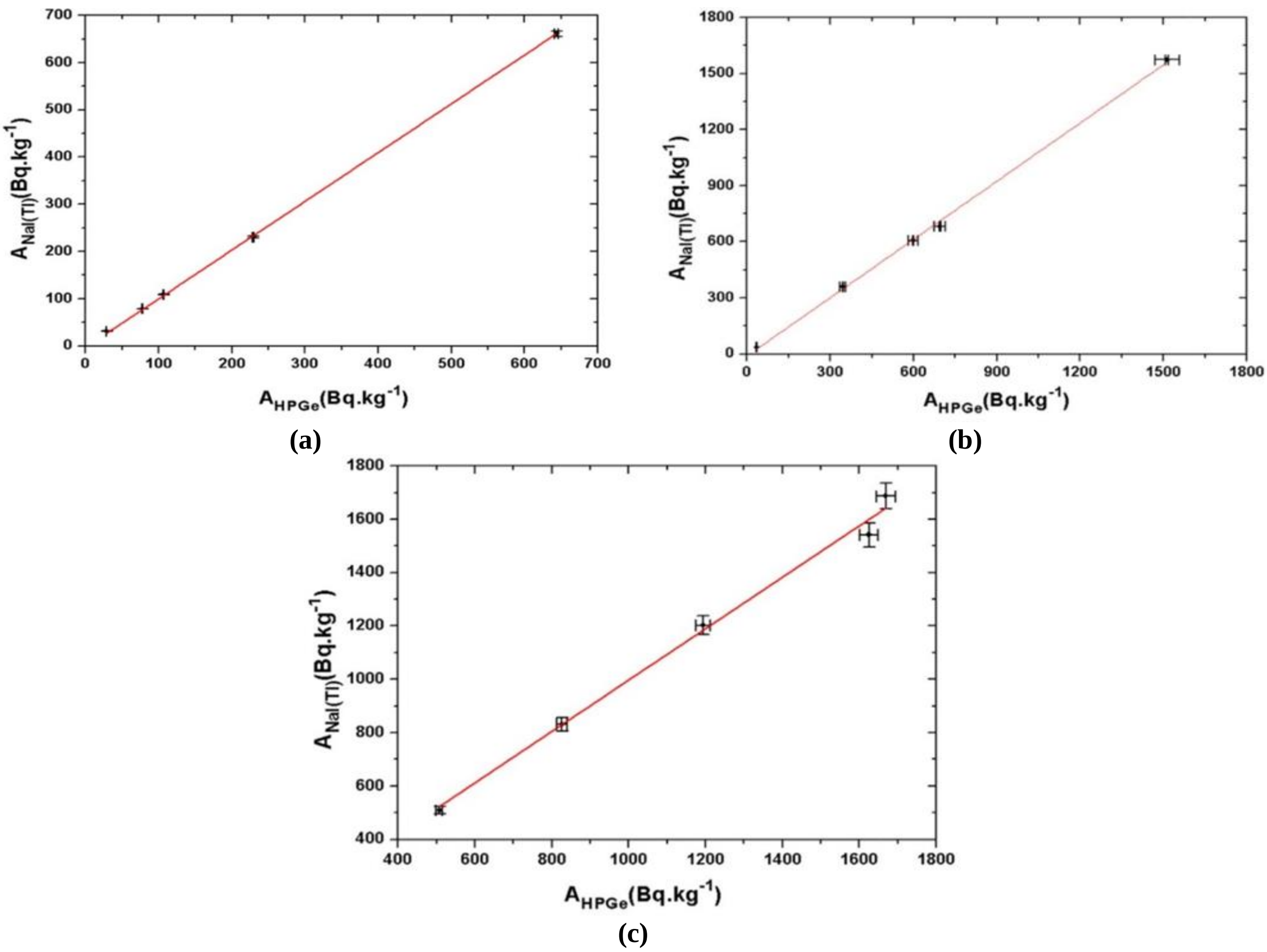

Figure 8. Relative function of radioactive of both detectors: **(a)** for 238U; **(b)** for 232Th; **(c)** for 40K respectively [63].

Table 3. Mass activities are measured using NaI(Tl) and HPGe detectors respectively [63].

	Mass activity (Bq·kg^{-1})					
	238U		**232Th**		**40K**	
Sample	**NaI(TI)**	**HPGe**	**NaI(TI)**	**HPGe**	**NaI(TI)**	**HPGe**
S1	78.65 ± 0.25	77.48 ± 0.52	681.84 ± 19.3	694.88 ± 2.49	1540.87 ± 44.54	1625.7 ± 23.8
S2	30.77 ± 0.77	28.58 ± 0.26	360.71 ± 10.38	345.3 ± 1.39	1202.4 ± 34.89	1193.54 ± 18.14
S3	230.28 ± 2.51	229.24 ± 1.21	606.43 ± 17.22	598.84 ± 2.21	1687.37 ± 48.74	1669.45 ± 24.45
S4	108.93 ± 0.53	106.83 ± 0.67	1573.62 ± 44.12	1513.33 ± 5.09	509.26 ± 15.06	507.37 ± 8.83
S5	661.29 ± 5.63	643.58 ± 3	35.32 ± 1.32	34.45 ± 0.28	831.3 ± 24.33	826.48 ± 13.45

3.2. Anomalous concentrations of radionuclides in the groundwater of Ede Area, southwestern Nigeria: A direct impact of geology

A case study by Adetunji et al. [71].

3.2.1. Methodology

In November (during the dry season), a study was conducted to sample groundwater in different zones of Ede. A total of 15 samples were collected utilizing a standardized sampling method. Out of these, ten samples were obtained from Ede town, whereas two samples each were collected from Iddo and Ekuro, and one sample from Iwoye communities. The sampling areas are denoted as S1–S15 on the geological map. Thirteen of the samples were taken from hand-dug wells, while the remaining two samples were extracted from boreholes. To guarantee the purity of the samples, plastic containers were used, which were first rinsed with distilled water to eliminate any foreign substances. Hence, the containers were further rinsed with the water sample collected from each particular area. To avoid any external contamination or mix-up with other water samples, the containers were firmly sealed and labeled accordingly.

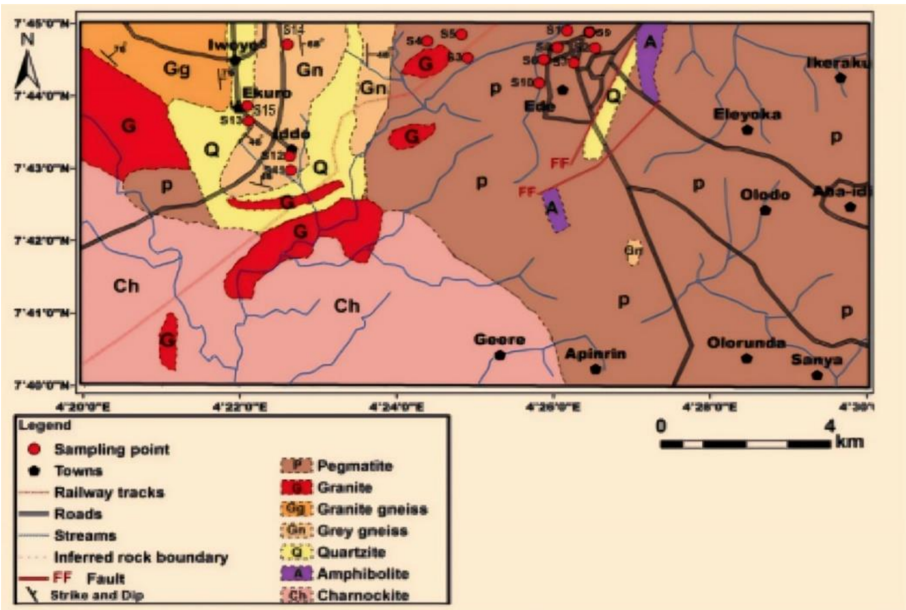

Figure 9. Geological map of Ede Area (the sampling points are indicated as S1–S15) [71].

The exact coordinates of sampling destinations were established utilizing a global positioning system (GPS) and, in this way, marked on the geological map of the research region (see **Figure 9**) [71].

The sodium iodide gamma spectrometer at the Centre for Energy Research and Development (CERD) at Obafemi Awolowo University, Ile-Ife, Nigeria, was utilized to determine the radionuclides present in the water. To prepare the water samples for analysis, hydrochloric acid was added. Each water sample, measuring 250 cm^3, was then carefully stored in an airtight and properly sealed container inside the laboratory for a duration of 28 days. This period permitted the establishment of secular equilibrium between isotopes and their respective daughters before conducting gamma-ray spectrometry analysis. It is worth noting that this specific technique has been broadly utilized by various analysts in the field [72–74].

After this time period, the hermetically sealed containers were individually positioned inside a strong lead enclosure and secured with a substantial seal. Attached to the lead enclosure was a sodium iodide radiation detector that produced electronic charges through ionization due to gamma-ray emissions. The spectrometer is comprised of a Canberra 7.6 cm by 7.6 cm NaI(TI) detector connected to a Canberra Series 10 Plus Multichannel Analyzer (MCA) through a preamplifier base. Protection of the environment from radiation was fulfilled by utilizing a Canberra 10-cm-thick lead castle [75].

Counting was conducted for a duration of 10 h due to the minimal natural activities of radionuclides present in the water. The spectrum was evaluated, and the calculation of the area underneath the photopeaks was carried out utilizing the MCA algorithm. The significant photo peaks detected in the samples' spectra were recognized as originating from radionuclides inside the natural decay series of 238U and 232Th, as well as the non-series 40K. To identify the gamma energy peaks, the spectra analysis software SAMPO 90 was utilized to compare them with a library of potential radionuclides [76–80].

3.2.2. Results

The data on radioactivity levels in the media samples are shown in **Table 4**. Radioactivity is measured in the Becquerel (Bq), with 1 Bq equivalent to 1 disintegration per second. The recommended levels for radioactivity in drinking water are expressed as the activity concentration of the radionuclide per liter, denoted as Bq/L. In the study area, the uranium-238 series (radon-222 and radium-228) were identified as the most predominant radionuclides in water. The activity concentration of the uranium series ranged from 7.24 ± 0.24 to 23.76 ± 0.31 Bq/L, with an average of 13.256 Bq/L over the four communities. Specifically, Ede had an average activity concentration of 13.645 Bq/L, ranging from 23.76 ± 0.31 to 7.24 ± 0.24 Bq/L. This shows that the average radioactivity level in Ede surpasses the regional average (13.256 Bq/L) for the whole area by roughly 0.389 Bq/L. Iddo and Ekuro had average values of 11.685 ± 0.3 Bq/L and 13.49 ± 0.7 Bq/L, respectively, while Iwoye recorded a value of 12.04 ± 0.23 Bq/L.

The concentration of thorium series activity in the whole area varies from 6.42 ± 0.53 to 20.97 ± 0.66 Bq/L, with an average value of 10.51 Bq/L. In contrast, samples collected from Ede display a range of values from 20.97 ± 0.66 Bq/L to 4.08 ± 0.89

Bq/L, with an average value of 11.182 Bq/L.

Table 4. Radionuclides concentrations in water samples from the study area [71].

S/no.	Location	Nature	Bed rock	40K (Bq/L)	238U (Bq/L)	232Th (Bq/L)
1	Ede	Hand dug	Pegmatite	9.03 ± 0.97	23.76 ± 0.31	10.10 ± 0.5
2	Ede	Hand dug	Pegmatite	15.71 ± 0.83	17.85 ± 0.22	7.30 ± 0.49
3	Ede	Hand dug	Pegmatite	23.82 ± 0.83	10.62 ± 0.22	19.84 ± 0.53
4	Ede	Hand dug	Pegmatite	10.08 ± 0.87	9.90 ± 0.23	14.62 ± 0.55
5	Ede	Hand dug	Pegmatite	27.74 ± 0.74	9.61 ± 0.302	8.38 ± 0.52
6	Ede	Hand dug	Pegmatite	21.58 ± 0.95	22.47 ± 0.30	20.97 ± 0.66
7	Ede	Hand dug	Pegmatite	16.61 ± 0.83	7.24 ± 0.24	11.14 ± 0.52
8	Ede	Hand dug	Pegmatite	17.18 ± 0.91	10.45 ± 0.25	8.54 ± 0.58
9	Ede	Hand dug	Pegmatite	13.63 ± 0.81	10.51 ± 0.25	4.08 ± 0.59
10	Ede	Hand dug	Pegmatite	16.11 ± 1.01	14.04 ± 0.23	6.58 ± 0.55
11	Iddo	Borehole	Grey gneiss	14.00 ± 0.96	13.46 ± 0.30	9.00 ± 0.55
12	Iddo	Borehole	Grey gneiss	4.53 ± 0.96	9.91 ± 0.29	6.58 ± 0.66
13	Ekuro	Hand dug	Quartzite	9.68 ± 0.77	15.21 ± 0.30	6.42 ± 0.53
14	Iwoye	Hand dug	Grey gneiss	21.21 ± 0.78	12.04 ± 0.23	12.25 ± 0.56
15	Ekuro	Hand dug	Quartzite	3.47 ± 1.01	11.77 ± 0.23	11.63 ± 0.67

This data demonstrates that Ede has a higher thorium-232 activity, surpassing the combined activity of the four other communities by around 0.632 Bq/L. The average activity values for Iddo and Ekuro are 7.79 ± 0.605 Bq/L and 9.025 ± 0.6 Bq/L, respectively. On the other hand, Iwoye demonstrates an activity value of 12.25 ± 0.56 Bq/L.

The analysis results demonstrated that the activity concentration for 40K varies from 3.47 ± 1.01 to 27.74 ± 0.74 Bq/L, with a normal of 14.96 Bq/L over the whole area. In Ede, the values range from 27.74 ± 0.74 to 9.03 ± 0.97 Bq/L, with an average of 17.149 Bq/L. The average concentration in Ede surpasses the regional average (average for all four communities). Samples from Iddo and Ekuro show average concentrations of 9.265 ± 0.96 Bq/L and 6.6 ± 0.89 Bq/L, respectively, while Iwoye has a concentration of 21.21 ± 0.78 Bq/L.

In general, there is increased activity observed in all of the samples, in spite of variations in the concentrations of the radionuclides across different locations. **Figure 10**. The concentration of potassium remains consistently high in about all of the samples, reaching its peak in sample 5 (Ede) and its lowest in sample 15 (Ekuro). The elevated activity of 40K can be attributed to the abundance of potassic or K-feldspar ($KAlSi_3O_8$), which is the second most predominant mineral in these felsic rocks. On the other hand, quartz (SiO_2), the most abundant mineral, does not host any other elements other than oxygen and silicon to a significant extent.

The uranium series exhibits its highest concentration in sample 1 (Ede) and its lowest concentration in sample 7 (Ede). Similarly, the thorium series reaches its peak concentration in sample 6 (Ede) and appears to have its least concentration in sample 9 (Ede). Notably, sample 6 in Ede demonstrates equal activity concentrations for all the radionuclides.

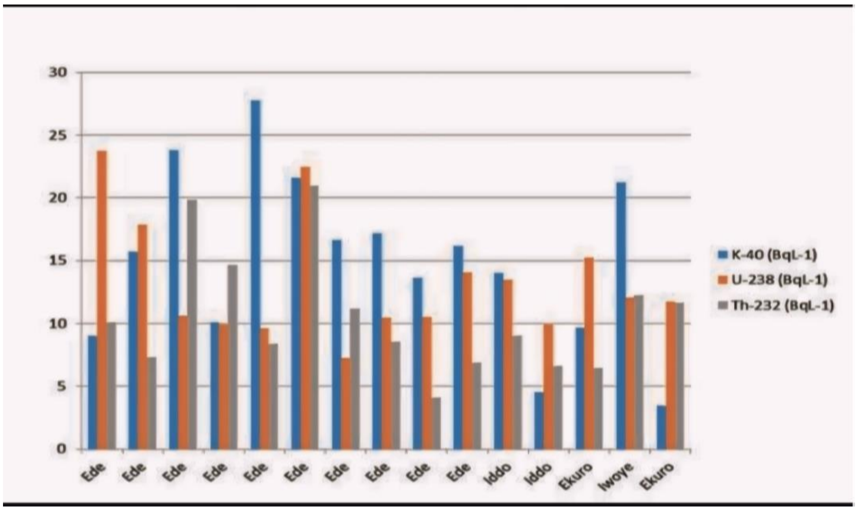

Figure 10. Bar chart showing radionuclides concentration in water samples from the study area [71].

3.3. Measurement of 226Ra in river water using liquid scintillation counting technique

A case study by Hamzah et al. [81].

Scintillation counting was used for measurement of 226Ra in water samples from Sungai Kelantan, mainly in the district of Kuala Krai.

3.3.1. Sampling site

Figure 11 shows a geological map of the Kelantan region, delineating the boundaries of the 10 area regions. The predominant geological features in Kelantan consist of undifferentiated acid intrusive rocks as well as formations from the Triassic and Permian periods. Furthermore, **Figure 12** outlines the particular areas where river water samples were collected within the Kuala Krai district.

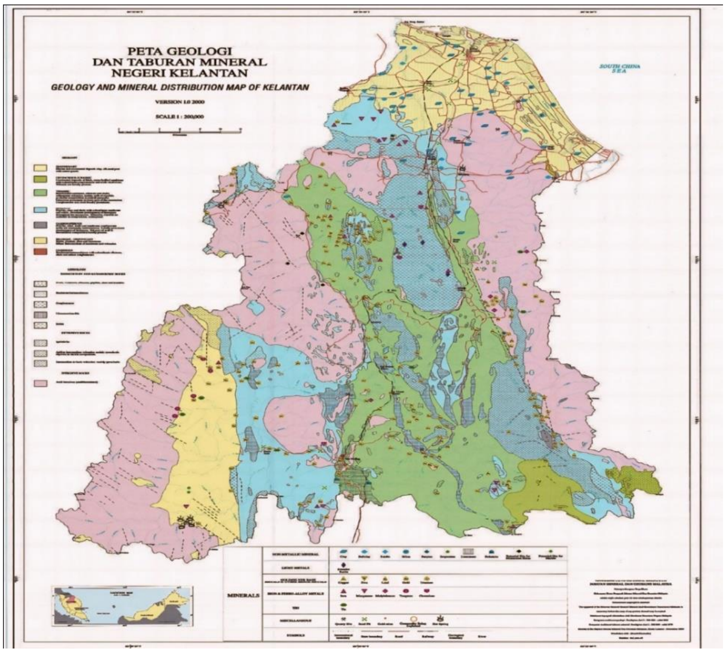

Figure 11. Geological map of Kelantan [81].

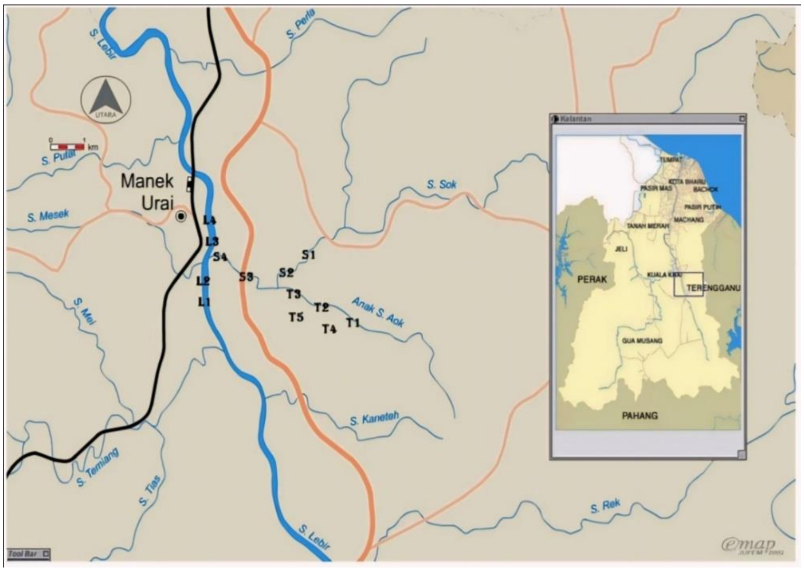

Figure 12. Area of sampling [81].

3.3.2. River water sample

To analyze the presence of 226Ra in a river sample, roughly 10 L of the untreated sample was carefully collected in a polyethylene bottle that had been completely cleaned with HNO_3 and distilled water. The collection of water samples was done at the midpoint of the river to guarantee their representativeness and to include the desired elements of interest, such as radionuclides. In order to protect the water and prevent any loss of radionuclides through sorption in the bottles, concentrated HNO_3 was promptly added to the raw sample at a ratio of 1 mL HNO_3 per 1 L of water [82].

These samples were obtained at a depth ranging from 0.01 to 0.3 m within the river. The water samples are passed through a membrane filter with a porosity of 0.47 µm and a diameter of 47 mm in order to remove suspended solids and impurities. In this way, 1 L of the filtered samples is transferred into Schott bottles, followed by the addition of 100 mL of scintillator to the samples.

3.3.3. Reagents and solutions

The scintillator was prepared by measuring 4.0 g of 2,5-diphenyloxazole (PPO) and 0.4 g of 1,4-bis(5-phenyloxazol-2-yl)-benzene (POPOP), which were then added to 1 liter of toluene of scintillation grade [83].

To guarantee a uniform dissolution in the solvent, the scintillator was stirred for a duration of 24 h. In this way, 100 mL of the scintillator was added to the 1 L water samples and allowed to incubate for a period of three weeks. Finally, 20.0 mL of the liquid scintillation cocktail was transferred into a polyethylene vial and promptly measured by liquid scintillation counting (LSC).

The liquid scintillation counter was utilized to measure the scintillation cocktail twice, with each cycle lasting 100 min. The counting method followed protocol 18 of Packard TRICAB 2700. The concentration of 226Ra was determined by calculating the total alpha peaks of 226Ra and its daughters (222Rn) in the alpha spectrum region [84].

3.3.4. Results

The range of these concentrations for the filtered sample is from 0.1095 Bq/L to

0.5483 Bq/L. Notably, the highest concentration is observed at the Manik Urai Bridge. It is worth saying that the activity concentrations of 226Ra from all 13 areas have surpassed the limit established by the Interim National Water Quality Standards for Malaysia (INWQS), which states that the activity concentration of 226Ra in water should not surpass 0.1 Bq/L. These findings suggest that 226Ra is dissolved in the water rather than merely being attached to suspended solids.

There are three particular sections of sampling in the study area, which are characterized by the small Sok River joining the Sok River and later joining the Lebir River. These rivers exhibit a progressive increase in size, starting from a small stream and gradually changing into a larger river. The collected information indicates a consistent pattern over all sections, where the activity concentration of 226Ra in each river section increases as the water flows downstream. This suggests that there may be a buildup of 226Ra in the water due to erosion within the river basin. **Figure 13a–c** depicts the measured activity concentrations of 226Ra in all sections of the study area.

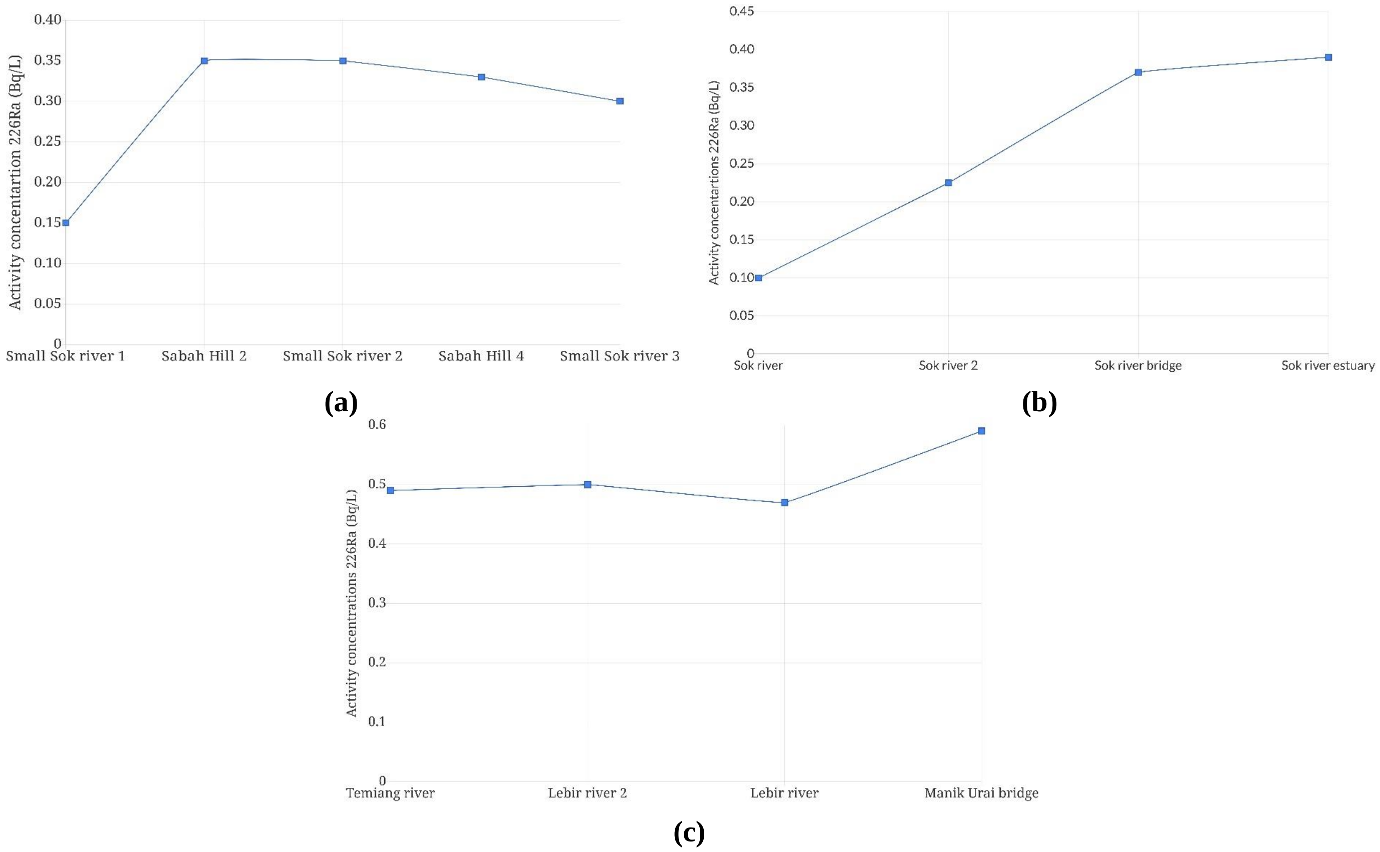

Figure 13. Activity concentrations of 226Ra measured along the 3 river sections in the study area [81].

Figure 14 illustrates the activity concentration of 226Ra over the three sections within the study area. The information reveals a recognizable pattern, with the highest activity concentration observed in the downstream sample. This suggests that various tributaries contribute varying amounts of 226Ra, influenced by the geological characteristics of the river basin. To find out the primary source of radium along this river, additional research is imperative.

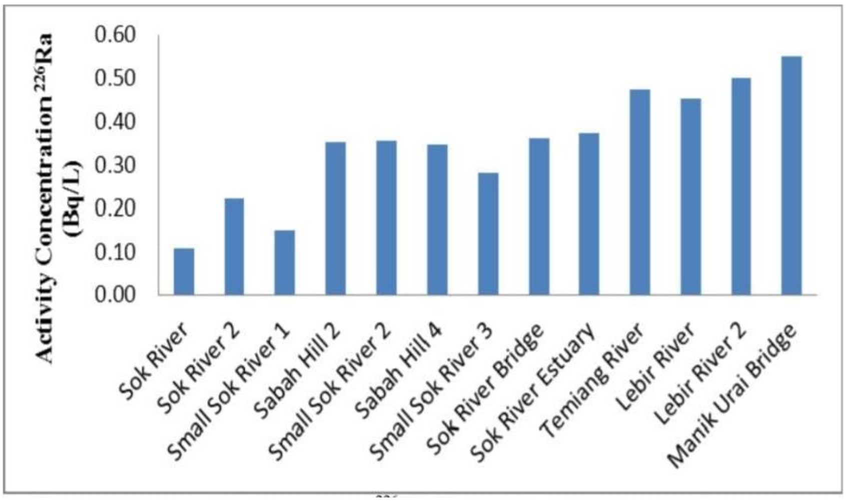

Figure 14. Activity concentration of 226Ra along 3 different sections in the study area [81].

In general, the samples show an activity concentration of 226Ra that surpasses the limit established in the INWQS. This can be attributed to the fact that the area, particularly the river basin, is situated within a granitic region that contains natural radionuclides. Among these radionuclides, 238U and 232Th play a significant role as they give rise to decay products that include 226Ra and 228Ra. However, due to its relatively short half-life, the contribution of 228Ra is considerably less significant compared to that of 226Ra. From a health risk perspective, the presence of radon and thoron, which are the decay products of radium, is of greater concern as they exist in gaseous form and can dissolve in water (**Table 5**).

Table 5. Activity concentration 222Rn and annual effective dose of 226Ra in river water from different locations in Kelantan [81].

Sample code	Ra (Bq/L)	Rn (Bq/L)	Estimated annual effective dose (mSv/year)
Lebir River			
L1	0.050 ± 0.7415	3.8911 ± 0.41	0.0964
L2	0.042 ± 0.4510	3.7540 ± 0.35	0.0922
L3	0.041 ± 0.4998	4.1577 ± 0.34	0.1022
L4	0.033 ± 0.5483	4.4326 ± 0.27	0.1121
Sok River			
S1	0.1095 ± 0.049	0.8836 ± 0.40	0.0224
S2	0.2203 ± 0.036	1.7834 ± 0.29	0.0450
S3	0.3613 ± 0.039	2.9056 ± 0.32	0.0739
S4	0.3732 ± 0.030	3.0353 ± 0.24	0.0763
Small Sok River			
T1	0.1491 ± 0.045	1.2073 ± 0.37	0.0305
T2	0.3569 ± 0.031	2.8880 ± 0.25	0.0730
T3	0.2803 ± 0.034	2.2652 ± 0.28	0.0573
T4	0.3524 ± 0.033	2.8400 ± 0.27	0.0720
T5	0.3466 ± 0.033	2.8211 ± 0.27	0.0708

When assessing the annual effective dose in the river water samples, it is expected that there will be a few contributions from naturally occurring radionuclides in the granitic area, as well as through the decay series of uranium and thorium in the soil [85].

The annual effective dose falls within the range of 0.0224–0.1531 mSv/year, as shown in **Table 1**, which is determined through the following equation: Yearly effective dose = 730 L/yr × 2.8 × 10^{-4} mSv/Bq × activity concentration of 226Ra (Bq/L).

The calculation of the annual effective dosage for water consumption by adults in this region, who depend on river water as their primary water supply, was conducted. It was determined that the annual drinking amount is 730 L/yr, assuming that an adult consumes 2 L of water per day. The dose conversion factor for 226Ra is 2.8 × 10^{-7} Sv/Bq [86]. As per the regulation set forth by the Polish Ministry of Health in 2002, the annually permissible effective dosage for all radionuclides, with the exception of tritium, must not surpass 0.010 mSv/year [86].

4. Health implications

The terrestrial environment is full of naturally occurring radioactive material, or NORM, which can be hazardous to human health [87]. Globally, the typical person receives 3.0 mSv annually. Radiation exposure from radon and thoron sources is the biggest source of dosage among all public radiation exposure sources. 42% of the annual absorbed dose globally is attributed to exposure to these radionuclides in the air and water. Upon entering the body, radionuclides are dispersed differently according to their shapes, chemical characteristics, and exposure pathways. When assessing the possible impacts of exposure, this causes variable accumulation and excretion that needs to be taken into consideration. It is significant to remember that, on average, NORM accounts for only about half of the radiation exposure that the general public experiences; the other half is attributed to man-made sources, mostly medical treatments [88].

The most concentrated dose of NORM is obtained from inhaling radon and thoron into the lungs. The decay of these radionuclides exposes the mouth, airways, and lung tissue to alpha particles directly after inhalation. Because of their incredibly short half-lives (microseconds to minutes), the decay products of radon and thoron can expose lung tissue to additional radiation in addition to the initial decay of these radionuclides in the lungs. They can even dissolve into the airway surface fluid and be absorbed into the blood stream through the lung [89]. The primary means of ingesting radionuclides is through contaminated drinking water and radionuclide-containing food. Once within the gastrointestinal tract, radionuclides can be taken up by active transport, passive diffusion, or both [90].

The largest single health effect of NORM exposure is the development and encouragement of cancer. The strongest evidence for the link between environmental exposure to NORM and cancer comes from exposure to 220Rn and 222Rn. Numerous epidemiological studies conducted on U miners and the general public indicate that there is probably a causal relationship between lung cancer and exposure to 220Rn/222Rn [91,92].

5. Conclusion

Understanding radioactivity begins with understanding its origin, whether it is primordial or cosmogenic. Radioactivity surrounds humans from each direction, and in this review, we tried to concentrate on its geological direction and how it can affect the environment and humans. Exposure to radiation can lead to many health risks by exceeding the permissible limit of radiation in the air, water, and dust. Spectrometry scientists have developed applications in which we can measure the emitted radiation emanating from rocks.

We shed light on some of the methodologies that are used to measure NORM radiation and how they work, their advantages and disadvantages, and their theories, semiconductor detectors like the high-Purity germanium detector and the thallium activated sodium iodide detector NaI(Tl), the liquid scintillation counting (LSC) technique.

Using the environmental samples matrix standard with both single-photon emitting nuclides mixed standard QCY40 containing 210Pb, 241Am, 109Cd, and 57Co, and the second QCY48 containing 241Am, 109Cd, Co57, 139Ce, 113Sn, 85Sr, 137Cs, 88Y, and 60Co, the absolute full-energy peak efficiency of high purity germanium (HPGe) detectors has been measured between (46, 54 and 1836) keV. The energy of the gamma rays, the geometry, the density, the height of the soil sample, and the detector characterization all affect efficiency.

In the first case study, the results of measuring radioactivity with a NaI(Tl) detector were compared to laboratory measurements made on geological samples using HPGe detectors. This is an important issue for analytical laboratories as it is the result of the IAEA procedure's proficiency test for all analytical determinations that are received as "acceptable" for all radionuclides. It should be mentioned that there are noticeable variations in both detector parameters' results. One possible cause of the mean mismatch between the NaI(Tl) and HPGe detectors could be an unidentified sample material.

Using a gamma ray spectrometer setup, the complete energy peak efficiencies of the NaI(Tl) detector were experimentally determined in the energy range of 1460 keV to 2614 keV. The results show that despite its poor energy resolution, a NaI(Tl) detector has a high efficiency, making it suitable for use in a variety of research applications.

In the second case study, the unusually high levels of radionuclides found in ground water in Ede and the surrounding settlements can only be attributed to geology, not to any other human activity. Therefore, it is necessary to conduct a regional radionuclide evaluation of groundwater in order to ascertain the spatial extent of these anomalous concentrations, the effects they have on local organic species, and any potential groundwater treatment plans before they are used. We also propose that comparable studies be conducted in pegmatite bedrock regions worldwide, since high activity might not be completely ruled out given that these rocks had a similar fractional crystallization sequence and focused on high concentrations of big ion lithophile elements.

In radionuclide metrology, liquid scintillation counting techniques are frequently applied for both the standardization of pure beta and an increasing number of radionuclides with more complex decay schemes. The primary benefit of LSC is its ability to quickly and simply prepare sources, which enables short-lived radionuclides to be standardized. The invention of the free parameter model allows one to use a tracer methodology, like the CIEMAT/NIST method, to determine detection efficiency. The majority of national radionuclide metrology laboratories currently employ LSC procedures, which have resulted in a growing number of radionuclides being standardized over time. While there is still need for improvement in quantitative LSC procedures, LSC standardization techniques have advanced significantly and are now widely used in radionuclide metrology.

In the third case study, the samples of river water show that the concentration of 226Ra in the samples is higher than the INTERIM National Water Quality Standards for Malaysia (0.1 Bq/L). The values for the annual effective dose of water have also surpassed the 0.01 mSv/yr international guideline value.

There are naturally occurring radioactive materials everywhere in the environment, and both the general population and radiation workers are at risk for health problems. With 220Rn and 222Rn gas accounting for 42% of the global public radiation dose, exposure to these gases in the air presents the greatest risk to public health among NORM. changes done to the environment, like resource extraction and drilling. Reducing the overall risk of cancer and limiting possible exposure require regulating the spread of NORM through human activities.

Conflict of interest: The authors declare no conflict of interest.

References

1. Martin JE. Naturally Occurring Radiation and Radioactivity. In: Physics for Radiation Protection. Wiley-VCH Verlag GmbH & Co. KGaA; 2013.
2. Isaksson M. Methods of measuring radioactivity in the environment (No. LUNFD6-NFFR--1017). Lund Univ. (Sweden). Dept. of Nuclear Physics; 1997.
3. Abedin MdJ, Khan R. NORMs distribution in the dust samples from the educational institutions of Megacity Dhaka, Bangladesh: Radiological risk assessment. Journal of Hazardous Materials Advances. 2022; 8: 100155. doi: 10.1016/j.hazadv.2022.100155
4. Abedin MdJ, Khan R. Primordial radionuclides in the dust samples from the educational institutions of central Bangladesh: radiological risk assessment. Heliyon. 2022; 8(11): e11446. doi: 10.1016/j.heliyon.2022.e11446
5. Khandaker MU, Mohd Nasir NL, Asaduzzaman K, et al. Evaluation of radionuclides transfer from soil-to-edible flora and estimation of radiological dose to the Malaysian populace. Chemosphere. 2016; 154: 528-536. doi: 10.1016/j.chemosphere.2016.03.121
6. Khandaker MU, Asaduzzaman K, Sulaiman AFB, et al. Elevated concentrations of naturally occurring radionuclides in heavy mineral-rich beach sands of Langkawi Island, Malaysia. Marine Pollution Bulletin. 2018; 127: 654-663. doi: 10.1016/j.marpolbul.2017.12.055
7. Khan R, Islam HMT, Apon MAS, et al. Environmental geochemistry of higher radioactivity in a transboundary Himalayan River sediment (Brahmaputra, Bangladesh): potential radiation exposure and health risks. Environmental Science and Pollution Research. 2022; 29(38): 57357-57375. doi: 10.1007/s11356-022-19735-5
8. Khan R, Haydar MA, Saha S, et al. (2022). Spatial distribution and radiological risk quantification of natural radioisotopes in the St. Martin's Island, Bangladesh. In: Soil Health and Environmental Sustainability: Application of geospatial technology. Cham: Springer International Publishing; pp. 369-388.
9. Habib MA, Basuki T, Miyashita S, et al. Distribution of naturally occurring radionuclides in soil around a coal-based power plant and their potential radiological risk assessment. Radiochimica Acta. 2018; 107(3): 243-259. doi: 10.1515/ract-2018-3044

10. Ionizing radiation and health effects. Available online: https://www.who.int/news-room/fact-sheets/detail/ionizing-radiation-and-health-effects (accessed on 3 April 2024).
11. Arogunjo AM, Höllriegl V, Giussani A, et al. Uranium and thorium in soils, mineral sands, water and food samples in a tin mining area in Nigeria with elevated activity. Journal of Environmental Radioactivity. 2009; 100(3): 232-240. doi: 10.1016/j.jenvrad.2008.12.004
12. Abbasi MN, Tufail M, Chaudhry MM. Assessment of heavy elements in suspended dust along the Murree Highway near capital city of Pakistan. World Applied Science Journal. 2013; 21(9): 1266-1275.
13. Kohman TP, Saito N. Radioactivity in Geology and Cosmology. Annual Review of Nuclear Science. 1954; 4(1): 401-462. doi: 10.1146/annurev.ns.04.120154.002153
14. Bastos RO, Appoloni CR, Pinese JPP, et al. Gamma Radiation Dose Rate in Air due to Terrestrial Radionuclides in Southern Brazil: Synthesis by Geological Units and Lithotypes Covered by the Serra do Mar Sul Aero-Geophysical Project. AIP Conference Proceedings. 2018; 1034(1): 403-406.
15. Bastos RO, Pascholati EM. Environmental gamma radiation in municipalities of Eastern of São Paulo State, Brazil. Terrae. 2005; 2(1-2): 37-45.
16. Dickson BL, Scott KM. Interpretation of aerial gamma-ray surveys-adding the geochemical factors. AGSO Journal of Australian Geology and Geophysics. 1997; 17.
17. Durrance EM. Radioactivity in geology: principles and applications. United States: N.; 1986.
18. Tarim UA, Gürler O. Source-to-detector distance dependence of efficiency and energy resolution of a 3"x3" NaI (Tl) detector. Avrupa Bilim ve Teknoloji Dergisi. 2018; (13): 103-107. doi: 10.31590/ejosat.443565
19. Sharma RK. Various spectroscopic techniques. Environmental Pollution: Monitoring Modelling and Control. Studium Press; 2017. pp. 181-206.
20. Vargas MJ, Timón AF, Díaz NC, Sánchez DP. Influence of the geometrical characteristics of an HpGe detector on its efficiency. Journal of Radioanalytical and Nuclear Chemistry. 2002; 253.
21. Alnour IA, Wagiran H, Ibrahim N, et al. New approach for calibration the efficiency of HpGe detectors. AIP conference proceedings. 2014; 1584(1): 38-44.
22. Knoll GF. Radiation detection and measurement. John Wiley & Sons; 2010.
23. Ngaram S, Baffa A, And I, Yunusa M. Determination of natural radionuclide using HPGe detectors. Journal of Environment, Technology & Sustainable Agriculture. 2017; 1: 14-22.
24. Guo Y, Wang Q, Kawazoe Y, et al. A New Silicon Phase with Direct Band Gap and Novel Optoelectronic Properties. Scientific Reports. 2015; 5(1). doi: 10.1038/srep14342
25. Leadbeater T. Lecture Notes on Particle Detectors. Birmingham: Physics and Astronomy. University of Birmingham; 2015.
26. Arif K, Malik AH. Monte Carlo EGS5 simulationsof High Purity Germanium (HPGe) detector. In: Proceedings of the 2015 Power Generation System and Renewable Energy Technologies (PGSRET). pp. 1-3.
27. High Purity Germanium Detectors—HPGe. Available online: https://www.nuclear-power.com/nuclear-engineering/radiation-detection/semiconductor-detectors/high-purity-germanium-detectors-hpge/ (accessed on 3 April 2024).
28. Saegusa J, Kawasaki K, Mihara A, et al. Determination of detection efficiency curves of HPGe detectors on radioactivity measurement of volume samples. Applied Radiation and Isotopes. 2004; 61(6): 1383-1390. doi: 10.1016/j.apradiso.2004.04.004
29. Vargas MJ, Timón AF, Dıaz NC, Sánchez DP. Monte Carlo simulation of the self-absorption corrections for natural samples in gamma-ray spectrometry. Applied Radiation and Isotopes. 2002; 57(6): 893-898.
30. Vargas MJ, Díaz NC, Sánchez DP. Efficiency transfer in the calibration of a coaxial p-type HpGe detector using the Monte Carlo method. Applied Radiation and Isotopes. 2003; 58(6): 707-712.
31. Vidmar T, Korun M, Likar A, Martinčič R. A semi-empirical model of the efficiency curve for extended sources in gamma-ray spectrometry. Nuclear Instruments and Methods in Physics Research Section A: Accelerators, Spectrometers, Detectors and Associated Equipment. 2001; 470(3): 533-547.
32. Al-Masri MS, Aba A, Al-Hamwi A, et al. Preparation of in-house reference soil sample containing high levels of naturally occurring radioactive materials from the oil industry. Applied Radiation and Isotopes. 2004; 61(6): 1397-1402. doi: 10.1016/j.apradiso.2004.04.007
33. Melquiades FL, Appoloni CR. Self-absorption correction for gamma spectrometry of powdered milk samples using Marinelli beaker. Applied Radiation and Isotopes. 2001; 55(5): 697-700.

34. San Miguel EG, Pérez-Moreno JP, Bolívar JP, et al. 210Pb determination by gamma spectrometry in voluminal samples (cylindrical geometry). Nuclear Instruments and Methods in Physics Research Section A: Accelerators, Spectrometers, Detectors and Associated Equipment. 2002; 493(1-2): 111-120.
35. Abbas MI, Selim YS. Calculation of relative full-energy peak efficiencies of well-type detectors. Nuclear Instruments and Methods in Physics Research Section A: Accelerators, Spectrometers, Detectors and Associated Equipment. 2002; 480(2-3): 651-657.
36. Harb S, Salahel Din K, Abbady A. Study of efficiency calibrations of HPGe detectors for radioactivity measurements of environmental samples. In: Proceedings of the 3rd Environmental Physics Conference; 19-23 February 2008; Aswan, Egypt.
37. Akkurt I, Gunoglu K, Arda SS. Detection Efficiency of NaI(Tl) Detector in 511–1332 keV Energy Range. Science and Technology of Nuclear Installations. 2014; 2014: 1-5. doi: 10.1155/2014/186798
38. El-Gamal H, Negm H, Hasabelnaby M. Detection efficiency of NaI (Tl) detector based on the fabricated calibration of HPGe detector. Journal of Radiation Research and Applied Sciences. 2019; 12(1): 360-366. doi: 10.1080/16878507.2019.1672313
39. Rathore V, Senis L, Andersson Sundén E, et al. Geometrical optimisation of a segmented HPGe detector for spectroscopic gamma emission tomography—A simulation study. Nuclear Instruments and Methods in Physics Research Section A: Accelerators, Spectrometers, Detectors and Associated Equipment. 2021; 998: 165164. doi: 10.1016/j.nima.2021.165164
40. Ahmadi S, Ashrafi S, Yazdansetad F, et al. A computational modelling of low-energy gamma ray detection efficiency of a cylindrical NaI(Tl) detector. Radiation Physics and Chemistry. 2021; 188: 109581. doi: 10.1016/j.radphyschem.2021.109581
41. Tsoulfanidis N. Nuclear Fission Reactors. Nuclear Technology. 1983; 63(1): 187-187. doi: 10.13182/nt83-a33318
42. Böhlen TT, Cerutti F, Chin MPW, et al. The FLUKA Code: Developments and Challenges for High Energy and Medical Applications. Nuclear Data Sheets. 2014; 120: 211-214. doi: 10.1016/j.nds.2014.07.049
43. Ferrari A, Sala PR, Fasso A, Ranft J. FLUKA: A Multi-particle Transport Code. Stanford Linear Accelerator Center, Stanford University; 2005.
44. Tekin HO. MCNP-X Monte Carlo Code Application for Mass Attenuation Coefficients of Concrete at Different Energies by Modeling 3 × 3 Inch NaI(Tl) Detector and Comparison with XCOM and Monte Carlo Data. Science and Technology of Nuclear Installations. 2016; 2016: 1-7. doi: 10.1155/2016/6547318
45. Akkurt İ, Tekin HO, Mesbahi A. Calculation of Detection Efficiency for the Gamma Detector using MCNPX. Acta Physica Polonica A. 2015; 128(2B): B-332-B-335. doi: 10.12693/aphyspola.128.b-332
46. Salgado CM, Brandão LEB, Schirru R, et al. Validation of a NaI(Tl) detector's model developed with MCNP-X code. Progress in Nuclear Energy. 2012; 59: 19-25. doi: 10.1016/j.pnucene.2012.03.006
47. Mouhti I, Elanique A, Messous MY, et al. Validation of a NaI(Tl) and LaBr3(Ce) detector's models via measurements and Monte Carlo simulations. Journal of Radiation Research and Applied Sciences. 2018; 11(4): 335-339. doi: 10.1016/j.jrras.2018.06.003
48. Akkurt İ, Waheed F, Akyildirim H, et al. Performance of NaI(Tl) detector for gamma-ray spectroscopy. Indian Journal of Physics. 2021; 96(10): 2941-2947. doi: 10.1007/s12648-021-02210-1
49. Tekin HO, ALMisned G, Issa SAM, et al. Calculation of NaI(Tl) detector efficiency using 226Ra, 232Th, and 40K radioisotopes: Three-phase Monte Carlo simulation study. Open Chemistry. 2022; 20(1): 541-549. doi: 10.1515/chem-2022-0169
50. Hendriks PHGM, Limburg J, De Meijer RJ. Full-spectrum analysis of natural γ-ray spectra. Journal of Environmental Radioactivity. 2001; 53(3): 365-380.
51. Løvborg L, Christiansen EM, Bøtter-Jensen L, Kirkegaard, P. Pad facility for the calibration of gamma-ray measurements on rocks (No. RISO-R—454). Risoe National Lab.; 1981.
52. Agency IE. The radiological accident in San Salvador: A Report. International Atomic Energy Agency; 1990.
53. Biere PE, Aina JO, Olaoye MO, et al. Calibration of a 5 × 5 NaI(Tl) for Prompt In-Situ Gamma-ray Spectrometry System. Materials and Geoenvironment. 2021; 68(1): 1-5. doi: 10.2478/rmzmag-2021-0001
54. Boson J. Improving accuracy of in situ gamma-ray spectrometry [PhD thesis]. Radiation Physics Umeå University; 2008.
55. Beck HL, Gogolak C, DeCampo J. In situ Ge (Li) and NaI (T1) gamma-ray spectrometry (No. HASL-258). United States Atomic Energy Commision, New York, NY (United States). Health and Safety Lab.; 1972.
56. Kallmann H. Scintillation Counting with Solutions. Physical Review. 1950; 78(5): 621-622. doi: 10.1103/physrev.78.621.2
57. Reynolds GT, Harrison FB, Salvini G. Liquid Scintillation Counters. Physical Review. 1950; 78(4): 488-488. doi: 10.1103/physrev.78.488

58. Pochwalski K, Radoszewski T. Disintegration rate determination by liquid scintillation counting using the triple to double coincidence ratio (TDCR) method. Institute of Nuclear Research, Warsaw, INR; 1848.
59. Malonda AG, Garcia-Toraño E. Evaluation of counting efficiency in liquid scintillation counting of pure β-ray emitters. The International Journal of Applied Radiation and Isotopes. 1982; 33(4): 249-253.
60. Introduction Liquid Scintillation—mn/safe/nukwik. Available online: https://wiki.uio.no/mn/safe/nukwik/index.php/Introduction_Liquid_Scintillation (accessed on 3 April 2024).
61. Broda R, Cassette P, Kossert K. Radionuclide metrology using liquid scintillation counting. Metrologia. 2007; 44(4): S36-S52. doi: 10.1088/0026-1394/44/4/s06
62. Peng CT, Li U. Analysis of solvent components in commercial liquid scintillation cocktails. LSC. 1992; 92: 157.
63. Hung NQ, Chuong HD, Vuong LQ, et al. Intercomparison NaI(Tl) and HPGe spectrometry to studies of natural radioactivity on geological samples. Journal of Environmental Radioactivity. 2016; 164: 197-201. doi: 10.1016/j.jenvrad.2016.07.035
64. Osprey® Universal Digital MCA Tube Base for Scintillation Spectrometry. Available online: https://www.mirion.com/products/technologies/spectroscopy-scientific-analysis/gamma-spectroscopy/detector-electronics/osprey-universal-digital-mca-tube-base-for-scintillation-spectrometry (accessed on 3 April 2024).
65. Lépy MC. Presentation of the COLEGRAM software. Note Technique LHNB/04/26. 2004. Available online: http://www.lnhb.fr/pdf/NT_04-26_Colegram.pdf (accessed on 12 January 2024).
66. IAEA. certification of IAEA gamma spectrometry reference materials, RGU-1, RGTh-1 and RGK-1, Report-IAEA/RL/148. International Atomic Energy Agency; 1987.
67. Gilmore G. Practical gamma-ray spectroscopy. John Wiley & Sons; 2008.
68. Lépy MC, Ferreux L, Hamon C, Plagnard J. ACORES yield curve adjustment software. Technical note LNHB. Available online: http://www.lnhb.fr/en/
69. GUM: Guide to the Expression of Uncertainty in Measurement—Evaluation of measurement data. Available online: https://www.bipm.org/documents/20126/2071204/JCGM_100_2008_E.pdf/cb0ef43f-baa5-11cf-3f85-4dcd86f77bd6 (accessed on 12 January 2024).
70. Shakhashiro A, Mabit L. Results of an IAEA inter-comparison exercise to assess 137Cs and total 210Pb analytical performance in soil. Applied Radiation and Isotopes. 2009; 67(1): 139-146. doi: 10.1016/j.apradiso.2008.07.014
71. Adetunji A, Olorunfemi AO, Abe O, et al. Anomalous concentrations of radionuclides in the groundwater of Ede area, southwestern Nigeria: a direct impact of geology. Environmental Earth Sciences. 2018; 77(17). doi: 10.1007/s12665-018-7799-2
72. Lydie RM, Nemba RM. Quantitative determination of 226Ra and 228Ra in reservoir and tap water in Yaoundé area, Cameroon. Glob. J. envir. Res. 2008; 2(3): 110-113.
73. Jibiri NN, Mbawanku AO, Oridata AA, Ujiagbedion C. Natural radionuclide concentration levels in soil and water around cement factory. Ewekoro, Ogun state. Nigeria Journal of physics. 1999; 11: 12-16.
74. Ajayi IR, Ajayi OS, Fusuyi AS. The natural radioactivity of surface soils in Ijero-Ekiti, Nigeria. Nig. J. Phys. 1995; 7: 101-103.
75. Farai IP, Sanni AO. Year-long variability of Rn-222 in a groundwater system in Nigeria. Journal of African Earth Sciences (and the Middle East). 1992; 15(3-4): 399-403.
76. Ahmed NK. Natural Radioactivity of Ground and Drinking Water in Some Areas of Upper Egypt. Turkish Journal of Engineering & Environmental Sciences. 2004; 28(6).
77. Nasirian M, Bahari I, Abdullah P. Assessment of natural radioactivity in water and sediment from Amang (tin tailing) processing ponds. Malays J Anal Sci. 2008; 12(1): 150-159.
78. Lydie RM, Nemba RM. The annual effective dose due to natural radionuclides in the reservoir and tap water in Yaoundé area, Cameroon. The South Pacific Journal of Natural and Applied Sciences. 2009; 27(1): 61. doi: 10.1071/sp09011
79. Ajayi OS, Adesida G. Radioactivity in some sachet drinking water samples produced in Nigeria. Iran. J. Radiat. Res. 2009; 7(3): 151-158.
80. Nwankwo LI. Study of natural radioactivity of groundwater in Sango-Ilorin, Nigeria. Journal of Physical Science and Application 2012; 2(8): 289.
81. Rahman SAA. Measurement of 226Ra in river water using liquid scintillation counting technique. Journal of Nuclear and Related Technologies. 2010; 7(02): 12-23.
82. de Oliveira J, Mazzilli BP, de Oliveira Sampa MH, Bambalas E. Natural radionuclides in drinking water supplies of Sao

Paulo State, Brazil and consequent population doses. Journal of Environmental Radioactivity. 2001; 53(1): 99-109.

83. Borai EH, Lasheen YF, El-Sofany EA, et al. Separation and subsequent determination of low radioactivity levels of radium by extraction scintillation. Journal of Hazardous Materials. 2008; 156(1-3): 123-128. doi: 10.1016/j.jhazmat.2007.12.004
84. Kim YJ, Kim CK, Lee JI. Simultaneous determination of 226Ra and 210Pb in groundwater and soil samples by using the liquid scintillation counter-suspension gel method. Applied Radiation and Isotopes. 2001; 54(2): 275-281.
85. Lasheen YF, Seliman AF, Abdel-Rassoul AA. Simultaneous measurement of 226Ra and 228Ra in natural water by liquid scintillation counting. Journal of Environmental Radioactivity. 2007; 95(2-3): 86-97. doi: 10.1016/j.jenvrad.2007.02.002
86. Kozłowska B, Walencik A, Dorda J, et al. Uranium, radium and 40K isotopes in bottled mineral waters from Outer Carpathians, Poland. Radiation Measurements. 2007; 42(8): 1380-1386. doi: 10.1016/j.radmeas.2007.03.004
87. May D, Schultz MK. Sources and Health Impacts of Chronic Exposure to Naturally Occurring Radioactive Material of Geologic Origins. Practical Applications of Medical Geology. 2021; 403-428.
88. NCRP. Ionizing radiation exposure of the population of the United States. NCRP; 2006.
89. Marsh JW, Bailey MR. A review of lung-to-blood absorption rates for radon progeny. Radiation Protection Dosimetry. 2013; 157(4): 499-514. doi: 10.1093/rpd/nct179
90. Taylor D, Bligh P, Duggan M. The absorption of calcium, strontium, barium and radium from the gastrointestinal tract of the rat. Biochemical Journal. 1962; 83(1): 25-29. doi: 10.1042/bj0830025
91. Lubin JH, Boice JD, Edling C, et al. Lung Cancer in Radon-Exposed Miners and Estimation of Risk from Indoor Exposure. JNCI Journal of the National Cancer Institute. 1995; 87(11): 817-827. doi: 10.1093/jnci/87.11.817
92. Field RW, Steck DJ, Smith BJ, et al. Residential Radon Gas Exposure and Lung Cancer: The Iowa Radon Lung Cancer Study. American Journal of Epidemiology. 2000; 151(11): 1091-1102. doi: 10.1093/oxfordjournals.aje.a010153